Lecture Notes in Physics 833

Henk N. W. Lekkerkerker
Remco Tuinier

Colloids and the Depletion Interaction

Springer

Lecture Notes in Physics

Volume 833

For further volumes:
http://www.springer.com/series/5304

The Lecture Notes in Physics

The series Lecture Notes in Physics (LNP), founded in 1969, reports new developments in physics research and teaching—quickly and informally, but with a high quality and the explicit aim to summarize and communicate current knowledge in an accessible way. Books published in this series are conceived as bridging material between advanced graduate textbooks and the forefront of research and to serve three purposes:

- to be a compact and modern up-to-date source of reference on a well-defined topic
- to serve as an accessible introduction to the field to postgraduate students and nonspecialist researchers from related areas
- to be a source of advanced teaching material for specialized seminars, courses and schools

Both monographs and multi-author volumes will be considered for publication. Edited volumes should, however, consist of a very limited number of contributions only. Proceedings will not be considered for LNP.

Volumes published in LNP are disseminated both in print and in electronic formats, the electronic archive being available at springerlink.com. The series content is indexed, abstracted and referenced by many abstracting and information services, bibliographic networks, subscription agencies, library networks, and consortia.

Proposals should be sent to a member of the Editorial Board, or directly to the managing editor at Springer:

Christian Caron
Springer Heidelberg
Physics Editorial Department I
Tiergartenstrasse 17
69121 Heidelberg/Germany
christian.caron@springer.com

Henk N. W. Lekkerkerker
Remco Tuinier

Colloids and the Depletion Interaction

Springer

Henk N. W. Lekkerkerker
Van 't Hoff Laboratory
Utrecht University
Padualaan 8
3584 CH Utrecht
The Netherlands
e-mail: h.n.w.lekkerkerker@uu.nl

Remco Tuinier
Colloids & Interfaces Group, Advanced Chemical Engineering Solutions
DSM Research
Urmonderbaan 22
6167 RD Geleen
The Netherlands
e-mail: remco.tuinier@dsm.com

ISSN 0075-8450 e-ISSN 1616-6361

ISBN 978-94-007-1222-5 e-ISBN 978-94-007-1223-2

DOI 10.1007/978-94-007-1223-2

Springer Dordrecht Heidelberg London New York

Comments and/or corrections are welcome at depletionbook@gmail.com

New graphic art was prepared by Mieke Kröner, Henk Lekkerkerker and Remco Tuinier

Cover design: eStudio Calamar, Berlin/Figueres

Printed on acid-free paper

Springer is part of Springer Science+Business Media (www.springer.com)

Preface

The physical properties of colloidal suspensions are strongly affected by the forces that act between the colloidal particles. Attempts to explain them in these terms go back to the beginning of the 20th century. Important and extensively studied forces in colloidal systems are Van der Waals forces, electrostatic forces, steric forces due to attached polymers and magnetic forces. In the last decades it has been observed that the stability of colloidal particles is also affected by non-adsorbing polymers in solution. The origin of this interaction was first explained successfully in 1954 by S. Asakura and F. Oosawa using the concept that the free volume available to non-adsorbing polymers increases whenever two hard particles approach sufficiently close such that their depletion zones overlap and the total depletion zone decreases.

However, a number of important applications were used in technology and medicine (long) before the depletion concept was introduced. For example, clustering of red blood cells due to serum proteins was already detected at the end of the 18th century and forms the basis of the blood sedimentation test still in use. Furthermore, creaming of colloidal particles to concentrate latex dispersions upon the addition of polysaccharides was first studied in the 1920s. Polysaccharides were also used in the isolation of plant viruses, starting in the 1940s. Systematic and fundamental investigations on the effect of depletion interactions in colloidal systems started with the work of B. Vincent in the UK, S. Hachisu in Japan, and A. Vrij in The Netherlands in the 1970s. Work on depletion interaction gained momentum after W.R. Russel and co-workers in the US clarified the relationship between the range and depth of the depletion interaction and the topology of the phase diagram in the 1980s. Since then the depletion field evolved rapidly.

This book aims at providing a self-contained treatment of the depletion interaction and the resulting phase behaviour in colloidal dispersions. It is hoped that the book may be equally useful to senior undergraduate students or beginning graduate students in physical chemistry, chemical and mechanical engineering, biophysicists or soft condensed matter physics. At the same time we hope that professional chemists and engineers dealing with colloidal suspensions may find it

a useful reference book to gain an understanding about the implications of the depletion interaction for the handling of suspensions.

In order to keep the size of the book within bounds a description of the interface between demixed phases has not been included and the discussion of phase transition kinetics is rather brief. Also we emphasize that the references quoted do not claim to be a complete list. If the reader prefers it, (s)he can read the book at three levels. For a general idea of depletion interactions and their implications not only in colloid science but also in systems of biological and technological interest it is recommended to study Chap. 1. At the second level one can study 2.1, 2.2, Chap. 3, 4.1, 4.2, 4.5 and 6.1–6.3, 6.5. This material could be used for 6–8 hour senior undergraduate or junior graduate course in physical chemistry or soft matter physics. The third level covers the complete text of this monograph.

Many people have stimulated us to write this book. Initially, we had hoped to write it with Dirk Aarts. His enthusiasm for the book project helped us greatly during the early stages but he was unable to reserve enough time for the book after his start in Oxford. We are indebted to him, to Jeroen van Duijneveldt and Gerard Fleer for commenting in detail on drafts of several chapters of the manuscript. It might well be that remaining errors and unclarities can be traced back to where we foolishly disagreed with them.

We were fortunate to have the meticulous help in the preparation of texts and figures of the manuscript by Mieke Kröner, while the illustrations benefited from the advice of Jeannette Kröner.

R.T. wishes to thank Jan Dhont and his Soft Matter group at the IFF of research center Jülich for their support during the initial stages leading to this book. The members of the Colloids & Interfaces group at DSM Research, Leon Bremer, Harm Langermans, Leo Vleugels, Benjamin Voogt, Jef Bisscheroux, and Feng Li, are acknowledged for the pleasant and stimulating interactions. Peter Jansens and Jeroen Kluytmans of DSM Research are thanked for supporting R.T. to finish the book. Collaborations with Martien Cohen Stuart, Tai-Hsi Fan, Kees de Kruif, Peter Schurtenberger, Takashi Taniguchi, and Agienus Vrij contributed to the evolution of this book.

H.N.W.L. wishes to thank the staff members and his PhD students and Postdocs at the Van 't Hoff laboratory with whom he had the privilege to work. He benefited from a long-term collaboration with Marc Baus, Louise Bailey, Mike Cates, Bob Evans, Seth Fraden, Daan Frenkel, Jean-Pierre Hansen, Joseph Indekeu, Geoff Maitland, Theo Odijk, Roberto Piazza, Wilson Poon, Peter Pusey, Bill Russel, Patrick Warren and Ben Widom. H.N.W.L. would like to thank the Royal Netherlands Academy of Arts and Sciences for the appointment as Academy Professor for the period 2006–2011, which made it possible to write this book.

Finally, we express our appreciation for the encouragement and pleasant cooperation with Maria Bellantone, Mieke van der Fluit and Liesbeth Mol of Springer Science + Business Media.

Geleen / Utrecht, April 2011

Remco Tuinier
Henk N. W. Lekkerkerker

Contents

List of Symbols

We refer to the section where the symbol was first used. An asterisk (*) refers to the fact that this symbol is only used in a single Chapter.

α	Free volume fraction (Sect. 3.3)
α_p	Static polarizability (Sect. 1.2)
β	Scaling factor in the concentration dependence of the depletion thickness (Sect. 4.3)
χ	Partition coefficient of polymers between a slit and the bulk (Sect. 2.2)
δ	Depletion layer thickness (Sect. 1.3)
ε	Minimum of the Lennard-Jones potential (Sect. 4.5)*
ε_0	Dielectric constant in vacuum (Sect. 1.2)
ε_r	Relative dielectric constant (Sect. 1.2)
ϕ	Colloid volume fraction (Sect. 2.3)
ϕ	Azimuthal angle (Sect. 5.3)*
ϕ_{cp}	Volume fraction at close packing (Sect. 3.2)
ϕ_d	Relative depletant concentration (Sect. 3.3)
ϕ_m	Melting volume fraction (Sect. 4.4)
ϕ_p	Relative polymer concentration (Sect. 1.2)
φ	Volume fraction of polymer segments (Sect. 1.2)
φ^*	Volume fraction of polymer segments at overlap (Sect. 1.2)
Γ	Adsorbed amount (Sect. 2.1)
γ	Aspect ratio $L/D + 1$ (Sect. 5.3)
γ	Angle between rods (Sect. 6.1)*
γ	Scaling exponent for the characteristic polymer size (Sect. 4.3)*
γ	Interfacial tension (Sect. 1.3)*
κ	Variational parameter in trial functions $f(\theta)$ (Sect. 6.1)
Λ	De Broglie wavelength (Sect. 3.2)
Λ	Characteristic length scale (Sect. 4.5)*
λ	Relative interparticle distance $(h - \sigma)/\sigma$ (Sect. 2.3)*

λ	Scaling parameter for the size of a particle (Sect. 3.3)
λ	Lagrange multiplier (Sect. 6.1)*
λ_m	Wavelength in a medium (Sect. 2.6)*
λ_B	Bjerrum length (Sect. 1.2)*
λ_D	Debye screening length (Sect. 1.2)
μ	Chemical potential (Sect. 2.1)
μ^{ex}	Excess chemical potential (Sect. 6.1)
$\tilde{\mu}$	Dimensionless chemical potential μ/kT (Sect. 3.2)
$\bar{\mu}$	Dipole moment (Sect. 1.2)
v	Overlap volume (Sect. 2.3)*
ν	Scaling exponent for the characteristic polymer size (Sect. 4.3)*
ν	Scaling parameter for the size of a rod (Sect. 5.3)
θ	Polar angle (Sect. 2.1)
θ_s	Scattering angle (Sect. 2.6)
ρ	Density (Sect. 1.2)
ρ	Packing parameter (Sect. 6.1)*
ϱ	Penetration depth of an evanescent wave (Sect. 2.6)*
σ	Diameter of a penetrable hard sphere (Sect. 2.1)
σ	Standard deviation (Sect. 4.4)*
$\sigma_{\max}$	Maximum standard deviation (Sect. 4.4)*
σ	Orientational parameter (Sect. 6.1)*
σ_a	Diameter of an atom (Sect. 1.2)*
σ_b	Brush anchor density (Sect. 1.2)*
σ_c	Surface charge density (Sect. 1.2)*
τ_B	Brownian time scale (Sect. 4.5)*
Ω	Grand potential (Sect. 3.3)
$\overline{\Omega}$	Approximate grand potential (Appendix)*
$\widetilde{\Omega}$	Normalised grand potential $\Omega v_0 /kTV$ (Sect. 3.3)
Ω	Solid angle (Sect. 5.3)
Ξ	Grand canonical partition function (Appendix)*
ξ	Correlation length (Sect. 4.3)
ψ_0	Surface potential (Sect. 1.2)*
ζ	Constant in combination rule for depletion thickness (Sect. 4.3)*
l	Characteristic length scale of depletion agent (Sect. 2.5)*
A	Hamaker constant (Sect. 1.2)*
A	Area (Sect. 2.2)
A_i	ith osmotic virial coefficient between polymer chains (Sect. 4.3)
a	Parameter in expression for α (Sect. 3.3)
B	Amplitude of the double layer repulsion (Sect. 1.2)
B_i	*i*th osmotic virial coefficient between colloids (Sect. 1.3)
b	Parameter in expression for α (Sect. 3.3)
b	Segment length (Sect. 2.2)
b	Excluded volume between two rods (Sect. 6.1)*
C	Coefficient in the dispersion attraction (Sect. 1.2)*
C_i	Curvature terms for the depletion thickness (Sect. 4.3)*

c	Concentration (Sect. 2.2)
c	Parameter in expression for α (Sect. 3.3)
D	Rod/platelet diameter (Sect. 2.4 and Sect. 2.5)
D_s	Self-diffusion coefficient (Sect. 4.5)*
d	Charge separation length scale (Sect. 1.2)*
d	Scaling exponent describing the scattering of aggregates (Sect. 4.5)*
d_f	Fractal dimensions describing the internal structure of aggregates (Sect. 4.5)*
E_i	Internal electric field (Sect. 1.2)*
E_e	External electric field (Sect. 1.2)*
$\overline{E}$	Electronic excitation energy (Sect. 1.2)*
e	The elementary charge (Sect. 1.2)
F	Helmholtz free energy (Sect. 2.1)
$\widetilde{F}$	Dimensionless Helmholtz free energy Fv_0/kTV (Sect. 3.3)
$\widetilde{f}$	Scattering scaling function (Sect. 4.5)*
f	Function for the distance dependence (Sect. 2.2)
$f(\theta)$	Orientational distribution function (Sect. 6.1)*
H	Distance between spherical surfaces (Sect. 2.1)
I	Ionic strength (Sect. 1.2)
I	Scattered intensity (Sect. 2.6)
h	Closest distance between the surfaces of two particles (Sect. 1.2)
K	Force between plates per unit area (Sect. 2.1)
K_s	Force between two spheres (Sect. 2.1)
K_{sp}	Force between a sphere and a flat plate (Sect. 2.1)
k	Boltzmann's constant (Sect. 3.1)
L	Rod length (Sect. 2.4)
L	Thickness of a platelet (Sect. 2.5)*
l_{sed}	Sedimentation length (Sect. 1.2)*
M	Number of monomers (Sect. 1.2)
M_{x}	Molar mass of polymer 'x' (Sect. 1.2)
N	Number of particles (Sect. 2.1)
$\widetilde{N}$	Normalisation constant (Sect. 6.1)
N_{av}	Avogadro's number (Sect. 1.2)
n	Number density (Sect. 1.2)
n_b	Bulk number density (Sect. 2.1)
n_d	Number density of depletants (Sect. 3.3)
n_i	Number density between plates (Sect. 2.2)
n_o	Contact number density outside plates (Sect. 2.3)
n_s	Salt number density (Sect. 1.2)
P	Pressure (Sect. 1.2)
P	Form factor (Sect. 2.6)*
$\widetilde{P}$	Dimensionless pressure Pv/kT (Sect. 3.2)
P_i	Osmotic pressure inside plates (Sect. 2.1)
P_o	Osmotic pressure outside plates (Sect. 2.1)
p	Probability (Sect. 1.4)

p_c	Number of elementary charges e on a surface area $2\pi\lambda_D\lambda_B$ (Sect. 1.2)
q	Size ratio of depletant over colloid size (Sect. 1.2)
q_e	Number of charges (Sect. 1.2)*
Q	Canonical partition function ((Appendix)*)
Q	Scattering wave vector (Sect. 2.6)
Q_m	Scattering wave vector where the scattering intensity I passes through a maximum (Sect. 4.5)
R	Radius of a sphere (Sect. 1.2)
R_d	Effective depletion radius hard-sphere radius (Sect. 2.1)
R_{eff}	Effective hard-sphere radius (Sect. 4.1)
$\sqrt{\langle \mathbf{R}^2 \rangle}$	End-to-end distance (Sect. 2.2)
$\langle \cdots \rangle$	Ensemble-averaged value of ... (Sect. 2.2)
R_g	Radius of gyration of a polymer chain (Sect. 1.2)
r	Center-to-center distance between two spheres (Sect. 2.1)
S	Nematic order parameter (Sect. 6.1)*
S	Structure factor (Sect. 2.6)
U_c	Interaction energy between colloids ((Appendix)*)
U_{cd}	Interaction between colloids and depletants ((Appendix)*)
V	Volume (Sect. 2.2)
V_{ov}	Overlap volume between depletion layers (Sect. 1.2)
$\langle V_{\text{free}} \rangle$	Ensemble-averaged free volume for the depletants (Sect. 3.3)
$\langle V_{\text{free}} \rangle_0$	Undistorted ensemble-averaged free volume (Sect. 3.3)
$\mathbf{v}$	Excluded volume of a polymer segment (Sect. 4.3)
v_d	Volume of a depletant (Sect. 3.3)
v_{excl}	Excluded volume (Sect. 5.3)
v_{o}	Hard sphere volume (Sect. 1.3)
v_p	Polymer coil volume (Sect. 1.2)
v_R	Volume of a rod (Sect. 6.1)
v_{rod}	Volume of a spherocylinder (Sect. 5.3)
v_s	Volume of a monomer (segment) (Sect. 1.2)
v^*	Free volume (Sect. 3.2)
W	Interaction potential (Sect. 1.2)
W	Particle insertion work (Sect. 3.3)
x	Distance from the surface (Sect. 2.2)
x^R	Property x in the reservoir (Sect. 3.1)
y	$\phi/(1-\phi)$ (Sect. 6.2)
Z	Number of ideal chains (Sect. 2.2)
z	Normalised distance from the surface (Sect. 2.1)

Chapter 1
Introduction

1.1 Colloids

In this book colloids are a central theme. We therefore first define what colloids are. According to IUPAC [1] the term colloidal refers to a state of subdivision, implying that the molecules or polymolecular particles dispersed in a medium have at least in one direction a dimension roughly between 1 nm and 1 μm, or that in a system discontinuities are found at distances of that order'. This means that colloidal particles are supramolecular submicron sized substances dispersed in a medium that can be a liquid or a gas, see [2–6]. Supramolecular implies that colloids are much bigger than 'normal' molecules (though they may be comparable in size to macromolecules). The lower length scale for a colloidal particle is close to a nm. The medium of low molecular mass substances in a colloidal suspension can often be regarded as 'background' with respect to the colloidal size range, then this medium may be approximated as a continuum.

From a physics point of view colloidal particles are characterized by observable Brownian motion, originating from a thermal energy of order of kT for each colloidal particle. Particles in a solvent are considered to be Brownian if sedimentation can be neglected with respect to thermal motion. This means that the sedimentation length, the ratio of thermal energy and gravity force,

$$l_{sed} = \frac{kT}{m^* g}, \tag{1.1}$$

should be larger than the colloid radius. Here the buoyant mass m^* equals $(4\pi/3)\Delta\rho R^3$ for a spherical colloid with radius R, where $\Delta\rho$ is the density difference between particle and solvent. Hence the upper colloidal size corresponds to the condition where $l_{sed} \approx R$. For $\Delta\rho$ = 100 kg/m^3 this implies an upper diameter of about 2 μm at 300 K.

Perrin [7] studied dispersed resin colloids and detected Brownian motion as visible manifestation of thermal motion, verifying Einstein's theoretical results [8].

H. N. W. Lekkerkerker and R. Tuinier, *Colloids and the Depletion Interaction*,
Lecture Notes in Physics, 833, DOI: 10.1007/978-94-007-1223-2_1,

The height distribution of the resin colloids in the field of gravity was shown to obey Boltzmann's law for the sedimentation equilibrium. The picture emerged that colloids behave as big atoms in many respects. Later, Onsager [9, 10] and McMillan and Mayer [11] laid down a statistical mechanics foundation for the colloid/atom analogy. They pointed out that the degrees of freedom of the solvent molecules in a colloidal dispersion can be eliminated, implying that the solvent can be considered as 'background'. The resulting description involves only colloidal particles interacting through an *effective* potential, the potential of mean force, that accounts for the presence of the solvent.

Often the interactions between small spherical atoms and some (rotationally-averaged) molecules similarly depend on the relative interparticle separation; the Lennard–Jones interaction [12] reasonably describes their pair interaction (see [13] for an in-depth critical discussion) for quite a number of substances. For these systems the phase diagrams scaled by the critical values of temperature, pressure and molar volume appear similar as well. The fact that the thermodynamic properties of all simple gases exhibit basic similarities is expressed by the law of corresponding states of Van der Waals. A statistical mechanical derivation of this law was provided by Pitzer [14].

Just as the pressure of an atomic gas is affected by the interaction between the atoms, the physical properties of a colloidal dispersion depend on the potential of mean force between colloidal particles. An extended law of corresponding states has been conjectured [15] stating that knowledge of the potential of mean force between spherical colloidal particles enables to predict the phase diagram (topology). Hence, one may therefore expect similarities between the phase diagrams of atomic and colloidal systems.

Apart from such similarities, there are also distinct differences between atoms and colloidal particles. In contrast to pair interactions between atoms, interactions between colloidal particles can be tuned by choosing particle type, temperature, solvent, by supplementing additives such as electrolytes, polymers or colloidal particles, or by modifying the particle surface. Since the 1970s it gradually became clear that adding small particles or polymers that do not adsorb onto the colloids opens up a wide variety of possibilities to tune the phase behaviour of colloidal dispersions. The interactions mediated by such non-adsorbing species and the resulting phase behaviour are at the core of this book.

Colloidal dispersions can be found in a wide range of environments and products. Industrial examples include emulsions (mayonnaise), foams (shaving cream), surfactant solutions (shampoo) or polymer latex dispersions (paint). The science of colloids is important for applications ranging from drug delivery and dairying to coating technology and drilling fluids. For practical reasons, mankind has always been interested in colloidal stability. Frequently, long-term stability of a colloidal dispersion is desired, for example in storage of paint or food, and often adjusting the particle surface chemically or via adsorption is applied to ensure this stability. For example, carbon is the oldest ink material known and in Egypt its use for writing can be dated back to 3400 BC [16]. The carbon used for making ink was soot in most cases. By mixing with gum arabic and water, soot was made into ink.

Without understanding the underlying principles, the Egyptians effectively used the stabilization of dispersions by adsorbed macromolecules [3, 17]. This is nowadays recognized as an example of polymeric stabilization, see Sect. 1.2.4. In this manner the Egyptians succeeded in engineering the soot particles as to be able to remain suspended for an indefinite period.

An example where the instability of colloids (clay) plays a role in nature is delta formation. Deltas [18] are formed due to precipitation of colloidal (clay) particles carried by the river as its flow meets the sea (or ocean), where the river water mixes with salty sea water. The delta formation process was already described by Barton [19] in 1918 before a clear understanding of the role of salt on colloidal stability had been established.

Milk is a natural colloidal dispersion that contains casein micelles, self-assembled protein associates with a diameter of about 200 nm [20]. The casein micelles are protected against flocculation by an assembly of dense 'hairs' (often called a 'brush') at their surfaces. Polymer brushes can thus provide steric stabilization of colloids. For millennia, man used the fact that milk flocculates and gels when it is acidified, as in yogurt production. Below $pH = 5$ macroscopic flocculation of the casein micelles in milk is observed [21]. This means that the interactions between casein micelles change from repulsive to attractive. The explanation is that acidification leads to collapse of the casein brushes [22]. In cheese-making the steric stabilization is removed by enzymes, which induce gelation into cheese curd.

Modest solvent composition changes can also affect the state of a colloidal dispersion. A charge-stabilized dispersion of polymer latex particles or gold colloids may flocculate irreversibly upon adding salt, while ion removal through dialysis may turn the dispersion into an ordered structure exhibiting Bragg reflection [23]. Obviously, the physical state of a colloidal dispersion is a function of the interactions between the colloidal particles.

In foods and paints and in biological systems such as the living cell, colloids and polymers are often present simultaneously. When the polymers do not adsorb onto the colloidal particles the result is a socalled depletion layer. As we shall see, overlap of depletion layers leads to an attractive depletion interaction between the colloidal particles. The term depletion derives from Latin meaning 'emptied out'. The verb 'plere' is 'to fill' [24]. Thus a 'pletion' force is due to accumulation of some substance between two colloids. The reversal, a 'depletion' force is due to the expulsion of material.

Mixing colloids with polymers or other colloids can lead to phase transitions or aggregation resulting in for instance gelation, crystallization, glass transition, flocculation, or fluid–fluid demixing of the dispersion. The type of instability depends on the range and strength of the particle interactions involved. The knowledge gained over the last few decades on depletion effects in mixtures of colloidal particles and polymers is of great interest for designers of new products. Insight into the factors determining the stability of mixtures changes product development from trial-and-error towards knowledge-driven innovation. This

book serves as a guide to help understanding what happens when colloids are mixed with polymers or other colloids.

This chapter gives an introduction into colloidal interactions, including the depletion force in a historical context, and provides examples of the manifestations of depletion effects. First, we start with a brief overview on colloidal interactions in Sect. 1.2 including the basic concept of the depletion interaction. We sketch the effects of unbalanced forces, amongst which depletion forces in colloidal dispersions from a historical perspective in Sect. 1.3. Finally, we discuss some consequences of depletion forces in Sect. 1.4, followed by a brief Outline of the other Chapters of this book in Sect. 1.5.

1.2 Colloidal Interactions

The basic understanding of colloidal interactions commenced in the 1940s. Then Derjaguin and Landau [25] in the former USSR and Verwey and Overbeek [26] in The Netherlands pointed out that in a dispersion of charged colloids in an electrolyte solution the Van der Waals attraction between two colloidal particles is opposed by a repulsion originating from electrical double layers. This foundation for the stability of colloids is known as the DLVO theory and has been remarkably successful in explaining the results of a vast number and broad range of experiments, including direct force measurements [27]. Polymers, either depleted from or adsorbed or anchored to colloidal surfaces also turned out to strongly influence colloidal interactions; these were not considered by DLVO.

In Sects. 1.2.1 and 1.2.2 we shall first qualitatively consider double layer and Van der Waals interactions, the two contributions to the DLVO potential (Sect. 1.2.3), and then discuss (polymeric) steric stabilization by end-attached polymer in Sect. 1.2.4. While not further discussed here we mention that adsorbing polymers, proteins or particles can also be used to protect colloids against flocculation. For protein adsorption, often used for instance in food emulsions, we refer to [28]. Using particles to stabilize colloids is referred to as Ramsden-Pickering stabilization [29]. Finally, the depletion interaction will be treated in Sect. 1.2.5.

1.2.1 Van der Waals Interaction

Dispersion or London–Van der Waals forces act between all atoms and molecules. This intermolecular attractive force arises from a cooperative oscillation of electron clouds when the molecules are at close range. Each colloidal particle consists of atoms. When two colloidal particles in a background medium are in close proximity, the Van der Waals interaction between all atoms contribute to an effective attraction termed colloidal Van der Waals interaction. This attraction follows from summation of all atomic Van der Waals interactions [30, 31]. The dielectric properties of the colloidal particles and the background medium

determine the strength of the interaction. For two colloidal spheres with radius R the Van der Waals attraction reads [32]

$$W_{VdW}(h) = -\frac{A}{6} f(h/R) \tag{1.2}$$

with

$$f(h/R) = \frac{2R^2}{h^2 + 4Rh} + \frac{2R^2}{h^2 + 4Rh + R^2} + \ln\left(\frac{h^2 + 4Rh}{h^2 + 4Rh + R^2}\right),$$

where A is the Hamaker constant and h is the closest distance between the surfaces of two spheres.

The Hamaker constant for the interaction between two colloidal particles without intervening medium is, to a good approximation, built up additively from pair interactions between the atoms (or molecules) which make up the colloidal particles. This leads to

$$A = C\pi^2 n^2, \tag{1.3}$$

where n is the number density of atoms. Here C is the coefficient for the dispersion interaction between the atoms of which the colloidal particles consist. According to the London theory [33, 34] for dispersion interactions this coefficient can, to a good approximation, be written as

$$C = \frac{3}{4}\overline{E}\left(\frac{\alpha_p}{4\pi\varepsilon_0}\right)^2. \tag{1.4}$$

Here $\overline{E}$ is a typical (average) electronic excitation energy, α_p is the static polarizability and ε_0 is the vacuum permittivity. As a primitive description for an atom we use Thomson's model [35] but now with a point nucleus (with $+q_e$ charges) surrounded by a charged spherical cloud ($-q_e$ charges) with diameter σ_a [36]. In the presence of an external electric field the nucleus will be shifted while the electron cloud moves in the opposite direction. Assuming that the electron cloud retains its spherical shape this leads to a dipole moment $\overline{\mu} = q_e d$, where d is the displacement of the nucleus from the center of the negative charge. The value d is determined by the balance of the forces acting on the nucleus due to the external field E_e and the internal field E_i caused by the displacement of the nucleus. The charge outside the sphere of radius d does not contribute to the force acting on the nucleus. The charge inside this sphere is $-q_e d^3/(\sigma_a/2)^3$ and acts on the nucleus as though it were concentrated at the centre and hence

$$E_i = -\frac{2q_e}{\pi\varepsilon_0}\frac{d^3}{\sigma_a^3}\frac{1}{d^2}. \tag{1.5}$$

Exercise Prove the statements above (1.5) using Gauss's law. Hint: consult Chap. 2 in [36].

The balance condition

$$E_e + E_i = 0, \tag{1.6}$$

leads to

$$\overline{\mu} = q_e d = \frac{\pi \varepsilon_0 \sigma_a^3}{2} E_e, \tag{1.7}$$

Since $\overline{\mu} = \alpha_p E_e$ it follows

$$\frac{\alpha_p}{4\pi\varepsilon_0} = \frac{\sigma_a^3}{8}. \tag{1.8}$$

Although this atomic model is extremely crude the result (1.7) is not too bad; it is accurate to within a factor four or so for many simple atoms. The number density scales as

$$n \simeq \frac{1}{\sigma_a^3}, \tag{1.9}$$

and so we obtain

$$A = \frac{3\pi^2}{256} \overline{E}. \tag{1.10}$$

Now using the fact that the typical electronic excitation energies lies in the range $1-5\,\mathrm{eV}$ we obtain $A = 0.12 - 0.6\,\mathrm{eV} = 2 - 10 \times 10^{-20}\,\mathrm{J}$, in good agreement with experiment. After expressing A in units kT ($\approx 4 \times 10^{-21}\,\mathrm{J}$ at room temperature), we obtain $A = 5 - 25\,\mathrm{kT}$. With a medium between the colloidal particles the value of A is typically reduced by a factor 3 to 10.

From (1.2) it follows that the Van der Waals attraction is very strong at short interparticle separations (small h, where $W_{VdW}(h) \sim -AR/h$). In order to stabilize a colloidal dispersion a significant repulsion is needed preventing the particles getting too close and flocculate irreversibly. The Van der Waals interaction is sketched schematically in Fig. 1.1 as the lower dashed curve.

1.2.2 Double Layer Interaction

A charged colloid is surrounded by a solution with an inhomogeneous distribution of ions. Co-ions (with the same charge as the colloids) are depleted from the colloid surface and counterions (with opposite charge) adsorb (accumulate) at the surface. Far from the colloidal surface the concentrations of the two ion types attain a constant averaged value. The inhomogeneous layer is termed double layer and its width depends on the ion concentration in the bulk solution: adding more ions screens the charges on the colloidal surfaces.

When two double layers overlap a repulsive pair potential develops which leads to a repulsive pressure. Dispersed like-charged colloids hence repel each other

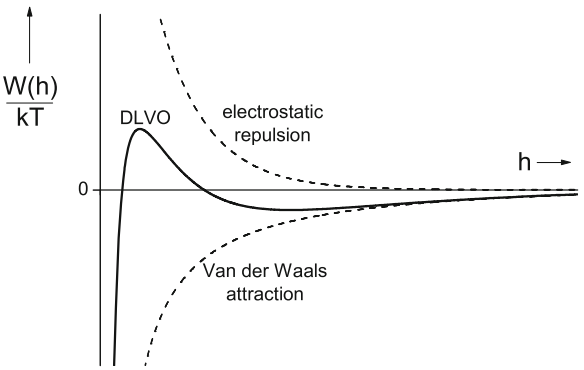

Fig. 1.1 Schematic plot of a typical double layer repulsion between charged colloidal spheres (*top*), of the Van der Waals attraction (*bottom*) and their sum, which is the DLVO interaction potential

upon approach due to screened-Coulomb or double layer repulsion. The length scale over which this force is operational is set by the Debye screening length λ_D

$$\lambda_D = \sqrt{\frac{1}{8\pi\lambda_B n_s}}, \tag{1.11}$$

where n_s is the salt number density and λ_B is the Bjerrum length,

$$\lambda_B = \frac{e^2}{4\pi\varepsilon_0\varepsilon_r\, kT}, \tag{1.12}$$

with e the elementary charge and ε_r the relative dielectric constant ($\approx$80 in water). The Bjerrum length is the distance between two elementary charges at which their interaction equals kT. In water at room temperature its value is ≈ 0.7 nm. For the Debye length we then find $\lambda_D = 0.3\sqrt{I}$ nm with the ionic strength I in mol/L.

The interparticle separation dependence of double layer repulsion is approximately exponential [26]

$$W_{DR}(h) = B\frac{R}{\lambda_B}\exp(-h/\lambda_D), \tag{1.13}$$

which shows that the range of the screened double layer repulsion is λ_D, and depends on ionic strength.

The quantity B can be expressed in terms of the surface charge density σ_c of the interacting colloids [26]

$$\frac{B}{kT} = \frac{8p_c^2}{1+p_c^2}, \tag{1.14}$$

where $p_c = 2\pi\lambda_D\lambda_B|\sigma_c/e|$, with p_c the number of elementary charges e on a surface area $2\pi\lambda_D\lambda_B$. Given the fact that $|\sigma_c|$ varies roughly between 0.1 and 2 e/nm^2, the value of p_c ranges from 0.1 to 10 and hence B has a typical value of $1-8$ kT. The quantity B can also be expressed as a function of the surface potential ψ_0 [26]:

$$\frac{B}{kT} = 8\left[\tanh\left(\frac{\psi_0}{4\,kT}\right)\right]^2. \tag{1.15}$$

The surface potential of a charged colloidal particle typically varies from 10 to 100 mV leading to B values in the same range as given above.

The double layer interaction between two like-charged colloidal particles is sketched in Fig. 1.1 (upper dashed curve).

1.2.3 DLVO Interaction

By assuming additivity of the interactions, the total DLVO potential is simply given by

$$W_{DLVO} = W_{VdW} + W_{DR}. \tag{1.16}$$

In Fig. 1.1 the DLVO interaction potential W_{DLVO} is schematically sketched together with its two contributions. If the maximum of W_{DLVO} is sufficiently high (larger than a few kT), flocculation is prevented. Flocculation does occur when the particles can get very close into the socalled primary minimum; this minimum is usually deep enough for irreversible flocculation.

For a given Van der Waals attraction and particle size the DLVO potential depends on the ionic strength. The DLVO potential is qualitatively represented in Fig. 1.2, with from (i) towards (iv) more added salt. At low salt concentration (i) the double layer repulsion dominates, the maximum of W_{DLVO} exceeds several kT and a stable colloidal dispersion is expected. In situation (ii) the salt concentration is larger but there is still a local maximum that may be significant, preventing the particles to irreversibly stick into the primary minimum. A shallow secondary minimum now manifests itself at large interparticle distances. If this local minimum is sufficiently deep (i.e. for large particles), weak flocculation can take place. Such weakly flocculated aggregates can be redispersed by shaking or by lowering the salt content. Adding still more salt (iii, iv) leads to irreversible

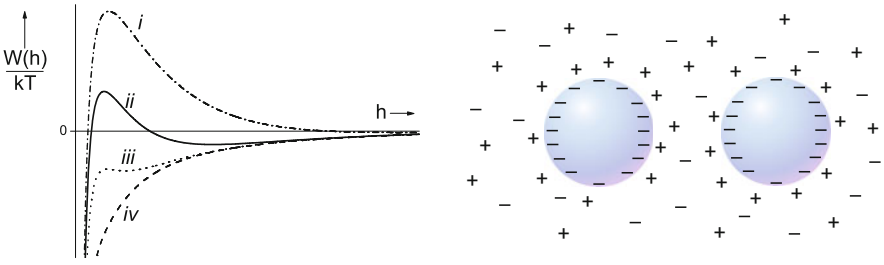

Fig. 1.2 Illustrative DLVO pair interactions (*left*) between two charged colloidal spheres (see sketch on the right) in an electrolyte solution as a function of adding more salt from $(i \rightarrow iv)$

aggregation: the Van der Waals attraction gets dominant and the colloidal dispersion will be unstable. DLVO theory is capable of accurately describing early stage aggregation of dilute charged colloidal spheres for $\lambda_D \gtrsim 3\,\text{nm}$ [37].

Using the surface force apparatus Israelachvili and Adams [38] measured a repulsive force in aqueous solution at short separations that could not be interpreted in terms of DLVO theory. This interaction is due to hydration forces caused by the ordering of water molecules. Its range is very short, typically below 2 nm. For a discussion on the limitations of DLVO theory and possible improvements, see for instance [39].

In the above descriptions we concentrated on situations where a polar background solvent was implicitly assumed. In apolar solvents double layer repulsion is difficult to achieve because dissociation, leading to charged surface groups, is less likely to occur and it becomes essential to stabilize colloids with polymers as to prevent instabilities. In the first decades after the establishment of the DLVO theory most papers on forces between colloidal particles focused on Van der Waals and double layer interactions. Forces of other origin such as polymeric steric stabilization [17], depletion [40] or effects of a critical solvent mixture [41] gained interest at a later stage.

1.2.4 Influence of Attached Polymers

Colloidal dispersions can be very well stabilized by polymers attached to the particle surfaces [17]. Here we consider polymer chains that are in a 'good solvent'. This means that the chains are swollen and repel each other. As two colloidal particles, protected with attached polymers, approach each other the local osmotic pressure increases dramatically due to steric hindrance of the polymer chains on both particles. This competition between the chains for the same volume leads to a repulsive interaction, as was realized already by Fischer [42].

Polymers can be attached to surfaces for instance as mushrooms, brushes or as adsorbed chains, see Fig. 1.3. In case of mushrooms and brushes the

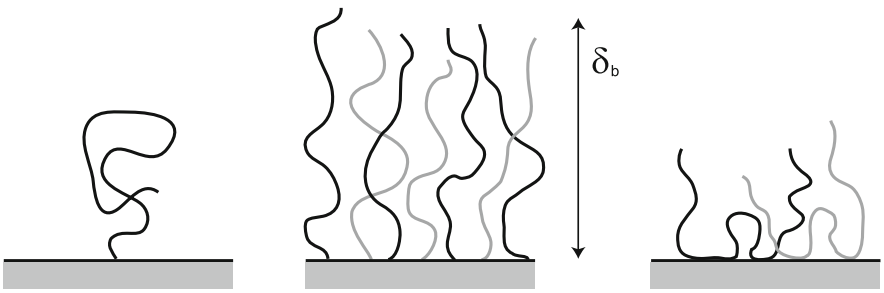

Fig. 1.3 Schematic pictures of polymers attached at a surface: a mushroom (*left*), a brush (*middle*), and a layer of adsorbed polymer (*right*)

(non-adsorbing) chains are chemically bound to the surface by one chain end. Brushes are characterized by a high packing density. When polymers adsorb at a surface many segments stick and densely pack at the interface. Attached polymers can contribute to a (significant) repulsive interaction between the particles. Upon overlap of the attached polymers the osmotic pressure between the surfaces strongly increases which leads to a repulsive interaction between the particles.

A simple picture emerges for polymer brushes, chains that are anchored to the surface by an end segment with a high anchor density; as a consequence the chains are highly stretched. The free energy of interaction between brushes consists of two terms: an osmotic repulsion contribution and a stretching factor. The Alexander–De Gennes theory [43–45] considers the repulsive interaction of overlapping brushes of thickness δ_b in a good solvent. This thickness scales as $M\sigma_b^{1/3}$, where M is the chain length and σ_b the anchor density. For $h \leq 2\delta_b$ the pressure P between two parallel plates with anchored brushes at separation h reads:

$$\frac{P(h)}{kT\,\sigma_b^{3/2}} \approx \left(\frac{2\delta_b}{h}\right)^{9/4} - \left(\frac{h}{2\delta_b}\right)^{3/4}. \tag{1.17}$$

The first positive term on the right-hand side represents the osmotic repulsion between the brushes and the second negative term originates from the elastic energy gain upon retraction of chains (less stretching). The repulsion dominates the interaction for $h < \delta_b$. As will become clear in Sect. 2.1, the pressure yields the interaction potential between two plates from which also the interaction between two spheres can be derived.

In Fig. 1.4 we qualitatively sketch the effect of adding a polymer brush to two (uncharged) colloidal spheres subject to Van der Waals attraction. Commonly, one assumes the total interaction is the sum of all pair interactions:

$$W_{tot} = \sum_i W_i. \tag{1.18}$$

So in Fig. 1.4 the total interaction potential is $W_{tot} = W_{VdW} + W_{brush}$. Without the anchored polymer chains the particles would coagulate spontaneously, since the

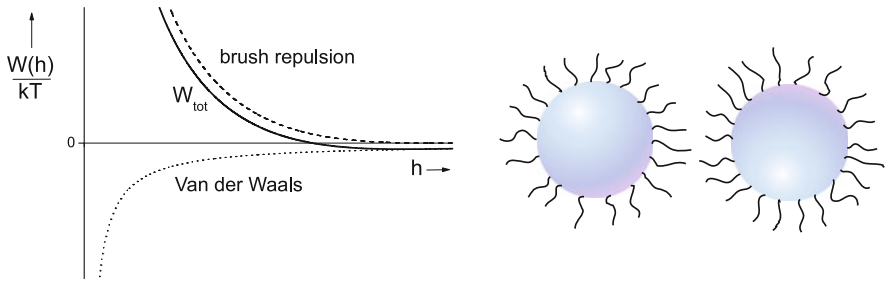

Fig. 1.4 Sketch of the influence of a brush repulsion on two spheres with Van der Waals attraction

Van der Waals attraction is very strong at small values of h. However, upon adding the polymer brush repulsion the total interaction (solid curve) is repulsive for a wide h-range with no significant attraction left.

The Van der Waals attraction can be reduced by choosing a solvent (mixture) that allows for refractive index matching of colloid and solvent. For model studies where one desires hard-sphere-like particles, refractive index matching is combined with attaching short hairs (a thin brush; $\delta_b \ll R$) to the colloidal particles. This leads to absence of effective attractions and only a short-ranged repulsion between the particles: basically we now have a system of hard spheres; imagine sub-micron sized billiard balls. The pair interaction may then be approximated as

$$\begin{aligned} W(h) &= \infty \quad h \leq 0 \\ &= 0 \quad h > 0 \end{aligned}, \tag{1.19}$$

the hard-sphere interaction, plotted in Fig. 1.5 (left panel). In the next section we consider the effect of non-adsorbing polymer in such a hard-sphere dispersion.

When the medium is a poor solvent for the attached polymers a rather different situation is encountered. The polymer chains then tend to assume collapsed configurations in order to minimize contact with solvent molecules and the polymer segments prefer to interact with each other. This results in (short-ranged) attraction between colloidal particles covered with polymer chains in a poor solvent (see Sect. 5.5 in [46]). The interaction of such sticky spheres (billiard balls with a thin layer of honey [47]) is often described in a simple manner using the adhesive hard sphere interaction (see right panel in Fig. 1.5)

$$\begin{aligned} W(h) &= \infty \quad h \leq 0 \\ &= -\varepsilon \quad 0 < h \leq \Delta, \\ &= 0 \quad h > \Delta \end{aligned} \tag{1.20}$$

where Δ is the range of the attraction set by the thickness of the polymer layers and ε is the strength of attraction upon overlap of the polymer layers. For $\Delta \ll R$ the sticky sphere model of Baxter [48] can be employed providing simple expressions for the second osmotic virial coefficient and the equation of state. When the attractions are sufficiently strong phase separation or aggregation occurs [49–52].

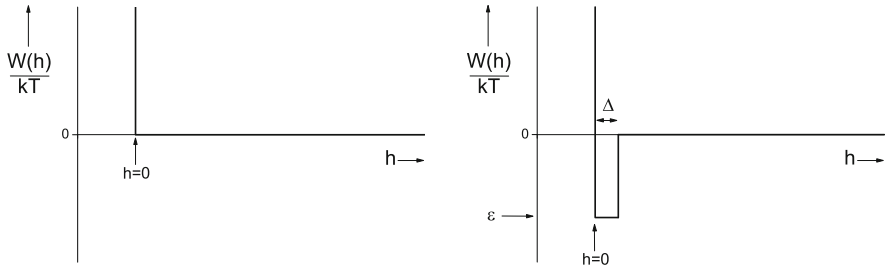

Fig. 1.5 Hard-sphere (*left*) and adhesive hard-sphere (*right*) interaction

1.2.5 Depletion Interaction

Consider a room in a restaurant on two different occasions, as sketched in Fig. 1.6. On regular evenings the staff arranges the tables in a typical dinner set-up. Sometimes the room is booked for a cocktail party with many people present. In such a busy cocktail party the tables are laden with drinks and snacks and the configuration of the tables is rather different. Obviously, when the number of visitors exceeds a certain value, people tend to push the tables close to each other near one wall in order to gain more translational freedom for the visitors. This 'phase separation' is driven by entropy only. The apparent attraction between the tables originates from purely repulsive interactions between the people: the visitors do not wish to be too close to each other (and can still fetch a drink from a table). It is, just like depletion, an example of, what Vrij (personal communication) refers to as 'attraction through repulsion'. Below we explain the origin of the depletion effect, first by regarding colloidal hard spheres in a solution of non-adsorbing polymer.

Suppose colloidal spheres are mixed with non-adsorbing polymers. Negative adsorption then results in an effective depletion layer near the surface due to a loss of configurational entropy of a polymer chain in that region. The mechanism that is responsible for the attraction originates from the presence of depletion layers. Consider the sketch depicted in Fig. 1.7 of a few colloidal spheres in a polymer solution. Depletion layers are indicated by the (dashed) circles around the spheres. When the depletion layers overlap (lower two spheres) the volume available for the polymer chains increases. It follows that the free energy of the polymers is minimized by states in which the colloidal spheres are close together. The effect of this is just as if there were an attractive force between the spheres even while the direct colloid–colloid and colloid–polymer interactions are both repulsive [40]. For small depletant concentrations the attraction equals the product of the osmotic pressure and the overlap volume, indicated by the hatched region between the lower spheres in Fig. 1.7. The picture sketched above became first clear in the 1950s through the work of Asakura and Oosawa [53, 54] and gained full attention

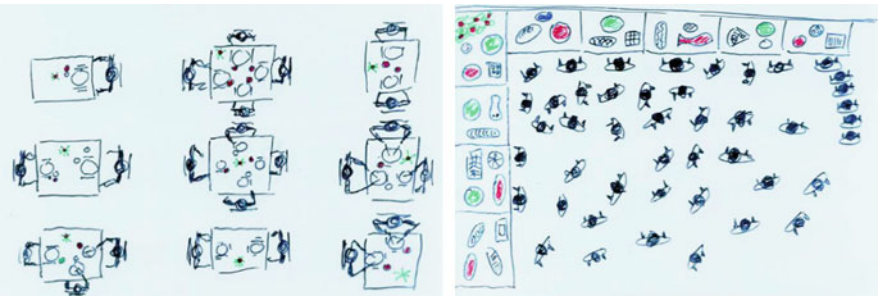

Fig. 1.6 *Left* dinner set-up in the restaurant on a quiet evening. *Right* buffet set-up in the same restaurant after 'phase separation'. Drawings by D. Frenkel (personal communication)

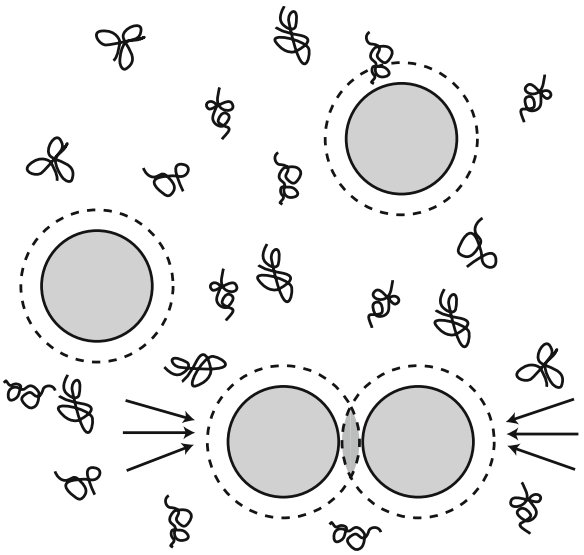

Fig. 1.7 Schematic picture of colloidal spheres in a polymer solution with non-adsorbing polymers. The depletion layers are indicated by the *short dashes*. When there is no overlap of depletion layers (*upper two spheres*) the osmotic pressure on the spheres due to the polymers is isotropic. For overlapping depletion layers (*lower two spheres*) the osmotic pressure on the spheres is unbalanced; the excess pressure is indicated by the *arrows*

only when Vincent et al. [55] and Vrij [40] started systematic experimental and theoretical work on colloid–polymer mixtures.

Anticipating a more rigorous treatment in Chap. 2, we already give the standard expression often used for the depletion interaction [40, 54]. Consider two colloidal spheres each with diameter $2R$, each surrounded by a depletion layer with thickness δ. In that case the depletion potential can be calculated from the product of $P = n_b\, kT$, the (ideal) osmotic pressure of depletants with bulk number density n_b, times V_{ov}, the overlap volume of the depletion layers. Hence the Asakura–Oosawa–Vrij (AOV) depletion potential equals:

$$\begin{aligned} W_{dep}(h) &= \infty && h<0 \\ &= -PV_{ov}(h) && 0 \le h \le 2\delta, \\ &= 0 && h \ge 2\delta \end{aligned} \tag{1.21}$$

with overlap volume $V_{ov}(h)$

$$V_{ov}(h) = \frac{\pi}{6}(2\delta - h)^2\,(3R + 2\delta + h/2). \tag{1.22}$$

In Fig. 1.8 the AOV interaction potential $W_{dep}(h)$ between two hard spheres in a solution containing free polymers is plotted. The minimum value of the potential W_{dep} is achieved when the particles touch ($h = 0$).

We note that in the original paper of Asakura and Oosawa [54], where expression (1.21) was first derived, the polymers were regarded as pure hard spheres. Vrij [40, 56] arrived at the same result by describing the polymer chains as penetrable hard spheres, see Sect. 2.1. Inspection of (1.21) and (1.22) reveals that the *range* of the depletion attraction is determined by the size 2δ of the

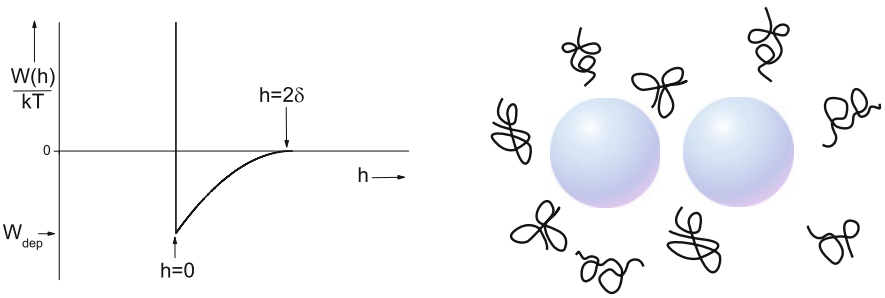

Fig. 1.8 Sketch of the depletion interaction between two hard spheres

depletant, whereas the *strength* of the attraction increases with the osmotic pressure, hence with the depletant concentration. Depletion effects offer the possibility to independently modify the range and the strength of attraction between colloids. In dilute polymer solutions, the depletion thickness δ is close to the polymer's radius of gyration R_g.

In a mixture of hard spheres and depletants a phase transition occurs upon exceeding a certain concentration of colloidal spheres and/or depletants. This is the subject of Chaps. 3–6 in this book. A key parameter in describing the phase stability of colloid–polymer mixtures is the size ratio q,

$$q = \frac{R_g}{R}. \tag{1.23}$$

Throughout, colloid–polymer mixtures are described in terms of the volume fraction of colloids ϕ and the *relative* polymer concentration:

$$\phi_p = \frac{n_b}{n_b^*} = \frac{\varphi}{\varphi^*}, \tag{1.24}$$

which is unity at the overlap concentration and can be regarded as the 'volume fraction' of polymer coils (and exceeds unity in the semi-dilute concentration regime). Here n_b is the bulk polymer number density and n_b^* is its value at which the polymer coils overlap. In terms of the volume fraction of polymer segments φ ($0 \leq \varphi \leq 1$), one then uses $\phi_p = \varphi/\varphi^*$, with φ^* the segment volume fraction where the chains start to overlap:

$$\varphi^* = \frac{M v_s}{v_p}, \tag{1.25}$$

where M is the number of monomers per chain, v_s is the monomer (segment) volume, and $v_p = (4\pi/3)R_g^3$ the coil volume, so $\varphi^* \sim M/R_g^3$. The overlap number density n_b^* hence follows as $n_b^* = 3/(4\pi R_g^3)$.

It has actually become a standard practice to normalize polymer concentrations in this way and use φ/φ^* (or n_b/n_b^*) as the parameter for 'polymer concentration'.

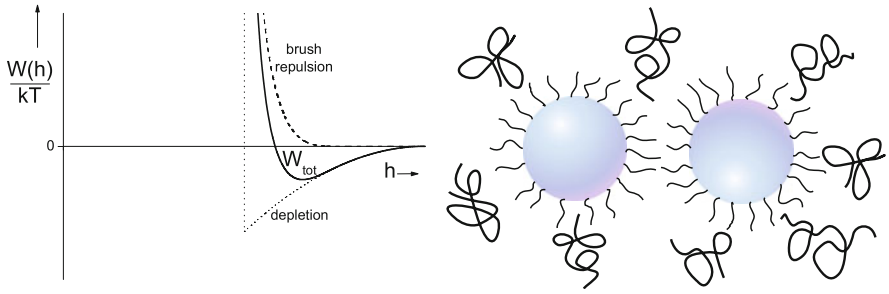

Fig. 1.9 Sketch of the total interaction potential between two spheres covered with polymer brushes in a good solvent in a solution containing non-adsorbing polymer chains

In terms of practical concentrations in kg/m^3 or g/L the overlap concentration follows as

$$\frac{3M_p}{4\pi R_g^3 N_{av}}, \tag{1.26}$$

where M_p is the polymer's molar mass and N_{av} is Avogadro's number. The pressure P in (1.21) can, using (1.24), be rewritten as $Pv_p/kT = \phi_p$.

Exercise
Show that, when using the approximation $\delta = R_g$, the attractive part of (1.21) can be written in normalized quantities as:

$$\frac{W_{dep}(h)}{kT} = q^{-3}\phi_p\left(q - \frac{h}{2R}\right)^2\left(\frac{3}{2} + q + \frac{h}{4R}\right).$$

In Fig. 1.9 we sketch the influence of a combined depletion attraction and a brush repulsion on the total interaction. The presence of brushes reduces the attraction and the minimum value of the attraction is found at $h > 0$ [57].

The fact that depletion forces enable to vary the range of attraction and its strength independently is helpful for studying fundamental properties of liquids, as well as crystallization and gelation phenomena, using colloidal systems instead of low molar mass substances. Another advantage of colloid–polymer mixtures is that colloids can be investigated using microscopy. Aarts et al. [58] could even detect capillary waves at the colloidal gas–liquid interface. Observations of wetting phenomena can also be studied at the particle level [59, 60].

1.3 Historical Overview on Depletion

In this book depletion in colloidal dispersions is a central theme. As we saw in Sect. 1.2.5 depletion effects in colloidal dispersions are caused by an unbalanced force. From a physics point of view the depletion force between colloidal particles

due to non-adsorbing polymer chains or small particles has common features with any other unbalanced force, whether of a colloidal nature or not. Before we focus on depletion effects on a mesoscopic level we first give two classical examples of unbalanced forces.

1.3.1 Early Interest in Unbalanced Forces

1.3.1.1 The Von Guericke Force

Halfway the 17th century a series of remarkable experiments were performed initiated by Otto Von Guericke. One took place in 1657 at the court of King Friedrich Wilhelm III of Brandenburg in Berlin, Germany. Two hollow copper hemispheres with a diameter of 51 cm were joined and air was pumped out so a partial vacuum was created. To each hemisphere teams of horses were harnessed, see Fig. 1.10. The teams of horses, which pull with a force of about 1,500 N each, could not pull apart the two joined hemispheres, demonstrating the tremendous force of air pressure. This proved the existence of the nothing we now call a vacuum.

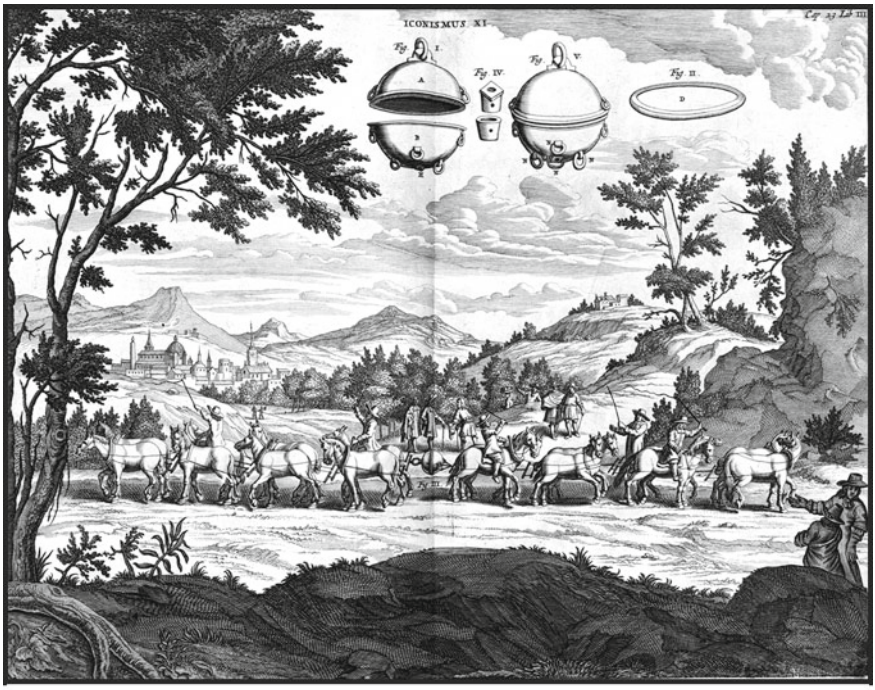

Fig. 1.10 Sketch by Caspar Schott (1602–1666) of the demonstration of the vacuum force by two teams of horses attempting to disengage the hemispheres

Exercise
Show that the force on the *hemispheres* due to air pressure is one order of magnitude larger than the force that can be produced by 24 horses.

This experiment was the brainchild of scientist, inventor, and politician Otto Von Gericke, later spelled Von Guericke, who lived between 1602 and 1686. The vacuum pump he used was invented by himself in 1650. His book on vacuum [61] reminds of the difficulties at the time on understanding vacuum. Von Guericke was able to abandon established views and developed an independent vision on vacuum [62]. The result of the 'horses' experiment showed that the surrounding air molecules push against the *Magdeburg* hemispheres (Von Guericke was the mayor of Magdeburg). The unbalanced force thus pulls the hemispheres together.

Exercise
Explain why the osmotic pressure of the polymer solution in a colloid–polymer mixture plays a similar role as air pressure in Von Guericke's experiment.

1.3.1.2 Le Sage's Gravitation Theory

In 1690 Nicolas de Fatio and later in 1748 Georges-Luis Le Sage proposed a mechanical theory for the explanation of Newton's gravitational force. This theory assumes the existence of 'ultramundane corpuscles'. Streams of such corpuscles are thought to impact on all materials from all directions. Now if two bodies of materials are close to one another they can partially shield each other from the incoming 'ultramundane corpuscles'; the bodies will be struck by less corpuscles from the side of the other body. This mutual shielding was then supposed to push the bodies together due to the unbalanced force of the colliding corpuscles. This line of reasoning was first formulated by de Fatio in a letter to Huygens [63]. Also Newton had contact with de Fatio on this matter. While Huygens, Newton and Leibniz were interested, they never accepted de Fatio's explanation as the driving force for gravity.

At a later stage, Le Sage published a similar, more refined version of the theory [64]. He was in contact with some of the greatest physicists and mathematicians of his time, including Euler and Bernouilli, who found the theory rather speculative. Inconsistencies in the theory were later revealed by for instance Laplace, Lord Kelvin, Lorentz and, for didactic reasons, more recently by Feynman [65]. Nowadays, Le Sage's theory is out of focus thanks to Einstein's theory of general relativity. Still, occasionally there is interest in Le Sage's theory [66]. This story reveals that physicists have always been triggered by the concept of an unbalanced force that brings objects together.

1.3.2 Experimental Observations on Depletion Before the 1950s

Long before Asakura and Oosawa rationalized the attractive interaction caused by depletants, the effects of depletion were already noted in various areas of specialization. In this overview we first give examples of such studies, and try to interpret them with our current knowledge of depletion forces. Subsequently, we will discuss several studies that were performed after the work of Asakura and Oosawa, often in light of the theoretical progress that is being made over, especially, the last decades. Although it is clearly impossible to cover all developments within the area of depletion phenomena in physics and chemistry, we aim at giving the reader a broad overview here.

1.3.2.1 Clustering of Red Blood Cells

Red blood cells (RBCs) are biconcave particles and their detailed shape and size depend on the RBC type. The human RBC may be considered a disc with a diameter of 6.6 μm and a thickness of 2 μm, its volume thus being of the order of 10^2 μm^3. The RBCs occupy about 40 to 50 vol % of our blood.

Exercise
Demonstrate stacking all red blood cells in a human being (having about 5 L of blood) in a single column provides a RBC cylinder with a height that is of the order of the earth's circumference.

Already in the 18th century it was known that RBCs tend to cluster, preferably with their flat sides facing each other. Such a side by side RBC aggregate reminds of the packing of 'a number of coins' [67]. These structures are commonly denoted as 'rouleaux'. In blood of healthy human beings the tendency of RBCs to aggregate is weak. In case of pregnancy or a wide range of illnesses aggregation is found to be enhanced, giving rather pronounced rouleaux, see Fig. 1.11. An impressive review on RBC clustering was written by Fåhraeus [67]. Another historical review, is due to Thysegen [68].

Enhanced RBC aggregation can be detected for instance by measuring the sedimentation rate. The sedimentation rate varies between 1 and 3 mm/h for healthy blood up to 100 mm/h in case of severe illnesses. The blood sedimentation test, based on monitoring aggregation of red blood cells, became a standard method for detecting illnesses. The relation between pathological condition, RBC aggregation and enhanced sedimentation rate, has been known for at least two centuries, as described in [69, 70].

Fåhraeus [67, 69] related enhanced aggregation of RBCs plus longer and stronger rouleaux to the concentration of the blood serum proteins fibrinogen, globulin and albumin. The tendency to promote aggregation depends on the type of protein. Rouleaux formation is most sensitive to increased serum concentrations of (rod-like) fibrinogen (molar mass 340 kg/mol) compared to (globular) β- and

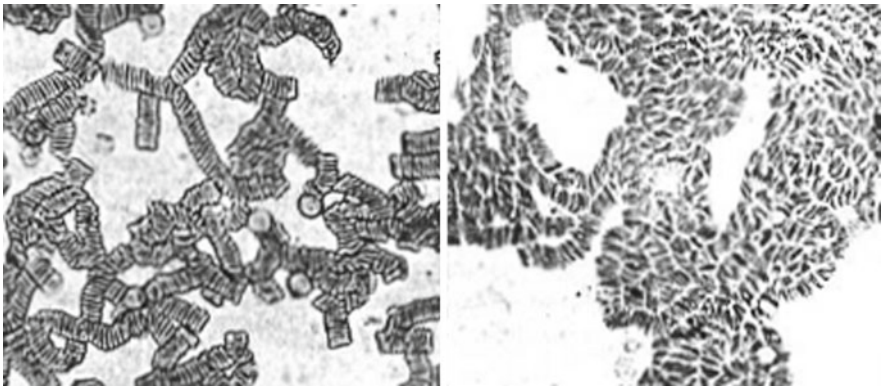

Fig. 1.11 Red blood cells in healthy blood (*right*) exhibiting weak aggregation and in blood of a pneumonia patient (*left*) in which rouleaux formation took place (strong aggregation) [67]. Picture reprinted from R. Fåhraeus, *Physiol. Rev*., 9:241, Copyright 1929, with permission from APS

γ-globulins (90 and 156 kg/mol, respectively). The globulins in turn lead to RBC aggregation at lower protein concentrations than albumin proteins (69 kg/mol). It has further been shown that adding other macromolecules such as dextrans also promote rouleaux formation. Asakura and Oosawa [54] suggested that RBC aggregation might be caused by depletion forces between the RBCs induced by serum proteins. This is in line with the finding that the sedimentation rate is more sensitive to larger serum proteins.

Some authors interpret rouleaux formation as being caused by bridging of RBCs by serum proteins. There is however no evidence for protein adsorption onto RBCs. A study on rouleaux formation in mixtures of human RBCs (diameter 6.6 μm) and rabbit RBCs (diameter 7.8 μm) resulted in rouleaux structures that consisted (mainly) of only a *single* type of RBC [71]. This can be explained by a depletion effect (the overlap volume, hence entropy, is maximized if similar RBCs stack onto each other). In case of bridging, however, mixed aggregates are expected, so there is little support for the bridging hypothesis [72]. The general picture is that red blood cells tend to cluster at elevated concentrations of the blood serum proteins, which act as depletants.

1.3.2.2 Mixing Biopolymers

Another manifestation of a depletion phenomenon was reported by the microbiologist Beijerinck [73] who tried to mix gelatin (denatured protein coil) with starch (polysaccharide) in aqueous solution in order to prepare new Petri dish growth media for bacteria. He reported that these biopolymers could not be mixed; 'emulsion droplets' appeared instead. With current knowledge [74] this can be regarded as an early detection of depletion-induced demixing. Tolstoguzov, Grinberg and coworkers extensively studied many mixtures of

polysaccharides and proteins and concluded that such mixtures tend to segregate [75–77], unless there are specific interactions such as opposite charges. They further found that adding salt decreases the miscibility region in protein/polysaccharide mixtures [75]. Obviously, double layer interactions also play a role on top of pure depletion forces in such mixtures. The separate liquid phases in demixed protein–polysaccharide mixtures can sometimes be characterized by a sharp liquid–liquid interface. The interfacial tension between the coexisting phases in protein–polysaccharide mixtures has been determined and is of O (μN/m) [78, 79].

1.3.2.3 Creaming of Particles in Latex

In the beginning of the 20th century large scale production of latex for rubber and paint production commenced. The term 'latex' is nowadays identified with a stable dispersion of polymeric particles in an aqueous medium. In order to lower transport costs there was a significant interest in concentrating the polymeric latex. Centrifugation is highly energy consuming and thus expensive.

Traube [80] showed that adding plant and seaweed polysaccharides led to a phase separation between an extremely dilute and a very concentrated phase. Since the particles are lighter than the solvent the concentrated phase, with volume fraction $0.5 \leq \phi \leq 0.8$, floats on top. The lower phase is clear and hardly contains particles. Baker [81] and Vester [82] systematically investigated the mechanism that leads to what they called (enhanced) creaming.

In Fig. 1.12 we show microscopic images of the latex dispersion investigated by Baker [81]. The images are for a 1% latex dispersion, first without added polymer (A). Images B and C were taken respectively 2 and 10 min after adding 0.3% of polymer (the polysaccharide tragon seed gum). After polymer addition, Baker reports an immediate slowing down of Brownian motion together with particle aggregation. After about 10 min particle aggregation discontinues and the aggregates start creaming. The entire creaming process takes about 1 day. Image D was taken in the cream layer. Upon diluting the cream layer till 1% of latex particles Brownian motion restarts, implicating the flocs segregated into individual particles again. From the work of Baker [81] it can thus be concluded that the particles aggregate reversibly; upon dilution the latex particles can be resuspended. This suggests that bridging, which can also cause creaming [83], is not the driving force for enhanced creaming.

Vester [82] reviewed ways to optimize the creaming speed of latices by using non-adsorbing polymer chains as depletants. He found that polymer addition can also lead to formation of emulsion droplets with diameters of $O(10-100)$ μm that are enriched in latex while the continuous phase is dilute in latex particles. Nowadays this is interpreted as a colloidal gas–liquid phase coexistence. A microscopic image of the resulting emulsion is given in Fig. 1.13 (left panel). Upon confining the emulsion the droplets deform very easily (right panel Fig. 1.13). This implies that the interfacial tension γ is very low. Indeed we do

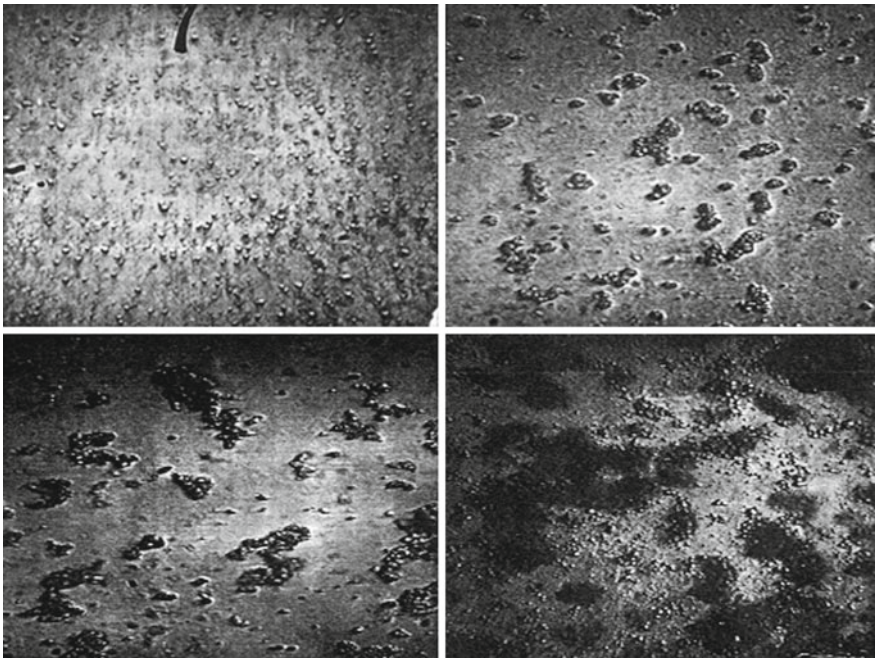

Fig. 1.12 Microscopic images of a rubber latex dispersion [81]. **a** 1% suspension without polymer; **b** 2 min after addition of 0.2% polysaccharide; **c** 10 min after addition of 0.2% polysaccharide; **d** image of the creaming layer. Size of the images are about 130 by 100 μm. Picture reprinted from H. C. Baker, *Inst. Rubber Ind.*, 13:70, 1937

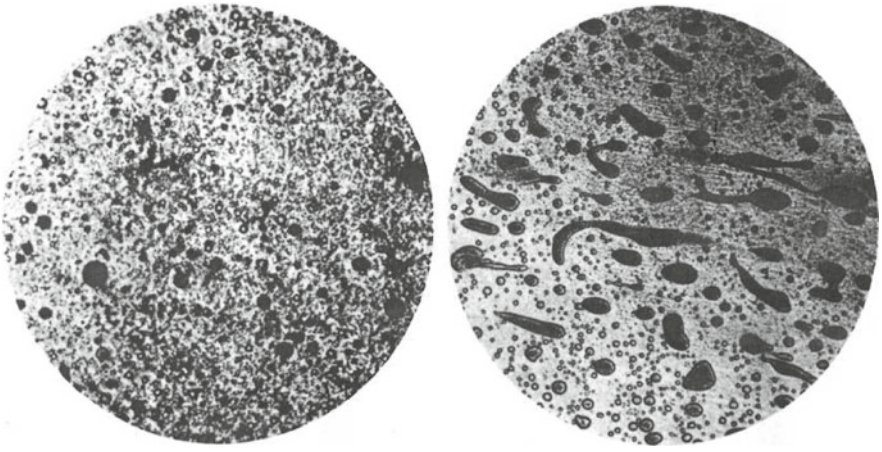

Fig. 1.13 Microscopic images (diameters correspond to 610 μm) of demixed dispersions of emulsion droplets (*black*) in a polymer solution. The *right panel* is the result of pressing the microscopic slide. Picture reprinted from C. F. Vester, *Kolloid Z.*, 84:63, Copyright 1938, with permission from Springer

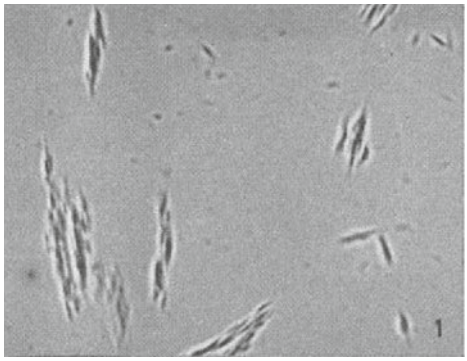

Fig. 1.14 Light microscopy image of TMV paracrystals upon adding heparin [85]. Size of image: 80 by 60 μm. Picture reprinted from S. S. Cohen, *J. Biol. Chem.*, 144:353, Copyright 1942, with permission from the American Society for Biochemistry and Molecular Biology

expect a small interfacial tension. The order of magnitude of a surface tension can be estimated from [84]

$$\gamma \approx \frac{kT}{R^2}, \tag{1.27}$$

where R is the particle radius. For molecular systems this yields values for γ of 10–100 mN/m, which agrees perfectly with measured surface tensions. In the colloidal size domain, for particles with for instance $R \approx 60$ nm an interfacial tension of only 1 μN/m is expected at room temperature. Indeed this is the order of magnitude of the ultralow interfacial tension measured in unmixed colloid–polymer mixtures that are in colloidal gas–liquid equilibrium, see Sect. 1.4.

1.3.2.4 Precipitation and Isolation of Viruses

Cohen [85] demonstrated that adding less than a percent of heparin to solutions of rod-like viruses results in the precipitation of the virus particles. The isolated precipitate phase consists of 'paracrystals'. The connection Cohen [85] makes with the work of Bernal and Farkuchen [86] suggests the phase appears liquid crystalline. This opens up the possibility to isolate and separate viruses [87, 88]. In Fig. 1.14 a microscopic image is shown of clusters of tobacco mosaic virus (TMV) particles in a dispersion with 0.5 wt% of heparin [85]. In Chap. 6 we consider depletion effects in colloidal rod dispersions.

1.3.2.5 Aggregation and Creaming of Emulsion Droplets

Cockbain [89] found that creaming of oil droplets in a surfactant-stabilized oil-in-water emulsion is enhanced when the surfactant concentration exceeds the critical

micelle concentration. This phenomenon was left unexplained at the time, but 30 years later Fairhurst et al. [90] made a connection with depletion interaction theories and suggested that the micelles play a similar role as non-adsorbing polymers or small colloidal particles as depletants (see Chap. 5).

1.3.3 1950–1969

In the early 1950s Noble Prize winner Paul J. Flory visited Nagoya University [91]. During this visit Asakura and Oosawa (see Fig. 1.15) reported unpublished theoretical results on two particles immersed in a solution containing non-adsorbing polymer chains, showing the chains impose an *attractive* interaction between the particles. The very positive response of Flory resulted in submission of this work, leading to a seminal paper in which Asakura and Oosawa [53] presented a statistical mechanical derivation of the interaction between two plates immersed in a solution of ideal non-adsorbing polymers. The segments of ideal polymer chains have no excluded volume; segments do not 'feel' other segments. The theory of Asakura and Oosawa [53] is the first theoretical prediction of a depletion force. It will be explained in more detail in Sect. 2.2.

They showed that adding non-adsorbing polymer chains induce an effective attraction between particles with a hard core interaction. It is a purely entropic effect; attraction originates from purely repulsive interactions.

Not long after the publication of the work of Oosawa, Sieglaff [92] demonstrated that a depletion-induced phase transition may occur upon adding polystyrene a dispersion of microgel spheres in toluene. This demonstrated that the attractive depletion force is sufficiently strong to induce a phase separation. Sieglaff rationalized his findings in terms of the theory of Asakura and Oosawa. It took several years before subsequent work was done. This study of Sieglaff was later extended by Clarke and Vincent [93].

Fig. 1.15 Oosawa (*left*) and Asakura (*right*) at Nagoya University in the 1960s [91]. Courtesy of Professor Fumio Oosawa

1.3.4 1970–1982

Early systematic studies with respect to phase stability for colloid–polymer mixtures were performed by Vincent and co-workers [55, 94, 95]. At ICI and in Bristol, they concentrated on mixtures of colloidal spheres (latex particles) plus non-adsorbing polymers such as polyethylene oxide (PEO). The work started when Vincent worked at ICI in Slough (1970–1972), where he investigated the origin of the flocculation of pigment particles in paint dispersions with F. Waite. In the papers of Vincent et al. there is of lot of attention for properly qualifying the demixing phenomena in colloid–polymer mixtures [94–98]. These experiments were ahead of a full theoretical understanding of the phase behaviour of colloid–polymer mixtures. One of the systems studied were polystyrene spheres with terminally attached PEO brushes dispersed in mixtures of free PEO and water for a wide range of concentrations. Both in pure water and in pure PEO melts the spherical particles were stable. However, in mixed solutions of PEO and water (for instance 50% water and 50% of PEO) a 'slow flocculation' of the particles was observed. The maximum flocculation rate was measured and was found to shift to lower PEO concentrations upon increasing the molar mass. This restabilisation at very high polymer concentrations (reported in a series of papers [94–99]) was also found in a dispersion of grafted silica spheres mixed with polydimethyl siloxane (PDMS) polymer chains. Only polymer melts that are sufficiently liquid-like allow studying such very high polymer concentrations because other polymers would be too viscous for a proper analysis of the phase behaviour.

In the same period, Hachisu et al. [100] investigated aqueous dispersions of negatively charged polystyrene latex particles that undergo a colloidal fluid-to-solid phase transition upon lowering the salt concentration using dialysis or increasing the particle concentration. Under conditions where the latex dispersion (particles with $R = 170\,\text{nm}$) is not ordered (fluid-like), Kose and Hachisu [101] added sodium polyacrylate to polystyrene latex particles (both components are negatively charged), and observed crystallization of the colloidal spheres, see Fig. 1.16. Since polymers and particles repel each other the crystallization process is probably induced by depletion interaction, although the authors themselves did not mention depletion as such. They do suggest that the ordering is due to 'some attractive force'. When the polymer concentration is increased crystallization occurs faster, see Fig. 1.17.

Theoretical work on depletion interactions and their effects on macroscopic properties such as phase stability commenced along various routes. First, Vrij [40] considered the depletion interaction between hard spheres due to dilute non-adsorbing polymers such as penetrable hard spheres (see Sect. 1.2.5 and Sect. 2.1). Vrij [40] referred to the work of Vester [82], Li-In-On et al. [55] and preliminary experiments at the Van't Hoff Laboratory on micro-emulsion droplets mixed with free polymer [40] for experimental evidence of depletion effects.

Progress on the depletion layer thickness was triggered by 1991 Noble Prize winner De Gennes. In his seminal book [102], De Gennes derived an expression

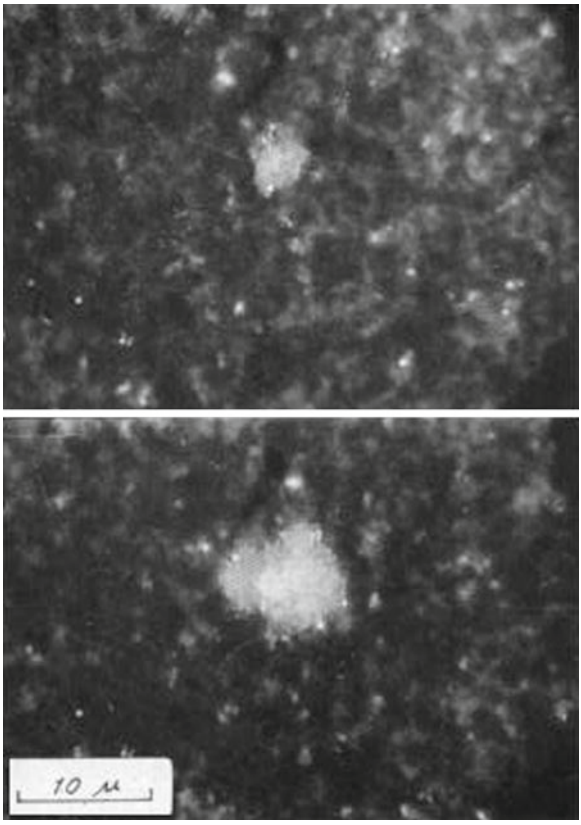

Fig. 1.16 Microscopic image of a mixture of monodisperse polystyrene latex particles 25 min (*top*) and 55 min (*bottom*) after adding 185 mg/L sodium polyacrylate polymers. Picture reprinted from A. Kose and S. Hachisu, *J. Colloid Interface Sci*., 55:487, 1976, with permission from Elsevier

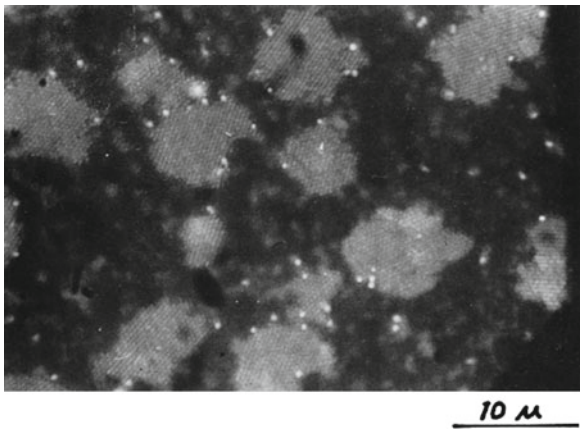

Fig. 1.17 Micrograph taken 25 min after mixing polystyrene latex particles with 370 mg/L sodium polyacrylate. Picture reprinted from A. Kose and S. Hachisu, *J. Colloid Interface Sci*., 55:487, 1976, with permission from Elsevier

for the density profile of a semi-dilute polymer solution near a (non-attractive) wall and demonstrated that the depletion thickness equals the correlation length, the length scale over which the polymer segments are correlated. In dilute polymer

solutions (below coil overlap) it is the radius of gyration. However, in semi-dilute solutions (above overlap) the correlation length becomes independent of the chain length and is a (decreasing) function of the polymer concentration. Hence, also the depletion thickness decreases with polymer concentration in the semi-dilute regime. De Gennes considered the depletion contact potential between two colloidal hard spheres in a semi-dilute polymer solution in a good solvent. For this case, where the only relevant length scales are the sphere radius R and the correlation length ξ, he derived the following scaling relation for the minimum of the interaction potential [103]:

$$\frac{W_{dep}(h=0)}{kT} \cong \begin{cases} -\frac{R}{\xi} & R \gg \xi \\ -\left(\frac{R}{\xi}\right)^{4/3} & R \ll \xi \end{cases}, \tag{1.28}$$

with an unknown prefactor $O(1)$.

Exercise
What is expected with respect to colloidal stability of large ($R \gg \xi$) and tiny ($R \ll \xi$) colloidal spheres in a semi-dilute polymer solution?

Depletion effects have been studied using mean-field methods since the end of the 1970s. Insights into polymer physics have increased tremendously through the development of mean-field theories, which allow both to include excluded-volume interactions and give insights in details of the configurations of polymers. A detailed analytical mean-field treatment for depletion interaction was made by Joanny et al. [104] who calculated the polymer segment concentration profile between two plates in the semi-dilute regime, in agreement with De Gennes' scaling prediction discussed above.

Using a Flory–Huggins-like mean-field model, Feigin and Napper [105] calculated the free energy of interaction between two flat plates mediated by non-adsorbing polymers and noted that a repulsive barrier is present for polymer concentrations in the concentrated regime. The potential at plate contact is, however, still attractive. These authors suggested that if the repulsive barrier is large enough this might lead to so-called depletion stabilization; a colloidal dispersion is destabilized at low polymer concentrations but restabilized at high concentrations. A conceivable intuitive explanation is kinetic: at high polymer concentrations it is hard to push polymer chains out of the gap between two particles. The bulk osmotic pressure is very high in a concentrated polymer solution. The polymer chains between the particles thus need to be transported towards a very steep osmotic pressure gradient.

Scheutjens and Fleer [106] developed a numerical self-consistent field (SCF) method that enables the calculation of equilibrium SCF concentration profiles near interfaces. This SCF method was applied to depletion effects in Ref. [107], showing that the depletion layer thickness is close to R_g at low polymer concentrations, but

decreases with increasing polymer concentration in the semi-dilute regime. In the concentrated regime, very close to the melt concentration, the polymer concentration between two parallel plates oscillates around the bulk polymer concentration. This finding is supported by Monte Carlo computer simulations of Broukhno et al. [108]. The interaction potential between the plates was calculated as well by Scheutjens and Fleer [107]. For dilute polymer solutions the range of the potential is close to $2R_g$ and the depth of the potential increases with increasing solvent quality. When the volume fraction of polymer segments in the system is 0.1 (a very high polymer concentration in practice), a weak repulsive part appears in the interaction potential appears as also found by Feigin and Napper [105]. This repulsion appears at lower concentrations for better solvent quality [17, 107].

A direct link between theoretical and experimental work on depletion-induced phase separation of a colloidal dispersion due to non-adsorbing polymers was made by De Hek and Vrij [56, 109]. They mixed sterically stabilized silica dispersions with polystyrene in cyclohexane and measured the 'limiting polymer concentration' (phase separation threshold). Commonly, one uses the binodal or spinodal as experimental phase boundary. A binodal denotes the condition (compositions, temperature) at which two or more distinct phases coexist, see Chap. 3. A tie-line connects two binodal points. A spinodal corresponds to the boundary of absolute instability of a system to decomposition. At or beyond the spinodal boundary infinitesimally small fluctuations in composition will lead to phase separation. De Hek and Vrij [56] used the pair potential (1.21) to estimate the stability of colloidal spheres in a polymer solution by calculating the second osmotic virial coefficient B_2:

$$B_2 = 2\pi \int_0^\infty r^2(1 - \exp[-W(r)/kT])dr, \tag{1.29}$$

where we used the centre-to-centre distance r between the spheres which equals $2R + h$. A simple argument was used to estimate the spinodal curve [56]. For colloid or polymer concentrations [110] exceeding the spinodal, phase separation occurs spontaneously. At the spinodal therefore,

$$\frac{\mathrm{d}P}{\mathrm{d}\phi} = 0. \tag{1.30}$$

The virial expansion for the osmotic pressure P of a colloidal dispersion reads

$$\frac{Pv_0}{kT} = \phi + B_2^*\phi^2 + \text{higher order } \phi\text{-terms}. \tag{1.31}$$

with $B_2^* = B_2/v_0$. Here v_0 is the volume of the colloidal sphere. In the limit of low ϕ, (1.30) and (1.31) provide

$$1 + 2B_2^*\phi^{sp} = 0. \tag{1.32}$$

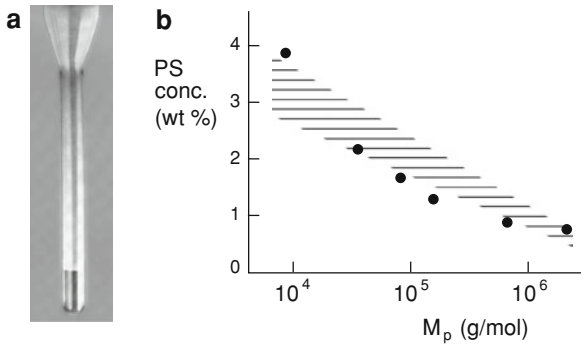

Fig. 1.18 **a** Photograph of a test tube containing a phase-separated mixture of polystyrene polymer chains (molar mass 32,410 g/mol) and sterically stabilized silica spheres ($R = 21$ nm) in cyclohexane. Initial concentrations: 1 wt % of silica spheres and 2.5 g/L polystyrene. The concentration below which no phase separation was found is 17 g/L. The two demixed phases are separated by a sharp interface. Picture reprinted from H. De Hek and A. Vrij, *J. Colloid Interface Sci.*, 70:592, Copyright 1979, with permission from Elsevier. **b** State diagram of 1 wt% silica spheres ($R = 46$ nm) in cyclohexane mixed with polystyrene polymer chains varying in molar mass M_p [56]. The limiting polystyrene concentrations below which no phase separation occurred are indicated as the filled circles. *Hatched region* theoretical limits between which the spinodal curve is situated

This relates the polymer activity (which determines B_2) to the colloid volume fraction ϕ^{sp} at the spinodal. De Hek and Vrij [56] could give a good description of the phase line of mixtures of polystyrene chains plus small volume fractions of (hard-sphere like) octadecyl silica spheres dispersed in cyclohexane [109].

In Fig. 1.18 we depict results obtained on a mixture of octadecyl silica spheres and polystyrene polymers in cyclohexane. Both separated phases are fluid. The limiting polymer concentration below which no phase separation occurs in a solution containing a given amount of silica is plotted versus the molar mass of the added polymer polystyrene. It was found that less polymer is required to induce a phase separation when the molar mass is larger. This experimental trend can be predicted by using the spinodal condition (1.32), but this is only a semi-quantitative test because in fact the binodal condition is required. Formally one should compare the stability curve with the binodal. The compositions of the phases in a demixed dispersion locate the binodal curve. The spinodal is however not too far off from the binodal and probably gives a good and simple estimate. For the smallest molar mass, the separated phase was gel-like instead of a fluid. A statistical mechanics calculation of ideal polymer chains between two walls by De Hek and Vrij [56] demonstrated that the range of attraction between two flat parallel plates due to ideal polymer chains is close to $2.25R_g$, implying a depletion thickness at each plate of about R_g.

A light scattering contrast variation study on elucidating the negative adsorption of polystyrene chains next to a silica sphere in cyclohexane solutions was

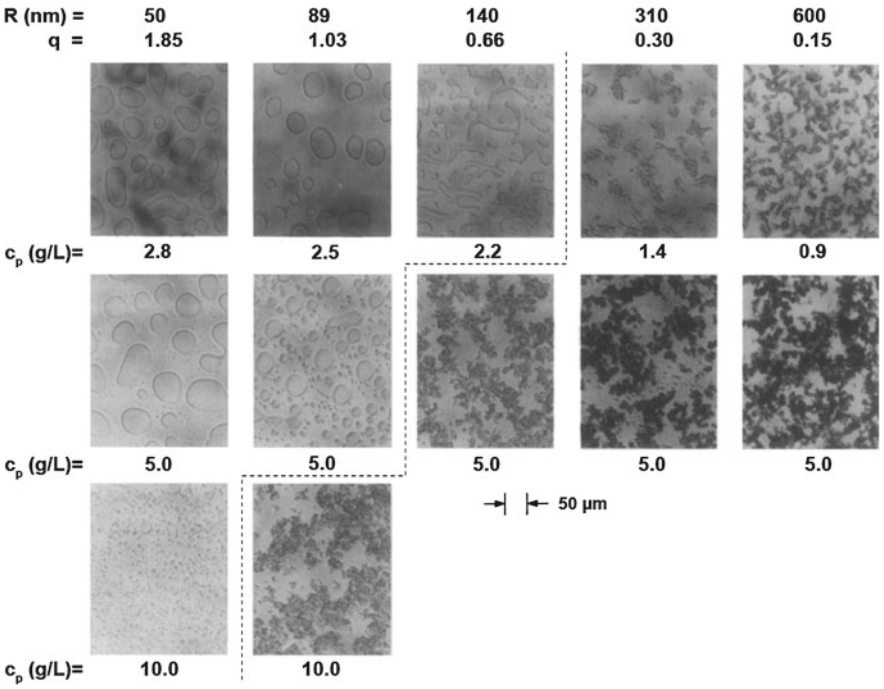

Fig. 1.19 Micrographs of latex colloids mixed with HEC by Sperry [112–114]. Picture reprinted from P. R. Sperry, *J. Colloid Interface Sci.*, 99:97, Copyright 1984, with permission from Elsevier

described in another paper by de Hek and Vrij [111]. This negative adsorption can be converted to a depletion thickness, which is close to the radius of gyration of polystyrene in cyclohexane. From the light scattering experiments the second virial coefficient of the silica particles could be determined and its value was shown to become negative (implying attraction between the spheres) when a sufficient amount of non-adsorbing polystyrene is added.

By mixing aqueous hydroxyethylcellulose (HEC) with latex, Sperry [112, 113] and coworkers [114] observed phase separation and made a study on the effect of the structure of the colloid-rich phase as a function of the colloid–polymer size ratio $q = R_g/R$. The micrographs in Fig. 1.19 of phase separating mixtures demonstrate how the morphology of the segregating systems varies upon changing q and polymer concentration. Unstable systems at large q and not too high polymer concentrations are characterized by smooth interfaces, implying colloidal gas–liquid coexistence. For small q, demixed systems are characterized by irregular interfaces that indicate (colloidal) fluid–solid coexistence. This suggests that the width of the region where a colloidal liquid is found in colloid–polymer mixtures is limited. We return to this issue in Sect. 4.3. As the polymer concentration is increased substantially, irregular interfaces are also detected for $q > 1/3$.

1.3.5 1983–1989

The work of Sperry inspired Gast, Hall and Russel to develop a theory which might explain the experimental phenomena. Gast et al. [115] used thermodynamic perturbation theory (TPT) [116] to derive the free energy of a mixture of colloidal particles and polymers (described as phs; penetrable hard spheres), based on pairwise additivity of the interactions between the colloids. This is an approach which is based upon a perturbation from the free energy of a pure colloidal dispersion due to depletion forces, with (1.21) as input. Using equations of state for the hard-sphere fluid and the fcc-crystal structure as references, they calculated the phase behaviour from the (perturbed) free energy. This made it possible to assign the nature (i.e. colloidal gas, liquid or solid) of the coexisting phases as a function of size ratio q, the concentration (or formally activity within their approach) of the polymers, and the volume fraction of colloids. For small values of q, say, $q = R_g/R < 0.3$, increasing the polymer concentration broadens the hard sphere fluid–solid coexistence region; a (stable) colloidal fluid–solid coexistence is expected if the polymer chains are significantly smaller than the colloidal spheres (low q). Inside the unstable regions a (metastable) colloidal gas–liquid branch is located. For intermediate values of q, the gas–liquid coexistence curve crosses the fluid–solid curve and for large q-values mainly gas–liquid coexistence is found for $\phi < 0.49$, where ϕ is the volume fraction of colloids [110]. The results are in agreement with the findings of Sperry [112–114]. Experimentally, Gast, Russel and Hall [117] later verified the predicted types of phase coexistence regions for a model colloid–polymer system. Colloid–polymer phase diagrams [110] are commonly plotted in terms of the volume fraction of colloids ϕ and the *relative* polymer concentration ϕ_p, defined in (1.24).

Exercise
Use the Gibbs phase rule and derive how many phase states a system can assume when it consists of two components.

In both the descriptions by De Hek and Vrij and by Gast, Russel and Hall, the depletion thickness δ was assumed to be equal to the radius of gyration. This assumption was rationalized by Eisenriegler [118]. He calculated the density profile of ideal chains near a flat surface and from this density profile it follows that $\delta/R_g = 2/\sqrt{\pi} \approx 1.13$ [119], see Sect. 2.2.

Experimental work on the determination of the depletion layer thickness commenced in this period. The depletion thickness δ of polystyrene at a non-adsorbing glass plate was measured using an evanescent wave technique by Allain et al. [120]. The value found for δ was indeed close to the radius of gyration of the polymer. Ausserré et al. [121] measured the depletion thickness of xanthan (a polysaccharide) at a quartz wall below and above the polymer overlap concentration. In dilute solutions, below overlap, δ was close to the radius of gyration of

xanthan, whereas in the semi-dilute regime, i.e. above overlap ($\phi_p > 1$), it decreases as $\delta \sim \phi_p^{-0.8}$. This is in accordance with what is expected theoretically, see Sects. 4.3.1 and 4.3.2.

Attempts to measure depletion forces were made by Luckham and Klein [122, 123] who could not measure a depletion force with the surface force apparatus. They measured the interaction between two mica plates in the presence of non-adsorbing polystyrene in toluene. Pashley and Ninham [124] did succeed in measuring the depletion potential between mica plates as induced by CTAB micelles.

1.3.6 1990–1999

The polymer density profile of ideal chains next to a hard sphere for arbitrary size ratio q was first calculated by Taniguchi et al. [125] and later independently by Eisenriegler et al. [126]. Eisenriegler also considered the pair interaction between two colloids for $R_g \ll R$ [127] and for $R_g \gg R$ [128], as well as the interaction between a sphere and a flat wall due to ideal chains [129]. Depletion of excluded volume polymer chains at a wall and near a sphere was considered by Hanke et al. [130]. One of their results is that the ratio δ/R_g at a flat plate, which is 1.13 for ideal chains [118, 119], is slightly smaller (1.07) for excluded-volume chains.

Inspired by the work of De Gennes [102, 103], fundamental work commenced on colloid–polymer mixtures in which the polymers are relatively large compared to the colloids. This regime is relevant for mixtures of polymer or polysaccharides mixed with proteins and is often denoted as the *protein limit* ($q > 1$). The opposite case (small q) is known as the *colloid limit*. We distinguish three regimes, see Fig. 1.20, in colloid–polymer mixtures: small q (also termed the 'colloid limit') of

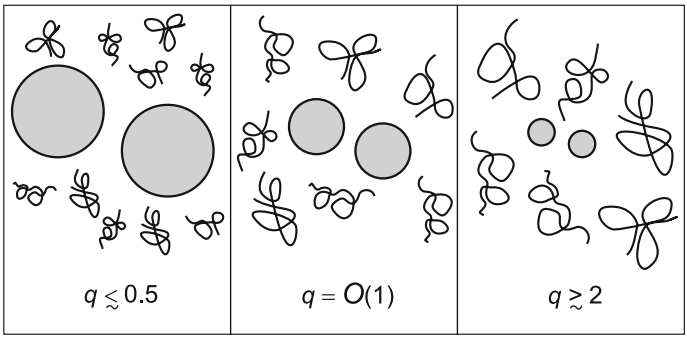

Fig. 1.20 Sketch of the different regimes size ratio in colloid–polymer mixtures. *Left* the 'colloid limit' of relatively small polymer chains. *Middle* the equal size regime. *Right* the 'protein limit' regime of relatively large polymer chains

$q \lesssim 0.5$, 'equal sized' $(0.5 < q < 2)$ and the large q regime (also termed the 'protein limit') of $q \lesssim 2$.

Odijk [131–134] published a relevant series of papers devoted to the protein limit $\xi \gg R$; he considered semi-dilute polymer solutions where the correlation length ξ scales as $\phi_p^{-3/4}$. He first calculated the density profile of a small colloid in a semi-dilute polymer solution with $\xi \gg R$ and found a very simple shape of the density profile that is independent of ξ and only depends on R [131]. By considering the second virial coefficient between a large polymer and a tiny colloid he concluded that phase separation is not expected in this case. This was confirmed later by Eisenriegler [135], who from renormalization group theory found that the second osmotic virial coefficient of small colloidal spheres, B_2, only marginally decreases with increasing polymer concentration up to the coil overlap concentration above which it increases. Odijk [132] also considered many-body effects by involving void–void correlations and statistical geometrical approaches [136]. He concluded that the depletion-induced interaction between small colloids due to large semi-dilute polymers levels off to a maximum attraction near a volume fraction $\phi \sim 0.3$. Odijk [134] and Eisenriegler [137–140] also extended the approach of polymer depletion and small colloids towards colloids with ellipsoidal shape to mimic proteins.

A semi-grand canonical treatment for the phase behaviour of colloidal spheres plus non-adsorbing polymers was proposed by Lekkerkerker [141], who developed 'free volume theory' (also called 'osmotic equilibrium theory'), see Chap. 3. The main difference with TPT [115] is that free volume theory (FVT) accounts for polymer partitioning between the phases and corrects for multiple overlap of depletion layers, hence avoids the assumption of pair-wise additivity which becomes inaccurate for relatively thick depletion layers. These effects are incorporated through scaled particle theory (see for instance [136] and references therein). The resulting free volume theory (FVT) phase diagrams calculated by Lekkerkerker et al. [142] revealed that for $q < 0.3$ coexisting fluid–solid phases are predicted, whereas at low colloid volume fractions a gas–liquid coexistence is found for $q > 0.3$, as was predicted by TPT.

A coexisting *three*-phase colloidal gas–liquid–solid region, not present in TPT phase diagrams, was predicted by FVT for $q > 0.3$ and gained much attention. Experimental work [143, 144] demonstrated that this three-phase region does indeed exist. Both Ilett et al. [143] and Leal-Calderon [144] measured phase diagrams of colloid–polymer mixtures as a function of the size ratio q. The topology of the phase diagrams correspond well to FVT predictions, as long as q is below 0.6, see Chap. 4.

As another example of a three-phase system, photographs of dispersions containing 16 vol% polystyrene latex spheres (with a diameter of 67 nm), published by Faers and Luckham [145], are reproduced in Fig. 1.21. The numbers shown represent the concentration (in wt%) of the polysaccharide hyroxyethylcellulose (HEC). In the dispersion with 0.3 wt% of HEC three phases coexist. From top to bottom colloidal gas, liquid and solid phases can be recognized. The rigidity of the

solid–liquid interface is demonstrated in the lower photographs where the tubes are tilted. The gas–liquid interface flows upon tilting the sample, for the gas–solid interface this is not the case. Using the theory of Lekkerkerker et al. [142] it is also possible to calculate the tie-lines along which the system demixes, enabling a comparison of the theory with experimental phase boundaries. For small q the theory describes the experimental phase diagrams rather accurately [143]. FVT for colloidal spheres mixed with penetrable hard spheres was tested with computer

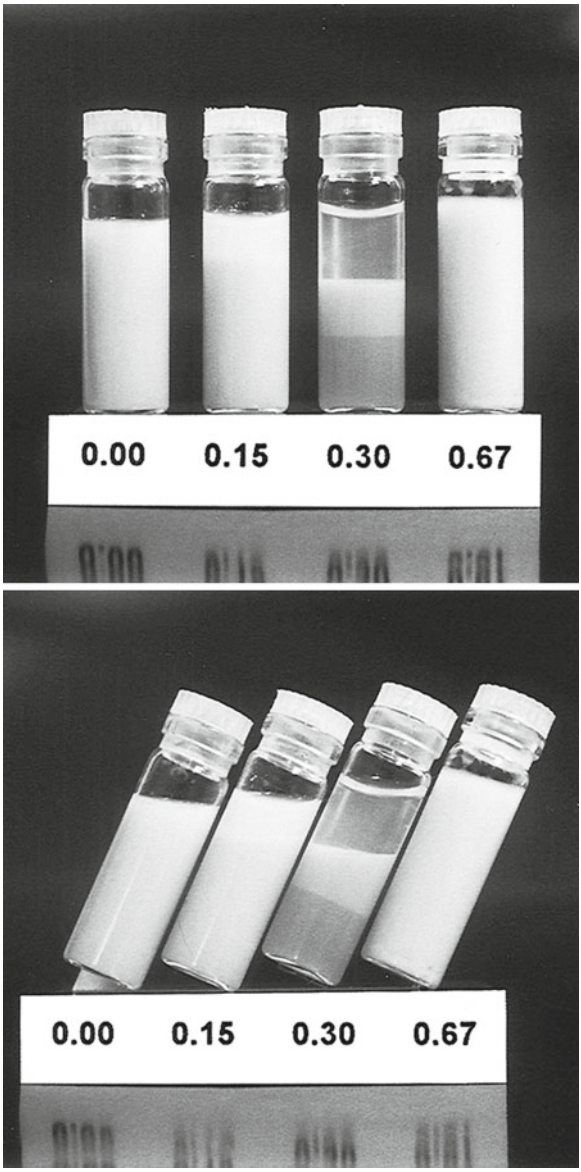

Fig. 1.21 Photograph of a polystyrene latex dispersion (16 vol%) in 10 mM NaCl at pH 7 with (as indicated in wt%) added hydroxyethyl cellulose (HEC) studied by Faers and Luckham [145]. In the lower photograph the tubes are tilted demonstrating the difference between rigid colloidal solid–liquid and fluid colloidal gas–liquid interfaces for the three-phase coexistence at 0.3 wt% HEC. Reprinted from M. A. Faers and P.F. Luckham, *Langmuir*, 13:2922, Copyright 1997, with permission from the American Chemical Society and the authors

simulations on a dispersion of spheres immersed in a solution of ideal lattice polymer chains by Meijer and Frenkel [146]. Their simulation results showed that for small values of q the agreement with the osmotic equilibrium theory of Lekkerkerker et al. [142] is very good.

Faers and Luckham [145] also studied the effect of the amount of polymer grafted onto the colloid surfaces. Decreasing the amount of grafted polymer increased the phase separation concentration of polymers at fixed colloid concentration, demonstrating that it is worthwhile to investigate the effect of the presence of brushes in combination with non-adsorbing polymers.

Polymers are often added to oil-in-water emulsions in order to impose a certain emulsion viscosity. This may however lead to instability problems as is known in food emulsions [28, 147]. Bibette et al. [148–150] were the first to quantitatively relate phase transitions in emulsions due to non-adsorbing polymers to depletion-induced forces. They showed that it is possible to size fractionate an emulsion with a depletion-induced phase transition. An interesting aspect of (micro) emulsion droplets is that they are not hard spheres, as assumed in FVT [142]. Several groups [40, 151–153] studied the phase behavior of droplets in a micro-emulsion mixed with non-adsorbing polymers. The phase behavior could be explained by describing the micro-emulsion itself as a collection of sticky hard spheres rather than pure hard spheres. The colloid–polymer mixture is then described as a mixture of sticky spheres mixed with non-adsorbing polymers [151, 152]. For emulsions mixed with polymers the theory of Lekkerkerker et al. [142] was found to agree as regards the phase behavior for the colloid limit, as studied for instance by Meller and Stavans [154]. The B_2-approach of Vrij [40, 56] could explain the phase line measured for an aqueous mixture of casein micelles plus non-adsorbing exocellular polysaccharides by Tuinier and de Kruif [155]. However, often the polymer is larger (protein limit) or has a similar size as the spherical droplets in polymer/micro-emulsion mixtures. Then phase transitions occur near or above the polymer overlap concentrations. Obviously, the assumption $\delta = R_g$ is then no longer correct. For a proper description of the phase behavior in this case the effect of interactions between the polymers must be taken into account: more accurate descriptions of the depletion thickness and osmotic pressure as a function of the polymer concentration are needed.

Depletion potentials were first measured indirectly using scattering techniques [156, 157] and can nowadays be probed directly with high precision using a wide range of techniques [158–161], see Sect. 2.6. Confocal microscopy also allows to measure the potential of mean force between colloids in colloid–polymer mixtures as first performed by Royall et al. [162]. Depletion effects can also be quantified by measuring the spin–spin nuclear resonance time. Cosgrove et al. [163] performed such a study using a dispersion of silica with added sodium polystyrene sulfonate (NaPSS). The resonance time could be related to the depletion thickness, which decreased with increasing concentration of NaPSS.

When a colloid–polymer mixture phase separates into a colloid-rich and polymer-rich phase an interface appears in between. For a colloidal gas–liquid

interface it is possible to measure the interfacial tension using a number of techniques. The value of the interfacial tension [164] is interesting since it is related to phase separation kinetics, see Sect. 4.5. The spinning drop method was successfully used in the past to determine the interfacial tensions in demixed colloid–polymer mixtures [165, 166], yielding tensions with values of a few μN/m corroborating the relation between the interfacial tension expressed in (1.27). The order of magnitude of the data of De Hoog and Lekkerkerker [166] were comparable with the theoretical results of Vrij [164], Van der Schoot [167] and of Brader and Evans [168]. From the results of Chen et al. [169] it follows that the interfacial tension increases with the distance from the critical point, in agreement with scaling theory [84]. Using ellipsometry and break-up of an elongated droplet in a centrifugal field De Hoog et al. [170, 171] demonstrated that the value of the measured interfacial tension was independent of the method used. Overall, it can be concluded that the colloidal and the 'molecular' gas–liquid interface behave similar. The difference is that the interface tension between a colloidal liquid and gas is ultralow.

1.3.7 2000–2010

Until the end of the 1990s most theoretical approaches were based on describing polymer chains as ideal or as penetrable hard spheres. Especially at the turn of the last century a wealth of different approaches were proposed to describe colloid–polymer mixtures in which interactions between polymer segments were accounted for. Essential was the progress made in Monte Carlo computer simulation studies on depletion effects [172–179] to test such theories.

Despite the success of FVT in predicting the phase diagram of colloid–polymer mixtures for the colloid limit (small q) (semi-)quantitatively, in the protein limit (high q) the FVT predictions were far less convincing: it could give only qualitative information for large q. Quantitative deviations from FVT appear for $q > 0.5$, as follows from comparing FVT with Monte Carlo computer simulations [176, 177] and experiment [143, 153, 166, 180–185]. In conclusion, FVT predicts binodal curves at too small polymer concentrations for large q, see Sect. 4.1.

Under conditions where the polymer chains are much larger than the colloidal particles, such as mixtures of proteins [186] or micro-emulsion droplets [153, 184] mixed with large polymers (or polysaccharides) instability does occur at rather high polymer concentration. In such situations it does not suffice to stick to the classical Asakura-Oosawa-Vrij description. Van der Schoot [187] showed that polymer collapse can take place when adding small colloids to a polymer solution. He derived an expression for the free energy of a polymer solution in a good solvent in the presence of small colloidal spheres and showed that adding colloids leads to a distortion of the conformational entropy of a polymer chain. Effectively, adding spheres thus turns the solvent quality from a good to a bad solvent. As a consequence, a polymer chain is expected to collapse above a certain colloid

concentration. This effect originates from the mutual exclusion of polymer segments and colloidal spheres. Experimental work confirms shrinkage of a polymer chain caused by adding nanospheres [188–190]. Computer simulations of large polymer chains in a system with random small obstacles by Wu et al. [191] are in line with polymer shrinkage due to added nanospheres: the size of the polymers was found to decrease when small particles are added.

The polymer reference interaction site model (PRISM) is a continuous space liquid state approach that allows to compute the equilibrium properties of polymeric systems [192]. Integral equations methods [12] are widely employed to understand structure, thermodynamics in atomic, colloidal, and small molecule fluids, and have been generalized to treat macromolecular materials in the 1990s. More recently, it has been extended towards a description for the structural and microscopic properties of colloid–polymer mixtures [193–195]. The results heavily rely on the accuracy of approximate closure relations. PRISM gives a good description of the second osmotic virial coefficient of proteins with added non-adsorbing polymer chains. Predictions of full phase diagrams including binodals are still too involved computationally. It can be used to predict spinodal curves, which are quite close to binodals. The measured binodals of Ramakrishnan et al. [196] agree well with spinodals computed with PRISM.

Several liquid state theories have been developed that are based on *effective* potentials [197] from which the thermodynamic properties of many-body systems can be computed. Louis and Bolhuis et al. [174, 198–202] developed a Gaussian core model (GCM) for interacting polymer chains. In this model the polymer chains are replaced with spherical particles with a soft repulsion. This model enables studying structure, depletion interactions and the full phase behaviour (in combination with Monte Carlo computer simulations). Basically, the theory is a liquid state approach. On the level of the depletion interaction mediated by interacting polymers they showed that their GCM agrees very well with Monte Carlo computer simulations [198, 202], except for a slight oscillation in the density profile in case of Gaussian cores due to their 'particle' character. In the colloid limit, GCM predictions for the phase diagram of colloid–polymer mixtures are similar to those for free volume theory. For larger q-values FVT predicts phase separation at smaller polymer concentrations as compared to the GCM.

Density functional theory [203] in combination with fundamental measure theory [204, 205] has been used to study the interactions in and structure and phase behaviour of colloidal systems [206], colloid–polymer mixtures [168, 207, 208] and star polymer plus polymer mixtures [209]. Within density functional theory (DFT) the polymers are commonly treated as penetrable hard spheres. Oversteegen and Roth [210] discussed the close analogy and discrepancies between FVT and fundamental measure theory. For asymmetric additive hard sphere mixtures DFT can be exploited to study the influence the degree of repulsive interaction (the 'additivity') between the small spheres on the interaction between the large spheres. From self-avoiding walk computer simulations it follows that the degree of additivity of excluded volume polymers is very small [198, 211]. Interestingly, DFT also allows studying the colloidal gas–liquid interface of a demixed

dispersion. This made it possible to evaluate the interfacial tension; for a review on the possibilities of DFT for studying colloid–colloid and colloid–polymer mixtures, see [212].

It appears that the phase diagram for very small q ($q < 0.3$) is much simpler than for larger q [144–145, 213, 214]. For small q the only effect of adding polymer chains to the pure hard-sphere dispersion is the widening of the fluid–solid coexistence region. A gas–liquid phase transition occurs at larger polymer concentrations above the fluid–solid phase line and is metastable, see Sect. 3.3.4. Only above a certain range of attraction, the (colloidal) gas–liquid phase transition shifts below the fluid–solid coexistence curve. For q close to 1/3 the critical point hits the fluid–solid coexistence curve. This critical point is the *critical endpoint*, which is rather insensitive to the shape of the interaction potential used [215].

In the protein limit ($q > 2$) the phase behaviour is dominated by the gas–liquid phase transition at low colloid volume fractions ϕ. Colloidal gas–liquid coexistence concentrations have been determined using Monte Carlo simulations by Bolhuis, Meijer and Louis [177] on hard spheres plus self-avoiding walk polymer chains consisting of segments with hard-sphere interactions. For three q-values coexistence data are shown in Fig. 1.22. Phase transitions then take place near and above the polymer overlap concentration ($\phi_p \geq 1$). In such cases a more detailed description of the physics of polymer solutions is required to describe depletion forces and the resulting phase transitions. TPT has been extended to incorporate interactions between the polymer chains [216]. This indeed shifts the binodal curves for larger q to higher relative polymer concentrations. It is also possible to extend FVT and incorporate the effects of interactions between the polymer chains [217–220], see Sect. 4.3. This generalized free volume theory (GFVT) includes the correct dependencies for the depletion thickness and the osmotic pressure on polymer concentration for interacting chains and gives a good description of colloid–polymer phase diagrams of model systems up to large q [220]. GFVT is in

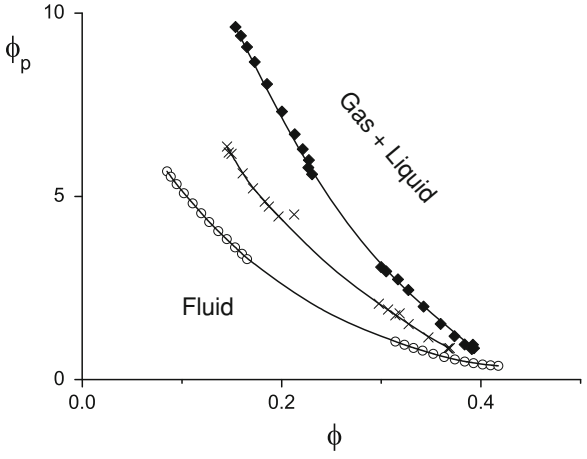

Fig. 1.22 Monte Carlo computer simulation results for the gas–liquid coexistences of hard spheres mixed with excluded volume polymers for q = 3.86 (*open circles*), 5.58 (*crosses*) and 7.78 (*filled diamonds*), redrawn from Bolhuis et al. [177]. The binodal curves are drawn to guide the eye

(semi)quantitative agreement with experiments and computer simulations [219, 220].

Most of the models for depletion of polymer are based upon the assumption that the polymer segments are always much smaller then the colloids. Depletion of freely-jointed chains near a spherical colloid can also be considered for arbitrary size of the segment, showing that depletion effects get weaker as the segments become longer (for a fixed value of the polymer's radius of gyration) [221]. This is in agreement with work of Paricaud, Varga and Jackson [222] who used Wertheim perturbation theory.

In this last decade also more insight was gained on the ultra-low interfacial tension at the colloidal gas–liquid interface in demixed dispersions containing colloids and polymers. It became clear that this ultra-low interfacial tension affects the relevant characteristic length- and timescales [223]. The capillary length [224] decreases down to the order of microns while the thermal length can become of the order of (sub)microns. The typical interface velocity in such systems is just a few microns per second. Inertial terms only become important at large length- and timescales. By means of confocal scanning laser microscopy Aarts et al. [59] studied the influence of the ultra-low interfacial tension on wetting of colloid–polymer mixtures on a solid surface and on capillary waves at the interface of a demixed colloid–polymer dispersion [225]. Studies on the bending rigidity of the colloidal gas–liquid interface in a demixed colloid–polymer dispersion are in progress [226].

In this overview on the history of depletion in colloidal dispersions we have focused on mixtures of colloidal spheres and non-adsorbing polymers, which have received most attention. Since the 1990s depletion phenomena have also been studied systematically in dispersions of colloidal rods [227, 228], platelets [229], rocks [230] (colloidal particles with an irregular surface) or cubes [231] plus non-adsorbing polymers or in mixtures of different colloids with large size asymmetry [232–235]. In Chap. 5 we concentrate on mixtures of colloidal large spheres plus added small spheres or added colloidal rods. Finally, in Chap. 6 we concentrate on the phase behaviour of colloidal rod plus polymer dispersions.

1.4 Manifestations of Depletion Effects of Biological and Technological Interest

By the addition of non-adsorbing polymers to colloidal suspensions the mixture phase separates into a colloid-rich and a polymer-rich phase, as discussed above. The understanding of this polymer-induced phase separation is very important, not only for colloid science but also for industrial systems, such as food dispersions [74, 77, 236, 237]) and paint [238]. In these systems colloids and polymers (or surfactants) are jointly present and influence the stability and hence related processing issues.

More recently, is has been realized that procedures based on the depletion interaction have the potential to enable fabrication of materials based on self-organized colloidal structures [239]. Also in biological systems, the importance of depletion effects are increasingly appreciated [240, 241]. To illustrate this, we discuss a few examples of depletion effects in systems of biological and technological interest in this section.

1.4.1 Depletion Effects in Biological Systems: Macromolecular Crowding

A longstanding question in molecular biology is the extent to which the behaviour of macromolecules observed in vitro accurately reflects their behavior in vivo [242]. The cytoplasm of a living cell contains a high concentration of macromolecules (up to 400 g/L), including proteins and nucleic acids. Over the last 30 years or so [243–245] it has been increasingly appreciated that the large volume fraction occupied by these macromolecules influences several intracellular processes [241, 246, 247], ranging from the bundling of biopolymers like DNA and actin to the phase separation in a bacterial cell. These effects are known amongst biochemists and biophysicists as *macromolecular crowding* (for reviews see [240, 248–250]).

Phase separation between a nucleoid and cytoplasm in bacterial cells is a striking example of macromolecular crowding [251–254]. Chromosomes in bacterial cells do not occur in dispersed form but are organized in the nucleoid as a separate phase. Depletion forces that originate from the presence of proteins can explain the phase separation [254]. As a result, the proteins partition over the cytoplasm and nucleoid phases. Their concentration in the cytoplasm is about two times larger than their concentration in the nucleoid phase [255], see Figs. 1.23 and 1.24.

Depletion forces can be of use in biomedical applications. Non-adsorbing polymer chains promote the adhesion of cells to surfaces [256] and enhance adsorption of lung surfactants at the air/water interface in lungs so as to help patients suffering from acute respiratory syndrome [257]. The physical properties of actin networks are affected by non-adsorbing polymers [258], which also modify phase transitions in virus dispersions [228].

1.4.2 Depletion Interactions and Protein Crystallization

In 1934 Desmond Bernal and Dorothy Crowfoot (later Hodgkin) discovered that crystals of pepsin, a digestive enzyme, give a well-resolved X-ray diffraction pattern [259]. It took 25 years before the first atomic structures of proteins using X-ray crystallography were determined. In 1958 Kendrew et al. published the

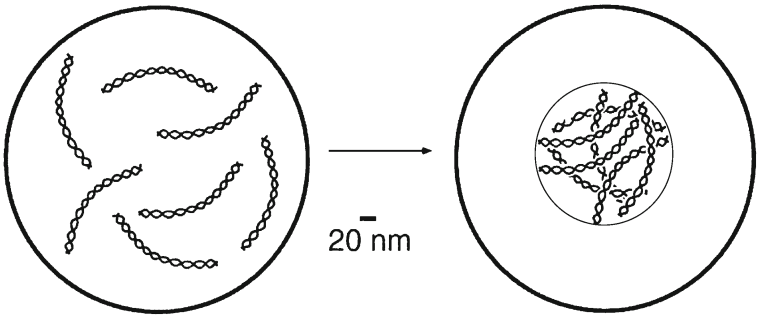

Fig. 1.23 Sketch of the cross-section of superhelical DNA in a cell. *Left* DNA is dispersed throughout the cell. *Right* DNA is confined within the nucleoid phase [255]. Reprinted from C. L. Woldringh and T. Odijk *in: Organization of the Prokaryotic Genome, R. L. Charlebois (Ed.)*. ASM Press, Amsterdam, Copyright 1999, with permission from ASM Press

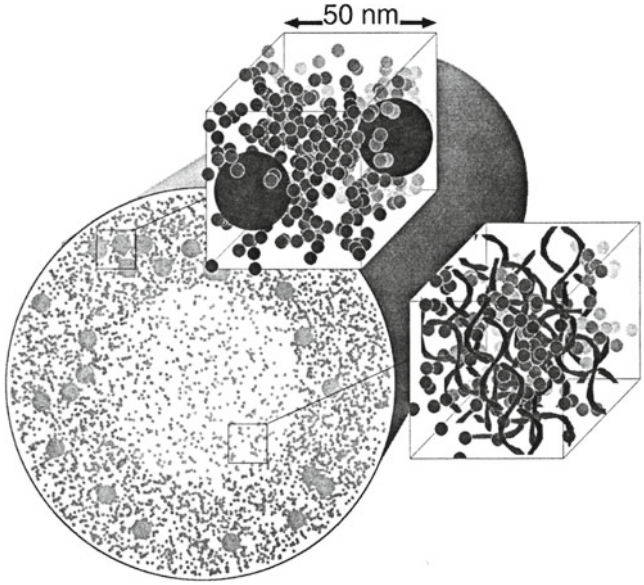

Fig. 1.24 Schematic picture of a cell containing phase separated nucleoid (cube on the *right*; magnifies DNA (*chains*) and proteins (*small spheres*) in this phase) and serum (*upper cube*; containing proteins and ribosomes as *big spheres*). Sketch by Woldringh and Odijk [255]. Reprinted from C. L. Woldringh and T. Odijk *in: Organization of the Prokaryotic Genome, R. L. Charlebois (Ed.)*. ASM Press, Amsterdam, Copyright 1999, with permission from ASM Press

structure of the protein myoglobulin [260], which stores oxygen in muscle cells and in 1960 Perutz et al. [261] reported the structure of the protein hemoglobin, which transports oxygen in blood.

The first requirement for protein structure determination with X-ray diffraction is to grow suitable crystals [262]. While great strides have been made in the

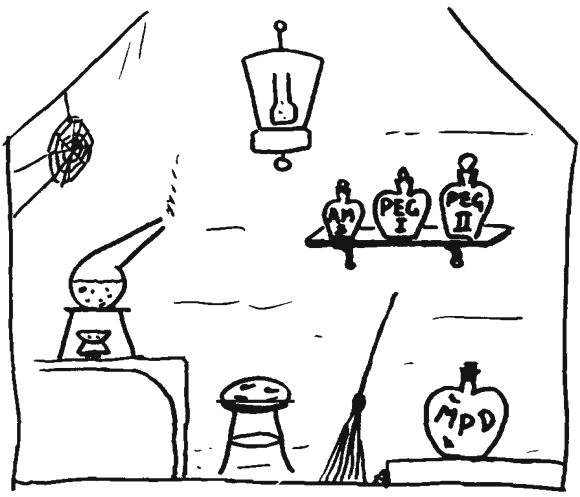

Fig. 1.25 View upon the 'art' of protein crystallization by J. Drenth [265]. Picture reprinted from J. Drenth, *J. Cryst. Growth*, 90:368, Copyright 1988, with permission from Elsevier

determination of protein structures (today about 60,000 protein structures have been resolved), protein crystallization, notwithstanding a history spanning more than 150 years [263, 264], remains somewhat magical.

Figure 1.25 characterizes the state of the art in protein crystallization in 1988 [265]. In recent years significant progress has been made in understanding protein crystallization on the basis of the phase diagram of protein solutions. The key observation which lies at the basis of this development was made by Benedek and co-workers [266, 267]. In the course of their investigations of proteins involved in maintaining the transparency of the eye lens, they discovered that in aqueous solutions of several calf lens proteins the solid–liquid phase boundary lies higher in temperature than the liquid–liquid coexistence curves. Thus, over a range of concentrations and temperatures for which liquid–liquid phase separation occurs, the coexistence of a protein crystal phase with a protein liquid solution phase is thermodynamically stable relative to the metastable separated liquid phases, see Fig. 1.26.

It was shown that this remarkable phase behaviour could be understood on the basis of the sensitivity to the form of the pair potential of the phase diagram of small attractive colloidal particles [268–270]. Moreover, it was soon realized that successful protein crystallization depends on the location (protein concentration and temperature) in the phase diagram [271–275]. Control of protein crystal nucleation around the metastable 'liquid–liquid' phase boundary appears key to the development of systematic crystallization strategies (for a concise review see [276]). This phase boundary can be manipulated by depletion interactions through the addition of non-adsorbing polymers such as polyethylene glycol.

To illustrate the role of non-adsorbing polymer chains on the protein solution phase behaviour we discuss the results of adding the polymer PEO (also termed PEG) to a solution with the protein apoferritin by Tanaka and Ataka [277]. Apoferritin is an iron storage protein consisting of 24 subunits. The effective radius

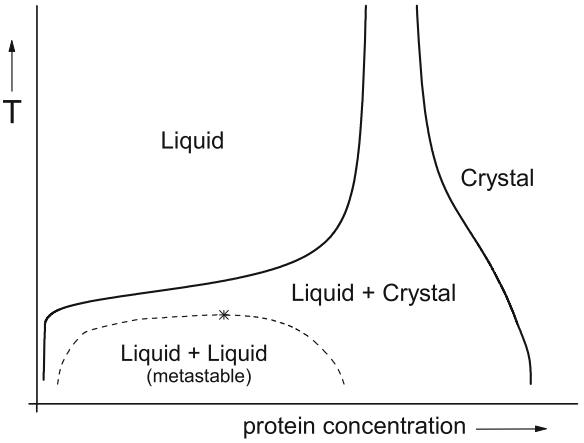

Fig. 1.26 Sketch of a typical phase diagram of a globular protein solution. The critical point is marked by the *asterisk*

is about 8 nm and the molar mass of apoferritin is 440 kg/mol. It is not easy to crystallize a solution of apoferritins by adding salt ions. Traditionally, a well-defined scale, known as the Hofmeister series [278], is used as a measure for the efficiency of precipitating proteins. A solution of apoferritin cannot be crystallized in the common manner with the usual salt ions as precipitating agents. Adding PEO, however, does make it possible to induce crystallization. In Fig. 1.27 the

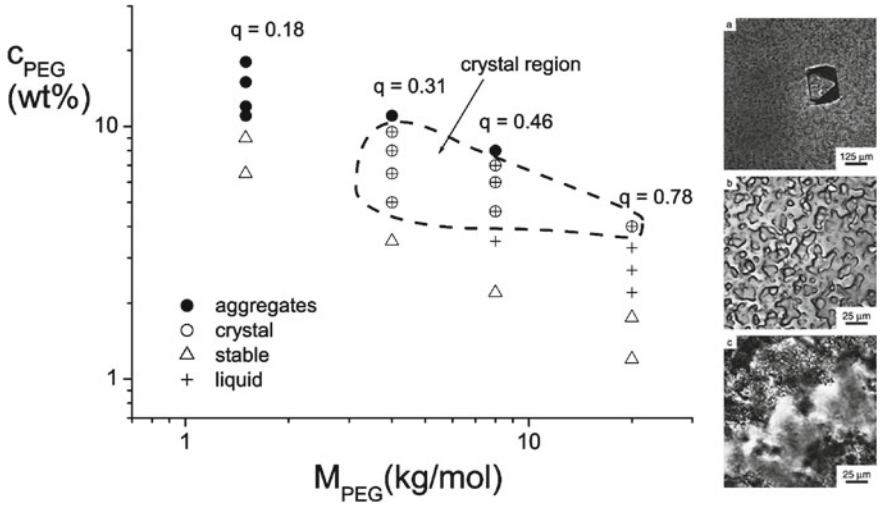

Fig. 1.27 Phase behavior of apoferritin with PEO. *Left* state diagram of apoferritin mixed with PEO of various molar masses. The apoferritin concentration was kept constant at 54 g/L and the molar mass and concentration of PEO was varied as indicated in the diagram. Results are redrawn from [277]. *Right* micrographs representing the various kinds of unstable solutions that were found in aqueous apoferritin–PEO mixtures: **a** crystals, **b** liquid domains and **c** random aggregates. Reprinted with permission from S. Tanaka and M. Ataka, *J. Chem. Phys*., 117:3504, Copyright 2002, American Institute of Physics

experimental data are shown that were obtained from visual and microscopic inspection of PEO-apoferritin in aqueous 0.6 M NaCl solutions. The concentration of apoferritin was fixed at 54 g/L. The PEO concentration and molar mass were varied. Four molar masses M_{PEG} (and radii of gyrations R_g) of the PEOs were used: 1.5 (1.4 nm), 4.0 (2.5 nm), 8.0 (3.7 nm) and 20 (6.2 nm) kg/mol, corresponding to $q = 0.18$, 0.31, 0.46, and 0.78. Four kinds of situations were observed after mixing PEO with apoferritins [277]. For sufficiently small concentrations (depending on M, hence q), the mixture was stable (triangles in the left panel of Fig. 1.27). Above a certain PEO concentration a phase transition took place. At $q = 0.18$ random aggregates (filled circles) were found, which is typical for a protein solution undergoing a fluid-to-solid transition, and does not give the proper conditions for obtaining good-quality crystals. The same happens for the highest concentrations at $q = 0.31$ and 0.46. For $q = 0.31$, 0.46 and 0.78 there was a region where liquid domains (plusses) were formed, indicative for a gas–liquid phase transition, usually referred to as liquid-liquid phase separation. For $q = 0.78$ liquid domains were found in the entire unstable regime. Finally, good quality crystals (open circles) were formed at $q = 0.31$ and 0.46 for intermediate PEO concentrations. For these q-values the critical point is close to the fluid-crystal coexistence line, in agreement with the findings of Ten Wolde and Frenkel [272]. It thus follows that adding PEO indeed allows providing conditions for good crystallization within a specific range of protein–polymer size ratios and polymer concentrations. The different states are illustrated with the micrographs in right panel of Fig. 1.27.

1.4.3 Shape and Size Selection

The depletion interaction, as argued in Sect. 1.2.5, depends on the concentration of the depletion agent and the overlap volume of the depletion zones. For a given concentration of depletant the only variable is the overlap volume, which in turn depends on the size and (see Chap. 2) shape of the colloidal particles. Tuning the

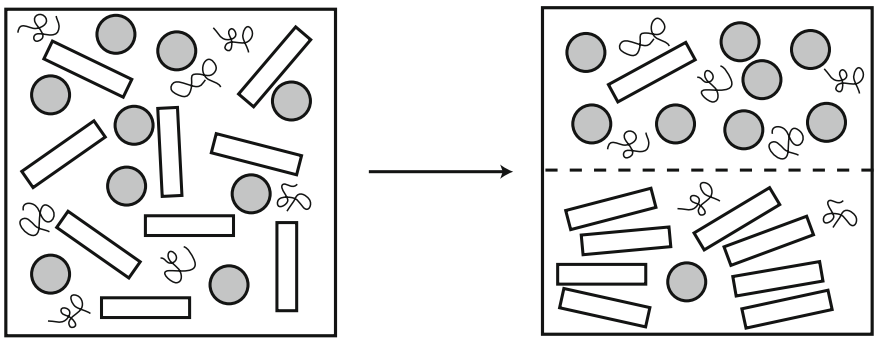

Fig. 1.28 Shape-selective separation induced by depletion forces

strength of the depletion interaction therefore allows to separate particles of different size and shape. For example, the separation of rod-like particles and spheres under the influence of polymers is schematically indicated in Fig. 1.28.

Unaware of the underlying principle this was first used by Cohen already in 1941 [87] to separate two viruses; Tobacco Mosaic Virus and Tobacco Necrosis Virus. Tobacco Mosaic Virus is a rod-like virus with a length of 300 nm and diameter of 18 nm and Tobacco Necrosis Virus a spherical virus with a diameter of about 26 nm. Cohen used the polysaccharide heparin as depletant to separate these viruses. Recently, this method to separate colloids of different size and shape has gained new impetus. For nano-based technologies particles with a specific size and shape are critical to optimize the nanostructure-dependent optical, electrical and magnetic properties.

While the self-organisation of nearly monodisperse spherical colloidal particles has been studied for a long time, the potential of self-assembly of anisometric colloidal particles (rods and plates) is far from being achieved. Nevertheless important advances have been made. For example, *CdSe* semiconductor nanorods have been shown to form nematic liquid crystals [279] that can potentially be used as functional components in electro-optical devices. Hence a tool for the effective separation of anisometric colloids from a mixture of particles of different sizes and shapes is highly desirable.

Recent studies have shown that depletion-induced shape and size selection of colloidal particles has the potential to be a powerful enabling method to achieve this in an effective way. For instance, Park et al. [280] reported the depletion-induced shape and size selection of gold rods and cubes. In Fig. 1.29 we show their transmission electron microscopy (TEM) images of gold rods (length $L = 77$ nm, diameter $D = 11$ nm) and cubes (size is 20 nm). In (a) the synthesized mixture is shown, (b) depicts the sediment concentrated in golds rods and (c) is an image of the supernatant enriched in cubes.

Baranov et al. [239] showed that the attractive depletion forces were effective in the shape selective separation of *CdSe*/*CdS*-rods from a mixture of rods and *CdSe* spheres. Mason [281] showed that the depletion interaction between plate-

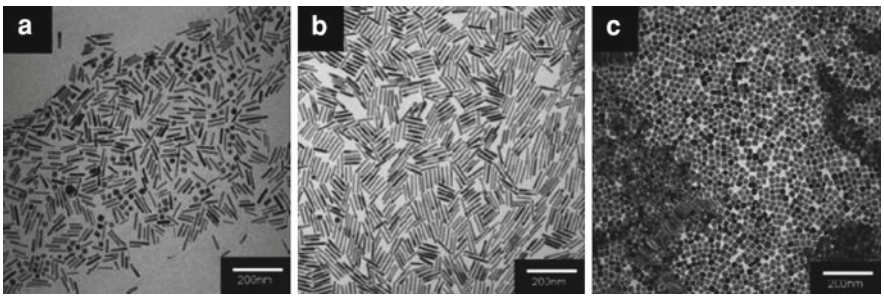

Fig. 1.29 TEM images of a dispersion of rod-like and cube-like gold colloids. **a** Synthesized mixture, **b** sediment, **c** supernatant. Picture reprinted from K. Park, H. Koerner, and R. A. Vaia, *Nano Lett*., 10:1433, Copyright 2010, with permission from the American Chemical Society

like particles is much stronger than between spheres, leading to a separation between a phase enriched in plates and a phase mainly concentrated in spheres. The dependence on size of the depletion interaction can also be used to fractionate a bidisperse population of colloidal spheres [282] or to obtain a monodisperse population of spheres from a collection of polydisperse spheres [149]. The monodisperse colloidal particles have the potential to self-organize in colloidal crystals, see Chap. 5 for more details. These procedures based on the depletion interaction have the potential to enable fabrication procedures for materials based on self-organized colloidal structures.

1.4.4 Directing Colloidal Self-assembly Using Surface Microstructures

As indicated in Sect. 1.4.3, the depletion interaction depends on the overlap volume for a given depletant concentration. This dependence leads to a difference in depletion interaction between particles of different size and shape and offers a powerful and cost-effective way to separate them.

The use of surface microstructures provides a promising route for creating colloidal assemblies via depletion forces. Dinsmore, Yodh and Pine [283] studied the interaction of large polystyrene spheres ($R = 203\,\text{nm}, \phi = 10^{-5}$) in a sea of small polystyrene spheres ($R = 41\,\text{nm}, \phi = 0.30$) with a wall with a step edge, see Fig. 1.30.

Clearly the overlap volume depends on the position of the big sphere with respect to the step edge. Since (1.21)

$$W_{dep}(h) = -nkTV_{ov}(h),$$

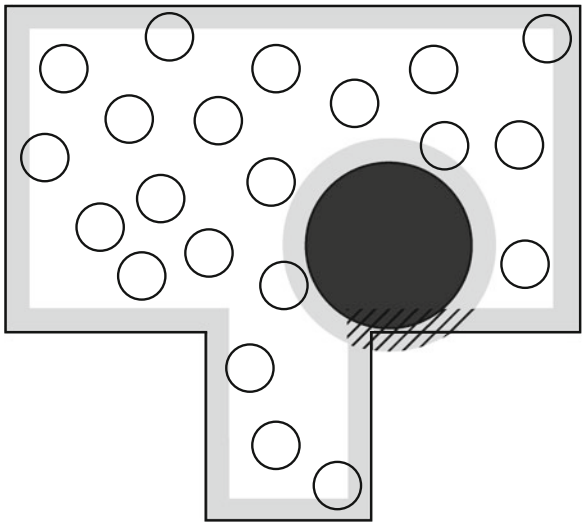

Fig. 1.30 A large colloidal sphere near a step edge in a sea of small spheres. The presence of the small spheres lead to depletion zones (*light grey regions*) near the walls of the container and around the big sphere. Overlap of depletion zones is indicated by the *hatched area*. This overlap volume increases the volume accessible to the small spheres, thereby increasing their entropy

where n is the number density of the small spheres, this difference in overlap volume directly translates in a different depletion interaction. By determining with optical microscopy the probability of the various positions of the big particles on the terrace with the step edge and relating this probability with the help of the Boltzmann relation

$$p(h) \sim \exp(-W_{dep}(h)kT), \tag{1.33}$$

the depletion interaction can be measured. For the system considered the differences in the overlap volume amount to a difference in the depletion potential of about twice the thermal energy of the particles.

Exercise
Rationalize why the big sphere in Fig. 1.30 will move to the right.

This indicates that surface structures can create localized force fields which can trap particles. An interesting application of this concept can be found in the recent work of Sacanna et al. [284]. They created, by clever colloid synthesis, 5 μm (diameter) polymerized silicon oil droplets with a well-defined spherical cavity. To these 'lock' particles they added appropriately sized spherical 'key' particles (silica, poly(methyl methacrylate) or polystyrene colloids) that can fit into the cavity. Nanometer sized non-adsorbing polymers were added to provide a depletion interaction. The depletion interaction, being proportional to the overlap volume of the depletion zones, attains a maximum when the key particle fits precisely into the spherical cavity of a lock particle, see Fig. 1.31. The depletion-driven self-assembly of lock and key particles is demonstrated in Fig. 1.32. This time series (from left to right) illustrates the site-specificity of the attraction.

Another way to manipulate the overlap volume of the depletion zones is to vary the roughness of the surface of the colloidal particles, see Fig. 1.33. The left

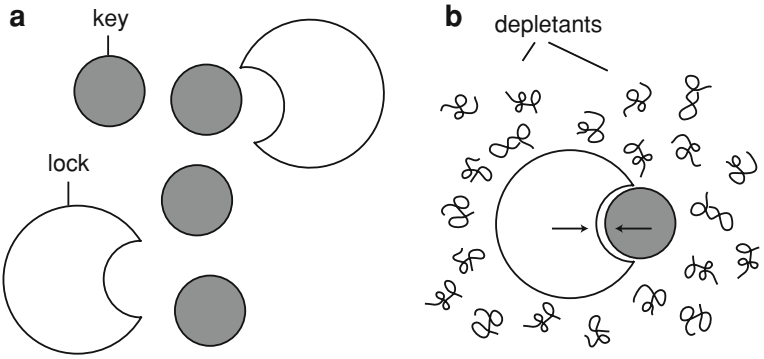

Fig. 1.31 **a** Colloidal 'lock' particles can be synthesized [284] containing a dimple into which 'key' particles, spherical colloids with appropriate size, can fit. **b** By adding depletants (polymer chains) a key can be pushed into a lock using the depletion force. Inspired by Solomon [285]

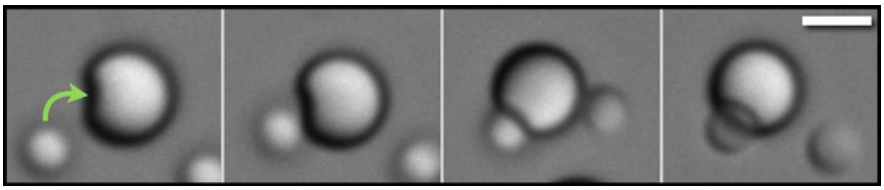

Fig. 1.32 Images of Sacanna et al. [284] demonstrating a colloidal sphere entering the lock of larger colloid. The curved arrow (*left*) indicates a successful lock-key binding. *Scale bar* is 2 μm. Picture reprinted from S. Sacanna, W. T. M. Irvine, P.M. Chaikin, and D. J. Pine, *Nature*, 464:575, Copyright 2010, with permission from Nature. Kindly provided by S. Sacanna

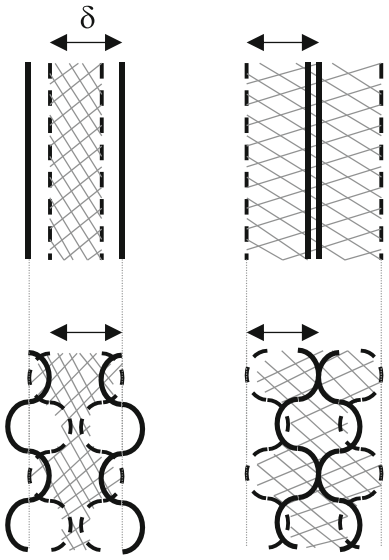

Fig. 1.33 Sketch of the overlap zones between flat surfaces (*upper*) and between roughened surfaces *lower*. Depletion thickness δ is indicated by the *arrows*. *Left drawings* intermediate overlap of depletion layers. *Right drawings* large overlap of depletion layers

drawings show that surface roughness does not affect the overlap volume for intermediate overlap of depletion zones. For large/maximum overlap, surface roughness prevents overlap of certain zones that do overlap in case of flat surfaces, see the sketches on the right. It is now possible to direct the self-assembly of particles by selectively controlling the roughness of different sides of colloidal particles. Badaire et al. [286, 287] demonstrated the potential of this method in the assembly of lithographically designed colloidal particles. In Fig. 1.34 we show the particles used by Badaire et al. [286, 287] that consist of roughened rounded side walls and flat ends. Upon adding surfactant micelles these particles will attract one another due to the depletion force. Since the attraction is stronger between the flat sides of the particles rod-like equilibrium structures are formed at a certain depletant concentration. An example is depicted in Fig. 1.35.

Zhao and Mason [288] demonstrated the same principle on plate-like particles with manipulated roughness.

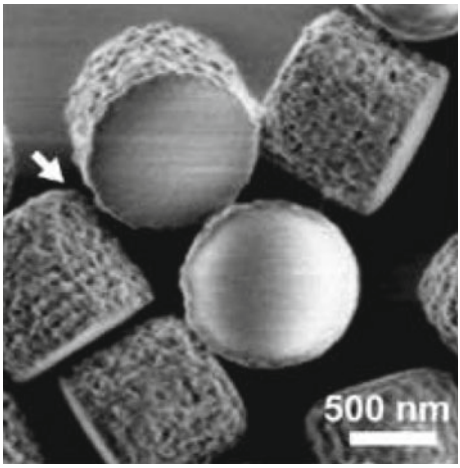

Fig. 1.34 Scanning electron microscopy (SEM) image of colloidal particles having sides with surfaces roughness and flat sides. Picture reprinted from S. Badaire, C. Cottin-Bizonne, and A. D. Stroock, *Langmuir*, 24:11451, Copyright 2008, with permission the American Chemical Society

Fig. 1.35 Aggregated state of the particles in Fig. 1.34 under the influence of depletion forces. Image size $50 \times 50\,\mu m^2$. Picture reprinted from S. Badaire, C. Cottin-Bizonne, and A. D. Stroock, *Langmuir*, 24:11451, Copyright 2008, with permission the American Chemical Society

1.4.5 Motion of a Sphere Through a Polymer Solution

Macromolecular crowding also has consequences for transport properties. One may wonder how protein transport occurs through a cell composed of a highly concentrated dispersion. The viscosity of a serum phase will be significantly larger than that of a physiological salt solution. The question arises what the friction is that a protein experiences as it moves through a cell. This relates to a fundamental problem in colloid physics: the dynamics of a colloidal sphere translating and rotating through a polymer solution.

As a colloidal particle diffuses or sediments through a solution containing non-adsorbing polymer chains, one may naively expect that the friction experienced by the particle is set by the bulk viscosity. In practice, it is smaller. An analysis of the

velocity profile of a non-adsorbing polymer solution near a flat surface shows that depletion leads to effective slip [289]. The depletion layer implies a non-uniform viscosity profile near the surface, which explains this slip.

Phillies and co-workers [290, 291] studied the translational self-diffusion of well-defined colloidal spheres through polymer solutions and showed that the interpretation of the measured friction coefficient of the particles is fairly complicated. For a spherical particle that moves through a medium containing small solvent molecules, the friction coefficient is proportional to the solvent viscosity. When the solvent is replaced by a polymer solution one may naively expect that the friction coefficient is proportional to the viscosity of polymer solution. Measurements indicate that this is only true when the chains are very small compared to the size of the particle.

Exercise
What viscosity is experienced by a tiny sphere in a dilute solution with very long polymer chains?

For polymer chains that are roughly as big as the particle, the apparent or effective viscosity experienced by a sphere is in between the viscosities of solvent and polymer solution. A similar finding was also reported for the rotational diffusion of colloidal particles [292] and for the sedimentation of colloids through a polymer solution [293].

The fact that the effective viscosity is intermediate between that of solvent and polymer solution can be rationalized as follows. Within the depletion layer, the viscosity is expected to follow the polymer density distribution [289] and it gradually increases from the solvent viscosity at the solid surface to the bulk viscosity far from the particle. Therefore, as a particle diffuses, the hydrodynamic resistance force is also in between the two limits. Fan et al. [294, 295] derived analytical expressions for the friction felt by a sphere when it moves through a macromolecular medium, and showed that the friction is strongly reduced compared to Stokes' law. This means that depletion-induced slip effects facilitate protein transport through crowded media.

1.5 Outline

In this chapter we provided an introduction to colloidal interactions, a historical perspective on early observations, and on later understanding of depletion effects and applications of depletion phenomena. In Chap. 2 we address the fundamentals of depletion interactions, including the effects of anisotropic depletants. The focus will be on small depletant concentrations which allow simple treatments using both the force method and the adsorption method to arrive at depletion potentials. The basics of phase behavior in colloidal dispersions with added depletants are set

out in Chap. 3. First, the equations of state of the hard-sphere fluid and the hard-sphere fcc crystal are discussed, leading to the phase diagram which in this case contains only the fluid-crystal equilibrium. Then the addition of depletants, using the simple penetrable hard sphere model, is considered within the framework of free volume theory; now a liquid phase enters. This is followed by extensions towards mixtures of spherical colloids and polymers in Chap. 4. Experimental phase diagrams of well-defined colloid–polymer mixtures are discussed and compared to theories for colloid–polymer mixtures. Phase separation kinetics and non-equilibrium states in colloid–polymer mixtures are treated as well. Chapter 5 deals with the phase behaviour of mixed colloids in the absence of non-adsorbing polymer and we will discuss the effect of adding small rod-like colloids or small spherical colloids to a suspension with colloidal spheres. Rod-like colloids are considered in Chap. 6, first without polymer: the physics of the isotropic to nematic phase transition is discussed in some detail. Finally, we describe the polymer-induced depletion effects for rod-like colloids. Throughout, the concepts will be illustrated by experimental and computer simulation results.

References

1. Manual of symbols and terminology for physicochemical quantities and units, appendix 2: Definitions, terminology and symbols in colloid and surface chemistry. Pure Appl. Chem. **31**, 7551 (1972)
2. D.H. Everett, *Basic Principles of Colloid Science* (The Royal Society of Chemistry, London, 1988)
3. W.B. Russel, D.A. Saville, W.R. Schowalter, *Colloidal Dispersions* (Cambridge Universtity Press, USA, 1999)
4. R.J. Hunter, *Foundations of Colloid Science*, 2nd edn. (Oxford University Press, Oxford, 2001)
5. D.F. Evans, H. Wennerström, *The Colloidal Domain: Where Physics, Chemistry, Biology, and Technology Meet*, 2nd edn. (Wiley-VCH, New York, 1999)
6. J. Lyklema, *Fundamentals in Colloid and Interface Science*, vol. 1–5. (Elsevier, Amsterdam, 1991–2005)
7. J. Perrin, Ann. de Chem. et de Phys. **18**, 5 (1909)
8. A. Einstein, Ann. Phys. **17**, 549 (1905)
9. L. Onsager, Chem. Rev. **13**, 73 (1933)
10. L. Onsager, Ann. NY. Acad Sci. **51**, 627 (1949)
11. W.G. McMillan, J.E. Mayer, J. Chem. Phys. **13**, 276 (1945)
12. J.-P. Hansen, I.R. McDonald, *Theory of Simple Liquids* (Academic Press, San Diego, 1986)
13. G.C. Maitland, M. Rigby, E.B. Smith, W.A. Wakeham, *Intermolecular Forces: Their Origin and Determination* (Clarendon Press, Oxford, 1981)
14. K.S. Pitzer, J. Chem. Phys. **7**, 583 (1939)
15. M.G. Noro, D. Frenkel, J. Chem. Phys. **113**, 2941 (2000)
16. A. Lucas, J. Harris, *Ancient Egyptian Materials and Industries* (Dover, London, 1999)
17. G.J. Fleer, M.A. Cohen Stuart, J.M.H.M. Scheutjens, T. Cosgrove, B. Vincent, *Polymers at Interfaces* (Chapman & Hall, New York, 1993)
18. The Greek historian Herodotus coined the term delta for the landform where the Nile river flows into the Mediterranean Sea; the sediment deposited at the river's mouth has the shape of the upper-case Greek letter Δ.

19. E.C. Barton, Geograph J. **51**, 100 (1918)
20. C.G. de Kruif, C. Holt, Casein micelle structure, functions and interactions, in: *Advanced Dairy Chemistry Proteins*, vol. 1, ed. by P.F. Fox, P.L.H. McSweeney (Kluwer, Plenum New York, 2002) pp. 233–276
21. P. Walstra, R. Jenness, *Dairy Chemistry and Physics* (Wiley, New York, 1984)
22. C.G. de Kruif, E.B. Zhulina, Colloids Surf. A. **117**, 151 (1996)
23. A. Kose, M. Ozka, K. Takano, Y. Kobayashi, S. Hachisu, J. Colloid Interface Sci. **44**, 330 (1973)
24. C. Soanes, A. Stevenson, *Oxford Dictionary of English* (Oxford University Press, New York, 2005)
25. B.V. Derjaguin, L. Landau, Acta Physicochimica USSR. **14**, 633 (1941)
26. E.J.W. Verwey, J. Th. Overbeek, *Theory of the Stability of Lyophobic Colloids* (Elsevier, Amsterdam, 1948)
27. J.N. Israelachvili, *Intermolecular and Surface Forces* (Academic, London, 1991)
28. P. Walstra, *Physical Chemistry of Foods* (Marcel Decker, New York, 2003)
29. R. Aveyard, B.P. Binks, J.H. Clint, Adv.Colloid Interface Sci. **100**, 503 (2003)
30. J.H. De Boer, Trans. Faraday. Soc. **32**, 21 (1936)
31. H.C. Hamaker, Physica. **4**, 1058 (1937)
32. J. Lyklema, *Fundamentals in Colloid and Interface Science*, vol. 1. (Elsevier, Amsterdam, 1991)
33. F. London, Z. Phys. B. **11**, 222 (1930)
34. R. Eisenschitz, F. London, Z. Phys. **60**, 491 (1930)
35. R. Becker, *Electromagnetic Fields and Interactions*, vol. II. (Blaisdell Publishing Company, New York, 1964)
36. D.J. Griffith, *Introduction to Electrodynamics* (Prentice-Hall, New Jersey, 1999)
37. S.H. Behrens, D.I. Christel, R. Emmerzael, P. Schurtenberger, M. Borkovec, Langmuir. **16**, 2566 (2000)
38. J.N. Israelachvili, G.E. Adams, J. Chem. Soc. Faraday Trans. **74**, 975 (1978)
39. B.W. Ninham, Adv. Colloid Interface Sci. **83**, 1 (1999)
40. A. Vrij, Pure Appl. Chem. **48**, 471 (1976)
41. C. Hertlein, L. Helden, A. Gambassi, S. Dietrich, C. Bechinger, Nature. **451**, 172 (2008)
42. E.W. Fischer, Kolloid Z. **160**, 120 (1958)
43. S.J. Alexander, J. Phys. Paris. **38**, 983 (1977)
44. P.G. De Gennes, C.R. Acad. Sc. Paris ser. B. **300**, 839 (1985)
45. P.G. De Gennes, Adv. Colloid Interface Sci. **27**, 189 (1987)
46. A. Vrij, R. Tuinier, Chapter 5 in Lyklema J (ed) *Fundamentals in Colloid and Interface Science*, vol. 4. (Elsevier, Amsterdam, 2005)
47. C.G. de Kruif, personal communication
48. R.J. Baxter, J. Chem. Phys. **49**, 2770 (1968)
49. P.W. Rouw, A. Vrij, C.G. de Kruif, Colloids Surf. **31**, 299 (1988)
50. P.W. Rouw, C.G. de Kruif, J. Chem. Phys. **88**, 7799 (1988)
51. P.W. Rouw, A. Vrij, C.G. de Kruif, Prog. Colloid Polym. Sci. **76**, 1 (1988)
52. E.G.M. Pelssers, M.A. Cohen Stuart, G.J. Fleer, J. Chem. Soc. Faraday Trans. **86**, 1355 (1990)
53. S. Asakura, F. Oosawa, J. Chem. Phys. **22**, 1255 (1954)
54. S. Asakura, F. Oosawa, J. Pol. Sci. **33**, 183 (1958)
55. R. Li-In-On, B. Vincent, F.A. Waite, ACS Symp. Ser. **9**, 165 (1975)
56. H. De Hek, A. Vrij, J. Colloid Interface Sci. **84**, 409 (1981)
57. C.M. Wijmans, E.B. Zhulina, G.J. Fleer, Macromolecules. **27**, 3238 (1994)
58. D.G.A.L. Aarts, M. Schmidt, H.N.W. Lekkerkerker, Science. **304**, 847 (2004)
59. D.G.A.L. Aarts, J.H. van der Wiel, H.N.W. Lekkerkerker, J. Phys Condens. Matter. **15**, S245 (2003)
60. W.K. Wijting, N.A.M. Besseling, M.A. Cohen Stuart, Phys. Rev. Lett. **90**, 196101 (2003)

61. O. Von Guericke, *Experimenta nova Magdeburgica de vacuo spatio* (Waesberge, Amsterdam, 1672)
62. E. Mach, *The Science of Mechanics* (The Open Court Publishing Company, IL, USA, 1960)
63. N. de Fatio Dullier, Oeuvres completes de Christiaan Huygens, The Hague. **9**, 381–389 (1888–1950)
64. G-L. Le Sage, Lettre á une académicien de Dijon Mercure de France: 153–171 (1756)
65. R.P. Feynman, *The Character of Physical Law*. in: The 1964 Messenger Lectures (Cambridge, MIT, 1967)
66. M.R. Edwards (ed), *Pushing Gravity: New Perspectives on Le Sage's Theory for Gravitation* (C. Roy Keys Inc., Montreal, 2002)
67. R. Fåhraeus, Physiol. Rev. **9**, 241 (1929)
68. J.E. Thysegen, Acta Med. Scand. Suppl. **134**, 1 (1942)
69. R. Fåhraeus, Acta. Med. Scand. **55**, 1 (1921)
70. S.E. Bedell, B.T. Booker, Am. J. Med. **78**, 1001 (1985)
71. D.R. Forsdyke, P.M. Ford, Biochem. J. **214**, 257 (1983)
72. J. Janzen, D.E. Brooks, Clin. Hemorheol. **9**, 695 (1989)
73. M.W. Beijerinck, Zentr. Bakteriol. Paras. Infektionskr. **2**, 697 (1896)
74. J.-L. Doublier, C. Garnier, C. Renard, C. Sanchez, Curr.Opin. Colloid Interface Sci. **5**, 184 (2000)
75. V.B. Tolstoguzov, Food Hydrocolloids. **4**, 429 (1991)
76. V.B. Tolstoguzov, Food Hydrocolloids. **11**, 181 (1997)
77. V. Ya. Grinberg, V.B. Tolstoguzov, Food Hydrocolloids. **11**, 145 (1997)
78. E. Scholten, R. Tuinier, R.H. Tromp, H.N.W. Lekkerkerker, Langmuir. **18**, 2234 (2002)
79. V.B. Tolstoguzov, A.L. Mzhel'sky, V. Ya. Gulov, Colloid Polym. Sci. **252**, 124 (1974)
80. J. Traube, Gummi Zeitung. **39**, 434 (1925)
81. H.C. Baker, Inst. Rubber Ind. **13**, 70 (1937)
82. C.F. Vester, Kolloid Z. **84**, 63 (1938)
83. E. Dickinson, Food Hydrocolloids. **17**, 25 (2003)
84. J.S. Rowlinson, B. Widom, *Molecular Theory of Capillarity* (Clarendon Press, Oxford, 1982)
85. S.S. Cohen, J. Biol. Chem. **144**, 353 (1942)
86. J.D. Bernal, I. Fankuchen, J. Gen. Physiol. **25**, 111 (1941)
87. S.S. Cohen, Proc. Soc. Exp. Biol. Med. **48**, 163 (1941)
88. R. Leberman, Virology. **30**, 341 (1966)
89. E.G. Cockbain, Trans. Faraday Soc. **48**, 185 (1952)
90. D. Fairhurst, M.P. Aronson, M.L. Ohm, E.D. Goddard, Colloids Surf. **7**, 153 (1983)
91. F. Oosawa, Hyo-Hyo Rakugaku (Autobiography, Nagoya, 2005)
92. C. Sieglaff, J. Polym. Sci. **41**, 319 (1959)
93. J. Clarke, B. Vincent, J. Chem. Soc. Faraday Trans. I. **77**, 1831 (1981)
94. C. Cowell, R. Li-In-On, B. Vincent, F.A. Waite, J. Chem. Soc. Faraday Trans. **74**, 337 (1978)
95. B. Vincent, P.F. Luckham, F.A. Waite, J. Colloid Interface Sci. **73**, 508 (1980)
96. B. Vincent, J. Edwards, S. Emmett, A. Jones, Colloids and Surfaces. **17**, 261 (1986)
97. B. Vincent, Colloids and Surfaces. **24**, 269 (1987)
98. B. Vincent, J. Edwards, S. Emmett, R. Croot, Colloids and Surfaces. **31**, 267 (1988)
99. S. Emmett, B. Vincent, Phase Trans. **21**, 197 (1990)
100. S. Hachisu, A. Kose, Y. Kobayashi, J Colloid Interface Sci. **55**, 499 (1976)
101. A. Kose, S. Hachisu, J. Colloid Interface Sci. **55**, 487 (1976)
102. P.G. De Gennes, *Scaling Concepts in Polymer Physics* (Cornell University Press, Ithaca, 1979)
103. P.G. De Gennes, C. R. Acad. Sc. Paris ser. B. **288**, 203 (1979)
104. J.F. Joanny, L. Leibler, P.G. De Gennes, J. Polymer Sci. Polym. Phys. **17**, 1073 (1979)
105. R.I. Feigin, D.H. Napper, J. Colloid Interface Sci. **75**, 525 (1981)
106. J.M.H.M. Scheutjens, G.J. Fleer, J. Phys. Chem. **83**, 1619 (1979)

107. J.M.H.M. Scheutjens, G.J. Fleer, Adv. Colloid Interface Sci. **16**, 361 (1982)
108. A. Broukhno, B. Jönsson, T. Åkesson, P.N. Vorontsov-Velyaminov, J. Chem. Phys. **113**, 5493 (2000)
109. H. De Hek, A. Vrij, J. Colloid Interface Sci. **70**, 592 (1979)
110. As dimensionless concentration variable ϕ is used throughout. In case of hard colloidal particles the quantity ϕ is the volume fraction. For polymers and penetrable hard spheres ϕ refers to the relative concentration with respect to overlap (see (1.24))
111. H. De Hek, A. Vrij, J. Colloid Interface Sci. **88**, 258 (1982)
112. P.R. Sperry, H.B. Hopfenberg, N.L. Thomas, J. Colloid Interface Sci. **82**, 62 (1981)
113. P.R. Sperry, J. Colloid Interface Sci. **87**, 375 (1982)
114. P.R. Sperry, J. Colloid Interface Sci. **99**, 97 (1984)
115. A.P. Gast, C.K. Hall, W.B. Russel, J. Colloid Interface Sci. **96**, 251 (1983)
116. J.A. Barker, D. Henderson, Rev. Mod. Phys. **48**, 587 (1976)
117. A.P. Gast, W.B. Russel, C.K. Hall, J. Colloid Interface Sci. **109**, 161 (1986)
118. E. Eisenriegler, J. Chem. Phys. **79**, 1052 (1983)
119. R. Tuinier, G.A. Vliegenthart, H.N.W. Lekkerkerker, J. Chem. Phys. **113**, 10768 (2000)
120. C. Allain, D. Ausserré, F. Rondelez, Phys. Rev. Lett. **49**, 1694 (1982)
121. D. Ausserré, H. Hervet, F. Rondelez, Macromolecules **19**, 85 (1986)
122. P.F. Luckham, J. Klein, Macromolecules **18**, 721 (1985)
123. P.F. Luckham, J. Klein, J. Colloid Interface Sci. **117**, 149 (1987)
124. R.M. Pashley, B.W. Ninham, J. Phys. Chem. **91**, 2902 (1987)
125. T. Taniguchi, T. Kawakatsu, K. Kawasaki, in: K. Kawasaki (ed). 'Slow dynamics in condensed matter' AIP series. **256**, 503 (1992)
126. E. Eisenriegler, A. Hanke, S. Dietrich, Phys. Rev. E. **54**, 1134 (1996)
127. E. Eisenriegler, Phys. Rev. E. **55**, 3116 (1997)
128. E. Eisenriegler, J. Phys. D: Condens. Matter **12**, A227 (2000)
129. A. Bringer, E. Eisenriegler, F. Schlesener, A. Hanke, Eur. Phys. J. B. **11**, 101 (1999)
130. A. Hanke, E. Eisenriegler, S. Dietrich, Phys. Rev. E. **59**, 6853 (1999)
131. T. Odijk, Macromolecules **29**, 1842 (1996)
132. T. Odijk, J. Chem. Phys. **106**, 3402 (1997)
133. T. Odijk, Langmuir **13**, 3579 (1997)
134. T. Odijk, Biophys. J. **79**, 2314 (2000)
135. E. Eisenriegler, J. Chem. Phys. **113**, 5091 (2000)
136. H. Reiss, J. Phys. Chem. **96**, 4736 (1992)
137. E. Eisenriegler, A. Bringer, J. Phys.: Condens. Matter. **17**, 1711 (2005)
138. E. Eisenriegler, J. Chem. Phys. **124**, 144912 (2006)
139. E. Eisenriegler, J. Chem. Phys. **125**, 204903 (2006)
140. E. Eisenriegler, A. Bringer, J. Chem. Phys. **127**, 034904 (2007)
141. H.N.W. Lekkerkerker, Colloids and Surfaces **51**, 419 (1990)
142. H.N.W. Lekkerkerker, W.C.K. Poon, P.N. Pusey, A. Stroobants, P.B. Warren, Europhys. Lett. **20**, 559 (1992)
143. S.M. Ilett , A. Orrock, W.C.K. Poon, P.N. Pusey, Phys. Rev. E. **51**, 1344 (1995)
144. F. Leal-Calderon, J. Bibette, J. Biais, Europhys. Lett. **23**, 653 (1993)
145. M.A. Faers, P.F. Luckham, Langmuir **13**, 2922 (1997)
146. E.J. Meijer, D. Frenkel, J. Chem. Phys. **100**, 6873 (1994)
147. E. Dickinson, Soft Matter. **2**, 642 (2006)
148. J. Bibette, D. Roux, F. Nallet, Phys. Rev. Lett. **65**, 2470 (1990)
149. J. Bibette, J. Colloid Interface Sci. **147**, 474 (1992)
150. J. Bibette, D. Roux, B. Pouligny, J. Phys. II. **2**, 401 (1992)
151. M.J. Snowden, P.A. Williams, M.J. Garvey, I.D. Robb, J. Colloid Interface Sci. **166**, 160 (1994)
152. K-Q. Xia, Y-B. Zhang, P. Tong, C. Wu, Phys. Rev. E **55**, 5792 (1997)
153. I. Lynch, S. Cornen, L. Piculell, J. Phys. Chem. B **108**, 5443 (2004)
154. A. Meller, J. Stavans, Langmuir **12**, 301 (1996)

155. R. Tuinier, de C.G. Kruif, J. Colloid Interface Sci. **218**, 201 (1999)
156. X. Ye, T. Narayanan, P. Tong, J.S. Huang, M.Y. Lin, B.L. Carvalho, L.J. Fetters, Phys. Rev. E. **54**, 6500 (1996)
157. K.D. Horner, M. Topper, M. Ballauff, Langmuir **13**, 551 (1997)
158. A. Sharma, J.Y. Walz, J. Chem. Soc. Faraday Trans. **92**, 4997 (1996)
159. D. Rudhardt, C. Bechinger, P. Leiderer, Phys. Rev. Lett. **81**, 1330 (1998)
160. R. Verma, J.C. Crocker, T.C. Lubensky, A.G. Yodh, Macromolecules. **33**, 177 (2000)
161. D. Kleshchanok, R. Tuinier, P.R. Lang, Langmuir **22**, 9121 (2007)
162. C.P. Royall, A.A. Louis, H. Tanaka, J. Chem. Phys. **127**, 044507 (2007)
163. T. Cosgrove, T.M. Obey, K. Ryan, Colloids Surf. **651**, 1 (1992)
164. A. Vrij, Physica A. **235**, 120 (1997)
165. G.A. Vliegenthart, H.N.W. Lekkerkerker, Prog. Colloid Polym. Sci. **105**, 27 (1997)
166. E.H.A. de Hoog, H.N.W. Lekkerkerker, J. Phys. Chem. B. **103**, 5274 (1999)
167. P. Van der Schoot, J. Phys. Chem. B. **103**, 8804 (1999)
168. J.M. Brader, R. Evans, Europhys. Lett. **49**, 678 (2000)
169. B.-H. Chen, B. Payandeh, M. Robert, Phys. Rev. E. **62**, 2369 (2000)
170. E.H.A. de Hoog, H.N.W. Lekkerkerker, J. Schulz, G.H. Findenegg, J. Phys. Chem. B. **103**, 10657 (1999)
171. E.H.A. de Hoog, H.N.W. Lekkerkerker, J. Phys. Chem. B. **105**, 11636 (2001)
172. M. Dijkstra, Curr. Opin. Colloid Interface Sci. **4**, 372 (2001)
173. P.G. Bolhuis, A. Stroobants, D. Frenkel, H.N.W. Lekkerkerker, J. Chem. Phys. **107**, 1551 (1997)
174. A.A. Louis, P.G. Bolhuis, J.P. Hansen, E.J. Meijer, Phys. Rev. Lett. **85**, 2522 (2000)
175. A. Moncho-Jorda, A.A. Louis, P.G. Bolhuis, R. Roth, J. Phys. Condens. Matter **15**, S3429 (2003)
176. P.G. Bolhuis, A.A. Louis, J.P. Hansen, Phys. Rev. Lett. **89**, 128302 (2002)
177. P.G. Bolhuis, E.J. Meijer, A.A. Louis, Phys. Rev. Lett. **90**, 068304 (2003)
178. M. Dijkstra, R. van Roij, R. Roth, A. Fortini, Phys. Rev. E. **73**, 041409 (2006)
179. A. Fortini, P.G. Bolhuis, M. Dijkstra, J. Chem. Phys. **128**, 024904 (2008)
180. I. Bodnár, J.K.G. Dhont, H.N.W. Lekkerkerker, J. Phys. Chem. **100**, 19614 (1994)
181. Y. Hennequin, M. Evens, C.M. Quezada Angulo, J.S. Van Duijneveldt, J. Chem. Phys. **123**, 054906 (2005)
182. Z.X. Zhang, J.S. van Duijneveldt, J. Chem. Phys. **124**, 154910 (2006)
183. Z.X. Zhang, J.S. van Duijneveldt, Langmuir **22**, 63 (2006)
184. J.S. Van Duijneveldt, K. Mutch, J. Eastoe, Soft Matter **3**, 155 (2007)
185. K.J. Mutch, J.S. van Duijneveldt, J. Eastoe, I. Grillo, R.K. Heenan, Langmuir **25**, 3944 (2009)
186. R. Tuinier, J.K.G. Dhont, C.G. de Kruif, Langmuir **16**, 1497 (2000)
187. P. Van der Schoot, Macromolecules. **31**, 4635 (1998)
188. T. Kramer, S. Scholz, M. Maskros, K. Huber, J. Colloid Interface Sci. **279**, 447 (2004)
189. T. Kramer, R. Schweins, K. Huber, J. Chem. Phys. **123**, 014903 (2005)
190. T. Kramer, R. Schweins, K. Huber, Macromolecules. **38**, 9783 (2005)
191. D. Wu, K. Hui, D. Chandler, J. Chem. Phys. **96**, 835 (1991)
192. K.S. Schweizer, J.G. Curro, Adv. Polym. Sci. **116**, 319 (1994)
193. M. Fuchs, K.S. Schweizer, Europhys. Lett. **51**, 621 (2000)
194. M. Fuchs, K.S. Schweizer, Phys. Rev. E. **64**, 021514 (2001)
195. M. Fuchs, K.S. Schweizer, J. Phys. Condens. Matter **14**, R239 (2002)
196. S. Ramakrishnan, M. Fuchs, K.S. Schweizer, C.F. Zukoski, J. Chem. Phys. **116**, 2201 (2002)
197. C.N. Likos, Phys. Rep. **348**, 267 (2001)
198. P.G. Bolhuis, A.A. Louis, J.P. Hansen, E.J. Meijer, J. Chem. Phys. **114**, 4296 (2001)
199. P.G. Bolhuis, A.A. Louis, J.P. Hansen, Phys. Rev. E. **6402**, 021801 (2001)
200. P.G. Bolhuis, A.A. Louis, Macromolecules. **35**, 1860 (2002)
201. A.A. Louis, P.G. Bolhuis, E.J. Meijer, J.-P. Hansen, J. Chem. Phys. **116**, 10547 (2002)
202. A.A. Louis, P.G. Bolhuis, E.J. Meijer, J.-P. Hansen, J. Chem. Phys. **117**, 1893 (2002)

203. R. Evans, Adv. Phys. **28**, 143 (1979)
204. Y. Rosenfeld, Phys. Rev. Lett. **63**, 980 (1989)
205. Y. Rosenfeld, J. Chem. Phys. **98**, 8126 (1993)
206. R. Roth, R. Evans, S. Dietrich, Phys. Rev. E. **62**, 62 (2000)
207. M. Schmidt, H. Löwen, J.M. Brader, R. Evans, Phys. Rev. Lett. **85**, 1934 (2000)
208. M. Schmidt, H. Löwen, J.M. Brader, R. Evans, J. Phys. Condens. Matt. **14**, 9353 (2002)
209. J. Dzubiella, C.N. Likos, H. Löwen, J. Chem. Phys. **116**, 9518 (2002)
210. S.M. Oversteegen, R. Roth, J. Chem. Phys. **122**, 214502 (2005)
211. R. Roth, R. Evans, Europhys. Lett. **53**, 271 (2001)
212. J.M. Brader, R. Evans, M. Schmidt, Mol. Phys. **101**, 3349 (2003)
213. W.C.K. Poon, F. Renth, R.M.L. Evans, D.J. Fairhurst, M.E. Cates, P.N. Pusey, Phys. Rev. Lett. **83**, 1239 (1999)
214. A. Moussaïd, W.C.K. Poon, P.N. Pusey, M.F. Soliva, Phys. Rev. Lett. **82**, 225 (1999)
215. G.J. Fleer, R. Tuinier, Physica A. **379**, 52 (2007)
216. B. Rotenberg, J. Dzubiella, J.-P. Hansen, A.A. Louis, Mol. Phys. **102**, 1 (2004)
217. D.G.A.L. Aarts, R. Tuinier, H.N.W. Lekkerkerker, J. Phys. Condens. Matter **14**, 7551 (2002)
218. G.J. Fleer, A.M. Skvortsov, R. Tuinier, Macromol. Theory Sim. **16**, 531 (2007)
219. R. Tuinier, P.A. Smith, W.C.K. Poon, S.U. Egelhaaf, D.G.A.L. Aarts, H.N.W. Lekkerkerker, G.J. Fleer, Europhys. Lett. **82**, 68002 (2008)
220. G.J. Fleer, R. Tuinier, Adv. Colloid Interface Sci. **143**, 1–47 (2008)
221. R. Tuinier, Eur. Phys. J. E. **10**, 123 (2003)
222. P. Paricaud, S. Varga, G.J. Jackson, J. Chem. Phys. **118**, 8525 (2003)
223. D.G.A.L. Aarts, R.P.A. Dullens, H.N.W. Lekkerkerker, New J. Phys. **7**, 40 (2005)
224. D.G.A.L Aarts, J. Phys. Chem. B **109**, 7407 (2005)
225. D.G.A.L Aarts, Soft Matter **3**, 19 (2007)
226. J. Kuipers, E.M. Blokhuis, J. Colloid Interface Sci. **315**, 270 (2007)
227. J. Buitenhuis, L.N. Donselaar, P.A. Buining, A. Stroobants, H.N.W. Lekkerkerker, J. Colloid Interface Sci. **175**, 46 (1995)
228. Z. Dogic, K.R. Purdy, E. Grelet, M. Adams, S. Fraden, Phys. Rev. E. **69**, 051702 (2004)
229. F.M. Van der Kooij, M. Vogel, H.N.W. Lekkerkerker, Phys. Rev. E. **62**, 5397 (2000)
230. C.P. Royall, R. Rice, To be published
231. L. Rossi, S. Sacanna, W.T.M. Irvine , P.M. Chaikin, D.J. Pine, A.P. Philipse, Soft Matter **7**, 4139 (2011)
232. H.H. Wensink, G.J. Vroege, H.N.W. Lekkerkerker, J. Chem. Phys. **115**, 7319 (2001)
233. H.H. Wensink, H.N.W. Lekkerkerker, Europhys. Lett. **66**, 125 (2004)
234. L. Harnau, S. Dietrich, Phys. Rev. E **71**, 011504 (2005)
235. S.M. Oversteegen, C. Vonk, J.E.G.J. Wijnhoven, H.N.W. Lekkerkerker, Phys. Rev. E **71**, 041406 (2005)
236. A. Syrbe, W.K. Bauer, H. Kostermeyer, Int. Dairy J. **8**, 179 (1998)
237. C.G. de Kruif, R. Tuinier, Food Hydrocolloids **15**, 555 (2001)
238. A. Overbeek, F. Bückmann, E. Martin, P. Steenwinkel, T. Annable, Progr. Org. Coat. **48**, 125 (2003)
239. D. Baranov, A. Fiore, M. van Huis, C. Giannini, A. Falqui, U. Lafont, H. Zandbergen, M. Zanella, R. Cingolani, L. Manna, Nano Lett. **10**, 743 (2010)
240. S.B. Zimmerman, A.P. Minton, Annu. Rev. Biophys. Biomol. Struc. **22**, 27 (1993)
241. A.P. Minton, Curr. Opin. Struct. Biol. **10**, 34 (2000)
242. S.R. McGuffee, A.H. Elcock, PLoS Comp. Biol. **6**, e1000694 (2010)
243. A.B. Fulton, Cell. **30**, 345 (1982)
244. G.B. Ralston, J. Chem. Edu. **67**, 857 (1990)
245. D.S. Goodsell, *The Machinery of Life* (Springer, New York, 1998)
246. K. Snoussi, B. Halle, Biophys. J. **88**, 2855 (2005)
247. M.S. Cheung, D. Klimov, D. Thirumalai, PNAS. **102**, 4753 (2005)
248. J. Herzfeld, Acc. Chem. Res. **29**, 31 (1996)

249. R.J. Ellis, Curr. Opin. Struct. Biol. **11**, 114 (2001)
250. R.J. Ellis, A.P. Minton, Nature **425**, 27 (2003)
251. F.J. Iborra, Theor. Med. Mod. **4**, 15 (2007)
252. J.A.C Valkenburg, C.L. Woldringh, J. Bacteriol. **160**, 1151 (1984)
253. H. Walter, D.E. Brooks, FEBS Lett. **361**, 135 (1995)
254. T. Odijk, Biophys. Chem. **73**, 4635 (1998)
255. C.L. Woldringh, T. Odijk, in *Organization of the Prokaryotic Genome*, ed. by R. L. Charlebois (ASM Press, Amsterdam, 1999)
256. B. Neu, H.J. Meiselman, Biochim. et Biophys. Acta. **1760**, 1772 (2006)
257. P.C. Stenger, J.A. Zasadzinski, Biophys. J. **92**, 3 (2007)
258. R. Tharmann, M.M.A.E. Claessens, A.R. Bausch, Biophys. J. **90**, 2622 (2006)
259. J.D. Bernal, D. Crowfoot, Nature **133**, 794 (1934)
260. J.C. Kendrew, G. Bodo, H.M. Dintzis, R.G. Parrish, H. Wyckoff, D.C. Phillips, Nature **181**, 662 (1958)
261. M.F. Perutz, M.G. Rossmann, A.F. Cullis, H. Muirhead, G. Will, Nature **185**, 416 (1960)
262. J. Drenth, *Principles of Protein X-Ray Crystallography* (Springer, Heidelberg, 2007)
263. A. McPherson, J. Cryst. Growth **110**, 1 (1991)
264. A. McPherson, Methods **34**, 254 (2004)
265. J. Drenth, J. Cryst. Growth. **90**, 368 (1988)
266. M.L. Broide, C.R. Berland, J. Pande, O. Ogun, G.B. Benedek, PNAS. **88**, 5660 (1991)
267. C.R. Berland, G.M. Thurston, M. Kondo, M.L. Broide, J. Pande, O. Ogun, G.B. Benedek, PNAS. **89**, 1214 (1992)
268. N. Asherie, A. Lomakin, G.B. Benedek, Phys. Rev. Lett. **77**, 4832 (1996)
269. D. Rosenbaum, P.C. Zamora, C.F. Zukoski, Phys. Rev. Lett. **76**, 150 (1996)
270. This could be considered as a contribution to the 'Wiedergutmachung' between colloid science in the colloid/macromolecule controversy with protein chemistry, see C. Tanford and J. Reynolds, Nature's Robots (Oxford University Press, New York, 2001)
271. W.C.K. Poon, Phys. Rev. E. **55**, 3762 (1997)
272. P.R. TenWolde, D. Frenkel, Science. **277**, 1975 (1997)
273. M. Muschol, F. Rosenberger, J. Chem. Phys. **107**, 1953 (1997)
274. C. Haas, J. Drenth, J. Cryst. Growth. **196**, 388 (1999)
275. O. Galkin, P.G. Vekilov, PNAS. **97**, 6277 (2000)
276. R. Piazza, Curr. Opinion Colloid Interface Sci. **5**, 38 (2000)
277. S. Tanaka, M. Ataka, J. Chem. Phys **117**, 3504 (2002)
278. see various papers in:. (2004) Curr. Opinion Colloid Interface Sci. 9:1–197
279. L.S. Li, J. Walda, L. Manna, A.P. Alivisatos, Nano Lett. **2**, 557 (2002)
280. K. Park, H. Koerner, R.A. Vaia, Nano Lett. **10**, 1433 (2010)
281. T.G. Mason, Phys. Rev. E. **66**, 60402 (2002)
282. R. Piazza, S. Iacopini, M. Pierno, E. Vignati, J. Phys.: Condens Matter **14**, 7563 (2002)
283. A.D. Dinsmore, A.G. Yodh, D.J. Pine, Nature **383**, 239 (1996)
284. S. Sacanna, W.T.M. Irvine, P.M. Chaikin, D.J. Pine, Nature **464**, 575 (2010)
285. M.J. Solomon, P.T. Spicer, Soft Matter **6**, 1391 (2010)
286. S. Badaire, C. Cottin-Bizonne, J.W. Woody, A. Yang, A.D. Stroock, J. Am. Chem. Soc. **129**, 40 (2007)
287. S. Badaire, C. Cottin-Bizonne, A.D. Stroock, Langmuir **24**, 11451 (2008)
288. K. Zhao, T.G. Mason, Phys. Rev. Lett. **99**, 268301 (2007)
289. R. Tuinier, T. Taniguchi, J. Phys. Condens. Matter **17**, L9 (2005)
290. T.H. Lin, G.D.J. Phillies, J. Phys. Chem. **86**, 4073 (1982)
291. G.S. Ullmann, K. Ullmann, R.M. Lindner, G.D.J. Phillies, J. Phys. Chem. **89**, 692 (1985)
292. G.H. Koenderink, S. Sacanna, D.G.A.L. Aarts, A.P. Philipse, Phys. Rev. E. **69**, 021804 (2004)
293. X. Ye, P. Tong, L.J. Fetters, Macromolecules **31**, 5785 (1998)
294. T-H. Fan, J.K.G. Dhont, R. Tuinier, Phys. Rev. E. **75**, 018803 (2007)
295. T-H. Fan, B. Xie, R. Tuinier, Phys. Rev. E. **76**, 051405 (2007)

Chapter 2
Depletion Interaction

In this chapter we consider the depletion interaction between two flat plates and between two spherical colloidal particles for different depletants (polymers, small colloidal spheres, rods and plates). First of all we focus on the depletion interaction due to a somewhat hypothetical model depletant, the penetrable hard sphere (phs), to mimic a (ideal) polymer molecule. This model, implicitly introduced by Asakura and Oosawa [1] and considered in detail by Vrij [2], is characterized by the fact that the spheres freely overlap each other but act as hard spheres with diameter σ when interacting with a wall or a colloidal particle. The thermodynamic properties of a system of hard spheres plus added penetrable hard spheres have been considered by Widom and Rowlinson [3] and provided much of the inspiration for the theory of phase behavior developed in Chap. 3.

The depletion potential is a *potential of mean force* and, as stressed by Onsager [4, 5], the system is considered at a given chemical potential of the solvent (and other solution) components; the relevant pressure is the osmotic pressure.

2.1 Depletion Interaction Due to Penetrable Hard Spheres

2.1.1 Depletion Interaction Between Two Flat Plates

2.1.1.1 Interaction Potential Between Two Flat Plates Using the Force Method

The force per unit area, $K(h)$, between two parallel plates separated by a distance h, is the difference between the osmotic pressure P_i inside the plates and the outside pressure P_o

$$K = P_i - P_o \tag{2.1}$$

H. N. W. Lekkerkerker and R. Tuinier, *Colloids and the Depletion Interaction*, Lecture Notes in Physics, 833, DOI: 10.1007/978-94-007-1223-2_2,

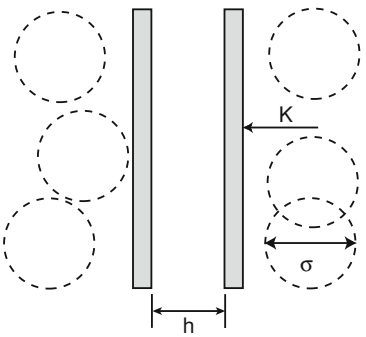

Fig. 2.1 Schematic picture of two parallel flat plates in the presence of penetrable hard spheres (*dashed circles*)

Since the penetrable hard spheres behave thermodynamically ideally the osmotic pressure outside the plates is given by the Van 't Hoff law

$$P_o = n_b kT,$$

where n_b is the bulk number density of the phs. When the plate separation h (see Fig. 2.1) is equal to or larger than the diameter σ of the penetrable hard spheres the osmotic pressure inside the plates is the same as outside:

$$P_i = P_o = n_b kT.$$

On the other hand, when the plate separation is less than the diameter of the penetrable hard spheres, no particles can enter the gap and

$$P_i = 0.$$

This means that

$$\begin{aligned} K(h) &= -n_b kT \quad h < \sigma \\ &= 0 \qquad\quad h \geq \sigma. \end{aligned} \tag{2.2}$$

This is the classical result derived by Asakura and Oosawa [1] more than 50 years ago.

Since $K = -\mathrm{d}W/\mathrm{d}h$, integration from ∞ to h yields the interaction potential per unit area $W(h)$ between the plates

$$\begin{aligned} W(h) &= -n_b kT(\sigma - h) \quad h < \sigma \\ &= 0 \qquad\qquad\quad h \geq \sigma. \end{aligned} \tag{2.3}$$

2.1.1.2 Interaction Potential Between Two Flat Plates Using the Extended Gibbs Adsorption Equation

An alternative and insightful way to obtain the interaction potential is from the extended Gibbs adsorption equation [6–8]. The natural thermodynamic potential to describe the system depicted in Fig. 2.2 is the grand potential $\Omega(T, V, \mu, h)$

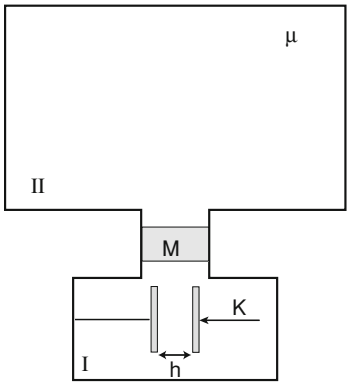

Fig. 2.2 Illustration of the (depletion) force between two plates in the system of interest (I) at given chemical potential of the depletant in the reservoir (II). The system is connected to the reservoir through a hypothetical membrane *M* that allows permeation of depletant

$$\Omega = F - \mu N, \tag{2.4}$$

where $F = F(T, V, N, h)$ is the Helmholtz (free) energy, N the number of penetrable hard spheres in the system and μ their chemical potential. At constant temperature and volume we have $\mathrm{d}F = \mu\,\mathrm{d}N - KA\,\mathrm{d}h$, so $\mathrm{d}\Omega$ is given by

$$\mathrm{d}\Omega = -KA\,\mathrm{d}h - N\,\mathrm{d}\mu, \tag{2.5}$$

where K is again the force per unit area between the plates and A is the area of the plates.

From cross-differentiating (2.5) we obtain

$$\left(\frac{\partial K}{\partial \mu}\right)_h = \frac{1}{A}\left(\frac{\partial N}{\partial h}\right)_\mu. \tag{2.6}$$

Combining this with

$$K = -\left(\frac{\partial W}{\partial h}\right)_\mu \tag{2.7}$$

we obtain

$$-\left(\frac{\partial}{\partial h}\left(\frac{\partial W}{\partial \mu}\right)_h\right)_\mu = \frac{1}{A}\left(\frac{\partial N}{\partial h}\right)_\mu. \tag{2.8}$$

Since the depletion potential W vanishes at infinite separation for all values of the chemical potential μ of the depletion agent, integration over h gives

$$-\left(\frac{\partial W}{\partial \mu}\right)_h = \frac{N(h) - N(\infty)}{A}, \tag{2.9}$$

where $N(h)$ is the number of penetrable hard spheres in the system when the plates are at separation h and $N(\infty)$ is that at infinite separation. The right-hand side of (2.9) can be conveniently written in terms of the surface adsorption

$$-\left(\frac{\partial W}{\partial \mu}\right)_h = \Gamma(h) - \Gamma(\infty), \tag{2.10}$$

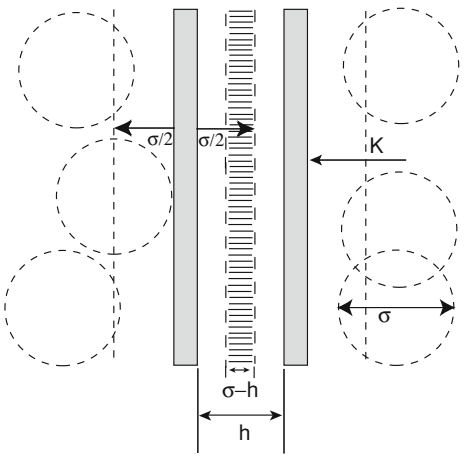

Fig. 2.3 The overlap volume (*hatched area*) of depletion layers due to penetrable hard spheres between two parallel flat plates equals $A(\sigma - h)$

where

$$\Gamma(h) = \int_0^h [n(x) - n_b]\mathrm{d}x, \tag{2.11}$$

and

$$\begin{aligned}\Gamma(\infty) &= 2\Gamma_{\text{single wall}} \\ &= 2\int_0^\infty [n(x) - n_b]\mathrm{d}x.\end{aligned} \tag{2.12}$$

In (2.12) $n(x)$ refers to the polymer segment concentration profile near a single wall whereas in (2.11) $n(x)$ is the profile between two walls. Expression (2.10) is the extension of the Gibbs adsorption equation for a single surface to the case of two surfaces at finite separation [6–8]. Integration of (2.10) gives

$$W(h) = -\int_{-\infty}^{\mu} [\Gamma(h) - \Gamma(\infty)]\mathrm{d}\mu. \tag{2.13}$$

The depletion thickness of penetrable hard spheres is $\sigma/2$ and $A\Gamma(h)$ equals the overlap volume $A(\sigma - h)$ times n_b (see Fig. 2.3)

$$\begin{aligned}\Gamma(h) - \Gamma(\infty) \quad &= n_b(\sigma - h) \quad h < \sigma \\ &= 0 \qquad\quad h \geq \sigma.\end{aligned} \tag{2.14}$$

The chemical potential of the penetrable hard spheres is

$$\mu = kT \ln n_b. \tag{2.15}$$

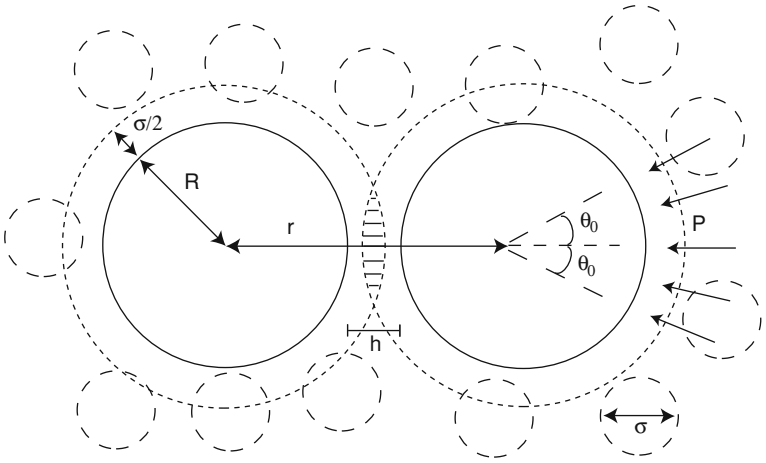

Fig. 2.4 Two hard spheres in the presence of penetrable hard spheres as depletants. The PHS impose an unbalanced pressure P between the hard spheres resulting in an attractive force between them. The overlap volume of depletion layers between the hard spheres (*hatched*) has the shape of a lens with width $\sigma - h$ and height $2H = 2R_d \tan\,\theta_0$, where θ_0 is given by $\cos\,\theta_0 = r/2R_d$

Inserting (2.14) and (2.15) into (2.13) yields (again) the interaction potential given by (2.3). The conceptual advantage of the calculation with the extended Gibbs adsorption equation is that it provides a direct link between the depletion of particles with the depletion potential, which is highly illuminating. The method also offers advantages to obtain physically motivated approximate expressions for the depletion interaction where an exact calculation is not possible.

2.1.2 Depletion Interaction Between Two Spheres

2.1.2.1 Interaction Potential Between Two Spheres Using the Force Method

When the depletion zones with thickness $\sigma/2$ around spherical colloidal particles with radius R start to overlap, i.e., when the distance r between the centers of the colloidal particles is smaller than $2R + \sigma = 2R_d$, a net force arises between the colloidal particles. For a convenient notation we defined an effective depletion radius R_d [9]

$$R_d = R + \sigma/2. \tag{2.16}$$

This (attractive) force originates from an uncompensated (osmotic) pressure due to the depletion of penetrable hard spheres from the gap between the colloidal particles. This is depicted in Fig. 2.4 from which we immediately deduce that the uncompensated pressure acts on the surface between $\theta = 0$ and $\theta_0 = \text{arc}\,\cos(r/2R_d)$.

For obvious symmetry reasons only the component along the line connecting the centers of the colloidal spheres contributes to the total force. For the angle θ this component is $P \cos\theta$ where the pressure is $P = n_b kT$. The surface on which this force acts between θ and $\theta + \mathrm{d}\theta$ equals $2\pi R_d^2 \sin\theta\,\mathrm{d}\theta$. The total force between the colloidal spheres is obtained by integration over θ from 0 to θ_0

$$\begin{aligned}\frac{K_s(r)}{n_b kT} &= -2\pi(R+\sigma/2)^2 \int_0^{\theta_0} \sin\theta\,\cos\theta\,\mathrm{d}\theta \\ &= -\pi R_d^2\left[1-(r/2R_d)^2\right] \quad 2R \le r < 2R_d \\ &= 0 \qquad\qquad\qquad\qquad\quad r \ge 2R_d.\end{aligned} \tag{2.17}$$

This result was also obtained by Asakura and Oosawa [1]. The minus sign in the right-hand side of (2.17) implies that the force is attractive.

Exercise
Show that (2.17) can also be written as the pressure times the area of the overlap of the depletion zones (see Fig. 2.4).

The depletion potential is now obtained by integration of the depletion force (2.17)

$$\begin{aligned}W_s(r) &= \int_r^{2R_d} K_s(r)\,\mathrm{d}r \\ &= -n_b kT V_{ov}(r) \quad 2R \le r < 2R_d \\ &= 0 \qquad\qquad\qquad\quad r \ge 2R_d,\end{aligned} \tag{2.18}$$

with

$$V_{ov}(r) = \frac{4\pi}{3} R_d^3 \left[1 - \frac{3}{4}\frac{r}{R_d} + \frac{1}{16}\left(\frac{r}{R_d}\right)^3\right] \tag{2.19a}$$

which can also be written as

$$V_{ov}(h) = \frac{\pi}{6}(\sigma - h)^2 (3R + \sigma + h/2) \tag{2.19b}$$

This result of (2.19a), in which r is the variable, was first obtained by Vrij [2]. In (2.19b) the variable is h and was already given (without explicit derivation) in (1.22). Both (2.19a) and (2.19b) are frequently used in the literature. Note that $W_s(r)$ in (2.18) is equal to pressure times the overlap volume V_{ov}. The reason for this simple form will become clearer after consideration of the interaction between two spheres using the extended Gibbs equation. In the limit that $\sigma/2 \ll R$ the force (2.17) and potential (2.18) between the spheres take very simple forms:

$$\frac{K_s(h)}{n_b kT} = -\pi R(\sigma - h) \tag{2.20}$$

and

$$\frac{W_s(h)}{n_b kT} = -\pi R \frac{1}{2}(\sigma - h)^2, \tag{2.21}$$

for separations $h = r - 2R$ smaller than σ

Exercise
Derive (2.20) and (2.21) from (2.17) and (2.18).

2.1.2.2 Interaction Potential Between Two Spheres from the Extended Gibbs Adsorption Equation

Applying exactly the same line of reasoning as for the derivation of the extended Gibbs adsorption equation for two flat plates, see (2.9), we now obtain

$$-\left(\frac{\partial W_s}{\partial \mu}\right) = N(r) - N(\infty), \tag{2.22}$$

where $N(r)$ is the number of penetrable hard spheres in the system when the colloidal spheres are at centre-to-centre separation r and $N(\infty)$ that at infinite separation. Clearly, the difference between $N(r)$ and $N(\infty)$ is caused by the overlap of the depletion zones

$$\begin{aligned} N(r) - N(\infty) &= n_b V_{ov}(r) \quad 2R \le r < 2R_d \\ &= 0 \qquad\qquad\quad r \ge 2R_d \end{aligned} \tag{2.23}$$

with V_{ov} defined in (2.19a, b). Integration of (2.22) using (2.23) and (2.15) immediately leads to the interaction potential (2.18). This route to the interaction potential makes it clear why the overlap volume of the depletion zones appears.

2.1.3 Depletion Interaction Between a Sphere and a Plate

The force method and the extended Gibbs adsorption equation can also be applied to obtain the depletion interaction between a sphere and a flat plate. For the Gibbs adsorption route we use (again)

$$-\left(\frac{\partial W_{sp}}{\partial \mu}\right) = N(h) - N(\infty), \tag{2.24}$$

where now $N(h)$ is the number of penetrable hard spheres in the system when the colloidal sphere is at a separation h from the plate and $N(\infty)$ is that at infinite

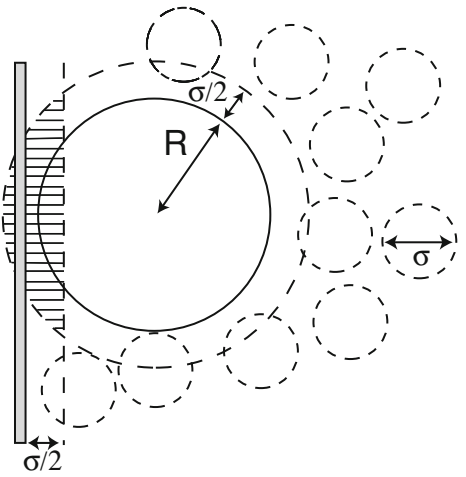

Fig. 2.5 Illustration of the overlap volume (*hatched*) of depletion layers between a hard wall and a hard sphere

separation. Again the difference between $N(h)$ and $N(\infty)$ is caused by the overlap of the depletion zones, now of the sphere and of the plate (see Fig. 2.5)

$$\begin{aligned}\frac{N(h)-N(\infty)}{n_b} &= V_{\mathrm{ov}}(h)\\ &= \frac{1}{3}\pi(\sigma-h)^2\left(3R+\frac{\sigma}{2}+h\right) \quad 0\le h<\sigma\\ &= 0 \qquad\qquad\qquad\qquad\qquad\quad h\ge\sigma,\end{aligned}$$

Integration of (2.24) now leads to

$$\begin{aligned}\frac{W_{\mathrm{sp}}(h)}{n_b kT} &= -\frac{1}{3}\pi(\sigma-h)^2\left(3R+\frac{\sigma}{2}+h\right) \quad 0\le h<\sigma\\ &= 0 \qquad\qquad\qquad\qquad\qquad\quad h\ge\sigma.\end{aligned} \tag{2.25}$$

For $R \gg \sigma$ (2.25) simplifies to

$$W_{\mathrm{sp}}(h) = -n_b kT\pi R(\sigma-h)^2 \quad 0\le h<\sigma, \tag{2.26}$$

which is twice (2.21).

2.1.4 Derjaguin Approximation

Some of the above results also follow directly from the so called Derjaguin approximation. Derjaguin [10] showed that there exists a simple (approximate) relation for the force between curved objects and the interaction potential between two flat plates. In the Derjaguin approximation the spherical surface is replaced by a collection of flat rings. Consider two spheres with radius R at a center-to-center

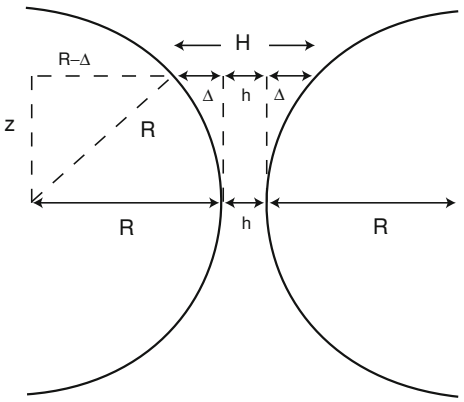

Fig. 2.6 Relevant length scales (see text) for describing the interaction force between two big spheres

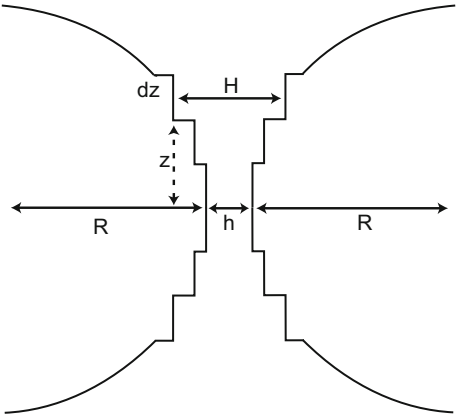

Fig. 2.7 Sketch of the Derjaguin approximation to the situation illustrated in Fig. 2.6

distance $r = 2R + h$. The distance H between the sphere surfaces at a distance z from the line joining the centers is $H = h + 2\Delta$, where $(R - \Delta)^2 + z^2 = R^2$ (see Fig. 2.6). When the range of interaction is short it is sufficient to consider only small values of h/R or z/R, see Fig. 2.7. For $z \ll R$ we can write to a good approximation $\Delta = z^2/2R$. Hence $H = h + z^2/R$ and thus $\mathrm{d}H = (2z/R)\mathrm{d}z$. The interaction between two spheres can now be written as the sum (integral) of the interactions of flat rings with radius z and surface $2\pi z\,\mathrm{d}z$ at a distance H from each other (see Fig. 2.7). Assuming that the interaction is sufficiently short-ranged, the contribution of rings with high values of H may be neglected, and thus the integration may be extended to $z = \infty$. We obtain

$$\begin{aligned} W_\mathrm{s}(h) &= \int_0^\infty W(H) 2\pi z\,\mathrm{d}z \\ &= \pi R \int_h^\infty W(H)\,\mathrm{d}H \end{aligned} \tag{2.27}$$

and hence

$$K_s(h) = -\frac{\partial W_s(h)}{\partial h} = \pi R W(h). \tag{2.28}$$

Here $W(h)$is the interaction potential between two flat plates at distance h. Clearly this approximate relation between the force for spheres and the interaction potential for plates is more accurate the larger the radius of the spheres compared to the range of the interaction. In this chapter we shall frequently use this Derjaguin approximation. It is a useful tool which, under the right conditions (see above), is very accurate but one has to be careful and be aware of its limitations.

With respect to the depletion interaction the Derjaguin approximation becomes accurate when considering a depletion agent which is small compared to the radius of the colloidal spheres. For example, applying the Derjaguin approximation to (2.3), the case of penetrable hard spheres, using (2.28) immediately leads to (2.20).

Applying the Derjaguin approximation to the interaction between a sphere and a flat plate provides

$$K_{sp}(h) = 2\pi R W(h). \tag{2.29}$$

This is an important relation as it allows one to obtain the interaction potential between two parallel plates from the measured force between a sphere and a wall (see Sect. 2.6)

Exercise
Derive equation (2.29).

From (2.29) it follows that

$$W_{sp}(h) = 2\pi R \int_h^\infty W(h')\mathrm{d}h'. \tag{2.30}$$

For the case of the penetrable hard sphere as depletion agent this leads to

$$\begin{aligned} W_{sp}(h) &= -n_b kT\pi R(\sigma - h)^2 \quad 0 \le h < \sigma \\ &= 0 \qquad\qquad\qquad\quad h \ge \sigma \end{aligned}, \tag{2.31}$$

in agreement with (2.26).

2.2 Depletion Interaction Due to Ideal Polymers

2.2.1 Depletion Interaction Between Two Flat Plates

2.2.1.1 Interaction Potential Between Two Flat Plates Using the Force Method

The simplest model to describe polymers is the ideal-chain model. For books on polymer physics where all the relevant background material can be found see [11–19]. In this model the polymer consists of M subunits, each with a fixed bond length b, and their orientation is completely independent of the orientation and positions of previous monomers, even to the extent that two different monomers can occupy the same position in space: there is no excluded volume. This model plays the same role in polymer physics as an ideal gas in molecular physics. It allows to describe the polymer chain as a (Gaussian) random walk of M steps, as depicted in Fig. 2.8.

The average value $\langle \mathbf{R} \rangle$ of the end-to-end vector $\mathbf{R}$ joining one end of the polymer to the other is zero, as 'negative' steps have the same probability as 'positive' ones. Mathematically, the probability of the end-to-end vector being $\mathbf{R}$ is the same as it being—$\mathbf{R}$ so that, for symmetry reasons, the two contributions cancel in the average. A straightforward calculation (see any of the references [11–14, 17, 19]) shows that $\langle \mathbf{R}^2 \rangle$, the average of the square of $\mathbf{R}$ is given by

$$\langle \mathbf{R}^2 \rangle = Mb^2. \tag{2.32}$$

This quantity is a measure of the size of the polymer chain. We see that the size of the ideal polymer chain, being proportional to $\sqrt{M}$, is much smaller than the total unfolded contour length Mb of the polymer.

Another commonly used and convenient quantity to describe the size of a polymer is the radius of gyration R_g, the root-mean-square of the average monomer position from the center of mass which becomes

$$R_g^2 = \frac{1}{6} Mb^2. \tag{2.33}$$

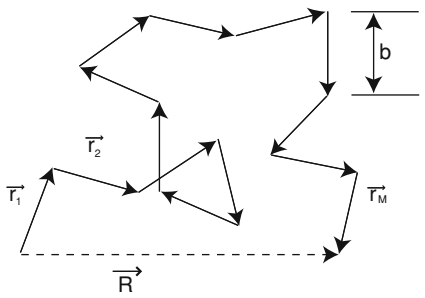

Fig. 2.8 Sketch of a random walk chain consisting of monomers with length b. For any given walk the end-to-end vector $\mathbf{R} = \sum r_i$

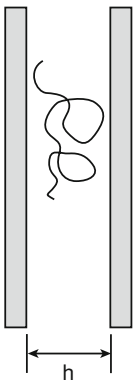

Fig. 2.9 An ideal chain confined between two parallel flat plates

The result $R_g = b\sqrt{M/6}$ holds for a Gaussian chain in the bulk solution.

We now consider an ideal Gaussian chain confined between two (large) flat plates with area A at a plate separation h, see Fig. 2.9.

For the computation of segment density profiles in polymer solutions near interfaces one can use the fact that there is a close analogy between the diffusion of a Brownian particle and the flight of a random walk [20, 21]. A diffusion-like equation can be derived to evaluate the partition function of polymer chains. Given the boundary condition this 'diffusion' equation can be solved. The partition function $z(h)$ of one confined chain is given by [1, 22, 23]

$$z(h) = V\chi(h), \tag{2.34}$$

where $V = A \cdot h$ is the volume of the system and

$$\chi(h) = \frac{8}{\pi^2} \sum_{n=1,3,5,\ldots} \frac{1}{n^2} \exp - \frac{n^2\pi^2 R_g^2}{h^2}. \tag{2.35}$$

For a derivation of the above expression see for instance [24] or Chap. 2 in [14]. Note that since

$$\sum_{n=1,3,5,\ldots} \frac{1}{n^2} = \frac{\pi^2}{8}$$

clearly

$$0 \le \chi(h) \le 1. \tag{2.36}$$

Exercise

Show that (2.35) can be approximated as [25]

$$\begin{aligned} \chi(h) &= \frac{8}{\pi^2} \mathrm{e}^{-\pi^2 R_g^2/h^2} \qquad 0 \le h \le \frac{8R_g}{\sqrt{\pi}} \\ &= 1 - \frac{4R_g}{h\sqrt{\pi}}, \qquad h > \frac{8R_g}{\sqrt{\pi}}. \end{aligned} \tag{2.37}$$

Since the ideal chains do not interact the partition function for N confined chains can be written as

$$Z(h) = \frac{z(h)^N}{N!}. \tag{2.38}$$

The Helmholtz energy is given by

$$F(h) = -kT \ \ln \ Z(h). \tag{2.39}$$

Hence the result

$$F(h) = NkT\left[\ln\left(\frac{N}{V}\right) - 1 - \ln \ \chi(h)\right] \tag{2.40}$$

is obtained after insertion of (2.38). This free energy can be written as

$$F(h) = F_{\text{unconfined}} - T\Delta S(h), \tag{2.41}$$

where $\Delta S(h)$ is the entropy of confinement:

$$\Delta S(h) = N\Delta s(h) = Nk \ \ln \ \chi(h). \tag{2.42}$$

From (2.36) it follows that the confinement entropy is negative, as expected, because confinement leads to a decrease of the entropy. From the free energy (2.39) we obtain for the pressure of the chains inside the plates

$$P_i = -\left(\frac{\partial F}{\partial V}\right) = kT\, n_i\left[1 + \frac{h}{\chi}\frac{\partial \chi}{\partial h}\right] \tag{2.43}$$

where $n_i = (N/V)_i$ is the number density of the ideal chains between the plates. The first term $kT\, n_i$ corresponds to the Van 't Hoff law. Likewise, the pressure of the ideal chains outside the plates is given by

$$P_o = n_b kT, \tag{2.44}$$

where n_b is the bulk number density of the polymer chains. Using Einstein fluctuation theory [26, 27] it follows immediately that

$$\begin{aligned} n_i &= \mathrm{e}^{\Delta s/k}\, n_b \\ &= \chi n_b. \end{aligned} \tag{2.45}$$

Exercise

Derive (2.45) by using the equality of the chemical potential of the ideal chains inside and outside the plates $\mu_i = \mu_o$.

Combining (2.1), (2.43), (2.44), and (2.45) we find for the force per unit area, $K(h)$, between the plates

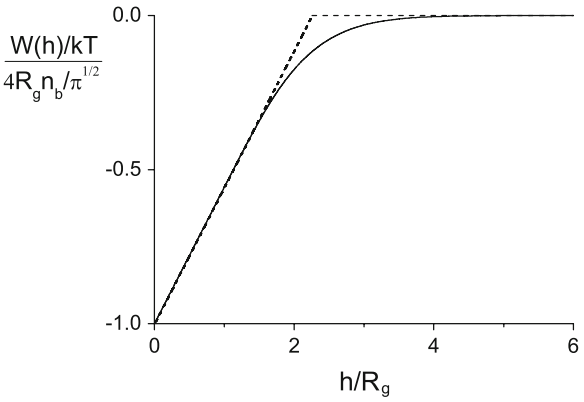

Fig. 2.10 Depletion potential $W(h)$ between two parallel flat plates caused by non-adsorbing ideal chains (*solid curve*). The *dotted lines* give $W(h)$ according to (2.3) with $\sigma = 4R_g/\sqrt{\pi}$

$$K(h) = P_i - P_o = -n_b kT\left[1 - \chi - h\frac{\partial \chi}{\partial h}\right]. \tag{2.46}$$

Again this result was first derived by Asakura and Oosawa [1]. Integration of (2.46) yields the interaction potential per unit area $W(h)$ between the plates [28]

$$W(h) = -n_b kT\left[\frac{4R_g}{\sqrt{\pi}} - h + h\chi(h)\right]. \tag{2.47}$$

Here we have used that

$$\lim_{h\to\infty}[h - h\chi(h)] = \frac{4R_g}{\sqrt{\pi}} \tag{2.48}$$

according to (2.37). Comparing (2.47) with the interaction potential (2.3) between flat plates due to penetrable hard spheres we find that the contact potentials ($h = 0$) match if we take $\sigma = 4R_g/\sqrt{\pi} = 2.26R_g$. A plot of the two potentials is given in Fig. 2.10. For small h, where $\chi(h)$ is negligible, the two potentials coincide: this is in the region $0 < h < 3R_g/2$. For $h > 2R_g$ the two potentials deviate because the discontinuous behaviour of (2.3) is replaced by the smooth crossover of (2.47). In the transition region ideal polymers have a longer range of attraction than penetrable hard spheres. Eisenriegler [29] has shown that (2.47) is identical to (2.3) (with $\sigma = 4R_g/\sqrt{\pi}$) up to and including terms of order h^4.

2.2.1.2 Interaction Potential Between Two Flat Plates from the Extended Gibbs Equation

From (2.45) and (2.11) it follows that

$$\Gamma(h) = [n_i(h) - n_b]h = n_b[\chi(h)h - h] \tag{2.49}$$

and hence, in view of (2.48)

$$\Gamma(\infty) = -n_b \frac{4R_g}{\sqrt{\pi}}. \tag{2.50}$$

Substituting (2.49) and (2.50) in (2.13) and using the fact that ideal chains show ideal thermodynamic behaviour, i.e.,

$$\mu = kT \ln n_b,$$

we obtain for the interaction potential per unit area $W(h)$ between two plates again the result given by (2.47). While the above thermodynamic route to the calculation of the adsorption is very efficient (as thermodynamics always is!) it is instructive (and useful for future reference) to consider the calculation of Γ starting from the polymer segment concentration profile $\varphi(x)$ near a single flat plate (with bulk concentration φ_b) and between two flat plates. Eisenriegler [30], and later Marques and Joanny [31], calculated the polymer concentration near one flat plate for ideal Gaussian ($M \gg 1$) chains and found the following expression for the relative polymer segment concentration $f(x) = \varphi(x)/\varphi_b$:

$$f(x) = 2\psi(z) - \psi(2z), \tag{2.51}$$

with

$$\psi(z) = \mathrm{erf}(z) + \frac{2z}{\sqrt{\pi}} e^{-z^2} - 2z^2 \mathrm{erfc}(z), \tag{2.52}$$

where z is defined as $x/(2R_g)$ and x is the distance from the surface. The (Gauss) error function $\mathrm{erf}(y)$ is defined as

$$\mathrm{erf}(y) = \frac{2}{\sqrt{\pi}} \int_0^y \mathrm{e}^{-t^2}\, \mathrm{d}t,$$

and the complimentary error function $\mathrm{erfc}(y) = 1 - \mathrm{erf}(y)$.

One can characterize the negative adsorption by the depletion layer thickness δ, which is defined as

$$\delta = \int_0^\infty \mathrm{d}x (1 - f(x)). \tag{2.53}$$

For the case of ideal polymer chains near a flat plate with the profile (2.51), we find

$$\delta = \frac{2R_g}{\sqrt{\pi}}. \tag{2.54}$$

This is in full agreement with (2.50) as $\Gamma(\infty) = 2\Gamma_{\text{single wall}} = -n_b 2\delta$.

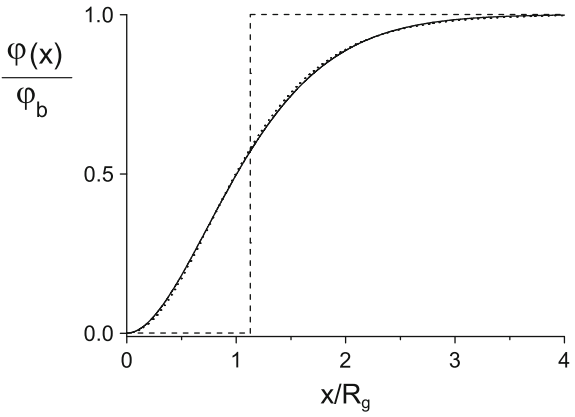

Fig. 2.11 Relative segment concentration of ideal chain segments (2.51) as a function of the distance from a flat plate (*solid curve*). *Dashed lines* represent the step function profile and the *dotted curve* is the approximation of (2.55)

Exercise
Derive $\delta = 2R_g/\sqrt{\pi}$ for ideal chains starting from its definition (2.53) and using the profile (2.51).

A simple approximation for the rather involved (2.51) is [28, 32]

$$f(x) = \tanh^2\left(\frac{x}{\delta}\right) \tag{2.55}$$

with δ given by (2.54).

In Fig. 2.11 we depict the concentration profile of an ideal polymer near a flat wall and its replacement by a step profile with width $\delta = 2R_g/\sqrt{\pi}$ (dashed). The simple approximation (2.55) reproduces the exact result within an accuracy of 1%.

Exercise
Show that the profile $f(x) = \tanh^2(x/\delta)$ has a depletion thickness δ.

For the concentration profile between two flat plates separated by a distance h the following product function approximation has been proposed [28]

$$\frac{\varphi(x)}{\varphi_b} = f(x)f(h-x). \tag{2.56}$$

In (2.56), $\varphi(x)$ is the polymer segment concentration between the plates and $f(x)$ and $f(h-x)$ are the individual one plate profiles given by (2.51) or, more simply by (2.55). The concentration near a single plate, say plate 1, can be expressed by a Boltzmann factor as $f(x) = \exp[-W_{\text{wall}}(x)/kT]$, where $W_{\text{wall}}(x)$ is the free energy giving rise to the profile. For the second plate, located at a distance h, we can then write $f(h-x) = \exp[-W_{\text{wall}}(h-x)/kT]$. Subsequently, the product function (2.56) follows from the superposition approximation:

$$W_{\text{wall,tot}}(x) = W_{\text{wall}}(x) + W_{\text{wall}}(h-x),$$

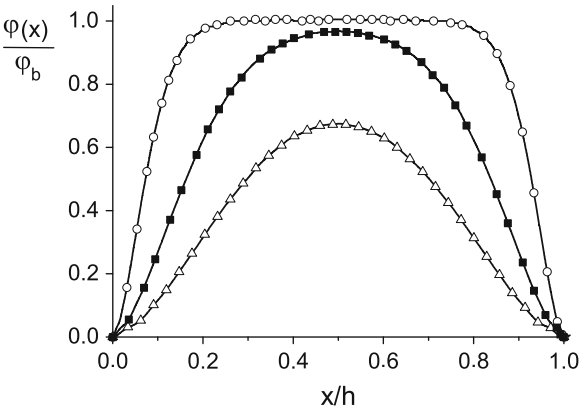

Fig. 2.12 Segment concentrations between two flat plates. Monte Carlo simulations with ideal chains of 100 segments for $h/R_g =$ 24.5 (*open circles*), 5.88 (*closed squares*), and 3.42 (*open triangles*) are compared with (2.56) as *solid curves*

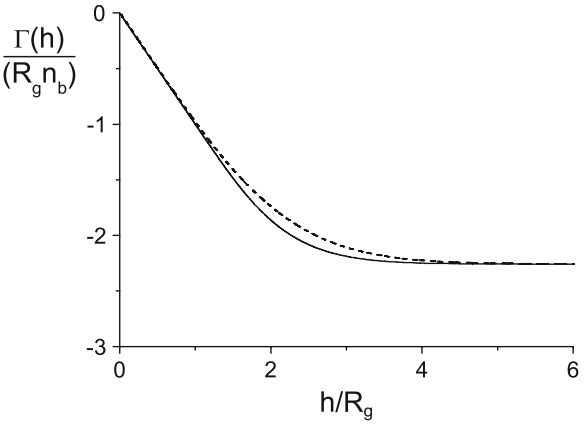

Fig. 2.13 (Negative) adsorption of ideal chains between two walls as a function of the distance between the walls. Exact result: *solid curve*. Product function approximation: *dashed curve*

which is expected to work well for sufficiently large h/R_g. This is indeed supported by computer simulations [28], see the comparison in Fig. 2.12. For $h/R_g < 3$, the product function overestimates the segment concentration between the plates. In such narrow slits the configurations of an ideal chain are then affected by both walls, which is not accounted for by the superposition approximation. While the relative deviation of the production function is largest for small plate separation h, for these distances $\Gamma(h) \to 0$ and hence the absolute error is small. The resulting adsorption is plotted in Fig. 2.13 (dashed curve). The exact result from (2.49) (with (2.35) for $\chi(h)$) is plotted as the solid curve. We conclude therefore that the product function gives overall a good prediction for the adsorption and we will use it to calculate the depletion interaction between two spheres due to ideal polymers using the extended Gibbs adsorption equation.

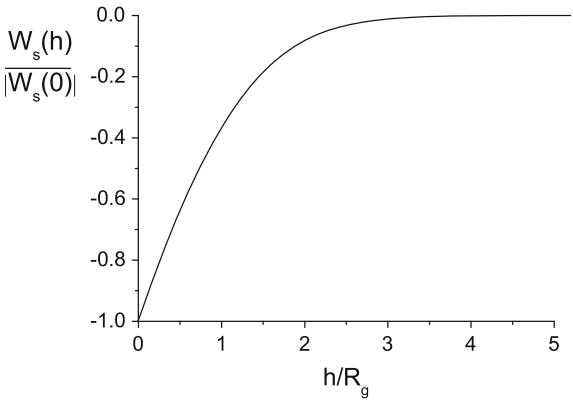

Fig. 2.14 Interaction potential between two big hard spheres as a function of the closest distance between the surfaces of the spheres

2.2.2 Interaction Between Two Spheres

2.2.2.1 Interaction Between Two Spheres from the Derjaguin Approximation

Using the Derjaguin approximation (2.27) for the force between two spheres the interaction potential between the spheres can be obtained from

$$W_s = \pi R \int_h^\infty W(h')\mathrm{d}h', \tag{2.57}$$

where $W(h)$ is the interaction potential per unit area between flat plates (2.47). The result for $q = 0.01$ is plotted in Fig. 2.14. Eisenriegler [29] obtained the following analytical expression

$$W_s(h) = -n_b kTRR_g^2\left(4\pi \ln 2 - 4\sqrt{\pi}\frac{h}{R_g} + \frac{\pi}{2}\frac{h^2}{R_g^2}\right) \tag{2.58}$$

for small values of h valid up to and including terms of order h^4. This equation matches the numerical results for $R/R_g = 100$ presented in Fig. 2.14 very closely for $h < (3/2)R_g$, see [28, 29].

Comparing the expression (2.21) for penetrable hard spheres and (2.58) for ideal chains reveals that we match the contact potentials for

$$\sigma = \sqrt{8\ \ln(2)}R_g$$

The result $\sigma = 2.35R_g$ agrees closely (within 5%) with the value $\sigma = 4R_g/\sqrt{\pi} = 2.26R_g$ for flat plates. Hence in the limit $R \gg R_g$ ideal polymers behave almost as penetrable hard spheres with a diameter $\sigma \simeq 2R_g$, just as for ideal chains between flat plates. In the next section we will see that this picture changes when $R \lesssim R_g$.

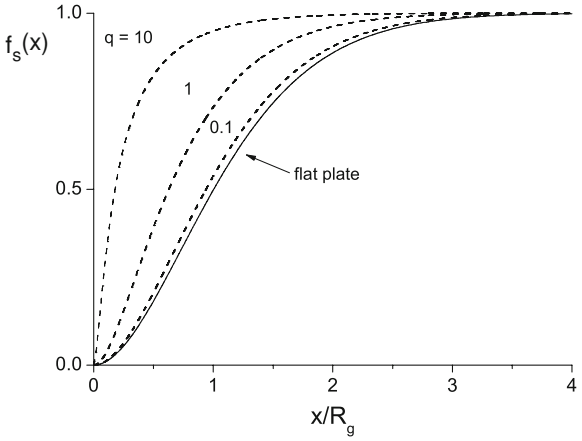

Fig. 2.15 Relative ideal chain segment concentrations at a wall and at a sphere for $q = 0.1$, $q = 1$, and $q = 10$ according to (2.59). With increasing q the profile shifts closer to the surface

2.2.2.2 Interaction Potential Between Two Spheres from the Extended Gibbs Equation

The limitation of the Derjaguin approximation is that it only provides reliable results for $R \geq R_g$. To obtain results for the interaction potential between spheres for arbitrary $q = R_g/R$ we use the extended Gibbs adsorption equation. Taniguchi et al. [33] and, independently, Eisenriegler et al. [34] found the concentration profile of Gaussian ideal polymer chains around a single hard sphere with radius R which reads

$$f_s(x) = \frac{\left(\frac{x}{R}\right)^2 + 2\left(\frac{x}{R}\right)\psi(z) + f(x)}{\left(\frac{x}{R} + 1\right)^2}, \tag{2.59}$$

where z again equals $x/2R_g$ and x is now the distance from the surface of the sphere; the functions $f(x)$ and $\psi(z)$ are defined in (2.51) and (2.52). A simpler, yet accurate, form of (2.59) is [32]

$$f_s(x) = \left(\frac{\frac{x}{R} + \tanh(x/\delta)}{\frac{x}{R} + 1}\right)^2. \tag{2.60}$$

For various ratios of $q = R_g/R$ we plotted the profiles $f_s(x)$ in Fig. 2.15. For $R \ll R_g$, the Odijk [35] result

$$f_s(x) = \left(\frac{x}{x + R}\right)^2$$

is recovered, which is independent of the polymer length scale. For large hard sphere radii $(q = 0.1)$ we see that the sphere profile approaches that of a flat plate.

However, for $R_g/R = 1$ the depletion layer thickness already becomes significantly smaller than $2R_g/\sqrt{\pi}$ and it further decreases with increasing q.

Exercise

(a) Show that in the limit $R \gg R_g$ the expression (2.59) for the profile around spheres becomes equal to the expression (2.51) for the profile at a flat plate.
(b) Give a physical argument why the concentration profile shifts towards the particle surface when R_g/R increases.

Starting from (2.59) we can obtain an analytical expression for the depletion thickness around a sphere δ_s, which is now defined by

$$\frac{4\pi}{3}\left[(R+\delta_s)^3 - R^3\right] = \int_0^\infty 4\pi(R+x)^2(1-f_s(x))\mathrm{d}x. \tag{2.61}$$

After carrying out the integration of the right-hand side of (2.61) we obtain [36, 37]

$$\frac{\delta_s}{R_g} = \left[\left(1+\frac{6q}{\sqrt{\pi}}+3q^2\right)^{1/3} - 1\right]/q. \tag{2.62}$$

Note that in the limit $q \to 0$, (2.62) yields, as expected, the flat plate result $\delta_s/R_g = 2/\sqrt{\pi}$. The result in (2.62) holds for Gaussian ideal chains, implying the segment size b is smaller than all other length scales, R_g and R. For freely-jointed ideal chains the depletion thickness also depends on the size ratio b/R for $R \lesssim 50b$ [38].

Exercise

(a) Show that in the limit $R \gg R_g$ (and hence $R \gg \delta_s$) expression (2.61) for δ_s reduces to the flat plate equation (2.53) for δ_s.
(b) Carry out the integrations in (2.61) and show that the result for δ is given by (2.62).

The result for the relative depletion thickness δ/R_g as a function of the size ratio $q = R_g/R$ is plotted in Fig. 2.16.

We showed in Sect. 2.2.1 that the product function (2.56) describes the polymer concentration profile between two flat plates quite well. Here we apply the product function Ansatz to calculate the concentration profile around two spheres. We assume that the local polymer concentration $n_s(\mathbf{r})$ in every point P (see Fig. 2.17) outside the spheres is given by

$$\frac{n_s(\mathbf{r})}{n_b} = f_s(x_1)f_s(x_2), \tag{2.63}$$

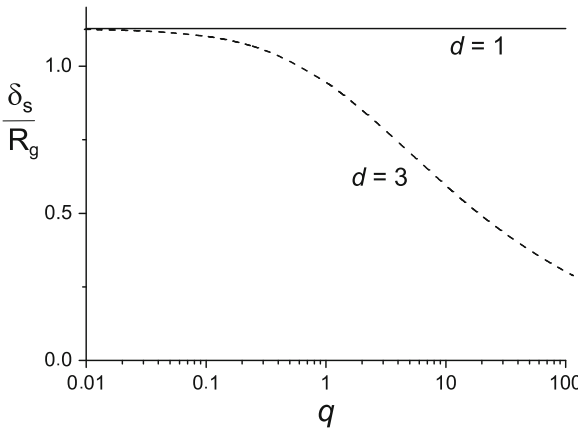

Fig. 2.16 Depletion thickness of ideal chains at a sphere ($d = 3$) as a function of the size ratio $q = R_g/a$. For comparison the flat wall case ($d = 1$) is given as *straight solid line*

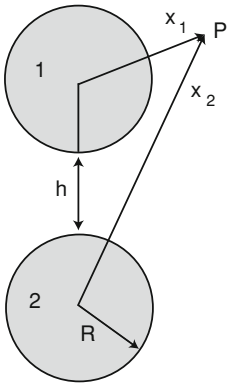

Fig. 2.17 Schematic picture of the geometry of two spheres separated by a distance h

where $f_s(x_i)$ is the polymer concentration profile around a sphere given by (2.59) with x_i the closest distance to the surface of the sphere (see Fig. 2.17). The interaction between two spheres can now be calculated from (2.22), which for ideal chains becomes

$$\frac{W_s(h)}{kT} = N(h) - N(\infty), \tag{2.64}$$

where $N(h)$ is the number of polymer molecules in the system when the colloidal particles are at a distance h (see Fig. 2.17) and $N(\infty)$ that when the colloidal particles are infinitely far apart. The quantity $N(h)$ can be calculated numerically from

$$N(h) = \int \mathrm{d}\mathbf{r}\, n_s(\mathbf{r}) \tag{2.65}$$

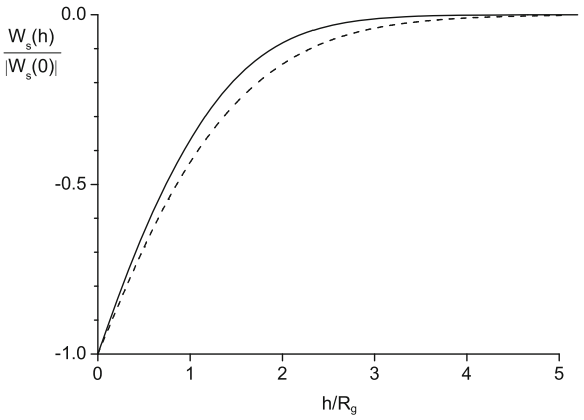

Fig. 2.18 Interaction potential between two spheres for $R/R_g = 100$. *Dashed curve*: (2.64) using (2.63). *Solid curve*: (2.58)

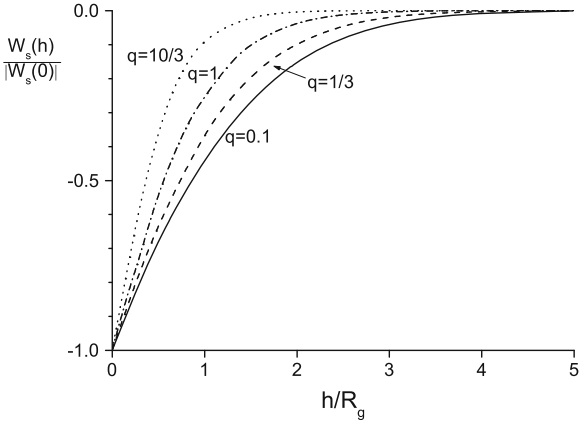

Fig. 2.19 Depletion potential as a function of the closest distance between the sphere surfaces for four size ratios $R/R_g = 10$ (*solid*), 3 (*dashed*), 1 (*dotted-dashed*), and 0.3 (*dotted*)

using the profile function (2.63) and obviously

$$N(\infty) = n_b\left(V - 2\frac{4\pi}{3}(R+\delta_s)^3\right).$$

The result for $q = 0.01$ is plotted in Fig. 2.18 (dashed curve). We normalised the interaction curve by dividing by the absolute value at contact. The depth of the interaction at contact can be computed and it is first compared to the result $W_s(0)/kT = -4\pi RR_g^2\ln(2)$ that follows from applying the Derjaguin approximation. We find a numerical value for $W_s(0)/kT$ of $-4\pi RR_g^2(0.76)$, which is close. In Fig. 2.19 we plot the results for different values of the size ratio q. We observe that the range of the interaction becomes smaller with decreasing colloid radius R in agreement with the decrease of the depletion thickness δ_s with decreasing colloid radius. In fact, by replacing in (2.18) $\sigma/2$ by δ_s given by (2.62) we obtain interaction curves in good agreement with the results presented in Fig. 2.19 obtained from the extended Gibbs adsorption equation using the product function (2.63).

This brings us to the conclusion that as far as the depletion interaction is concerned ideal polymer chains to a good approximation can be replaced by penetrable hard spheres with a diameter $\sigma = 2\delta_s$, where the depletion thickness δ_s now depends on the size ratio $q = R_g/R$. In dilute polymer solutions the ideal chain description suffices to describe depletion effects. In Chap. 4 we shall see that for polymers with excluded volume the depletion thickness not only depends on the size ration q but also on the polymer concentration, see also [36, 39–41]. Also the (osmotic) pressure is no longer given by the ideal (Van 't Hoff) expression. Both features significantly affect depletion effects.

2.3 Depletion Interaction Due to Colloid Hard Spheres

2.3.1 Concentration Profiles Near a Hard Wall and Between Two Hard Walls

We now consider the depletion interaction due to (small) colloidal hard spheres with diameter σ. At very low concentration, where we may neglect the interaction between the spheres so the system can considered to be thermodynamically ideal, the results for the depletion interaction are identical to those for penetrable hard spheres. At higher concentrations, say at volume fractions larger than a few percent, the interactions between the spheres cannot be neglected. This has two important consequences for the depletion interaction. First of all the pressure and chemical potential are no longer given by the ideal expressions. The corrections to ideal behaviour can be written in terms of the virial series (see textbooks on statistical thermodynamics, e.g., Hill [42] or Widom [43]):

$$\frac{P}{n_b kT} = 1 + B_2 n_b + \cdots \tag{2.66}$$

$$\frac{\mu}{kT} = \ln n_b + 2B_2 n_b + \cdots \tag{2.67}$$

Now n_b is the bulk concentration of (small) hard spheres. The quantity B_2 is the second osmotic virial coefficient

$$B_2 = \frac{2\pi\sigma^3}{3} = 4v_0, \tag{2.68}$$

where $v_0 = \pi\sigma^3/6$ is the volume of a hard sphere. Secondly, the interactions between the particles among themselves and with a wall leads to a concentration profile near the wall. Obviously, in a layer at the wall with thickness $\sigma/2$ no centers of the hard spheres can penetrate. In the case of penetrable hard spheres the concentration takes on the bulk value n_b outside the depletion layer. However, in the case of hard spheres the interactions lead to an effective attraction between a

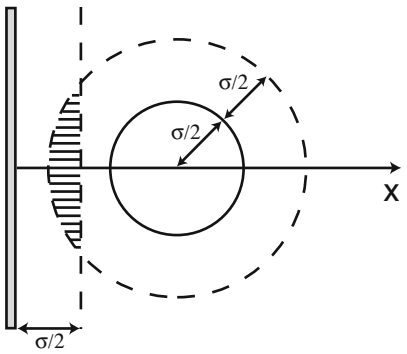

Fig. 2.20 Overlap volume (*hatched*) between a hard wall and a hard sphere

sphere and the wall and the concentration profile at distance $x = \sigma/2 + y$ from the wall can be written as

$$n(x) = n_b \exp[-W_{\text{wall}}(x)/kT], \tag{2.69}$$

where $W_{\text{wall}}(x)$ is the effective interaction between the hard sphere and the wall. In fact this is the potential of mean force between the sphere and the wall due to the other hard spheres. To lowest order in density we can write

$$W_{\text{wall}}(x) = -n_b kT v(y) \tag{2.70}$$

where $v(y)$ is the overlap volume of the depletion zone around the sphere and the depletion layer of the wall depicted in Fig. 2.20,

$$v(y) = \frac{\pi}{3}\left(2\sigma^3 - 3\sigma^2 y + y^3\right) \quad 0 \le y \le \sigma. \tag{2.71}$$

or

$$n_b v(y) = \phi\left(4 - 6\frac{y}{\sigma} + 2\frac{y^3}{\sigma^3}\right) \quad 0 \le y \le \sigma. \tag{2.72}$$

Here $\phi = n_b \pi\sigma^3/6$ is the volume fraction of the (small) spheres.
From (2.69–2.71) we obtain the lowest order in density $n(x)$

$$\begin{aligned} \frac{n(x)}{n_b} &= 0 && 0 \le x < \sigma/2 \\ &= 1 + n_b v(y) && \sigma/2 \le x \le 3\sigma/2 \end{aligned} \tag{2.73}$$

This profile of hard spheres at a single wall to order n_b^2 is depicted in Fig. 2.21. We see that in addition to the depletion layer there is also an 'accumulation' layer, where $n(x) > n_b$. The hard spheres located close to the depletion layer tend to 'push' one another into the layer next to the excluded depletion layer resulting in the accumulation. As we will see later this layer has important consequences for the depletion interaction. The concentration profile at a single wall to order n_b^3 was calculated by Fisher [44].

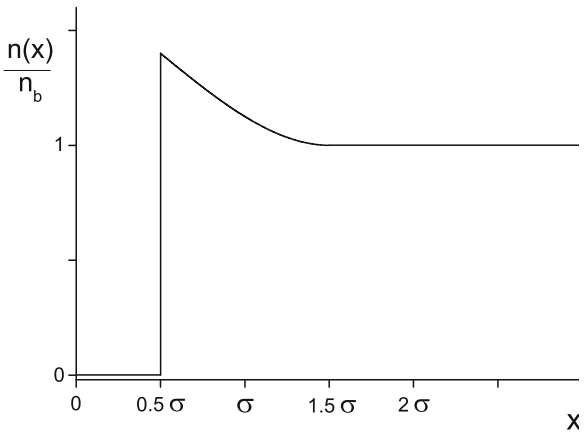

Fig. 2.21 Density profile $n(x)$ of hard spheres with $\phi = 0.1$ as a function of the distance from the wall x (2.73)

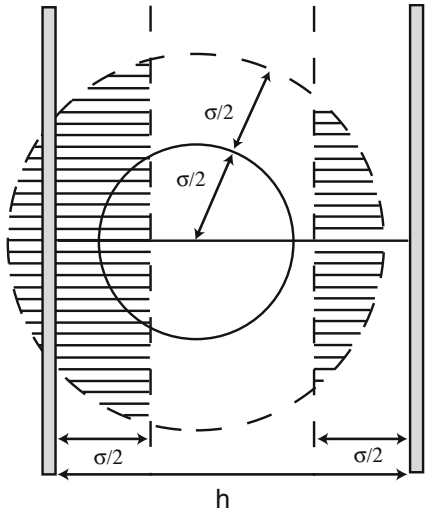

Fig. 2.22 A sphere between two walls. *Hatched areas* are the overlap volume between the hard sphere and the hard walls

For the calculation of the depletion interaction due to hard spheres we need the concentration profile between two confining walls. This problem was treated analytically by Glandt [45] and by Antonchenko et al. [46] using Monte Carlo computer simulations. Like for a single wall we present the calculation of the concentration profile between two confining walls to order n_b^2. For $h < \sigma$, no spheres can penetrate between the walls and hence the concentration is zero. For $\sigma \leq h \leq 2\sigma$, the depletion zone of a sphere overlaps with the depletion zones of both walls (see Fig. 2.22) and we can write

$$\frac{n(x)}{n_b} = 1 + n_b v(y) + n_b v(h - \sigma - y) \quad 0 \leq y \leq h - \sigma, \tag{2.74}$$

with $n_b v$ defined in (2.72).

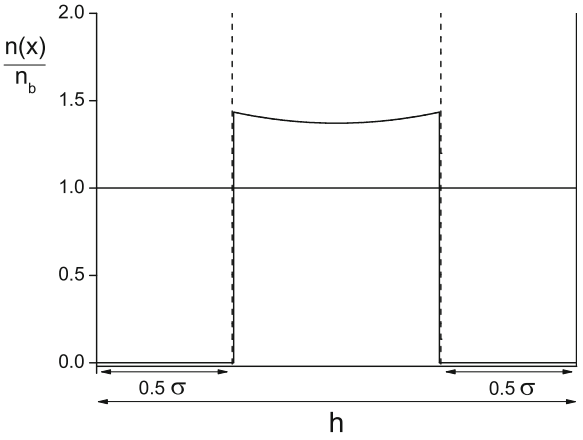

Fig. 2.23 Density profile of hard spheres between two hard walls for $h = 7\sigma/4$ and $\phi = 0.1$

The profile of hard spheres between two confining walls to order n_b^2 for $\sigma \leq h \leq 2\sigma$ is depicted in Fig. 2.23. For $h > 2\sigma$ there is no longer simultaneous overlap of the depletion layer of a sphere with the depletion layers of the confining walls. The profile then simply is the sum of the profiles of the two separate walls; there is no depletion-induced attraction.

2.3.2 Depletion Interaction Between Two Flat Plates

2.3.2.1 Interaction Potential Between Two Flat Plates from the Force Method

We follow the work of Mao et al. [47]. The same results as presented here were obtained earlier by Walz and Sharma [48] using a somewhat different method. The starting point for our treatment is a result by Henderson [49] that the force per unit area between two parallel hard plates immersed in a suspension of hard spheres is given by

$$K = P_i - P_o = kT(n_i - n_o), \tag{2.75}$$

where n_i and n_o are the *contact densities* of the hard spheres inside and outside the plates. A contact density is ensemble-averaged the density *at* the surface. This result can be explained as follows. The particle velocities are separable degrees of freedom and therefore always obey the Maxwell–Boltzmann distribution. The force per unit area on a hard plate is therefore given rigorously by elementary kinetic theory as [50]

$$P = n^* kT, \tag{2.76}$$

where n^* is the number density of particles at a distance corresponding to the point of impact (the position at which a particle hits the surface). This is, of course, the contact density. This argument applies whenever there is a hard interaction between the particles and the plate [50]. The generality of (2.75) will also be exploited in Sects. 2.4 and 2.5, where we consider the depletion interaction due to hard rods and hard disks. Up to order n_b^2 we find from (2.73) that

$$\begin{aligned} \frac{P_o}{kT} = n_o &= n_b[1 + n_b v(0)] \\ &= n_b\left[1 + n_b \frac{2\pi\sigma^3}{3}\right], \end{aligned} \tag{2.77}$$

or, in terms of ϕ,

$$\frac{P_o v_0}{kT} = \phi + 4\phi^2. \tag{2.78}$$

This is in agreement with the virial series (2.66) using the second virial coefficient (2.68). Between the plates we find

$$\begin{aligned} \frac{P_i}{kT} &= 0 && 0 \le h < \sigma \\ &= n_b[1 + n_b v(0) + n_b v(h - \sigma)] && \sigma \le h < 2\sigma \\ &= n_b[1 + n_b v(0)] && h \ge 2\sigma \end{aligned} \tag{2.79}$$

Hence

$$\begin{aligned} \frac{K(h)}{n_b kT} &= -1 - 4\phi && 0 \le h < \sigma \\ &= \phi\left[4 - 6\lambda + 2\lambda^3\right] && \sigma \le h < 2\sigma \\ &= 0 && h \ge 2\sigma \end{aligned} \tag{2.80}$$

where $\lambda = (h - \sigma)/\sigma$, which runs from 0 at $h = \sigma$ to 1 at $h = 2\sigma$.

The depletion force depicted in Fig. 2.24 jumps from negative (attractive) at $h = \sigma^-$ to positive (repulsive) at $h = \sigma^+$. The key idea behind the origin of the repulsive part of the depletion force is that for small λ the mutual repulsion of spheres is substantially reduced due to the fact that the excluded volumes of the spheres are hidden behind the depletion zones of the walls. In the limit $h = \sigma^+$, the spheres behave effectively thermodynamically ideal. To match the chemical potential (2.67) of the spheres in the bulk the number density inside the gap must be

$$n_i = n_b[1 + 2B_2 n_b], \tag{2.81}$$

and hence for $h = \sigma^+$

$$P_i = kTn_b[1 + 2B_2 n_b], \tag{2.82}$$

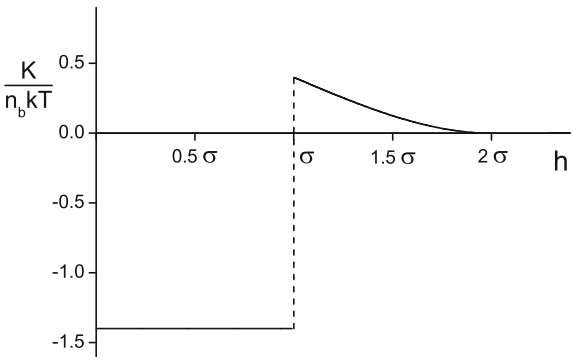

Fig. 2.24 Depletion force between two hard plates due to small hard spheres ($\phi = 0.1$)

giving rise to a maximum repulsive depletion force

$$\begin{aligned} K_{\max}(h = \sigma^+) &= P_i - P_o \\ &= 44kTn_b\phi \end{aligned} \tag{2.83}$$

Exercise
Derive (2.81)

Integrating the force (2.80) yields the interaction potential per unit area $W(h)$ between the plates

$$\begin{aligned} \frac{W(h)}{kTn_b} &= \sigma\left(\lambda + \frac{3}{2}\phi + 4\lambda\phi\right) && 0 \le h < \sigma \\ &= \sigma\phi\left(\frac{3}{2} - 4\lambda + 3\lambda^2 - \frac{1}{2}\lambda^4\right) && \sigma \le h < 2\sigma \\ &= 0 && h \ge 2\sigma \end{aligned} \tag{2.84}$$

In Fig. 2.25 we present the interaction potential which has a significant attraction at small separation distance h, but also has a repulsive part of the potential.

Exercise
(a) Explain why, whereas the force K has a discontinuity at $h = \sigma$, the interaction potential W is continuous at that point.
(b) Why is the interaction potential still repulsive for h just below σ, while the force is attractive?

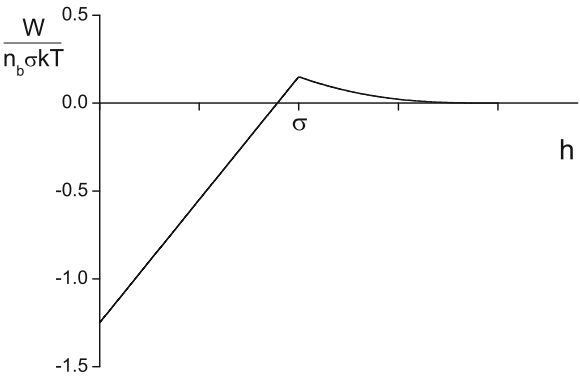

Fig. 2.25 Interaction potential between two hard plates due to small hard spheres ($\phi = 0.1$)

2.3.2.2 Interaction Potential Between Two Flat Plates from the Extended Gibbs Equation

From the depletion layer with thickness $\sigma/2$ and concentration profile (2.73) it follows that the adsorption on a single plate is given by

$$\begin{aligned}\Gamma_{\text{single wall}} &= -\frac{\sigma}{2}n_b + n_b^2\int_0^{\sigma} v(x)\mathrm{d}x \\ &= -\frac{\sigma}{2}n_b + n_b^2\frac{\pi}{4}\sigma^4\end{aligned} \tag{2.85}$$

Hence

$$\begin{aligned}\Gamma(\infty) &= 2\Gamma_{\text{single wall}} \\ &= -\sigma n_b + n_b^2\frac{\pi}{2}\sigma^4 \\ &= \sigma n_b(3\phi - 1)\end{aligned} \tag{2.86}$$

For two confining walls it is clear that for $h < \sigma$ no spheres can penetrate the gap between the walls. Hence

$$\Gamma(h) = \sigma n_b(3\phi - 1) \tag{2.87}$$

Using the concentration profile (2.74) we obtain for $\sigma \le h < 2\sigma$

$$\begin{aligned}\Gamma(h) &= -\sigma n_b + n_b^2\int_0^{h-\sigma}[v(x) + v(h-\sigma-x)]\mathrm{d}x \\ &= -\sigma n_b + \frac{2\pi}{3}n_b^2\sigma^4\left[2\lambda - \frac{3}{2}\lambda^2 + \frac{1}{4}\lambda^4\right]\end{aligned} \tag{2.88}$$

or

$$\frac{\Gamma(h)}{n_b\sigma} = \phi\left[8\lambda - 6\lambda^2 + \lambda^4\right] - 1 \tag{2.89}$$

For $h \geq 2\sigma$

$$\Gamma(h) = \Gamma(\infty). \tag{2.90}$$

Combining (2.86–2.90) gives

$$\begin{aligned} \frac{\Gamma(h) - \Gamma(\infty)}{n_b\sigma} &= 1 - \frac{h}{\sigma} - 3\phi; && 0 \leq h < \sigma \\ &= -\phi\left[3 - 8\lambda + 6\lambda^2 - \lambda^4\right]; && \sigma \leq h < 2\sigma \\ &= 0; && h \geq 2\sigma \end{aligned} \tag{2.91}$$

Taking into account that the chemical potential is now given by (2.67) we obtain from (2.13)

$$W(h) = -kT \int_0^{n_b} [\Gamma(h) - \Gamma(\infty)] \left[\frac{1}{n_b} + 2B_2\right] \mathrm{d}n_b. \tag{2.92}$$

Substituting (2.91) in (2.92) after some algebra yields (2.84). Note that in all cases considered so far (penetrable hard spheres, polymers) the quantity $[\Gamma(h) - \Gamma(\infty)]$ was always positive (or zero) for all values for h. Here we see that due to accumulation effects in the concentration profiles $[\Gamma(h) - \Gamma(\infty)]$ is negative for a certain range of h values. This leads to a positive interaction energy as is clear from (2.92).

Such a repulsive contribution to the depletion interaction originates from excluded volume interactions between the depletants; in case of ideal polymers and penetrable hard spheres it is absent. One might expect accumulation effects also in the case of interacting polymers. From Monte Carlo simulation studies [51] and numerical self-consistent field computations [52, 53] it follows that interacting polymers do contribute to repulsive depletion interactions but with a strength of the repulsion that is nearly imperceptible.

2.3.3 Depletion Interaction Between Two (Big) Spheres

Using the Derjaguin approximation (2.27) we obtain the interaction between two big spheres due to the small spheres by integration:

$$W_s(h) = \pi R \int_h^{2\sigma} W(h')\mathrm{d}h'. \tag{2.93}$$

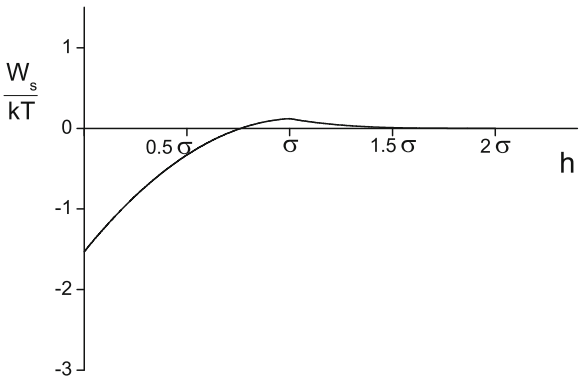

Fig. 2.26 Depletion potential between two hard spheres ($R = 5\sigma$) mediated by small hard spheres with $\phi = 0.1$

Using (2.84) for the interaction potential per unit area in (2.93) we obtain

$$\begin{aligned}\frac{W_s(h)}{kT} &= -\frac{R}{\sigma}\left[3\phi\lambda^2 - \phi^2(12 - 45\lambda - 60\lambda^2)\right] \qquad 0 \le h < \sigma \\ &= \frac{R\phi^2}{5\sigma}\left[12 - 45\lambda + 60\lambda^2 - 30\lambda^3 + 3\lambda^5\right] \quad \sigma \le h < 2\sigma \\ &= 0 \qquad\qquad\qquad\qquad\qquad\qquad\qquad\qquad h \ge 2\sigma, \end{aligned} \tag{2.94}$$

which has a positive maximum value of

$$\frac{W_{s,\max}}{kT} = \frac{12R}{5\sigma}\phi^2 \quad \text{at} \quad h = \sigma\left(1 - \frac{3}{2}\phi\right),$$

and a minimum value at contact

$$\frac{W_{s,\min}}{kT} = -3\frac{R}{\sigma}\left(\phi + \frac{1}{5}\phi^2\right). \tag{2.95}$$

In Fig. 2.26 we present the interaction potential between spheres (valid up to n_b^2 or, equivalently, up to ϕ^2). In [47] results are presented for the interaction valid up to n_b^3 including a comparison with the computer simulation results of Biben et al. [54].

Exercise

(a) Derive the interaction potential between spheres (2.94) from the extended Gibbs adsorption equation in the limit $R \gg \sigma$ (as is implicit when using the Derjaguin approximation).

(b) Show that (2.94) in the limit of first order ϕ equals (2.21).

2.4 Depletion Interaction Due to Colloidal Hard Rods

Asakura and Oosawa [1, 55] already recognized that rod-like macromolecules are very efficient depletion agents. In retrospect the observations of Fåhraeus [56] that the rod-like protein fibrinogen has, on a weight basis, the strongest effect on the aggregation of red blood cells can be understood on the basis of its high efficiency as a depletion agent associated with its rod-like shape. Here we consider the interaction caused by rod-like colloids as depletants and focus on a simple case; infinitely thin hard rods of length L. These rods have no excluded volume with respect to each other and hence behave thermodynamically ideally.

2.4.1 Depletion Interaction Between Two Flat Plates

2.4.1.1 Interaction Potential Between Two Flat Plates Using the Force Method

As we are dealing with hard plates and a hard wall we can again use (2.75) to calculate the force. The contact densities this time follow by considering the angles of the rods as a function of distance from the wall that lead to contact of an end point with the wall. First of all to make contact with the wall the distance of the center of the rod from the wall should be smaller than $L/2$. At a distance from the wall $x<L/2$ the angle that leads to contact is given by

$$\theta_x = \text{arc cos}\frac{x}{L/2}. \tag{2.96}$$

(see Fig. 2.27). Outside the confining walls x runs from $L/2$ to 0. Hence θ_x runs from 0 to $\pi/2$, so using spherical coordinates we obtain

$$n_o = n_b \int_0^{\pi/2} \sin\,\theta\,\mathrm{d}\theta = n_b$$

giving

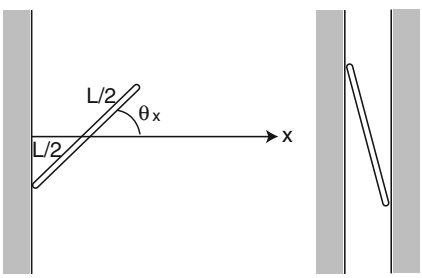

Fig. 2.27 Hard rod at a (hard) wall (*left*) and confined between two walls (*right*)

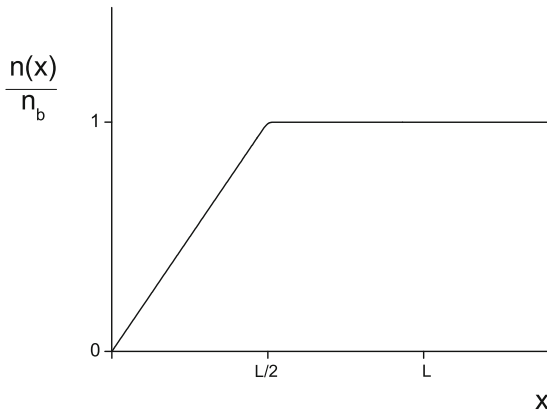

Fig. 2.28 Density profile of hard rods at a hard wall

$$P_o = n_b kT. \tag{2.97}$$

This result could have been written down at once as the infinitely thin rods behave ideally. Between two confining walls separated by a distance $h < L$ the second wall prevents contact configurations with the first wall for distances $x \geq h/2$. Hence

$$\begin{aligned} n_i = n_b \int_{\theta_{h/2}}^{\pi/2} \sin\,\theta\,\mathrm{d}\theta &= n_b \frac{h}{L} \quad 0 \leq h \leq L \\ &= n_b \qquad h > L \end{aligned}$$

From this result (plotted in Fig. 2.28) it follows using (2.76) that

$$\begin{aligned} P_i &= n_b kT \frac{h}{L} \quad 0 \leq h \leq L \\ &= n_b kT \qquad h > L \end{aligned} \tag{2.98}$$

By combining (2.97) and (2.98) we obtain for the force

$$\begin{aligned} K(h) &= P_i - P_o \\ &= -n_b kT[1 - h/L] \quad 0 \leq h \leq L \\ &= 0 \qquad\qquad\qquad h > L \end{aligned} \tag{2.99}$$

Integration of the force (2.99) yields the interaction potential per unit area $W(h)$ between the plates

$$\begin{aligned} W(h) &= -\frac{1}{2} n_b kT \frac{(L-h)^2}{L} \quad 0 \leq h \leq L \\ &= 0 \qquad\qquad\qquad\quad h > L \end{aligned} \tag{2.100}$$

This result was first obtained by Asakura and Oosawa [55] (see also Auvray [57]). Mao et al. [58, 59] considered the depletion interaction due to long thin rods with a finite diameter D. Then the system is no longer ideal and the interaction potential contains higher order terms in n_b. Like in the case of hard spheres the interactions between the rods themselves and with the wall results in the accumulation of rods at the wall which in turn leads to a repulsive contribution to the depletion interaction. For details we refer to the papers by Mao et al. [58, 59].

2.4.1.2 Interaction Potential Between Two Flat Plates from the Extended Gibbs Equation

The concentration profile of the rods near a wall also follows by considering the allowed angles. For a rod at a distance $x<L/2$ from a single wall the angles ranging from θ_x (defined by (2.96)) to $\pi/2$ are allowed (see Fig. 2.27).

Hence

$$n(x) = n_b \int_{\theta_x}^{\pi/2} \sin\,\theta\,\mathrm{d}\theta = n_b \frac{x}{L/2}. \tag{2.101}$$

(see Figs. 2.27 and 2.28). This provides an adsorbed amount at one wall

$$\Gamma_{\text{single wall}} = \int_0^{L/2} [n(x) - n_b]\mathrm{d}x = -n_b\, L/4,$$

and thus

$$\Gamma(\infty) = 2\Gamma_{\text{single wall}} = -n_b\, L/2. \tag{2.102}$$

For two confining walls separated by a distance $h<L$

$$\begin{aligned} n(x) &= n_b \frac{x}{L/2} \qquad 0 \le x \le h/2 \\ &= n_b \frac{h-x}{L/2} \qquad h/2 \le x \le h \end{aligned} \tag{2.103}$$

(see Fig. 2.29). Hence

$$\begin{aligned} \Gamma(h) = \int_0^h [n(x) - n_b]\mathrm{d}x &= n_b \left[\frac{h^2}{2L} - h\right] \qquad 0 \le h \le L \\ &= -n_b \frac{L}{2} \qquad\qquad h > L \end{aligned} \tag{2.104}$$

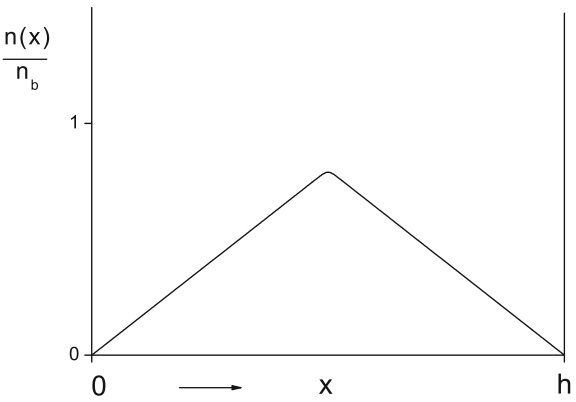

Fig. 2.29 Density of hard rods between two hard walls for $h = 4/5L$

Consequently,

$$\begin{aligned} \Gamma(h) - \Gamma(\infty) &= n_b \frac{[L-h]^2}{2L} \qquad 0 \le h \le L \\ &= 0 \qquad\qquad\quad h > L \end{aligned} \tag{2.105}$$

Substituting (2.105) in (2.13) and carrying out the integration, taking account that $\mu = kT \ln n_b$ (ideal behaviour) immediately results in the interaction potential (2.100). For the calculation and simulation of concentration profiles at walls of rods of finite thickness and the evaluation of the resulting depletion interaction to higher orders of n_b, we refer to Mao et al. [60].

2.4.2 *Interaction Between Two (Big) Colloidal Spheres Using the Derjaguin Approximation*

Using the Derjaguin approximation (2.27) we obtain the interaction between two big spheres with radius $R \gg L$ by integration

$$W_s(h) = \pi R \int_h^L W(h')\mathrm{d}h'.$$

Using (2.100) for the interaction potential per unit area in the above integration we obtain

$$W_s(h) = -n_b kT \pi R \frac{(L-h)^3}{6L}. \tag{2.106}$$

This expression for the interaction potential is also valid to order n_b for long thin rods with a finite diameter D and we can then write (2.106) in the form

$$W_s(h) = -\frac{2}{3}kT\phi\frac{R}{D}\frac{L}{D}\left(1-\frac{h}{L}\right)^3, \tag{2.107}$$

where

$$\phi = n_b\frac{\pi}{4}LD^2 \tag{2.108}$$

is the volume fraction of the rods. Comparing this expression for the depletion interaction between two big spheres with that for small spheres as depletant (2.94) for low ϕ reveals that the factor L/D, which usually is significantly larger than unity, is an important difference. Take as an example $R = 1\,\mu\text{m}$, $L = 200\,\text{nm}$ and $D = 10\,\text{nm}$. Then the factor

$$\frac{R}{D}\frac{L}{D} = 2000,$$

which implies that for a volume fraction of rods as low as 0.1% the depletion interaction will already be of order kT. For small colloidal spheres with $\sigma = 10\,\text{nm}$ this would require a volume fraction of about 1%.

The higher order terms calculated by Mao et al. [59], result, as in the case of small spheres as a depletion agent, in a repulsive barrier in the depletion interaction.

2.5 Depletion Interaction Due to Thin Colloidal Disks

Thin colloidal disks provide another example of an anisometric colloidal particle as an efficient depletion agent. This problem was first considered by Piech and Walz [61]. At the end of this section, where we compare spheres, rods and disks as depletion agents, we will see that the disk is intermediate in efficiency to induce depletion attraction between spheres and rods. Here we consider disks of diameter D and thickness L, see Fig. 2.30. Notice that for the simplest case, i.e., infinitely thin hard disks, the excluded volume of the disks with respect to each other is non-zero and only in limit of the concentration going to zero will the disks behave thermodynamically ideal. We restrict ourselves to this limiting case.

2.5.1 Depletion Interaction Between Two Flat Plates

2.5.1.1 Interaction Potential Between Two Flat Plates from the Force Method

We again use (2.75) as the starting point for the calculation of the force. To make contact with the wall, the distance of the center of the disks from the wall should

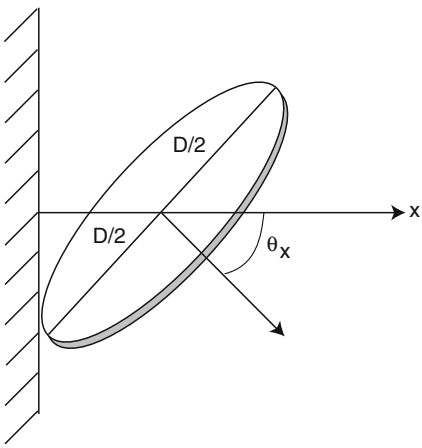

Fig. 2.30 Platelet at a hard wall. The *grey area* represents the thickness L

be smaller than $D/2$. At a distance from the wall $x < D/2$ the angle between the normal of the disk and the normal of the wall that leads to contact is now given by

$$\theta_x = \text{arc sin}\left(\frac{x}{D/2}\right). \tag{2.109}$$

(see Fig. 2.30). Outside the confining walls x runs from 0 to $D/2$. The contact density n_o follows as

$$n_o = n_b \int_0^{\pi/2} \sin\theta \, \mathrm{d}\theta = n_b$$

and hence (2.76)

$$P_o = n_b kT.$$

Between two confining walls separated by a distance $h < D$ the second wall prevents contact configurations with the first wall for distances $x \geq h/2$. Hence

$$n_i = n_b \int_0^{\theta_{h/2}} \sin\theta \, \mathrm{d}\theta = n_b \left[1 - \sqrt{1 - (h/D)^2}\right] \quad 0 \leq h \leq D$$
$$= n_b \qquad\qquad\qquad\qquad\qquad\qquad h > D$$

and hence

$$P_i = n_b kT \left[1 - \sqrt{1 - (h/D)^2}\right] \quad 0 \leq h \leq D$$
$$= n_b kT \qquad\qquad\qquad\qquad\qquad\qquad h > D$$

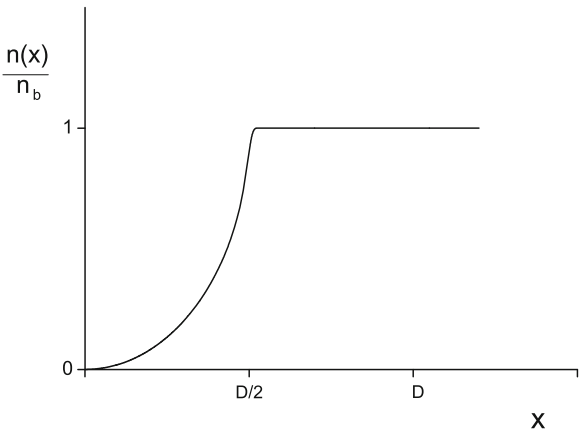

Fig. 2.31 Density profile of hard platelets at a hard wall

This leads to the following expression for the force between the plates

$$\begin{aligned} K(h) &= P_i - P_o \\ &= -n_b kT\sqrt{1-(h/D)^2} \quad 0 \le h \le D \\ &= 0 \qquad\qquad\qquad\qquad\quad h > D \end{aligned} \tag{2.110}$$

Integration of the force (2.110) yields the interaction potential per unit area $W(h)$ between the plates

$$W(h) = -n_b kT\,\frac{D}{2}\left[\frac{\pi}{2} - \frac{h}{D}\sqrt{1-\left(\frac{h}{D}\right)^2} - \text{arc sin}\left(\frac{h}{D}\right)\right]. \tag{2.111}$$

Exercise
Derive the interaction potential (2.111) from the force (2.110).

2.5.1.2 Interaction Potential Between Two Flat Plates from the Extended Gibbs Equation

The concentration profile of the disks near a wall also follows by considering the allowed angles [57]. For a disk at a distance $x < D/2$ from a single wall the angles ranging from 0 to θ_x (defined by (2.109)) are allowed (see Fig. 2.30).

Hence

$$n(x) = n_b \int_0^{\theta_x} \sin\,\theta\,\mathrm{d}\theta = n_b\left[1 - \sqrt{1-\left(\frac{x}{D/2}\right)^2}\right] \tag{2.112}$$

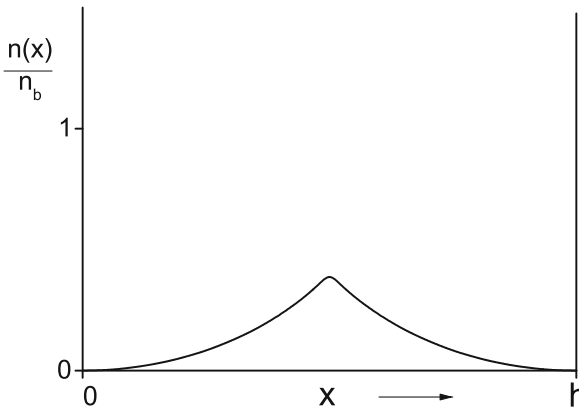

Fig. 2.32 Density profile of hard platelets between two walls for $h = 4D/5$

(see Fig. 2.31). Hence

$$\Gamma_{\text{single wall}} = \int_0^{D/2} [n(x) - n_b]\mathrm{d}x = -n_b D\frac{\pi}{8},$$

and thus

$$\Gamma(\infty) = 2\Gamma_{\text{single wall}} = -n_b D\frac{\pi}{4}. \tag{2.113}$$

For two confining walls separated by a distance $h < D$

$$\begin{aligned} n(x) &= n_b\left[1 - \sqrt{1 - \left(\frac{x}{D/2}\right)^2}\right] \qquad 0 \le x \le \frac{h}{2} \\ &= n_b\left[1 - \sqrt{1 - \left(\frac{h-x}{D/2}\right)^2}\right] \qquad \frac{h}{2} \le x \le h \end{aligned} \tag{2.114}$$

(see Fig. 2.32). Hence

$$\begin{aligned} \Gamma(h) &= \int_0^h [n(x) - n_b]\mathrm{d}x \\ &= -n_b\frac{D}{2}\left[\left(\frac{h}{D}\right)\sqrt{1 - \left(\frac{h}{D}\right)^2} + \frac{1}{2}\arcsin\left(\frac{h}{D}\right)\right] \qquad 0 \le h \le D \\ &= -n_b D\frac{\pi}{4} \qquad\qquad\qquad\qquad\qquad\qquad\qquad\quad h > D \end{aligned} \tag{2.115}$$

Combining (2.113) and (2.115) we obtain for $0 \leq h \leq D$

$$\Gamma(h) - \Gamma(\infty) = n_b \frac{D}{2} \left[\frac{\pi}{2} - \left(\frac{h}{D}\right) \sqrt{1 - \left(\frac{h}{D}\right)^2} - \text{arc sin} \left(\frac{h}{D}\right) \right]. \tag{2.116}$$

Substituting (2.116) in (2.13) and carrying out the integration with $\mu = kT \ln n_b$ once again yields the interaction potential (2.111).

2.5.2 *Interaction Between Two (Big) Colloidal Spheres Using the Derjaguin Approximation*

Using the Derjaguin approximation (2.27) we obtain the interaction between two big spheres with radius $R \gg D$ by integration

$$W_s(h) = \pi R \int_h^D W(h') \mathrm{d}h'.$$

Using (2.111) for the interaction potential per unit area in the above integration we obtain

$$W_s(h) = -n_b kT \frac{\pi}{3} RD^2 \times \left[-\frac{3}{4}\pi \frac{h}{D} + \frac{3}{2}\frac{h}{D} \text{arc sin} \left(\frac{h}{D}\right) + \left(1 + \frac{1}{2}\left(\frac{h}{D}\right)^2\right) \sqrt{1 - \left(\frac{h}{D}\right)^2} \right]. \tag{2.117}$$

This result obtained for infinitely thin disks will presumably also be valid for disks with finite thickness L to lowest order in n_b (although such a calculation has not been carried out) and we can then write (2.117) in the form

$$W_s(h) = -\frac{4}{3} kT \phi \frac{R}{L} \times \left[-\frac{3}{4}\pi \frac{h}{D} + \frac{3}{2}\frac{h}{D} \text{arc sin} \left(\frac{h}{D}\right) + \left(1 + \frac{1}{2}\left(\frac{h}{D}\right)^2\right) \sqrt{1 - \left(\frac{h}{D}\right)^2} \right], \tag{2.118}$$

where

$$\phi = n_b (\pi/4) LD^2. \tag{2.119}$$

Table 2.1 Characteristic parameters for C, ℓ and f in (2.120)

Depletion agent	C	ℓ	f
Sphere	$\pi/2$	σ	$(1-h/\ell)^2$
Rod	$\pi/6$	L	$(1-h/\ell)^3$
Disk	$\pi/3$	D	$\frac{3}{2}\left(\frac{h}{\ell}\right)\arcsin\left(\frac{h}{\ell}\right)-\frac{3}{4}\pi\left(\frac{h}{\ell}\right)+\left(1+\frac{1}{2}\left(\frac{h}{\ell}\right)^2\right)\sqrt{1-\left(\frac{h}{\ell}\right)^2}$
Ideal polymer	$\pi/2$	$R_g\sqrt{8\ln 2}$	$\left(1-\sqrt{\frac{8}{\pi\ln 2}}(h/\ell)+(h/\ell)^2+\cdots\right)$

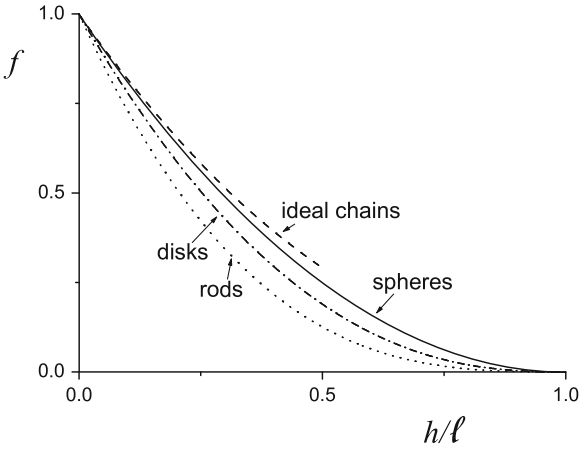

Fig. 2.33 Sketch of the function f in (2.120) for rods (*dotted*), disks (*dashed-dotted*), spheres (*solid*) and ideal chains (*dashed*), see Table 2.1

For thin disks L is small so R/L is large. Assume $R = 1\,\mu\text{m}$, $D = 200\,\text{nm}$ and $L = 1\,\text{nm}$ then $R/L = 1000$ implies that for volume fractions ϕ of the disks of 0.1% the depletion interaction is already of the order kT.

Comparison of the depletion potentials due to spheres (2.94), rods (2.107), disks (2.117) and ideal polymers (2.58) reveals that to lowest order in the depletant density they all have the general form

$$W_s(h) = -n_b kTRC\ell^2 f\left(\frac{h}{\ell}\right), \tag{2.120}$$

where ℓ is the characteristic length scale of the depletion agent, the prefactor C determines the depth of the potential and the function f sets the distance dependence normalized such that $f(0) = 1$ and $f(1) = 0$. This is summarized in Table 2.1.

Because for the ideal chain result higher-order h/R_g terms are not available the $f(1) = 0$ limit can not be accessed. In Fig. 2.33 we present the functions f for ideal chains (small h), spheres, rods and plates. It is clear that the dependence on the interparticle separation $f(h/\ell)$ is similar for greatly different depletants. The results for depletion interaction between big spheres discussed here are based on the Derjaguin approximation valid for $R \gg \ell$ ($\ell = \sigma, L, D$ for spheres, rods and disks).

In [62] an analysis of the accuracy of the Derjaguin approximation for depletion potentials is presented. From this analysis it follows that the depletion potential of large spheres due to small spheres is underestimated by the Derjaguin approximation, is surprisingly accurate for disks and is overestimated for rod-like depletion agents. A statistical mechanical analysis of the Derjaguin approximation applied to depletion interactions in colloidal fluids is presented by Henderson [63].

2.6 Measurements of Depletion Interactions

In this section we summarize experimental methods that enable measuring (depletion) interaction potentials between particles [64]. We distinguish pair interactions (Sects. 2.6.1–2.6.3) and many-body interactions (Sect. 2.6.4). The latter can be measured indirectly using scattering techniques or microscopy, whereas for pair interactions direct methods are available. Common instruments for investigating such pair interactions are the surface force apparatus (SFA) [65], optical tweezers [66, 67], atomic force microscopy (AFM) [68], and total internal reflection microscopy (TIRM) [69, 70].

The SFA was the first method allowing to measure forces between particles. It was developed by Tabor and Winterton [71] for two cylindrical surfaces in air or vacuum. An upgrade of the apparatus enabling measurements in liquids was constructed by Israelachvili and Adams [72, 73]. An advantage of SFA is the high spatial resolution of 0.1 nm when using molecularly smooth mica sheets; SFA is mainly used for model surfaces. Unfortunately, the force resolution is small ($O(10^{-8}\,N)$) and the contact area between the surfaces needs to be very large ($O(1\,\mu m^2)$). Overall, it turned out SFA is less suitable for measuring depletion forces and therefore we restrict ourselves here to AFM, TIRM and optical tweezers and briefly introduce these techniques below. A few arbitrarily chosen experimental examples of potentials in the presence of depletants are given as illustrations.

The effective pair interactions measured with these techniques are the direct pair interactions between two colloidal particles plus the interactions mediated by the depletants. In practice depletants are polydisperse, for which there are sometimes theoretical results available. For the interaction potential between hard spheres we quote references for the depletion interaction in the presence of polydisperse penetrable hard spheres [74], polydisperse ideal chains [75], polydisperse hard spheres [76] and polydisperse thin rods [77].

2.6.1 Atomic Force Microscopy

The atomic force microscope (AFM) was designed for high-resolution surface topography analysis. The basic measuring principle is sketched in Fig. 2.34. A sample is scanned by a sharp tip attached to a sensitive cantilever spring via a

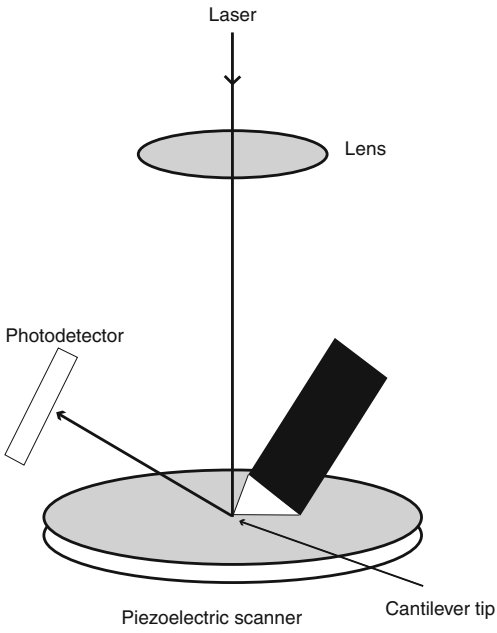

Fig. 2.34 Schematic picture of an atomic force microscope. The sample of interest is placed on the piezoelectric scanner and a laser is reflected off the upper side of the cantilever and guided to a split photo detector. In this way, vertical and horizontal deflection signals can be measured. A well-defined colloidal particle can be glued to the tip of the cantilever as to measure the force between that particle and the surface

piezo electric positioner. Forces on the tip lead to spring deflection, which is detected optically [78]. Topographic images of the sample are obtained by plotting the deflection of the cantilever as a function of the sample position. Alternatively, a feedback loop can be used to fix the spring deflection, and response of the piezoelectric positioner generates the image [68]. The pair interactions between a colloidal sphere and a surface by free depletants can be studied with a colloidal probe particle attached to the cantilever tip [79].

Interactions between a spherical colloid and a wall can be measured by bringing probe and substrate together and monitoring the cantilever deflection as a function of the interparticle distance. The photodetector voltage versus piezo position curve can be converted into a force–distance curve. The force acting on the cantilever follows from the deflection of the cantilever and its known spring constant. The zero force is defined by the deflection of the cantilever as the colloidal probe is far from the surface of the substrate. To obtain the force–distance dependence on an absolute scale the zero distance, i.e., where the colloid touches the wall, has to be determined. Commonly, the zero distance is obtained from the force curve itself and not through an independent method [68].

In practice, the position where the motion of the probe complies with the piezo movement defines the point of zero distance. Force–distance curves recorded with AFM depend on the specific geometry of the probe and the surface. Usually, the interaction is displayed as the force divided by the radius of the colloid, R, in units N/m. The Derjaguin approximation relates this quantity to the interaction potential per unit area between equivalent flat surfaces at given separation distance, see (2.29).

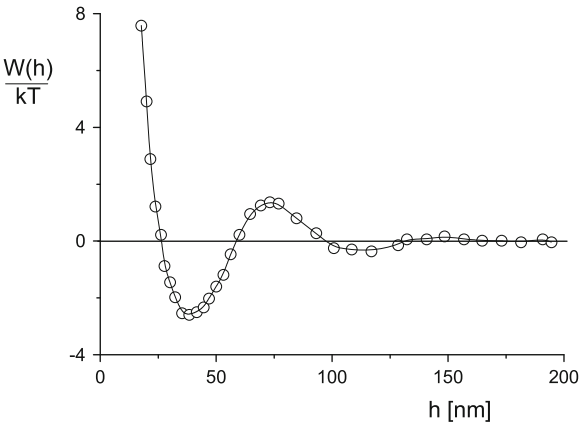

Fig. 2.35 Force measured between a flat silica surface and a silica sphere ($R = 2.2\,\mu m$) in the presence of 1.5 vol% Ludox spheres (radius 11 nm) as depletants at pH 5.6. The ionic strength was 0.76 mM. Redrawn from Piech and Walz [80]. Curve guides the eye

Since AFM is widely used for imaging, the technology is well-developed. Due to its high lateral resolution of $\sim 1\,nm$ small samples can be used and material inhomogeneities can be mapped and imaged. The small contact areas ($\sim 10\,nm^2$) reduce the probability of experimental artifacts due to surface contamination and roughness [68]. The high spatial resolution capability makes AFM a complementary approach to the SFA which has been used to measure interfacial forces between proximal surfaces over areas on the order of $\sim 1\,\mu m^2$. Moreover, the force resolution of AFM is better than that of the SFA.

The determination of the zero separation distance using AFM remains a complicated issue in some cases. This makes it often difficult to fully quantify depletion interactions. The force sensitivity is limited as compared to TIRM. This makes AFM only suitable for measuring strong depletion forces.

In Fig. 2.35 we show the measured force oscillating between a silicon wafer and a silica sphere (radius $R = 2.2\,\mu m$) attached to a cantilever spring in the presence of Ludox silica spheres with a radius of 11 nm [80]. The volume fraction of the Ludox spheres was 1.5%. The effective volume fraction is much larger due to repulsive double layer interactions.

2.6.2 Total Internal Reflection Microscopy

The interaction potentials between a single particle and a wall can be obtained using evanescent field scattering in total internal reflection microscopy (TIRM) [69, 70]. The fluctuations of the separation distance resulting from thermal motion can be directly detected from the scattered intensity. In a typical TIRM set-up a laser beam is directed via a prism to the glass/solution interface as sketched in Fig. 2.36, with an incident angle that is chosen such that total reflection occurs. The electric field of the laser beam penetrates the interface causing an

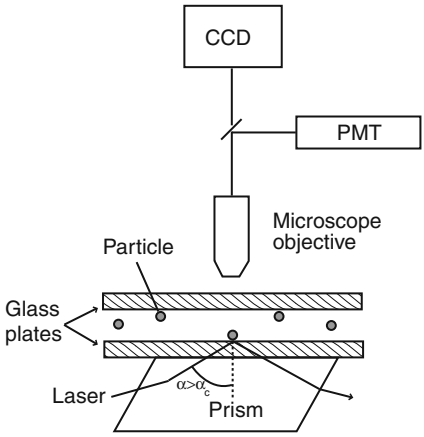

Fig. 2.36 Sketch of a TIRM set-up. Whenever the incident angle is larger than the critical angle the incident beam is totally reflected at the glass–fluid interface and an evanescent wave penetrates into the fluid. A colloidal particle located close to the surface will scatter light from the evanescent wave, which is collected by a photomultiplier and provides the probability density of separation distances between the particle and the wall. A CCD camera is used to image the field of view

evanescent wave, the amplitude of which decays exponentially along the normal to the interface. A single colloidal sphere in the field of gravity, interacting with this evanescent wave, will scatter light depending on its position h as [81]

$$I_s(h) = I(h = 0) \exp[-h/\varrho], \tag{2.121}$$

where ϱ is the penetration depth of the evanescent wave.

Exercise
Why does the scattered intensity due to a colloid decrease with increasing distance from the surface?

A photomultiplier is used to monitor the time dependence of the scattered intensity, with a resolution in the millisecond range. A sufficient number of data points allows to convert a histogram of intensities to the probability density distribution of the intensity. Through (2.121) the intensity histogram can be converted a probability density distribution (*pdf*) of separation distances. Using Boltzmann's law $\ln[pdf(h)] \sim -U(h)/kT$, this *pdf* provides the potential energy $U(h)$. Usually, a charged sphere is used with a size of the order of a μm. The solvent often is an aqueous salt solution. In this way double layer repulsion between particle and like-charged surface counterbalances gravity, enabling the particle to fluctuate near the wall. From $U(h)$ the bare pair depletion potential can be found by subtraction of double layer repulsion and gravity.

An optical trap can be set up to prevent the colloidal particle from moving out of the microscope's observation area. For this purpose a second laser beam has to

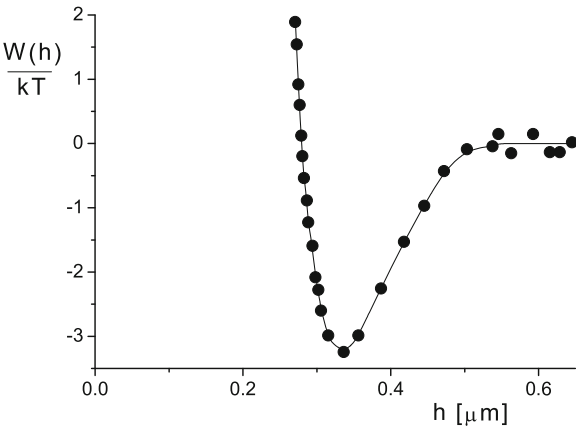

Fig. 2.37 Interaction potential between a flat silica surface and a polystyrene sphere ($R = 1.85\,\mu m$) mediated by polydisperse boehmite rods (0.09 vol%) with averaged length of 200 nm. Redrawn from Helden et al. [82]

be focused directly at the particle. It is recommended to use *p*-polarized light and a penetration depth below 150 nm.

Major advantages of TIRM relative to AFM and SFA for studying depletion potentials are its outstanding force sensitivity and its non-invasive nature. With TIRM it is possible to investigate the interactions of a single, freely moving, Brownian particle. This method enables measurements of forces as small as 10^{-14} N. The reason for this high sensitivity is the use of a molecular gauge for energy (kT) instead of a mechanical gauge for the force determined by a spring constant, as it is used in AFM and SFA [70].

TIRM is less suited for measuring strong depletion potentials. When the repulsion between the particle and the wall is bigger than 5 kT the *pdf* for finding the particle in this range becomes virtually zero. Therefore, the error in determining $pdf(h)$ becomes very large. If the attraction between the sphere and the wall becomes too strong, the intensity histogram becomes narrower than the range set by the electronic noise of the photomultiplier [70].

An example of a pair potential measured using TIRM is given in Fig. 2.37. The data are measured wall-sphere potentials between a flat silica surface and a polystyrene sphere ($R = 1.85\,\mu m$) in the presence of non-adsorbing polydisperse, charged boehmite rods (averaged length $L = 200\,nm$) [82]. The range of the potential is obviously close to the length of the rods. The volume fraction of the rods is 0.09%.

2.6.3 Optical Tweezers

Around 1970 it was found that laser radiation forces can be used to trap and manipulate small dielectric particles [83]. A laser beam can push a particle towards the centre of the beam, provided the particle has a higher refractive index than the surrounding medium. Thus, optical tweezers allow to pick up and manipulate

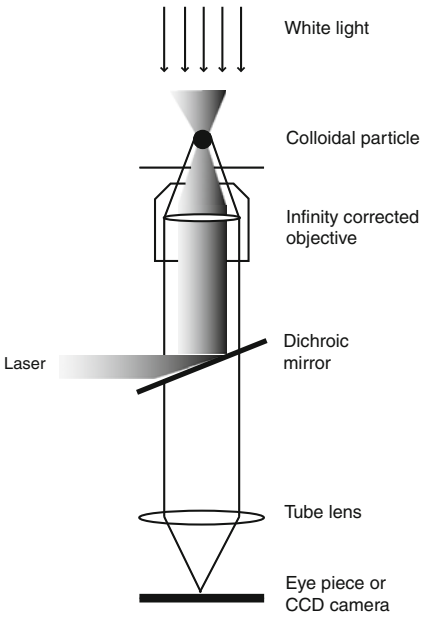

Fig. 2.38 Sketch of a simple optical tweezers arrangement. The microscope objective lens enables the tight focusing of the laser beam and imaging of trapped particles

colloidal particles; experts nowadays can even spell your name with a single optical tweezer and colloidal particles. This technique found a broad application in biology as well as in colloid science [84, 85]. Figure 2.38 illustrates a typical optical tweezer arrangement. The laser beam is tightly focused using the microscope objective lens, which also gives the possibility to image trapped particles with a camera. Optical tweezers can be configured using multiple beams to trap many particles simultaneously. This can be implemented in the following manner. Firstly, a single beam is used to rapidly scan two or more trap positions. Next, the beam is split at an early stage in the optical circuit to produce two separate light paths which are then recombined before entering the microscope. Finally, computer-generated holograms are used to generate multiple beams simultaneously.

Boltzmann's law is used to find the interaction potential between the trapped particles using the measured probability density as a function of separation distance. Position detection results either from particle tracking using video microscopy or back focal plane interferometry [67]. Accurate video microscopy requires the acquisition of bright field or fluorescent images from the microscope [86]. Particle centre separations can then be determined with a sub-pixel resolution through image-processing operations [86]. A spatial resolution of $\sim 10\,\text{nm}$ can be achieved. Back focal plane interferometry enables reducing the spatial resolution to $\sim 1\,\text{nm}$.

A major advantage of optical tweezers is that the detected forces range between 10^{-13} and $10^{-10}\,\text{N}$. Like TIRM, optical tweezers enable studying colloidal interactions in a non-invasive manner. Complementary to TIRM it enables to measure the interaction potentials between two colloidal particles, whereas TIRM and AFM

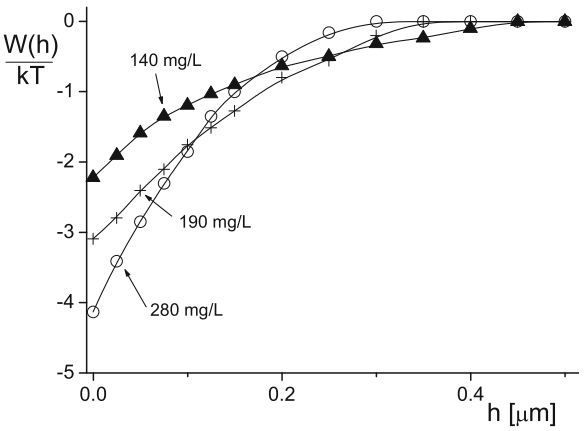

Fig. 2.39 Interaction potential between two silica spheres ($R = 0.63\,\mu m$) mediated by DNA chains ($R_g = 500\,nm$) [89]. The DNA concentrations are indicated in the plot

are restricted to wall-particle potentials. The main problems that can arise when making measurements with optical tweezers is that the results are susceptible to misinterpretations due to image processing problems [87, 88].

The pair interaction measured using optical tweezers between two silica spheres in the presence of rather monodisperse, non-adsorbing DNA chains [89] is plotted in Fig. 2.39. Data are given for three DNA concentrations beyond the coil overlap concentration indicated in the plot.

2.6.4 Scattering and Microscopy

One of the manifestations of depletion effects in a colloidal dispersion is that its fluid structure is affected by the presence of non-adsorbing depletants (for instance polymer chains). This is reflected in the radial distribution function $g(r)$; the local concentration of particle centers from a distance r to a fixed particle center. Statistical mechanics links $g(r)$ to the potential of mean force W_{mf} [90],

$$W_{mf}(r) = -kT \ln g(r). \tag{2.122}$$

For a dilute colloidal dispersion, $g(r) = \exp[-W(r)/kT]$, where $W(r)$ is the *pair* interaction. The quantity $g(r)$ can be measured using confocal laser scanning microscopy. This method allows to perform quantitative three-dimensional real space measurements of the positions of the (fluorescently labeled) colloidal particles. Analysis of the positions of the particles yields $g(r)$. This means that confocal microscopy enables to indirectly measure both the potential of mean force and (using a dilute dispersion) the pair interaction in a mixture of colloids and depletants. Royall et al. [91] have performed such a study in a colloid–polymer mixture with free polymers as depletants.

Scattering techniques allow to measure the structure factor $S(Q)$ as a function of the wave vector Q of colloidal dispersions defined as

$$Q = \frac{4\pi}{\lambda_m} \sin\left(\frac{\theta_s}{2}\right). \tag{2.123}$$

Here λ_m is the wavelength of radiation through the medium and θ_s the scattering angle. Statistical mechanics relates the structure factor $S(Q)$ to the radial distribution function $g(r)$ [92]:

$$S(Q) = 1 + \frac{\phi}{v_0} \int_0^\infty 4\pi r^2 [g(r) - 1] \frac{\sin Qr}{Qr} \, \mathrm{d}r. \tag{2.124}$$

Hence, via (2.122), (2.124) reveals $S(Q)$ contains the potential of mean force in the long wavelength limit ($Q \to 0$).

In the case of a colloid plus depletant mixture in which the depletant is made 'invisible' by contrast matching, the scattered intensity $I(Q)$ reads

$$I(Q) \sim \phi P(Q) S(Q), \tag{2.125}$$

where $P(Q)$ is the particle scattering form factor. The proportionality constant is the squared particle scattering amplitude. The structure factor then follows from (2.125) as

$$S(Q) = \frac{I(Q)}{I_0(Q)} \frac{\phi_0}{\phi}, \tag{2.126}$$

where ϕ_0 is the volume fraction of and $I_0(Q)$ is the scattered intensity in a very dilute dispersion. Here the fact was used that $S(Q)$ equals unity in a very dilute dispersion.

Following an early light scattering study of De Hek and Vrij [93], Ye et al. [94] made a small-angle neutron scattering (SANS) study on mixtures of $CaCO_3$ particles, stabilized with alkylbenzene sulfonate, plus polyethylene propylene (PEP) copolymers with $R_g = 8.3$ nm. Here $R = 4.8$ nm so $q = 2.1$. SANS allows contrast matching as to independently measure the structure factors of the free polymers or the colloids, see [95, 96] for a theoretical analysis. Further SANS is much less sensitive to multiple scattering problems as encountered in light scattering.

In Fig. 2.40 a few representative measured structure factors $S(Q)$ of colloidal spheres at a colloid volume fraction $\phi = 0.086$ are plotted at a few PEP concentrations. Clearly, the measured structure factor increases upon adding more free polymer at $Q < 0.2$ nm^{-1}, corresponding to an increase of the attraction between the colloids. This increase of $S(Q)$ at small Q has been found also in a few other studies [97–99]. Mutch et al. [99] showed it is possible to rescale structure factors at high q (relatively large polymers) to obtain a universal $S(Q)$ behaviour.

PRISM [100, 101] would be quite useful in quantifying these experimental data. Static and dynamic light scattering can be used also on colloid–polymer mixtures

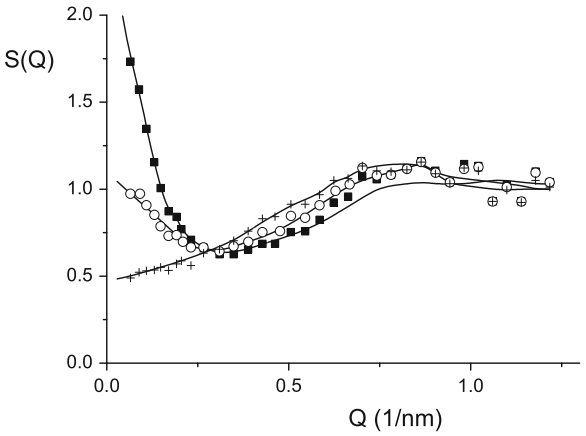

Fig. 2.40 Measured colloidal structure factor $S(Q)$ of colloid-PEP mixtures ($R = 4.8\,\text{nm},\ q = 2.1$) at 17.5 *wt*% of colloids (corresponding to $\phi = 0.086$) at polymer concentrations (in g/L) of 3.8 (*plusses*), 23.3 (*open circles*), and 65.2 (*filled squares*). *Curves* are drawn to guide the eye

to quantify the spinodal, defined at $1/S(Q \to 0) \equiv 0$ using extrapolation [97]. When the attraction becomes very strong the structure factor diverges at small Q and the dispersion starts to decompose. This demixing will be considered in Sect. 4.5.

Exercise
Why does $1/S(Q \to 0) \equiv 0$ correspond to the spinodal? Hint: check (1.30)

References

1. S. Asakura, F. Oosawa, J. Chem. Phys. **22**, 1255 (1954)
2. A. Vrij, Pure Appl. Chem. **48**, 471 (1976)
3. B. Widom, J.S. Rowlinson, J. Chem. Phys. **52**, 1670 (1970)
4. L. Onsager, Chem. Rev. **13**, 73 (1933)
5. L. Onsager, Ann. NY. Acad. Sci. **51**, 627 (1949)
6. D.G. Hall, J. Chem. Soc. Faraday. Trans. **68**(1), 2169 (1972)
7. S.G. Ash, D.H. Everett, C. Radke, J. Chem. Soc. Faraday. Trans. **69**(1), 1256 (1973)
8. R. Evans, U.M.B. Marconi, J. Chem. Phys. **86**, 7138 (1987)
9. T. Odijk, J. Chem. Phys. **106**, 3402 (1997)
10. B.V. Derjaguin, Kolloidn. Zh. **69**, 155 (1934)
11. P.J. Flory, *Principles of Polymer Chemistry* (Cornell University Press, New York, 1953)
12. H. Yamakawa, *Modern Theory of Polymer Solutions* (Harper and Row, New York, 1971)
13. P.G. De Gennes, *Scaling Concepts in Polymer Physics* (Cornell University Press, Ithaca, 1979)
14. M. Doi, S.F. Edwards, *The Theory of Polymer Dynamics* (Clarendon Press, Oxford, 1986)
15. J. des Cloizeaux, G. Jannink, *Polymers in Solution* (Oxford University Press, Oxford, 1990)
16. H. Fujita, *Polymer Solutions* (Elsevier, New York, 1990)
17. A.Y. Grosberg, A.R. Khoklov, *Statistical Physics of Macromolecules* (AIP, New York, 1994)
18. M. Doi, *Introduction to Polymer Physics* (Oxford University Press, Oxford, 1995)
19. L. Schäfer, *Excluded Volume Effects in Polymer Solutions* (Springer-Verlag, Heidelberg, 1999)

20. S.F. Edwards, Proc Phys Soc **85**, 613 (1965)
21. S.F. Edwards, K.F. Freed, J. Phys. A. **2**, 145 (1969)
22. E.F. Casassa, J. Polym. Sci. **5**, 773 (1967)
23. E.F. Casassa, Y. Tagami, Macromolecules **2**, 14 (1969)
24. P. Richmond, M. Lal, Chem. Phys. Lett. **24**, 594 (1974)
25. R. Tuinier, G.J. Fleer, Macromolecules **37**, 8764 (2004)
26. A. Einstein, Ann. Phys. (IV Folge) **22**, 569 (1907)
27. A. Einstein, Ann Phys (IV Folge) **33**, 1275 (1910)
28. R. Tuinier, G.A. Vliegenthart, H.N.W. Lekkerkerker, J. Chem. Phys. **113**, 10768 (2000)
29. E. Eisenriegler, Phys. Rev. E. **55**, 3116 (1997)
30. E. Eisenriegler, J. Chem. Phys. **79**, 1052 (1983)
31. C.M. Marques, J.F. Joanny, Macromolecules **23**, 268 (1990)
32. G.J. Fleer, A.M. Skvortsov, R. Tuinier, Macromolecules **36**, 7857 (2003)
33. T. Taniguchi, T. Kawakatsu, K. Kawasaki, in:'Slow dynamics in condensed matter'. ed. by K. Kawasaki. AIP series, **256**, 503 (1992)
34. E. Eisenriegler, A. Hanke, S. Dietrich, Phys. Rev. E. **54**, 1134 (1996)
35. T. Odijk, Macromolecules **29**, 1842 (1996)
36. A.A. Louis, P.G. Bolhuis, E.J. Meijer, J.-P. Hansen, J. Chem. Phys. **116**, 10547 (2002)
37. D.G.A.L. Aarts, R. Tuinier, H.N.W. Lekkerkerker, J. Phys. Condens Matter **14**, 7551 (2002)
38. R. Tuinier, Eur. Phys. J. E. **10**, 123 (2003)
39. A.A. Louis, P.G. Bolhuis, E.J. Meijer, J.-P. Hansen, J. Chem. Phys. **117**, 1893 (2002)
40. R. Tuinier, D.G.A.L. Aarts, H.H. Wensink, H.N.W. Lekkerkerker, Phys. Chem. Chem. Phys. **5**, 3707 (2003)
41. R. Tuinier, G.J. Fleer, Macromolecules **37**, 8754 (2004)
42. T.L. Hill, *An Introduction to Statistical Thermodynamics* (Addison-Wesley, New York, 1962)
43. B. Widom, *Statistical Mechanics: A Concise Introduction for Chemists* (Cambridge University Press, Cambridge, 2002)
44. I.Z. Fisher, *Statistical Theory of Liquids* (The University of Chicago Press, Chicago, 1964)
45. E.D. Glandt, J. Colloid Interface Sci. **77**, 512 (1980)
46. V.Y. Antonchenko, V.V. Ilyin, N.N. Makovsky, A.N. Pavlov, V.P. Sokhan, Mol. Phys. **52**, 345 (1984)
47. Y. Mao, M.E. Cates, H.N.W. Lekkerkerker, Physica A. **222**, 10 (1995)
48. J.Y. Walz, A. Sharma, J. Colloid Interface Sci. **168**, 485 (1994)
49. J.R. Henderson, Mol. Phys. **59**, 89 (1986)
50. R. Holyst, Mol. Phys. **68**, 391 (1989)
51. A.A. Louis, P.G. Bolhuis, J.P. Hansen, E.J. Meijer, Phys. Rev. Lett. **85**, 2522 (2000)
52. G.J. Fleer, M.A. Cohen Stuart, J.M.H.M. Scheutjens, T. Cosgrove, B. Vincent, *Polymers at Interfaces* (Chapman and Hall, New York, 1993)
53. J. van der Gucht, N.A.M. Besseling, van J. Male, M.A. Cohen Stuart, J. Chem. Phys. **112**, 2886 (2000)
54. T. Biben, P. Bladon, D. Frenkel, J. Phys. Condens Matter. **8**, 10799 (1996)
55. S. Asakura, F. Oosawa, J. Pol. Sci. **33**, 183 (1958)
56. R. Fåhraeus, Physiol Rev. **9**, 241 (1929)
57. L. Auvray, J. Phys. (Paris) **42**, 79 (1981)
58. Y. Mao, M.E. Cates, H.N.W. Lekkerkerker, Phys. Rev. Lett. **75**, 4548 (1995)
59. Y. Mao, M.E. Cates, H.N.W. Lekkerkerker, J. Chem. Phys. **106**, 3721 (1997)
60. Y. Mao, P. Bladon, H.N.W. Lekkerkerker, M.E. Cates, Mol. Phys. **92**, 151 (1997)
61. M. Piech, J.Y. Walz, J. Colloid Interface Sci. **232**, 86 (2000)
62. S.M. Oversteegen, H.N.W. Lekkerkerker, Physica A. **341**, 23 (2004)
63. J.R. Henderson, Physica A. **313**, 321 (2002)
64. D. Kleshchanok, R. Tuinier, P.R. Lang, J. Phys. Condens Matt. **20**, 073101 (2008)
65. J.N. Israelachvili, *Intermolecular and Surface Forces* (Academic, London, 1991)
66. D.G. Grier, Opin. Colloid Interface Sci. **2**, 264 (1997)

67. E.M. Furst, Soft Mater **1**, 167 (2003)
68. H.J. Butt, B. Cappella, M. Kappl, Surf. Sci. Rep. **59**, 1 (2005)
69. J.Y. Walz, Curr. Opin. Colloid Interface Sci. **2**, 600 (1997)
70. D.C. Prieve, Adv. Colloid Interface Sci. **82**, 93 (1999)
71. D. Tabor, R.H.S. Winterton, Nature **219**, 1120 (1968)
72. J.N. Israelachvili, G.E. Adams, Nature **262**, 774 (1976)
73. J.N. Israelachvili, G.E. Adams, J. Chem. Soc. Faraday Trans. **74**, 975 (1978)
74. D. Goulding, J.P. Hansen, Mol. Phys. **99**, 865 (2001)
75. R. Tuinier, A.V. Pethukhov, Macromol. Theory Simul. **11**, 975 (2002)
76. Y. Mao, J. Physique. **5**, 1761 (1995)
77. P.R. Lang, J. Chem. Phys. **127**, 124906 (2007)
78. J. Ralston, I. Larson, M.W. Rutland, A.A. Feiler, M. Kleijn, Pure Appl. Chem. **77**, 2149 (2005)
79. W.A. Ducker, T.J. Senden, R.M. Pashley, Nature **353**, 239 (1991)
80. M. Piech, J.Y. Walz, J. Phys. Chem. B. **108**, 9177 (2004)
81. D.C. Prieve, J.Y. Walz, Appl. Opt. **32**, 1629 (1993)
82. L. Helden, G.H. Koenderink, P. Leiderer, C. Bechinger, Langmuir **20**, 5662 (2004)
83. A. Askin, Phys. Rev. Lett. **24**, 156 (1970)
84. K. Svoboda, S.M. Block, Annu. Rev. Biophys. Biomol. Struct. **23**, 247 (1994)
85. C.F. Schmidt, *A practical guide to optical tweezers in: Soft Condensed Matter Physics in Molecular and Cell Biology* (Taylor and Francis, New York, 2006)
86. J.C. Crocker, D.G. Grier, J. Colloid Interface Sci. **179**, 298 (1996)
87. Y.L. Han, D.G. Grier, Phys. Rev. Lett. **91**, 038302 (2003)
88. J. Baumgärtl, C. Bechinger, Europhys. Lett. **71**, 487 (2005)
89. R. Verma, J.C. Crocker, T.C. Lubensky, A.G. Yodh, Macromolecules **33**, 177 (2000)
90. D.A. McQuarrie, *Statistical Mechanics* (University Science Books, Sausalito, CA, USA, 2000)
91. C.P. Royall, A.A. Louis, H. Tanaka, J. Chem. Phys. **127**, 044507 (2007)
92. J.G. Kirkwood, J. Chem. Phys. **7**, 919 (1939)
93. H. De Hek, A. Vrij, J. Colloid Interface Sci. **88**, 258 (1982)
94. X. Ye, T. Narayanan, P. Tong, J.S. Huang, M.Y. Lin, B.L. Carvalho, L.J. Fetters, Phys. Rev. E. **54**, 6500 (1996)
95. A. Vrij, J. Chem. Phys. **112**, 9489 (2000)
96. A. Vrij, Colloids Surf. A. **213**, 117 (2003)
97. I. Bodnár, J.K.G. Dhont, H.N.W. Lekkerkerker, J. Phys. Chem. **100**, 19614 (1994)
98. R. Tuinier, J.K.G. Dhont, de C.G. Kruif, Langmuir **16**, 1497 (2000)
99. K.J. Mutch, van J.S. Duijneveldt, J. Eastoe, I. Grillo, R.K. Heenan, Langmuir **26**, 1630 (2010)
100. M. Fuchs, K.S. Schweizer, Phys. Rev. E. **64**, 021514 (2001)
101. M. Fuchs, K.S. Schweizer, J. Phys. Condens Matter. **14**, R239 (2002)

Chapter 3
Phase Transitions of Hard Spheres Plus Depletants; Basics

In this chapter we discuss the basics of the phase behaviour of hard spheres plus depletants. Phase transitions are the result of physical properties of a collection of particles depending on many-body interactions. In Chap. 2 we focused on two-body interactions. As we shall see, depletion effects are commonly not pair-wise additive. Therefore, the prediction of phase transitions of particles with depletion interaction is not straightforward. As a starting point a description is required for the thermodynamic properties of the pure colloidal dispersion. Here the colloid-atom analogy, recognized by Einstein and exploited by Perrin in his classical experiments, is very useful. Subsequently, we explain the basics of the free volume theory for the phase behaviour of colloids + depletants. In this chapter we treat only simplest type of depletant, the penetrable hard sphere.

3.1 Introduction: Colloid/Atom Analogy

In his seminal 1905 paper on Brownian motion, Einstein [1] recognized and used that colloidal particles in a suspension obey the same statistical thermodynamics as atoms in an assembly of atoms. A well-known example of this colloid-atom analogy is the striking similarity between the ideal gas law for the pressure of a dilute gas and the Van 't Hoff law for the osmotic pressure of a dilute suspension. The colloid-atom analogy was exploited by Perrin [2] with simple, yet brilliant, experiments. Using an ordinary light microscope, Perrin verified that the equilibrium concentration of colloidal particles in a dilute suspension in the gravitational field varies exponentially with height. By applying Boltzmann's law to this height distribution he was able to determine the Boltzmann constant k and Avogadro's number N_{av}. For this work Perrin received the 1926 Nobel Prize for Physics.

The colloid-atom analogy can also be applied to interacting systems. The direct interaction potentials between atoms then have to be replaced by the *potential of mean force* between the dispersed colloidal particles. In the calculation of the

H. N. W. Lekkerkerker and R. Tuinier, *Colloids and the Depletion Interaction*, Lecture Notes in Physics, 833, DOI: 10.1007/978-94-007-1223-2_3,

potential of mean force one takes a statistical average over all possible configurations of the solvent components. In the previous chapter we treated the calculation of the potential of mean force due to dissolved non-adsorbing polymers and (small) colloidal particles.

The concept 'potential of mean force' was used by Onsager [3] in his theory for the isotropic-nematic phase transition in suspensions of rod-like particles. Since the 1980s the field of phase transitions in colloidal suspensions has shown a tremendous development. The fact that the potential of mean force can be varied both in range and depth has given rise to new and fascinating phase behaviour in colloidal suspensions [4]. In particular, sterically stabilized colloidal spheres with interactions close to those between hard spheres [5] have received ample attention.

The phase behaviour of such colloidal suspensions should be nearly the same as those of the hypothetical hard-sphere atomic system. Kirkwood [6] stated that when a hard sphere system is gradually compressed, the system will show a transition towards a state of long-range order long before close-packing is reached. In 1957, Wood and Jacobson [7] and Alder and Wainwright [8] showed by computer simulations that systems of purely repulsive hard spheres indeed exhibit a well-defined fluid–crystal transition. It has taken some time before the fluid–crystal transition of hard spheres became widely accepted. There is no exact proof that the transition occurs. Its existence has been inferred from numerical simulations or from approximate theories as treated in this chapter. However, this transition has been observed in hard-sphere-like colloidal suspensions [9].

The hard sphere fluid–crystal transition plays an important role as a reference point in the development of theories for the liquid and solid states and their phase behaviour [10]. We consider it in some detail in the next section; here the phase behaviour is relatively simple as there is no gas–liquid (GL) coexistence. After that we discuss the phase behaviour under the influence of the attraction caused by the depletion interaction; now there is such GL transition. We illustrate the enrichment of the phase behaviour in the somewhat hypothetical system consisting of an assembly of hard spheres and (non-adsorbing) penetrable hard spheres.

3.2 The Hard-Sphere Fluid–Crystal Transition

Following the work of Wood and Jacobson [7] and Alder and Wainwright [8], the location of the hard sphere fluid–crystal transition was determined from computer simulations by Hoover and Ree [11]. They found that the volume fractions of the coexisting fluid (f) and face centered cubic crystal (s) are given by $\phi_f = v_0 n = 0.494$ and $\phi_s = v_0 n = 0.545$ at a coexistence pressure $Pv_0/kT = 6.12$. Here $v_0 = (4\pi/3)R^3$, with R the radius of the hard sphere, is the hard sphere volume. As in Chap. 2, $n = N/V$ refers to the number density of N particles in a volume V.

We present a simple theoretical treatment of the hard sphere fluid–crystal transition that will also serve as a reference framework for our treatment of phase transitions in a system of colloids with depletion attraction.

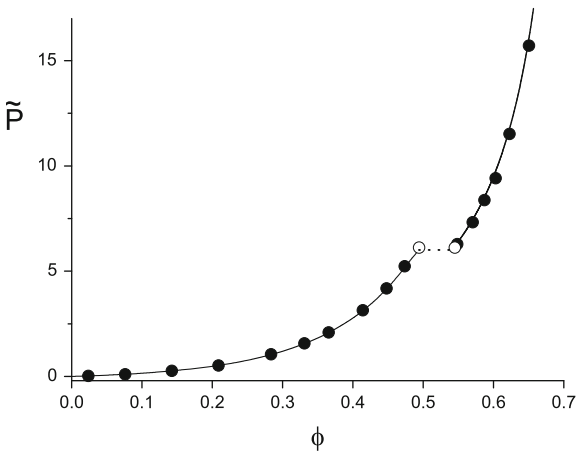

Fig. 3.1 The pressure of hard spheres. The *curves* are the Carnahan–Starling expression (3.1) for a fluid ($\phi \leq 0.494$) and the cell model result (3.12) for an fcc crystal (*solid curves*; $\phi \geq 0.545$). The *closed symbols* are Monte Carlo computer simulation results [13]. The *two open symbols* correspond to the fluid–solid coexistence from simulation [11], the *dotted line* is the theoretical result (see Sect. 3.2.3)

3.2.1 Hard-Sphere Fluid

We start with the equation of state for the fluid phase of hard spheres interacting through (1.19). An accurate expression for hard spheres is the so called Carnahan–Starling equation of state [12] which can be written in terms of the dimensionless pressure $\widetilde{P}_f$ as

$$\widetilde{P}_f = \frac{Pv_0}{kT} = \frac{\phi + \phi^2 + \phi^3 - \phi^4}{(1-\phi)^3}. \tag{3.1}$$

In Fig. 3.1 (left part) we compare the pressure given by the Carnahan–Starling equation of state (3.1) with computer simulations. We see that (3.1) is indeed very accurate.

A 'simple' way to derive this equation of state is to start from the virial expansion of the pressure [14]

$$\frac{P}{nkT} = 1 + \sum_{m=2} B_m n^{m-1}, \tag{3.2}$$

and use the fact that, to a good approximation, the virial coefficients can be written as [12]

$$B_{m+1} = (m^2 + 3m)v_0^m. \tag{3.3}$$

Together with (3.2) this yields (3.1). For hard spheres it is possible to calculate exact values of $B_2 - B_4$ and to perform numerical calculations for B_5 and beyond using statistical mechanics [15]. In Table 3.1. we compare exact (B_2, B_3, B_4) and

Table 3.1 State-of-the-art values for the second up to the tenth virial coefficient of hard spheres [16] in comparison with the Carnahan–Starling result (3.3)

m	Exact/numerical	CS (3.3)
2	4	4
3	10	10
4	18.36	18
5	28.22	28
6	39.82	40
7	53.34	54
8	68.53	70
9	85.81	88
10	105.8	108

The numbers in the second and third column are B_m/v_0^{m-1} for $m = 2...10$.

numerically highly accurate [16] $(B_5, B_6, B_7, B_8, B_9, B_{10})$ virial coefficients with the approximation given by (3.3)

Exercise Show that the summation on the right-hand side of (3.2) with (3.3) for the virial coefficients indeed leads to the equation of state (3.1)

From the Gibbs-Duhem relation $S\mathrm{d}T - V\mathrm{d}P + N\mathrm{d}\mu = 0$ we can calculate the chemical potential from the pressure. For constant T this relation may be written as

$$\mathrm{d}P = n\mathrm{d}\mu = \frac{\phi}{v_0}\mathrm{d}\mu \tag{3.4}$$

so that μ follows as

$$\mu = kT\ln\frac{\Lambda^3}{v_0} + v_0\int_0^{\phi}\frac{1}{\phi'}\frac{\mathrm{d}P}{\mathrm{d}\phi'}\mathrm{d}\phi' \tag{3.5}$$

where $\mathrm{d}P/\mathrm{d}\phi$ can be calculated from (3.1) for a fluid of hard spheres. The first (constant) term follows from the ideal gas reference state [15]; Λ is the De Broglie wavelength $\Lambda = h/\sqrt{2\pi m_c kT}$, with the colloid mass m_c and Planck's constant h. The result for the chemical potential of a hard sphere in a fluid with volume fraction of hard spheres ϕ is

$$\mu_f = kT\left[\ln\frac{\Lambda^3}{v_0} + \ln\,\phi + \frac{(8 - 9\phi + 3\phi^2)\phi}{(1-\phi)^3}\right]. \tag{3.6}$$

After simplification and defining the dimensionless chemical potential $\widetilde{\mu} = \mu/kT$ the simpler form

$$\widetilde{\mu}_f = \ln\frac{\Lambda^3}{v_0} + \ln\,\phi + \frac{3-\phi}{(1-\phi)^3} - 3 \tag{3.7}$$

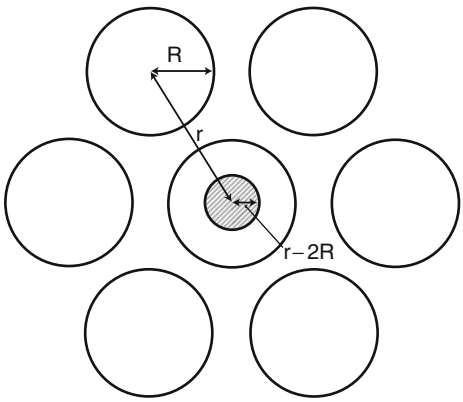

Fig. 3.2 Illustration of the free volume of a hard sphere (*hatched area*) in the cage of its nearest neighbours in the approximation of the inscribed sphere (*dashed line* radius $r - 2R$). The *hatched area* identifies the available volume for the center of the central sphere

is obtained. Finally, using the standard thermodynamic result $\widetilde{P} = \phi\widetilde{\mu} - \widetilde{F}$, the resulting canonical free energy of the pure hard-sphere dispersion of a fluid is:

$$\widetilde{F} = \phi\left[\ln(\phi\Lambda^3/v_0) - 1\right] + \frac{4\phi^2 - 3\phi^3}{(1-\phi)^2}. \tag{3.8}$$

Here we have introduced the normalized Helmholtz energy $\widetilde{F} = Fv_0/kTV$. The first term on the right-hand side of (3.8) is the ideal contribution, while the second hard-sphere interaction term is the Carnahan–Starling equation of state [12].

3.2.2 Hard-Sphere Crystal

To obtain the thermodynamic functions of the hard-sphere crystal we use the cell model of Lennard-Jones and Devonshire [17]. The idea of the cell model is that a given particle moves in a free volume v^* set by its neighbours which are located on their lattice positions (see Fig. 3.2). Then the partition function Q takes the form

$$Q = \frac{(v^*)^N}{\Lambda^{3N}}. \tag{3.9}$$

The 'exact' free volumes have a complicated geometry [18] but here we will use the simple approximation of the inscribed sphere. This yields

$$v^* = \frac{4\pi}{3}(r - 2R)^3, \tag{3.10}$$

where r is the centre-to-centre distance between the nearest neighbours. Using the relations

$$n\frac{\pi}{6}(2R)^3 = \phi$$

and

$$n\frac{\pi}{6}r^3 = \phi_{cp},$$

where $\phi_{cp} = \pi/3\sqrt{2} \simeq 0.74$ is the volume fraction at close packing, the free volume can be written as

$$v^* = 8v_0\left[\left(\frac{\phi_{cp}}{\phi}\right)^{1/3} - 1\right]^3.$$

We now obtain for the free energy

$$\begin{aligned} F &= -kT\ \ln\ Q \\ &= NkT\left\{\ln\left(\frac{27\Lambda^3}{8v_0}\right) - 3\ \ln\left[\left(\frac{\phi_{cp}}{\phi}\right) - 1\right]\right\}. \end{aligned} \tag{3.11}$$

In writing down (3.11) we used the approximation

$$\left(\frac{\phi_{cp}}{\phi}\right)^{1/3} - 1 = \frac{1}{3}\left(\frac{\phi_{cp}}{\phi} - 1\right).$$

Using the standard thermodynamic relations

$$P = -\left(\frac{\partial F}{\partial V}\right)_{N,T},$$

and

$$\mu = -\left(\frac{\partial F}{\partial N}\right)_{V,T},$$

we obtain for the dimensionless pressure and chemical potential

$$\widetilde{P}_s = \frac{3\phi}{1 - \phi/\phi_{cp}}, \tag{3.12}$$

and

$$\widetilde{\mu}_s = \ln\frac{\Lambda^3}{v_0} + \left[\frac{27}{8(\phi_{cp})^3}\right] + 3\ \ln\left[\frac{\phi}{1 - (\phi/\phi_{cp})}\right] + \frac{3}{1 - (\phi/\phi_{cp})}. \tag{3.13}$$

The pressure given by (3.12) can be compared to computer simulation data (e.g. [19]) and, as can be seen in Fig. 3.1 (right part), turns out to be highly accurate. The result for the chemical potential given by (3.13) is close to the computer simulation results of Frenkel and Ladd [20]. The constant on the right-hand side

$$\ln\left[\frac{27}{8(\phi_{cp})^3}\right] = 2.1178$$

is quite close to 2.1306, which can be abstracted from computer simulations. The full free energy expression for the hard-sphere solid phase is

$$\widetilde{F} = 2.1178\phi + 3\phi \ \ln\left(\frac{\phi}{1-\phi/\phi_{cp}}\right) + \ \phi \ \ln\left(\Lambda^3/v_0\right). \tag{3.14}$$

3.2.3 Fluid–Crystal Coexistence

Solving the coexistence conditions

$$\begin{aligned} \widetilde{P}_f(\phi_f) &= \widetilde{P}_s(\phi_s) \\ \widetilde{\mu}_f(\phi_f) &= \widetilde{\mu}_s(\phi_s), \end{aligned} \tag{3.15}$$

yields coexisting volume fractions $\phi_f = 0.491$, $\phi_s = 0.541$ and a coexistence pressure $\widetilde{P} = 6.01$. These values are indeed very close to the computer simulation results, see the comparison in Fig. 3.1.

The equilibrium configuration of hard spheres is the one that maximizes the entropy of the system. At low densities the configurations of maximum entropy correspond to disordered arrangements. As the density increases, the number of disordered arrangements is severely reduced due to the inefficiency of 'packing' them into the fixed volume. Then crystalline arrangements lead to a more efficient packing and make more arrangements possible. This is schematically depicted in Fig. 3.3.

Hence, the thermodynamic stability of the hard sphere crystal can be 'explained' on a purely entropic basis. Starting in the 1950s the fluid–crystal transition has been observed in suspensions of monodisperse repulsive colloidal particles [21–23]. Particularly, the work on sterically stabilized silica particles [24] and sterically stabilized PMMA particles [9] has served as a reference point. Figures 3.4 and 3.5 illustrate the phase behaviour of dispersed PMMA colloids as studied by Pusey and Van Megen [9]. In addition to the fluid–crystal transition these authors observed, above a volume fraction $\phi = 0.58$, an amorphous glassy phase that did not crystallize over several months. The explanation for this phenomenon is that for these high volume fractions the particles become so tightly trapped or caged by their neighbours that they are unable to move far enough to nucleate crystallization. Instead, long-lived metastable states called colloidal glasses are obtained. We return to glasses in Sect. 4.5.2.

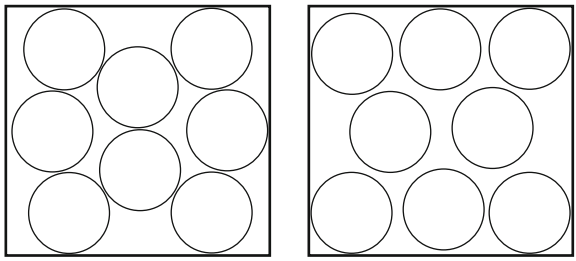

Fig. 3.3 Schematic pictures of a hard-sphere fluid (*left*) and hard spheres with 'crystalline' order (*right*); free volume entropy drives freezing

Fig. 3.4 Dispersions with hard-sphere like PMMA spheres at volume fractions around the fluid–solid phase transition. From Pusey and Van Megen [9]. Samples are denoted from left to right as samples a, b,... i. See Fig. 3.5 for the state of each sample. Picture reprinted from Pusey and Van Megen [9], Copyright 1986, with permission from Nature. Kindly provided by P.N. Pusey

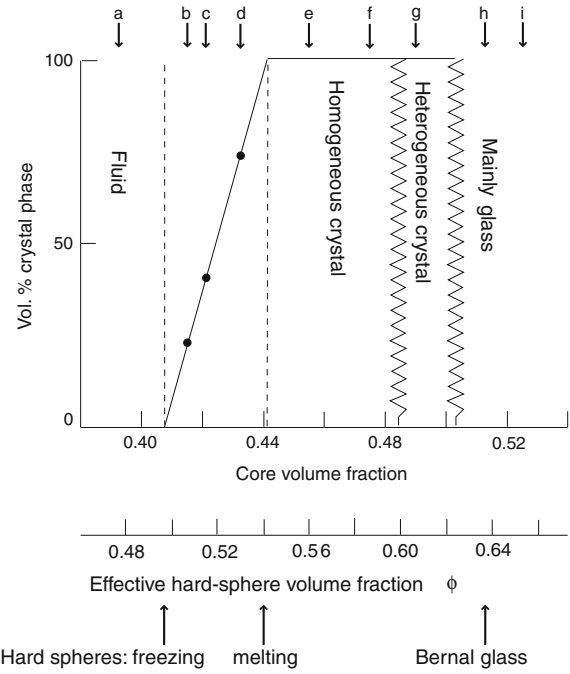

Fig. 3.5 Representation of the states of the colloidal PMMA dispersions shown in Fig. 3.4. The *abscissa* indicates the measured volume fraction of PMMA cores, which is smaller than the effective volume fraction of hard spheres that includes the short stabilizing brushes

3.3 Free Volume Theory of Hard Spheres and Depletants

3.3.1 System

Several theories have been developed that enable calculations of phase transitions in systems with depletion interactions. The first successful treatment accounting for depletion interactions in a many-body system [25, 26] is thermodynamic perturbation theory [14, 15]. In this classical approach depletion effects can be treated as a perturbation to the hard-sphere free energy, as was done by Gast et al. [25]. Their important work predicted that for a sufficient depletant concentration, the depletion interaction leads to a phase diagram with stable colloidal gas, liquid and solid phases for $\delta/R \geq 0.3$. For small depletants with $\delta/R \leq 0.3$ only colloidal fluid and solid phases are thermodynamically stable, and the gas–liquid transition is meta-stable. Although implementation of this theory is straightforward, it has the drawback that it does not account for depletant partitioning over the coexisting phases.

In the early nineties of the last century a theory that accounts for depletant partitioning over the coexisting phases was developed [27], which nowadays is commonly referred to as free volume theory (FVT) [28]. This theory is based on the osmotic equilibrium between a (hypothetical) depletant and the colloid + depletant system. The depletants were simplified as penetrable hard spheres. A pictorial representation is given in Fig. 3.6.

This theory has the advantage that the depletant concentrations in the coexisting phases follow directly from the (semi-)grand potential which describes the colloid + depletant system. As illustrated in Fig. 3.7, the system tries to arrange itself such as to provide a large free volume for the depletant. This (entropic) physical origin of the phase transitions induced by depletion interactions is incorporated in the theory in a natural way.

In FVT multiple overlap of depletion zones with thickness δ, see Fig. 3.8, is taken into account. Multiple overlap occurs for

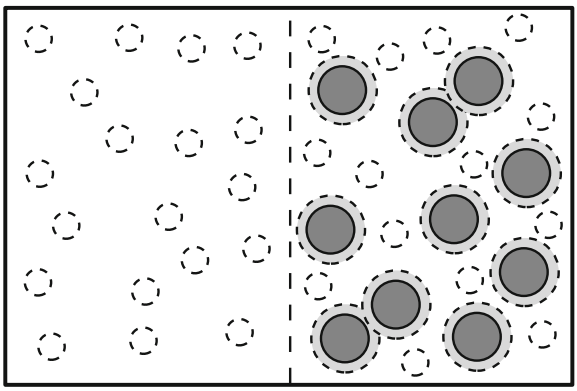

Fig. 3.6 A system (*right*) that contains colloids and penetrable hard spheres (phs) in osmotic equilibrium with a reservoir (*left*) only consisting of phs. A hypothetical membrane that allows permeation of solvent and phs but not of colloids is indicated by the *dashed line*. Solvent is considered as 'background'.

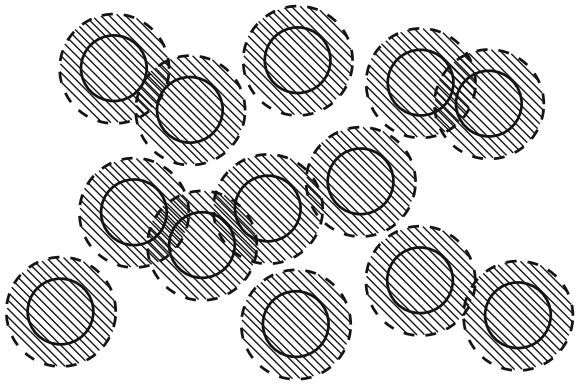

Fig. 3.7 Illustration of the free volume V_{free}: it is the unshaded volume not occupied by the colloids plus (partially overlapping) depletion layers

$$\frac{\delta}{R} > \frac{2}{3}\sqrt{3} - 1 \simeq 0.15,$$

where three depletion zones start to overlap, see Fig. 3.8. Only for $\delta/R < 0.15$ is a colloid/depletant mixture pair-wise additive. This has a considerable influence on the topology of the phase diagram [29]. Multiple overlap of depletion layers widens the liquid window, which is the parameter range with phase transitions that include a stable liquid, in comparison with a pair-wise additive system [28].

Exercise Show that multiple overlap only occurs for $\frac{\delta}{R} > \frac{2}{3}\sqrt{3} - 1$.

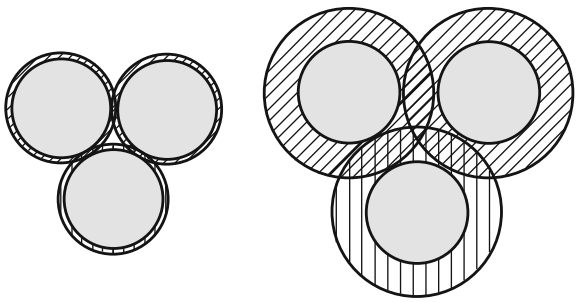

Fig. 3.8 Three hard spheres surrounded by depletion layers (*hatched areas*). When the depletion layers are thin (*left*) there is no multiple overlap of depletion layers; the system is pair-wise additive. For thicker depletion layers (*right*) multiple overlap of depletion layers occurs and depends on more than two-body contributions. The lowest value for δ/R where multiple overlap occurs follows from considering the triangle formed by the three particle centres; its edge is $2R + h$ at particle separation h. Multiple overlap starts when the centre of the triangle is a distance $R + \delta$ from the corners

3.3.2 Thermodynamics

The starting point of FVT is the calculation of the semi-grand potential describing the system of N_c colloidal spheres plus N_d depletants as depicted in Fig. 3.6.

$$\Omega(N_c, V, T, \mu_d) = F(N_c, N_d, V, T) - \mu_d N_d. \tag{3.16}$$

Using the thermodynamic relation

$$\left(\frac{\partial \Omega}{\partial \mu_d}\right)_{N_c,V,T} = -N_d, \tag{3.17}$$

we can write

$$\Omega(N_c, V, T, \mu_d) = F_0(N_c, V, T) - \int_{-\infty}^{\mu_d} N_d(\mu_d')\mathrm{d}\mu_d'. \tag{3.18}$$

Here $F_0(N_c, V, T)$ is the free energy of the colloidal particle system without added depletant as given by (3.8) (fluid) or (3.14) (solid).

The key step now is the calculation of the number of depletants in the colloid + depletant system as a function of the chemical potential μ_d imposed by the depletants in the reservoir. In the calculations presented below we model the colloidal particles as hard spheres with diameter $2R$ and the depletants by penetrable hard spheres with diameter σ.

For the calculation of N_d we make use of the Widom insertion theorem [30] according to which the chemical potential of the depletants in the hard sphere + depletant system can be written as

$$\mu_d = \text{const} + kT \ln \frac{N_d}{\langle V_{\text{free}} \rangle}. \tag{3.19}$$

Here $\langle V_{\text{free}} \rangle$ is the ensemble-averaged free volume for the depletants in the system of hard spheres, illustrated in Fig. 3.7

The chemical potential of the depletants in the reservoir is simply

$$\mu_d = \text{const} + kT \ln n_d^R, \tag{3.20}$$

where n_d^R is the number density of the depletants in the reservoir. By equating the depletant chemical potentials (3.19) and (3.20) we obtain

$$N_d = n_d^R \langle V_{\text{free}} \rangle. \tag{3.21}$$

The average free volume obviously depends on the volume fraction of the hard spheres in the system but also on the chemical potential of the depletants. The activity of the depletants affects the average configuration of the hard spheres. We now make the key approximation to replace $\langle V_{\text{free}} \rangle$ by the free volume in the pure hard sphere dispersion $\langle V_{\text{free}} \rangle_0$:

$$N_d = n_d^R \langle V_{\text{free}} \rangle_0. \tag{3.22}$$

This expression is correct in the limit of low depletant activity but is only an approximation for higher depletant concentrations. Substituting the approximation (3.22) in (3.18) and using the Gibbs-Duhem relation,

$$n_d^R \mathrm{d}\mu_d = \mathrm{d}P^R, \tag{3.23}$$

gives

$$\Omega(N_c, V, T, \mu_p) = F_0(N_c, V, T) - P^R \langle V_{\text{free}} \rangle_0, \tag{3.24}$$

where $P^R = n_d kT$ is the (osmotic) pressure of the depletants in the reservoir.

As we have expressions for the free energy of the hard sphere system (both in the fluid and solid state, see Sect. 3.2) and for the pressure of the reservoir, the only remaining quantity to calculate is $\langle V_{\text{free}} \rangle_0$. This can be done by using the Widom insertion Theorem at low depletant concentration:

$$\mu_d = \text{const} + kT \ln \frac{N_d}{\langle V_{\text{free}} \rangle_0}. \tag{3.25}$$

But we can also write the chemical potential μ_d as

$$\mu_d = \text{const} + kT \ln \frac{N_d}{V} + W, \tag{3.26}$$

where W is the reversible work required for inserting the depletant in the hard sphere dispersion. Combining (3.25) and (3.26) we find for the fraction α of free volume

$$\alpha = \frac{\langle V_{\text{free}} \rangle_0}{V} = e^{-W/kT}. \tag{3.27}$$

3.3.3 Scaled Particle Theory

An expression for the work of insertion W can be obtained from scaled particle theory (SPT) [31]. SPT was developed to derive expressions for the chemical potential and pressure of hard sphere fluids by relating them to the reversible work needed to insert an additional particle in the system. This work W is calculated is by expanding (scaling) the size of the sphere to be inserted from zero to its final size: the size of the scaled particle is $\lambda\sigma$, with λ running from 0 to 1. In the limit $\lambda \to 0$, the inserted sphere approaches a point particle. In this limiting case it is very unlikely that the depletion layers overlap. The free volume fraction in this limit can therefore be written as

$$\alpha = \frac{V - N_c \frac{\pi}{6}(2R + \lambda\sigma)^3}{V} = 1 - n_c \frac{\pi}{6}(2R + \lambda\sigma)^3.$$

It then follows from (3.27) that

$$W = -kT \ln\left[1 - n_c \frac{\pi}{6}(2R + \lambda\sigma)^3\right] \quad \text{for } \lambda \ll 1. \tag{3.28}$$

In the opposite limit $\lambda \gg 1$, when the size of the inserted scaled particle is very large, W to a good approximation is equal to the volume work needed to create a cavity $\frac{\pi}{6}(\lambda\sigma)^3$ and is given by

$$W = \frac{\pi}{6}(\lambda\sigma)^3 P \quad \text{for } \lambda \gg 1, \tag{3.29}$$

where P is the (osmotic) pressure of the hard sphere dispersion. In SPT the above two limiting cases are connected by expanding W as a series in λ:

$$W(\lambda) = W(0) + \left(\frac{\partial W}{\partial \lambda}\right)_{\lambda=0} \lambda + \frac{1}{2}\left(\frac{\partial^2 W}{\partial \lambda^2}\right)_{\lambda=0} \lambda^2 + \frac{\pi}{6}(\lambda\sigma)^3 P. \tag{3.30}$$

This yields

$$\frac{W(\lambda = 1)}{kT} = -\ln[1 - \phi] + \frac{3q\phi}{1 - \phi} + \frac{1}{2}\left[\frac{6q^2\phi}{1 - \phi} + \frac{9q^2\phi^2}{(1 - \phi)^2}\right] + \frac{\frac{\pi}{6}q^3(2R)^3 P}{kT}, \tag{3.31}$$

where q is the size ratio between the depletant with diameter σ and the hard sphere with diameter $2R$

$$q = \frac{\sigma}{2R}. \tag{3.32}$$

As was the original objective of SPT [31], the pressure P of the hard sphere system can be obtained from the reversible work of inserting an identical sphere ($q = 1$)

$$\frac{W}{kT} = -\ln[1 - \phi] + \frac{6\phi}{1 - \phi} + \frac{9\phi^2}{2(1 - \phi)^2} + \frac{\pi(2R)^3 P}{6kT}, \tag{3.33}$$

to obtain the chemical potential of the hard spheres

$$\mu_c = \text{const} + kT \ln\frac{N_c}{V} + W. \tag{3.34}$$

Applying the Gibbs-Duhem relation

$$\frac{\partial P}{\partial n_c} = n_c \frac{\partial \mu_c}{\partial n_c}$$

one obtains

$$\frac{P v_0}{kT} = \frac{\phi + \phi^2 + \phi^3}{(1-\phi)^3}, \tag{3.35}$$

which is the famous SPT expression for the pressure of a hard sphere fluid [31], which preceded the slightly more accurate Carnahan–Starling equation (3.1) (that contains an additional term ϕ^4). Inserting (3.35) into (3.31) and using (3.27) yields

$$\alpha = (1-\phi)\exp[-Q(\phi)], \tag{3.36}$$

where

$$\begin{aligned} Q(\phi) &= ay + by^2 + cy^3 \\ y &= \phi/(1-\phi) \\ a &= 3q + 3q^2 + q^3 \;=\; (1+q)^3 - 1 \\ b &= \frac{9}{2}q^2 + 3q^3 \\ c &= 3q^3. \end{aligned}$$

In Fig. 3.9 we present a comparison of the free volume fraction predicted by SPT (3.36) and computer simulations [32] on hard spheres plus penetrable hard spheres for $q = 0.5$ as a function of ϕ. As can be seen the agreement is very good. In the limit of small depletants the λ^2 and λ^3 terms of (3.30) can be omitted giving:

$$\alpha = (1-\phi)\exp\left[-3q\frac{\phi}{1-\phi}\right], \tag{3.37}$$

which is (3.36) with $Q = 3qy$. This equation will be used for hard sphere mixtures with large size asymmetry in chapter . We now have all the ingredients to compile the semi-grand potential Ω given by (3.24).

From Ω the pressure and chemical potential of the hard spheres in the hard sphere + depletant system at given μ_p are obtained:

$$P = -\left(\frac{\partial \Omega}{\partial V}\right)_{N_c,T,\mu_p} = P^0 + P^R\left(\alpha - n_c\frac{\partial \alpha}{\partial n_c}\right) \tag{3.38}$$

$$\mu_c = \left(\frac{\partial \Omega}{\partial N_c}\right)_{V,T,\mu_p} = \mu_c^0 - P^R\frac{\partial \alpha}{\partial n_c}. \tag{3.39}$$

For non-interacting depletants P^R is simply given by Van 't Hoff's law $P^R = n_d^R kT$ or

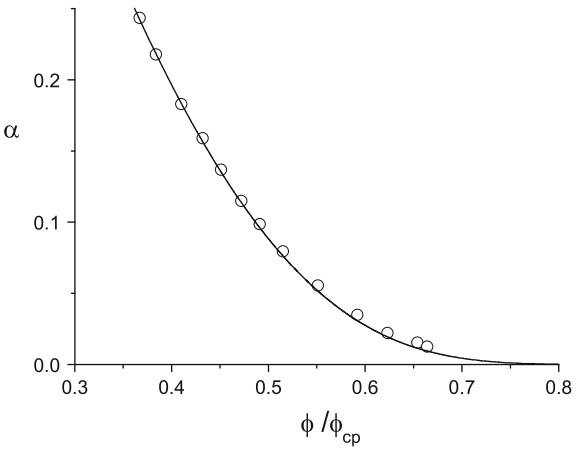

Fig. 3.9 Free volume fraction for penetrable hard spheres in a hard sphere dispersion for $q = \sigma/2R = 0.5$ as function of the hard sphere concentration. Data points are redrawn from Meijer [32]. Curve is the SPT prediction (3.36)

$$\widetilde{P}^R = \frac{P^R v_0}{kT} = n_d^R v_d q^{-3} = \phi_d^R q^{-3}, \tag{3.40}$$

with ϕ_d^R the relative reservoir depletant concentration $n_d^R v_d$, where v_d is the volume of a depletant sphere.

3.3.4 Phase Diagrams

We can now calculate the phase behaviour of a system of hard spheres and depletants by solving the coexistence equations for a phase I in equilibrium with a phase II

$$\mu_c^I(n_c^I, \mu_d) = \mu_c^{II}(n_c^{II}, \mu_d), \tag{3.41}$$

$$P^I(n_c^I, \mu_d) = P^{II}(n_c^{II}, \mu_d). \tag{3.42}$$

For numerical computations of phase coexistence, it is convenient to work with dimensionless quantities. The dimensionless version of the free volume expression (3.24) for the grand potential is

$$\widetilde{\Omega} = \widetilde{F}_0 - \alpha \widetilde{P}^R, \tag{3.43}$$

where $\widetilde{\Omega} = \Omega v_0/kTV$.

In Fig. 3.10 the semi-grand potential is presented as a function of the colloid volume fraction for given depletant reservoir concentration and size ratio q. Four possible scenarios are considered. Indicated are the common tangent constructions that allow to determine conditions where two (or three) phases coexist. A first criterion for two coexisting binodal composition is equality of the slope because it

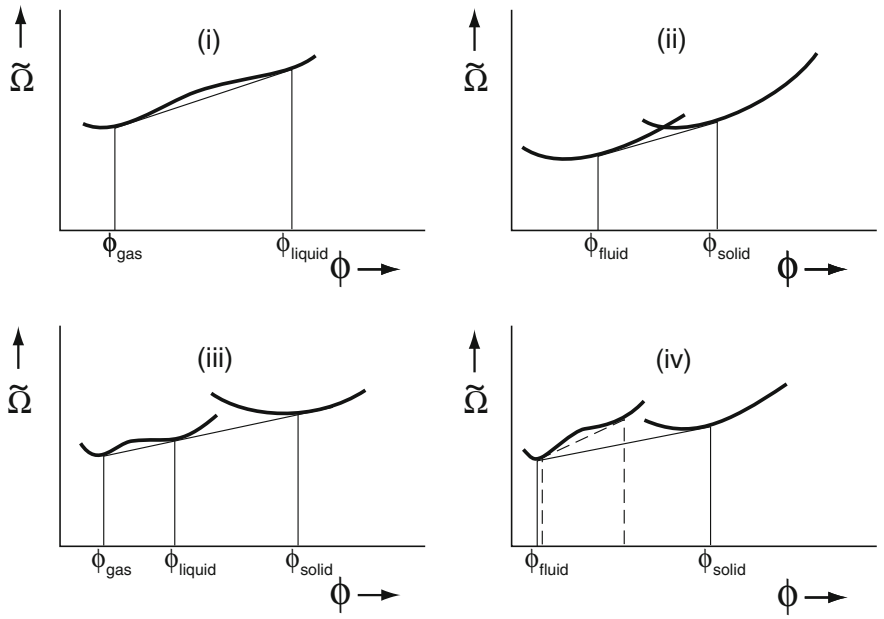

Fig. 3.10 The dimensionless semi-grand potential $\widetilde{\Omega}$ as a function of volume fraction ϕ. Schematic view of the common tangent construction (*straight lines*) to determine the phase coexistence in mixtures of colloidal hard spheres and phs. (i) gas–liquid coexistence, (ii) fluid–solid coexistence, (iii) gas–liquid–solid triple coexistence, and (iv) fluid–solid coexistence near a metastable (*dashed lines* represent the common tangent construction for this case) gas–liquid coexistence

corresponds to the chemical potential. The chemical potential of the colloids $\widetilde{\mu}_c$ can generally be expressed using the standard thermodynamic relation

$$\widetilde{\mu}_c = \left(\frac{\partial \widetilde{\Omega}}{\partial \phi}\right)_{\widetilde{P}^R,T,V}, \tag{3.44}$$

which shows that the slopes along the curves in Fig. 3.10 indeed correspond to $\widetilde{\mu}_c$. The (total) pressure is found from

$$\widetilde{P} = \phi \widetilde{\mu}_c - \widetilde{\Omega}. \tag{3.45}$$

When two compositions can be connected through the common tangent (the thin straight lines in the figures connecting these compositions), binodal points are found; the intercepts of the extrapolated lines correspond to the total pressure $-\widetilde{P}$. Scenario (i) in Fig. 3.10 corresponds to gas–liquid coexistence. In situation (ii) $\widetilde{\Omega}(\phi)$ are given for both the fluid state and for the solid state and the common tangent shows the compositions where fluid and solid coexist. A combination of (i)

and (ii) is possible under conditions where the curve for the fluid state shows an instability itself and the gas and liquid compositions coexist with a solid phase (termed a triple point) as exemplified by (iii). Finally, situation (iv) refers to an instability of the fluid state within the concentration region where fluid and solid coexist. Here the value for the chemical potential of the colloidal particles at gas–liquid coexistence is larger than the chemical potential of the fluid–solid coexistence as follows from the slopes. Hence gas–liquid coexistence is metastable in such a case. For each polymer concentration the binodal compositions can be found in this manner; full phase diagrams can be constructed from such binodals.

For non-interacting depletants such as penetrable hard spheres the μ's and P's in the phase coexistence equations (3.41) and (3.42) can be written such that binodal colloid concentrations follow from solving one equation in a single unknown [28]. We rewrite (3.38) and (3.39) as

$$\widetilde{\mu} = \widetilde{\mu}^0 + \widetilde{P}^R \, g(\phi) \tag{3.46}$$

$$\widetilde{P} = \widetilde{P}^0 + \widetilde{P}^R \, h(\phi), \tag{3.47}$$

where $g = -\partial\alpha/\partial\phi$ and $h = \alpha + g\phi$. The functions g and h may be written as

$$g(\phi) = e^{-Q(\phi)}\left\{1 + [1+y][a + 2by + 3cy^2]\right\} \tag{3.48}$$

and

$$h(\phi) = e^{-Q(\phi)}\left\{1 + ay + 2by^2 + 3cy^3\right\}. \tag{3.49}$$

The gas–liquid binodal can be solved from the second and third parts of

$$\widetilde{P}^R = \frac{\widetilde{\mu}_f^0(\phi_l) - \widetilde{\mu}_f^0(\phi_g)}{g(\phi_g) - g(\phi_l)} = \frac{\widetilde{P}_f^0(\phi_l) - \widetilde{P}_f^0(\phi_g)}{h(\phi_g) - h(\phi_l)}, \tag{3.50}$$

where $\widetilde{\mu}_f^0$ and $\widetilde{P}_f^0$ are only a function of ϕ, see (3.1) and (3.7). Hence, (3.50) gives a unique relation $\phi_l(\phi_g)$ at given q.

Exercise Derive (3.48), (3.49) and (3.50).

For some value of ϕ_g, within the region of ϕ_g values where a colloidal gas coexists with a colloidal liquid, the corresponding value of ϕ_l follows from the second equality of (3.50). The corresponding binodal depletant reservoir pressure $\widetilde{P}^R$ then follows from the first equality.

Similarly, the fluid–solid binodal can be obtained from

$$\widetilde{P}^R = \frac{\widetilde{\mu}_s^0(\phi_s) - \widetilde{\mu}_f^0(\phi_f)}{g(\phi_f) - g(\phi_s)} = \frac{\widetilde{P}_s^0(\phi_s) - \widetilde{P}_f^0(\phi_f)}{h(\phi_f) - h(\phi_s)}, \tag{3.51}$$

where again $\widetilde{\mu}_f^0$ is given by (3.7) and $\widetilde{P}_f^0$ by (3.1); these are the fluid contributions. For colloidal dispersions in the solid state $\widetilde{P}_s^0(\phi)$ and $\widetilde{\mu}_s^0(\phi)$ are given by (3.12) and (3.13), respectively.

Triple points have equal pressures and chemical potentials at colloidal gas, liquid *and* solid compositions. At the triple point expressions (3.50) and (3.51) are connected through equal values for $\widetilde{P}^R$ and, in principle, form a set of four equations from which the four coordinates of the triple point $(\phi_g, \phi_l, \phi_s, \widetilde{P}^R)$ follow. However, for the present phs-system the problem can be reduced to solving one equation in one unknown [28].

For large q $(q \geq 0.6)$, the triple point can be approximated easily from (3.46) and (3.47). It can be observed that the fluid–solid coexistence of the triple point occurs at nearly similar colloid concentrations as the pure hard sphere phase transition. For large q values, (3.46) and (3.47) can be written as $\widetilde{\mu}_f = \widetilde{\mu}_f^0 = \widetilde{\mu}_s^0$ and $\widetilde{P}_f = \widetilde{P}_f^0 = \widetilde{P}_s^0$, because $g(\phi)$ and $h(\phi)$ vanish for large q. In the coexisting colloidal gas phase the colloid concentration is then extremely small so $\widetilde{P}_g = \widetilde{P}^R$, since $h(\phi) \to 1$, implying $\widetilde{P}^R = \widetilde{P}_f^0 = \widetilde{P}_s^0 = 6.01$ at the triple point. Hence, for large q the fluid–solid coexistence of the triple point occurs at nearly the same colloid concentrations as for the pure hard-sphere phase transition.

The relative depletant concentration at the triple point now follows as $\phi_d^R \simeq \widetilde{P}^R q^3 = 6.01 q^3$. As can be seen in Figs. 3.11 $(q = 1.0)$ and 3.12 this is rather accurate.

The critical point can be found also as one equation in one unknown, for details we refer to [28]. The same applies to the *critical endpoint* (CEP), which corresponds to the q value where CP and TP coincide; it is the lowest q where stable liquid is possible. See the extended discussions on liquid windows as related to the CEP in [28, 29].

In Fig. 3.11 we present phase diagrams for $q = 0.1$, $q = 0.4$ and $q = 1.0$. As was already found by Gast et al. [25], for $q = 0.1$ there is only a fluid–crystal transition. For $\phi_d = 0$ the demixing gap is $0.491 < \phi < 0.541$ (see Sect. 3.2.3); with increasing depletant concentration this gap widens. For $q = 0.4$ there are a critical point (CP) and a triple point (TP) in the phase diagram, analogous to those found in simple atomic systems. At high depletant concentrations in the reservoir (above TP) a very dilute fluid (colloidal gas), coexists with a highly concentrated colloidal solid. Between TP and CP a colloidal gas (dilute fluid) coexists with a colloidal liquid (more concentrated fluid). At high packing fractions below the triple line, a colloidal liquid coexists with a colloidal solid phase.

In the absence of depletant only the fluid–solid phase transition of a pure hard sphere dispersion remains. Increasing the depletant activity now plays a role similar to lowering the temperature in atomic systems. For larger q (see $q = 1.0$) the qualitative picture remains the same while the liquid window expands.

In the top diagrams of Fig. 3.11 the ordinate axis is the depletant concentration in the reservoir. The depletant concentrations in the system of coexisting phases can be obtained by using the relation

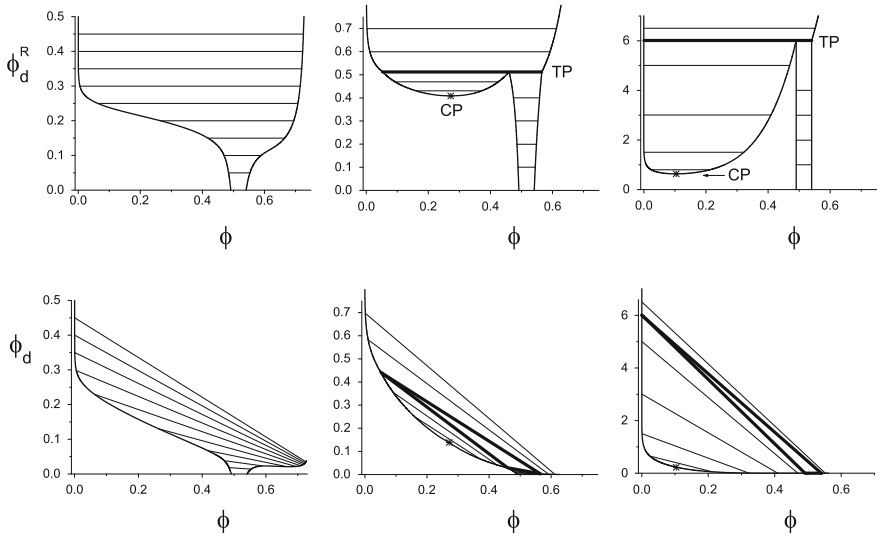

Fig. 3.11 Free volume theory predictions for the phase diagrams for hard spheres as depletants following Lekkerkerker et al. [27]. The *left diagrams* are for $q = 0.1$, *middle* $q = 0.4$, and *right diagrams* $q = 1.0$. *Upper diagrams* have depletant reservoir concentrations ϕ_d^R as ordinates, *lower diagrams* are in system depletant concentrations. *Triple lines* and *triangles* are indicated as thick lines. *TP* triple point, *CP* critical point (*Asterisks* refer to the critical points). A few representative tie-lines are plotted as thin lines

$$\frac{N_d}{V} = -\frac{1}{V}\left(\frac{\partial \Omega}{\partial \mu_d}\right)_{N_c,V,T} = \alpha n_d^R$$

or

$$\phi_d = \alpha \phi_d^R.$$

Coexisting phases of course have the same μ_d and hence the same n_d^R but since the volume fractions of hard spheres and, hence, the free volume fractions α are different, n_d in the two (or three) phases are not the same, so the tie-lines are no longer horizontal. This is illustrated in the bottom diagrams of Fig. 3.11; now the ordinate axis gives the relative 'internal' or system concentrations ϕ_d. A few selected tie-lines are drawn to give an impression of depletant partitioning over the phases. Interestingly, the horizontal triple line in the presentation of the phase diagram at constant chemical potential μ_d (field-density representation) is now converted into a three-phase triangle system representation.

As discussed in Sect. 3.2.3, the free volume theory is approximate in the sense that $\langle V_{\text{free}} \rangle$ is replaced by $\langle V_{\text{free}} \rangle_0$. To get an idea of the accuracy of the phase diagrams calculated with free volume theory we compare in Fig. 3.12 the results for $q = 0.6$ with recent computer simulations [33]. The agreement is, given the

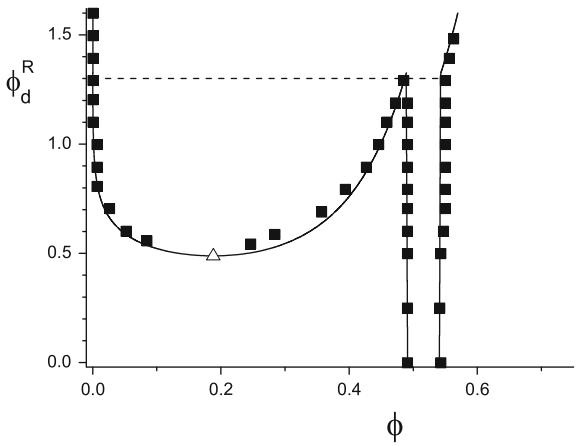

Fig. 3.12 Comparison of free volume theory (*curves*) with Monte Carlo computer simulations (data; [33]) for $q = 0.6$. *Open triangle* theoretical critical point

fact that the free volume theory is approximate, very good. Also for $q = 0.1 - 1.0$ [33] and large q values [34] the agreement with simulations is striking.

In this chapter we have presented the free volume theory for hard spheres plus depletants and focused on the simplest possible case of hard spheres + penetrable hard spheres. In the next chapters we will extend the free volume theory to more realistic situations (Chap. 4; hard spheres + polymers, Chap. 5; hard spheres + small colloidal particles, Chap. 6; hard rods + polymers) and compare the results with experiments and simulations.

References

1. A. Einstein, Ann. Phys. **17**, 549 (1905)
2. J. Perrin, Ann. de Chem. et de Phys. **18**, 5 (1909)
3. L. Onsager, Ann. N. Y. Acad. Sci. **51**, 627 (1949)
4. M. Baus, L.F. Rull, J.P. Ryckaert (eds.), *Observation and Simulation of Phase Transitions in Complex Fluids* (Kluwer Academic Publishers, Dordrecht, 1995)
5. A.K. Arora, B.V.R. Tata (eds.), *Phase Transitions in Charge Stabilized Colloids* (VCH Publishers, New York, 1996)
6. J.G. Kirkwood, J. Chem. Phys. **7**, 919 (1939)
7. W.W. Wood, J.D. Jacobson, J. Chem. Phys. **27**, 1207 (1957)
8. B.J. Alder, T.E. Wainwright, J. Chem. Phys. **27**, 1208 (1957)
9. P.N. Pusey, W. Van Megen, Nature **320**, 340 (1986)
10. W.B. Russel, D.A. Saville, W.R. Schowalter, Colloidal Dispersions. (Cambridge Universtity Press, Cambridge, 1999)
11. W.G. Hoover, F.H. Ree, J. Chem. Phys. **49**, 3609 (1968)
12. N.F. Carnahan, K.E. Starling, J. Chem. Phys. **51**, 635 (1969)
13. A. Fortini, M. Dijkstra, R. Tuinier, J. Phys. Condens. Matter. **17**, 7783–7803 (2005)
14. J.-P. Hansen, I.R. McDonald, Theory of Simple Liquids. (Academic Press, San Diego, 1986)
15. D.A. McQuarrie, Statistical Mechanics. (University Science Books, Sausalito, 2000)
16. A. Malijevský, J. Kolafa, Introduction to the thermodynamics of hard spheres and related systems, in *Theory and Simulation of Hard-Sphere Fluids and Related Systems*, Lecture Notes in Physics, vol. 753 (Springer, Berlin, 2008)

17. J.E. Lennard-Jones, A.F. Devonshire, Proc. Roy. Soc. **163**, 53 (1937)
18. R.J. Buehler, R.H. Wentorf, J.O. Hirschfelder, C.F. Curtis, J. Chem. Phys. **19**, 61 (1951)
19. B.J. Alder, W.G. Hoover, D.A. Young, J. Chem. Phys. **49**, 3688 (1968)
20. D. Frenkel, A.J.C. Ladd, J. Chem. Phys. **81**, 3188 (1984)
21. T. Alfrey, E.B. Bradford, J.F. Vanderhof, G. Oster, J. Opt. Soc. Amer. **44**, 603 (1954)
22. E.W. Fischer, Kolloid Z **160**, 120 (1958)
23. W. Luck, M. Klier, H. Weslau, Ber Buns. Phys. Chem. **67**, 75 (1963)
24. C.G. de Kruif, P.W. Rouw, J.W. Jansen, A. Vrij, J. de Phys. **46**, C3-295 (1985)
25. A.P. Gast, C.K. Hall, W.B. Russel, J. Colloid Interface Sci. **96**, 251 (1983)
26. B. Vincent, J. Edwards, S. Emmett, R. Croot, Colloids and Surf. **31**, 267 (1988)
27. H.N.W. Lekkerkerker, W.C.K. Poon, P.N. Pusey, A. Stroobants, P.B. Warren, Europhys. Lett. **20**, 559 (1992)
28. G.J. Fleer, R. Tuinier, Adv. Colloid Interface Sci. **143**, 1–47 (2008)
29. G.J. Fleer, R. Tuinier, Phys. A **379**, 52 (2007)
30. B. Widom, J. Chem. Phys. **39**, 2808 (1963)
31. H. Reiss, H.L. Frisch, J.L. Lebowitz, J. Chem. Phys. **31**, 369 (1959)
32. E.J. Meijer, Computer simulation of molecular solids and colloidal dispersions, PhD thesis, Utrecht University, Utrecht (1993)
33. M. Dijkstra, R. van Roij, R. Roth, A. Fortini, Phys. Rev. E **73**, 041409 (2006)
34. A. Moncho-Jorda, A.A. Louis, P.G. Bolhuis, R. Roth, J. Phys. Condens. Matter. **15**, S3429 (2003)

Chapter 4
Stability of Colloid–Polymer Mixtures

When a dispersion containing spherical colloids is mixed with a polymer solution two kinds of instabilities can occur as depicted in Fig. 4.1: bridging flocculation (1) caused by adsorbing polymer or unmixing driven by the depletion force (2). The type of instability encountered depends on whether the polymers adsorb onto the colloidal surfaces. Polymer adsorption occurs when the contact between the colloid surface and the polymer segments is energetically favorable to such a degree that the loss of configurational entropy is compensated [1]. When the amount of adsorbing polymer in the system does not suffice to fully cover all available surface area on the colloids, so-called bridging flocculation occurs [2]. Some polymers then attach to more than a single particle leading to aggregates or complexes (see Fig. 4.1), which tend to sediment when they are large (situation '1'). Such a flocculation with both colloids and polymers concentrated in one part of a container indicates polymer adsorption. When all particle surfaces are saturated with adsorbed polymers in a good solvent (see Fig. 4.2), the particle interactions are effectively repulsive because dense polymer layers overlap upon close approach giving rise to steric repulsion, which kinetically stabilizes the dispersion (see Chap. 10 in [1]).

In the introductory chapter we saw that many systematic depletion studies were performed on mixtures of spherical colloids plus non-adsorbing or free polymers. The reason is obvious: spherical colloids are of industrial and fundamental relevance, and can be prepared in a relatively controlled way (rather monodisperse, hard-sphere like), while polymers are ubiquitous, and are efficient depletants.

To verify whether polymers adsorb or not there are various experimental methods. The typical adsorbed amount at saturation $\Gamma \sim 1\,\mathrm{mg\ m^{-2}}$ [1]. It is possible to investigate whether a polymer adsorbs onto a colloid by measuring the friction coefficient that a sphere experiences by for instance sedimentation or dynamic light scattering [3, 4].

H. N. W. Lekkerkerker and R. Tuinier, *Colloids and the Depletion Interaction*, Lecture Notes in Physics, 833, DOI: 10.1007/978-94-007-1223-2_4,

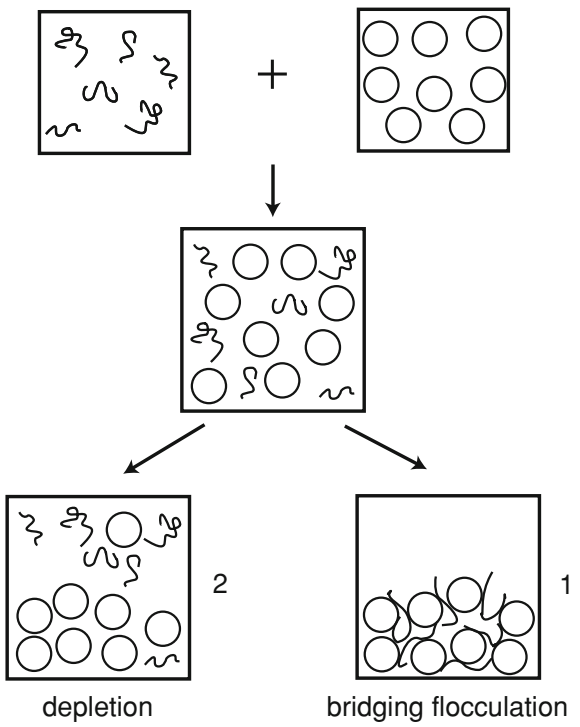

Fig. 4.1 Types of instability that occur after mixing a colloidal dispersion with a polymer solution. When the polymer chains do not adsorb depletion leads to partitioning of colloids and polymers over different phases (*2*). In case of adsorption (and low polymer concentrations) bridging between different particles can induce flocculation (*1*)

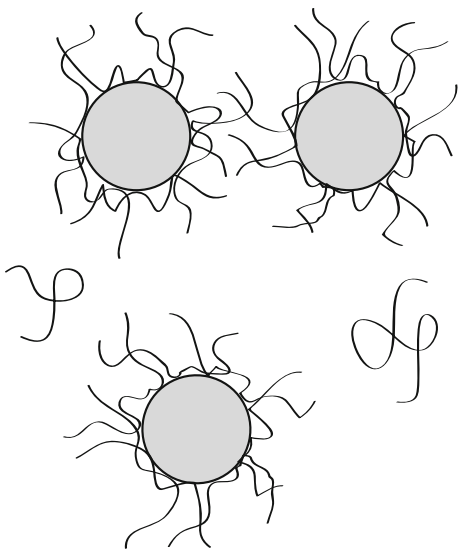

Fig. 4.2 Sketch of colloidal particles that are sterically stabilized through polymer adsorption

Exercise
Verify that the polymer concentration c_p (in g/L) required to fully cover all spheres with radii R in a dispersion with volume fraction ϕ can be expressed as

$$c_p = \frac{3\phi\Gamma}{R}.$$

Hint: assume that all added polymer adsorbs.

When the effective size, due to adsorption, increases, this results in a larger friction as follows from the Stokes friction coefficient $f = 6\pi\eta^{\text{eff}}R$. We stress that any study on colloid–polymer mixtures should be preceded with an analysis of whether the polymers adsorb or not. Analysis of the composition of the two phases can be used to verify whether depletion interaction is responsible for demixing.

When the colloidal particles are completely covered with adsorbing polymer, adding more polymer gives rise to excess polymer in the bulk solution, which is thus not adsorbed. This non-adsorbing polymer may lead to depletion interaction as well. In such a case depletion effects are weaker for two reasons. Firstly, more polymer is required before depletion-induced instability of the dispersion occurs because polymer is first consumed in order to cover the particles [1]. Secondly, the depletion interaction is weak due to the soft repulsion between the adsorbed polymer layers. It is known that depletion effects between such soft surfaces are rather small [1, 5].

For depleting polymer at hard surfaces, exceeding a certain polymer concentration may lead to phase separation into a polymer-enriched phase coexisting with a particle-enriched phase (see Fig. 4.1). For colloidal gas–liquid phase separation, the degree of partitioning over the two phases depends on how far the system is from the critical point. Although the focus in this chapter is on equilibrium phase behaviour, we also pay attention to nonequilibrium phenomena, ranging from polymer depletion-induced phase separation kinetics to colloidal (transient) gel and glass formation. Such effects are of significant practical relevance and are discussed in Sect. 4.5.

In Chap. 3 we introduced the phase behaviour of hard spheres mixed with penetrable hard spheres (phs). This provides a starting point for describing the phase behaviour of colloid–polymer mixtures. In Sect. 4.1 we show that the phs-description using penetrable hard spheres is adequate for mixtures in the colloid-limit: small q with polymer chains smaller than the particle radius. In Sect. 4.2 we treat the modifications for the case that the polymers are treated as ideal chains. More advanced treatments accounting for non-ideal behaviour of depletion thickness and osmotic pressure for interacting polymer chains enable to also describe intermediate and large q situations. This is the topic of Sect. 4.3. In Sect. 4.4 we qualitatively consider work available on the effects of polydispersity on

depletion interaction and phase behaviour as well as the influence of charges on depletion effects. Finally, we consider non-equilibrium states in colloid–polymer mixtures in Sect. 4.5.

4.1 Experimental State Diagrams of Model Colloid–Polymer Mixtures

In several groups well-defined colloids with a lyophilic surface coating and a steep repulsive interaction have been developed. Dispersions of such particles in appropriate solvents can be approximated as hard-sphere fluids (or solids above some concentration). Spherical silica particles in cyclohexane [6–8], in which the particles were made lyophilic by covering the surface with a layer of terminally anchored octadecyl chains, are a first example of such a model dispersion. In this system the refractive indices of silica (1.45) and cyclohexane (1.42) are close, so multiple light scattering effects are avoided and the Van der Waals attraction between the particles is small. Cyclohexane was chosen since it is a good solvent for octadecyl chains; the surface layers of two encountering particles will repel each other sterically, see Sect. 1.2.4. This results in a fairly steep pseudo hard-sphere interaction that can be described through (1.19):

$$\begin{aligned} W(r) &= \infty \quad r \leq 2R_{\text{eff}} \\ &= 0 \quad r > 2R_{\text{eff}}, \end{aligned} \tag{4.1}$$

where r is the centre-to-centre distance between the spheres ($= 2R_{\text{eff}} + h$). Here R_{eff} is the effective hard-sphere radius: the sphere radius plus the thickness of the terminally anchored chains.

Another interesting model system is a dispersion of polymethylmetacrylate (PMMA) particles that are sterically stabilized with poly-12-hydroxy stearic acid in solvents such as decalin, sometimes mixed with tetralin in order to match solvent and particle refractive indices. Early synthesis of and studies with these particles were performed in Bristol [9, 10]. These systems exhibit fluid to solid phase transitions when the particle volume fraction exceeds about 0.5.

Well-defined dispersions of hard-sphere-like PMMA colloids and non-adsorbing polymers were extensively studied in Edinburgh [11]. These PMMA particles can be synthesized with a size polydispersity below 5%, and behave almost like perfect hard spheres [12], see Sect. 3.2.

Polystyrene (PS) polymer is one of the well-characterized random coil polymers used in combination with PMMA spheres. PS can be synthesized with polydispersities as small as $M_W/M_N \approx 1.02$. The physical properties of PS in solution have been characterized in a wide range of solvents [13]. Optical tweezer experiments [14] on a pair of PMMA spheres in a PS solution were consistent with the presence of depletion layers of PS surrounding the spheres. Also DLS measurements showed that adsorption does not occur [3]. Hence, the model system of

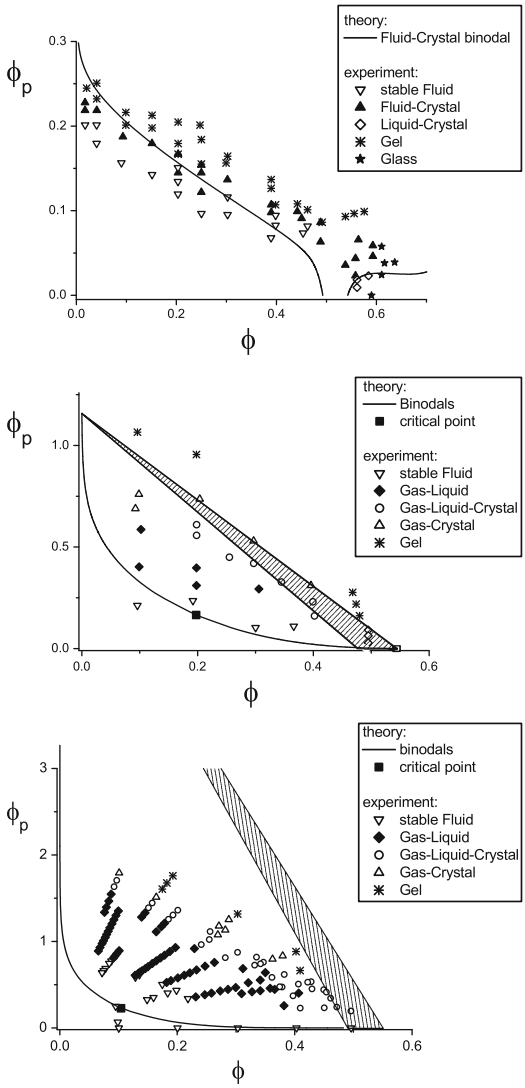

Fig. 4.3 State diagrams of colloid–polymer mixtures for $q = 0.08$ (*top*), $q = 0.57$ (*middle*) and $q = 1.0$ (*bottom*). Experimental data: PMMA spheres plus polystyrene polymers in *cis*-decalin [16, 17]. *Curves*: free volume theory [18] with $\delta = R_g$. For high q a triple triangle (*hatched*) is predicted by the theory

PMMA plus PS offers an excellent tool for studying the phase behaviour of hard spheres plus free polymers [15].

In Fig. 4.3 state diagrams are plotted that were measured by Poon et al. [16, 17] for three size ratios $q = R_g/R = 0.08, 0.57$ and 1. Here ϕ_p is the polymer concentration relative to overlap, see (1.24). At $\phi < 0.49$ and low polymer concentrations the mixtures appear as single-state fluid phases. At zero polymer content the hard-sphere fluid–crystal phase transition is found when the colloids occupy about half of the volume. Upon addition of polymer the fluid–crystal coexistence region expands for $q = 0.08$; then a colloidal fluid at smaller volume fraction

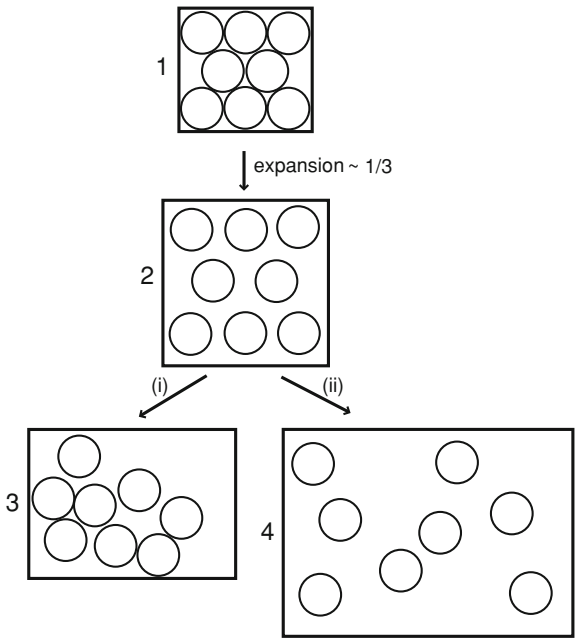

Fig. 4.4 Schematic picture of the expansion of a colloidal crystal phase (*1*) towards (*2*), at the melting volume fraction (~ 0.55). After melting, for a short-ranged attraction (ii) a colloidal gas (*4*) is more favourable upon further expansion. In case of a long-ranged attraction with appropriate strength, a colloidal liquid (*3*) is the stable state (i)

coexists with a denser colloidal crystal. Slanted tie-lines were observed that indicate polymer partitioning over the two phases [16]. These findings are consistent with the small-q predictions in Chap. 3 for hard spheres mixed with penetrable hard spheres [18] for small q. For larger q values ($q \gtrsim 0.3$), a critical point appears in the phase diagram, identifying the onset of the gas–liquid coexistence region. This is observed in the phase diagrams for $q = 0.57$ and 1 in Fig. 4.3 and is also found for larger q values [19–23]. Large q implies a long-ranged attraction.

The absence of a liquid state in phase diagrams for a collection of particles with short-ranged attractions is a general finding [24, 25] for which Pusey and Poon gave the following simple physical argument [15, 26]. Consider a close-packed crystal $\phi \approx 0.74$ of adhesive hard spheres that have a mutual attraction (see Fig. 4.4). Upon adding solvent, the crystalline structure expands in volume. At $\phi = 0.545$, the point of loss of rigidity is attained and a fluid state becomes possible. Liquid configurations require that the particles attract one another sufficiently strong as they are moving. For weak attraction (weaker than the attraction at the critical point) thermal energy overcomes this attraction and a liquid state is impossible. For stronger attractions (exceeding the critical value) the state depends on the range of attraction. For short-ranged attractions the particles are directly out of their range of attraction so a low density gas is the most stable situation upon dilution. Gas–liquid equilibria are then metastable. It has been shown that such 'hidden' gas–liquid coexistence regions have their impact on dynamics and phase separation kinetics and play a role in crystallisation phenomena [27–31]. Fortini et al. [32] studied the relationship between equilibrium and nonequilibrium phase diagrams of a system

of hard spheres with a short-ranged attraction using Monte Carlo and Brownian dynamics simulations. They found that crystallization is enhanced for attractions that are sufficiently strong to enter the metastable gas–liquid binodal. Then formation of a dense liquid is observed followed by nucleation of the crystallites within the dense fluid. Only at larger colloid concentrations a percolating network structure due to an arrested gas–liquid phase separation is found.

For sufficiently long-ranged attraction the particles still attract one another at the loss of rigidity point so a liquid state then is possible.

Exercise
What does it take to make a stable liquid?

In colloid–polymer mixtures there is no direct attraction between the colloids but the attraction enters through repulsion. Attraction is caused by overlap of depletion layers rather than through direct pair interactions. For $q > 0.15$, multiple overlap of depletion layers (see Fig. 3.8) occurs which is expected to promote the occurrence of a colloidal liquid. The critical point at which the range of attraction is just sufficient for a stable liquid state is termed the critical end point [25]. For a shorter range of attraction no critical point borders a stable fluid phase. Theory and computer simulations point out that the critical end point generally corresponds to a range of attraction close to $1/3$ of the particle diameter [25].

We now return to Fig. 4.3 and focus on the state diagrams for $q = 0.57$ and 1. Adding polymer leads to gas–liquid coexistence as discussed, followed by a region where a gas–liquid–crystal equilibrium (open circles) is found. For $q = 0.57$ this three-phase coexistence region corresponds roughly to the theoretical prediction of the free volume theory (FVT) as outlined in Chap. 3, with penetrable hard spheres playing the role of the polymer chains. Above the three-phase coexistence region a gas–crystal binodal is found which is also predicted by FVT. At even higher polymer concentrations crystallisation did not occur anymore while dense solid sediments of particles appeared. This nonequilibrium behaviour is also found for $q = 0.08$ at high polymer concentrations where (metastable) gel or glassy states are observed. A colloidal glass refers to a state where the particles are topologically trapped ('caged') by their neighbours. The term gel is identified as a disordered arrested state which does not flow but exhibits solid-like rheological properties such as an elastic shear modulus [33]. We return to these nonequilibrium states of colloid–polymer mixtures in Sect. 4.5.

In Fig. 4.3 we also plot the (equilibrium) binodals using FVT outlined in Chap. 3 for hard spheres plus penetrable hard spheres with diameters of $2R_g$. Qualitatively, the phase diagram topology is quite well predicted. For $q = 0.08$, only equilibrium fluid, crystal and fluid + crystal regions are found and predicted. Both for $q = 0.57$ and 1 the phase diagram contains fluid, gas, liquid and crystalline (equilibrium) phases. In the different unmixing regions one now finds gas–liquid coexistence with a critical point, three-phase gas–liquid–crystal and

gas–crystal coexistences. The observed q-dependence of the phase diagram topology outlined above is not limited to the PMMA model system. Similar findings were reported for the phase behaviour of for instance polystyrene latex spheres mixed with hydroxy-ethyl cellulose in water [34, 35].

Next we make a more quantitative comparison between theory and experiment. We observe in Fig. 4.3 that the quantitative agreement between FVT and the experimental data becomes less upon increasing q. For $q = 0.08$ the fluid–crystal binodal is in nearly quantitative agreement with the experimental results with a slight, nearly imperceptible, overestimation of the binodal. The $q = 0.57$ data are in fair agreement with the FVT predictions (middle panel of Fig. 4.3). The triple region lies somewhat above the experimental data, especially at low ϕ, and the FVT gas–liquid binodal curve lies slightly below the experimental binodal. Hence the width of the gas–liquid coexistence region is overestimated. Whereas for $q = 0.08$ the relevant concentration regime of the FVT prediction is located at $\phi_p < 0.3$, the relative polymer concentrations are much closer to the overlap concentration for $q = 0.57$. This means that one has to take into account the excluded volume interactions between the polymer chains. Regarding them as penetrable hard spheres only suffices for small q ($\sim \phi_p$).

For $q = 1.0$ (lower panel of Fig. 4.3) classical FVT fails. The FVT gas–liquid binodal now lies far below the experimental phase transition and the FVT triple region (approaching $\phi_p \approx 6$) at the gas corner of the triple region, see Fig. 3.11 (lower right panel), largely exceeds the experimental one. In Sect. 4.3 we generalize FVT by incorporating polymeric interactions between the polymer chains and we compare these results to the experimental equilibrium phase diagrams for $q = 0.57$ and 1.0.

To summarize, theory and experiment clearly demonstrate that the types of phase equilibria encountered in unmixed colloid–polymer mixtures are rather sensitive to the size ratio q. For sufficiently large q ($\gtrsim 0.3$) a colloidal gas–liquid phase separation is encountered. For $q \gtrsim 0.4$, the simple model of hard spheres plus penetrable hard spheres fails to accurately describe the phase behaviour of well-defined hard-sphere colloid plus polymer mixtures. For large q-values it is essential to improve the simple description of polymer chains as penetrable hard spheres.

4.2 Phase Behaviour of Colloid + Ideal Polymer Mixtures

The first step in taking into account more appropriate polymer physics compared to the simple description of penetrable hard spheres is by considering the polymers as ideal chains. Then one needs to incorporate the correct depletion thickness of non-adsorbing ideal chains near a colloidal hard sphere into free volume theory.

In Chap. 2 we saw that an analytical expression (2.62) can be derived for the depletion thickness around a sphere due to ideal polymer chains:

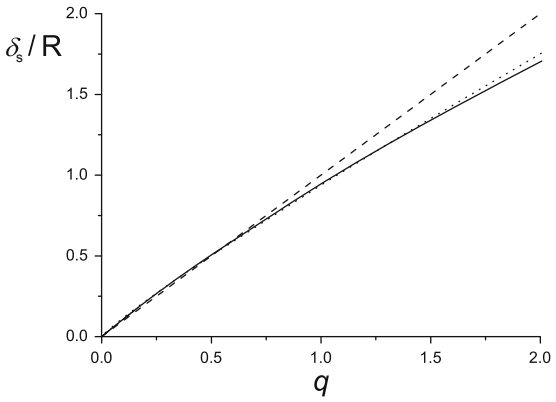

Fig. 4.5 Depletion thickness of ideal polymer chains around a sphere (*solid curve*) as a function of the polymer-to-sphere size ratio q. *Solid curve*: (4.2), *dashed line* is the classical penetrable hard-sphere approach $\delta_s = R_g$ and the *dotted curve* follows the approximation $\delta/R = 0.938q^{0.9}$, see (4.24)

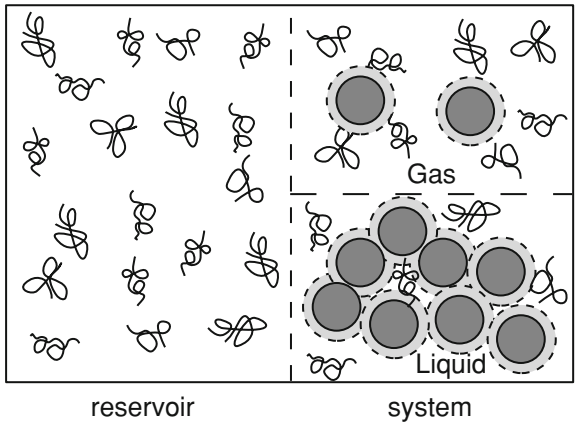

Fig. 4.6 Osmotic equilibrium between a reservoir containing polymer chains and a system of colloids plus polymers where (in this example) unmixing resulted in a colloidal gas in equilibrium with a colloidal liquid

$$\frac{\delta_s}{R} = \left(1 + \frac{6q}{\sqrt{\pi}} + 3q^2\right)^{1/3} - 1. \tag{4.2}$$

In Fig. 2.16 we plotted (4.2). It follows that the depletion thickness, normalised as δ_s/R, drops with increasing q. For $q < 1$ the depletion thickness is larger than R_g but not much: the maximum is $2/\sqrt{\pi} \approx 1.13$ times R_g in the limit $q \to 0$. For $q \gtrsim 1$ the depletion thickness is smaller than R_g. In Fig. 4.5, δ_s as normalized with the sphere radius R is plotted as a function of q.

We now incorporate the correct depletion thickness into free volume theory presented in Sect. 3.3. We consider the osmotic equilibrium between a polymer solution (reservoir) and the colloid–polymer mixture (system) of interest, see Fig. 4.6. The general expression for the semi-grand potential for N_c hard spheres plus interacting polymers as depletants, see (3.18), is

$$\Omega(N_c, V, T, \mu_p) = F_0(N_c, V, T) + \int_{-\infty}^{\mu_p^R} \frac{\partial \Omega}{\partial \mu_p^{R'}} \, \mathrm{d}\mu_p^{R'}, \tag{4.3}$$

with F_0 the free energy of the pure hard-sphere dispersion. Just as in Chap. 3 we define the dimensionless free energies, chemical potential and pressure

$$\widetilde{F}_0 = \frac{F_0 v_0}{VkT}, \quad \widetilde{\Omega} = \frac{\Omega v_0}{VkT}, \quad \widetilde{\mu} = \frac{\mu}{kT}, \quad \widetilde{P}^{(R)} = \frac{P^{(R)} v_0}{kT}.$$

We drop the explicit dependencies (N_c, V, T, μ_p) in (3.18) and can write

$$\widetilde{\Omega} = \widetilde{F}_0 - \int_0^{\phi_p} \alpha \left(\frac{\partial \widetilde{P}^R}{\partial \phi_p^{R'}} \right) \mathrm{d}\phi_p^{R'}, \tag{4.4}$$

using the free volume theory approximations discussed in Chap. 3. Since for ideal polymers $\widetilde{P}^R = \phi_p^R q^{-3}$ and α is independent of ϕ_p we arrive at (3.43)

$$\widetilde{\Omega} = \widetilde{F}_0 - \alpha \widetilde{P}^R = \widetilde{F}_0 - \alpha \phi_p^R q^{-3}. \tag{4.5}$$

Exercise
Derive (4.4) by starting from (3.16), using $\partial\Omega/\partial\mu_p = -N_p$, the Gibbs–Duhem relation $\mathrm{d}\mu_p^R = (v_p/\phi_p^R)\,\mathrm{d}P^R$ and $\widetilde{P}^R = P^R v_0/kT$.

For the free volume fraction α we recall (3.36),

$$\alpha = (1-\phi)\exp[-ay - by^2 - cy^3], \tag{4.6}$$

with

$$y = \frac{\phi}{1-\phi}$$

and revised definitions of a, b and c:

$$\begin{aligned} a &= 3\frac{\delta_s}{R} + 3\left(\frac{\delta_s}{R}\right)^2 + \left(\frac{\delta_s}{R}\right)^3, \\ b &= \frac{9}{2}\left(\frac{\delta_s}{R}\right)^2 + 3\left(\frac{\delta_s}{R}\right)^3, \\ c &= 3\left(\frac{\delta_s}{R}\right)^3. \end{aligned} \tag{4.7}$$

Inserting (4.2) into (4.6) gives the corrected free volume fraction in a mixture of ideal chains and colloidal spheres. Inspection of the gas–liquid coexistence binodals for $q = 1$ and smaller q reveals that replacing penetrable hard spheres with ideal chains does not give significant differences.

Exercise
Why does replacing penetrable hard spheres with ideal chains result in a polymer concentration shift upwards (at low colloid volume fractions ϕ) of the gas–liquid binodals for large q?

It follows from Fig. 4.5 and the detailed comparison in [36] that this corrected description for $q > 1$ does affect the phase diagram. For such high q values, however, it becomes essential to account for interactions between the polymer segments, whereby δ becomes a function of the polymer concentration and the osmotic pressure is no longer ideal.

4.3 Mixtures of Spheres Plus Interacting Polymer Mixtures

In this section we consider the phase behaviour of dispersions containing spherical colloids and *interacting* polymer chains in a common solvent. For small polymer-to-colloid size ratios, $q \lesssim 0.4$, the relevant part of the phase diagram lies below the polymer overlap concentration ($\phi_p^R < 1$). Then accounting for interactions between the polymers is not essential to properly describe the phase diagram and it is still sufficient to approximate the polymer-induced osmotic pressure by the ideal gas law as assumed within free volume theory [18]. However, for $q \gtrsim 0.4$, the polymer concentrations where phase transitions occur are of the order of and above the polymer overlap concentration: in that case interactions between the polymer segments should be accounted for.

We treat the extension of FVT and incorporate correct expressions for the (polymer concentration-dependent) depletion thickness and osmotic pressure, resulting in generalized free volume theory (GFVT). Expression (4.4) for the semi-grand potential is still valid in GFVT: it does not contain any assumption as yet on the physical properties of the depletants or the colloids. But now we need to specify the quantities α and $\widetilde{P}^R$ for interacting polymers. We thus need the osmotic pressure and depletion thickness (that determines α, see (4.6) and (4.7)). These will be considered in Sects. 4.3.2 and 4.3.3. First we start in Sect. 4.3.1 with some basics on the physics of polymer solutions in the dilute and semi-dilute concentration regimes.

4.3.1 Characteristic Length Scales in Polymer Solutions

In Sect. 2.2 we considered the concept of ghost or ideal chains. The segments of such chains do not feel each other. Here we consider excluded volume interactions between the segments Throughout Sect. 4.3 we consider two limiting cases of interacting polymer chains; the excluded volume limit (good solvent) and the

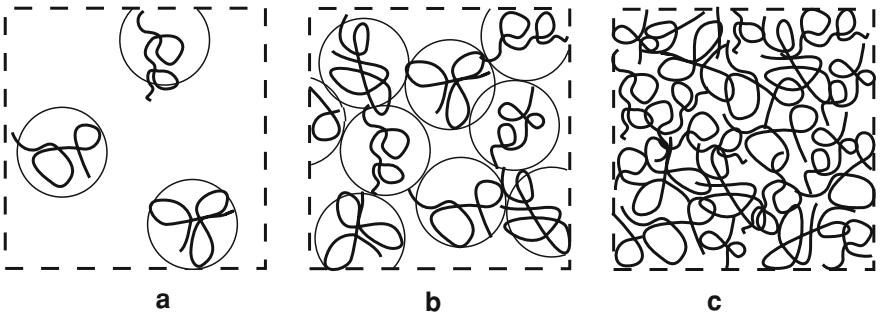

Fig. 4.7 Sketch of the various concentration regimes in polymer solutions, **a** dilute ($\phi_p < 1$), **b** near overlap ($\phi_p \approx 1$), **c** semi-dilute ($\phi_p > 1$)

Θ-solvent situation. The good solvent condition refers to the situation where the segments of the polymer chains effectively repel other segments so that chains in a good solvent will swell due to excluded volume interactions.

A special situation occurs when the attraction between the segments *exactly* compensates the (hard-core) excluded volume effect. In dilute solutions the chains then behave quasi-ideal. This situation is commonly referred to as the Θ-solvent condition.

Both under good and Θ-solvent conditions the physical properties of the polymer solution depend on the concentration regime. The characteristic length scale is the correlation length ξ. In the dilute concentration regime this is the radius of gyration of the coils, which depends on chain length M but not on concentration. Beyond the overlap concentration of polymer coils the correlation length decreases with increasing polymer concentration and is independent of M. Figure 4.7 gives a sketch of the various polymer concentration regimes.

4.3.1.1 Dilute Polymer Concentration

For long chains the following scaling relation holds [37]

$$R_g \sim M^{\nu}, \tag{4.8}$$

with

$$\begin{aligned} \nu &= \frac{1}{2} && \Theta\text{-solvent} \\ &= 0.588 && \text{good solvent,} \end{aligned} \tag{4.9}$$

where the scaling exponent ν is known as the Flory exponent. In a Θ-solvent the chains are ideal so R_g is proportional to $\sqrt{M}$. Then we have

$$R_g = b\sqrt{\frac{M}{6}},$$

where b is the segment size. For a good solvent the exponent ν follows from the Renormalization Group Theory (further on denoted as RGT) result [38].

For shorter chains an approximate expression for any solvency may be derived using the Flory excluded-volume parameter $\mathbf{v}$, which is unity when the segments experience hard-core repulsion and vanishes in case of a Θ-solvent. Based on Flory's result [37] for the expansion coefficient, the coil size can be written as [39]:

$$R_g = 0.31bM^{1/2}\left[1+\sqrt{1+6.5\mathbf{v}M^{1/2}}\right]^{0.352}, \tag{4.10}$$

where we adjusted the Flory scaling exponent $2/5$ in the last factor to 0.352 to achieve the correct scaling behaviour [38] of (4.9).

Exercise
Show that for $M \gg 1$ this expression reduces to the scaling limits of (4.8) and (4.9).

4.3.1.2 Semi-Dilute Polymer Concentration

In the dilute regime (Fig. 4.7a) each polymer coil occupies a volume $v_p = (4\pi/3)R_g^3$. When $v_p n_b$ becomes unity the solution is completely filled with polymer coils (Fig. 4.7b). For $v_p n_b > 1$ the chains overlap. Therefore overlap in terms of the number density is defined as $n_b^* = 1/v_p$. It is convenient to define a relative polymer concentration (1.24):

$$\phi_p = v_p n_b = \frac{\varphi}{\varphi^*}, \tag{4.11}$$

which is unity at the overlap concentration. Here φ is the polymer segment volume fraction, often used in polymer physics. Using this polymer segment volume fraction $\varphi = n_b M v_s$ the overlap volume fraction φ^* follows as

$$\varphi^* = M\frac{v_s}{v_p}. \tag{4.12}$$

Above the polymer overlap concentration we enter the semi-dilute regime (Fig. 4.7c). The length scale over which the polymer segments are correlated is denoted as correlation length ξ. Below overlap ($\varphi < \varphi^*$) this quantity is the coil size R_g which depends only on M (and solvency). Above overlap ($\varphi > \varphi^*$) we have the famous De Gennes scaling law [40]

$$\xi \sim \varphi^{-\gamma}, \tag{4.13}$$

which does not depend on chain length, The scaling exponent γ is given by

$$\begin{aligned} \gamma &= 1 \qquad \Theta\text{-solvent} \\ &= 0.77 \quad \text{good solvent.} \end{aligned} \tag{4.14}$$

Near the overlap concentration we have $\xi \approx R_g$ and $\varphi \approx \varphi^*$, so $R_g \sim (\varphi^*)^{-\gamma}$. Consequently,

$$\frac{\xi}{R_g} \sim \phi_p^{-\gamma}. \tag{4.15}$$

Since $\varphi^* \sim M/v_p \sim R_g^{1/\nu-3}$ (4.12) and $\varphi^* \sim R_g^{-1/\gamma}$, we have the following general relation between the Flory and De Gennes exponents

$$\frac{1}{\gamma} + \frac{1}{\nu} = 3. \tag{4.16}$$

To incorporate the crossover from dilute to the semi-dilute polymer concentrations, Fleer et al. [41] have derived approximate but accurate expressions for the polymer concentration-dependent depletion thickness δ and osmotic pressure P by interpolating between the exactly known dilute limit and scaling relations at semi-dilute polymer concentrations using combination rules. These are discussed in Sect. 4.3.2 (δ) and Sect. 4.3.3 (P).

4.3.2 Depletion Thickness

4.3.2.1 Concentration Profile at a Hard Wall

In the semi-dilute limit, De Gennes [40] made a mean-field analysis of the polymer concentration at a non-adsorbing hard wall. He used the ground state approximation (GSA) to approximate the Edwards equation [42–45] for polymer trajectories in an external field. The GSA basically simplifies chains in the sense that the spatial distribution of the segments is assumed to be independent of the ranking number of the segments: there is no difference between, for instance, an end segment and a middle segment of the chains. Especially in the semi-dilute concentration regime the GSA is powerful [46]. The GSA concentration profile is simple

$$f(x) = \tanh^2\left(\frac{x}{\xi}\right). \tag{4.17}$$

Applying (2.53)

$$\delta = \int_0^\infty \mathrm{d}x[1 - f(x)],$$

results in $\delta = \xi$. It follows that the correlation length sets the length scale over which polymer segments are depleted from the wall. Beyond a distance of the

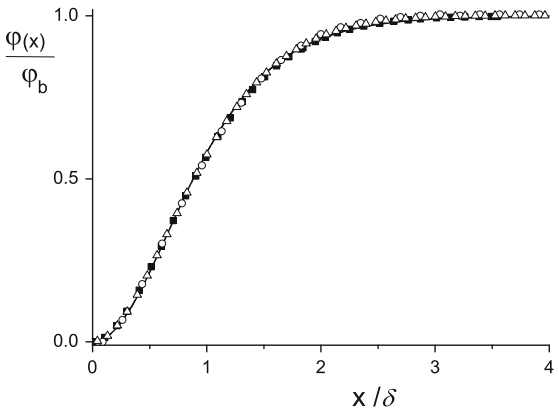

Fig. 4.8 Segment density profiles at a flat wall for non-adsorbing polymers described as ideal chains (*filled squares*) mean-field chains (*open circles*) and excluded volume chains (*open triangles*) compared to the $\tanh^2$ profile (*solid curve*) of (4.18)

correlation length from a colloidal surface the segments are 'unaware' of a non-adsorbing surface.

Exercise
Rationalize the shape of the profile $f(x) = \tanh^2(x/\xi)$ from the Van der Waals density profile at a gas–liquid interface. Hint: use the relation between the order parameter and the density profile.

For other cases (depleted dilute ideal or excluded volume chains, semi-dilute chains with fluctuation effects) density profiles are substantially more involved in comparison with a $\tanh^2$ profile. Surprisingly, the expression (2.55)

$$\frac{\varphi(x)}{\varphi_b} = \tanh^2\left(\frac{x}{\delta}\right), \tag{4.18}$$

where $\varphi(x)$ is the local polymer segment concentration and φ_b its value in the bulk, turns out to be very accurate in general as long as the correct correlation length δ is inserted, see Fig. 4.8.

4.3.2.2 Depletion Thickness at a Hard Wall

For ideal chains (or dilute chains in a Θ-solvent) we have seen, (2.51) plus (2.53), that the depletion thickness at a hard wall equals $\delta_0 = 2R_g\sqrt{\pi} \approx 1.13R_g$ [47, 48], where the subscript 0 now refers to the dilute (ideal) limit.

A general expression for dilute polymer solutions is

$$\delta_0 = pR_g \quad \text{with } p \approx \begin{cases} 1.13 & \Theta\text{-solvent} \\ 1.07 & \text{good solvent} \end{cases} \tag{4.19}$$

The good solvent result was derived by Hanke et al. [49] using RGT.

As we have seen the De Gennes result for the semi-dilute limit provides $\delta = \xi$. A GSA analysis of mean-field polymer chains in a slit [45] enables to combine the dilute and semi-dilute limits and provides a very simple and accurate relationship:

$$\delta^{-2} = \delta_0^{-2} + \xi^{-2}. \tag{4.20}$$

This result was derived from a mean-field treatment, where the semi-dilute scaling behaviour is $\xi \sim \phi_p^{-1}$ (Θ-solvent) or $\xi \sim \phi_p^{-1/2}$ (good solvent). The scaling exponent -1 is valid for chains in a Θ-solvent but $-1/2$ is incorrect for good solvent conditions. Expression (4.20) can, however, be generalised to include the correct scaling exponents by inserting the correct scaling (4.15) with (4.14), with the appropriate numerical prefactor, into (4.20). The result is [41]

$$\left(\frac{\delta_0}{\delta}\right)^2 = 1 + \beta\phi_p^{2\gamma} \tag{4.21}$$

with

$$\begin{aligned} \beta &= 6.02 \quad \Theta\text{-solvent} \\ &= 3.95 \quad \text{good solvent.} \end{aligned}$$

For a Θ-solvent with $\gamma = 1$ (4.21) is in quantitative with numerical self-consistent field results. For a good solvent with $\gamma = 0.77$ (4.21) compares favourably with computer simulation results, see [41].

4.3.2.3 Depletion Thickness Around a Hard Sphere

Converting the depletion thickness δ at a hard wall δ to its value δ_s around a hard sphere is a geometrical issue. In Sect. 2.2.2 we saw that the concentration profile of ideal polymer chains around a sphere gives (2.62), which can be rewritten in the form:

$$\frac{\delta_s}{R} = \left[1 + 3\frac{\delta}{R} + \frac{3\pi}{4}\left(\frac{\delta}{R}\right)^2\right]^{1/3} - 1. \tag{4.22}$$

For dilute chains in the excluded volume limit the following expansion has been found:

$$\frac{\delta_s}{R} = \left[1 + C_1\frac{\delta}{R} + C_2\left(\frac{\delta}{R}\right)^2 + C_3\left(\frac{\delta}{R}\right)^3 + \cdots\right]^{1/3} - 1, \tag{4.23}$$

with the flat wall result $C_1 = 3$. The curvature terms $C_2 \approx 2.273$ (which is close to $3\pi/4$) and the small value $C_3 \approx -0.0975$ were computed using RGT [49].

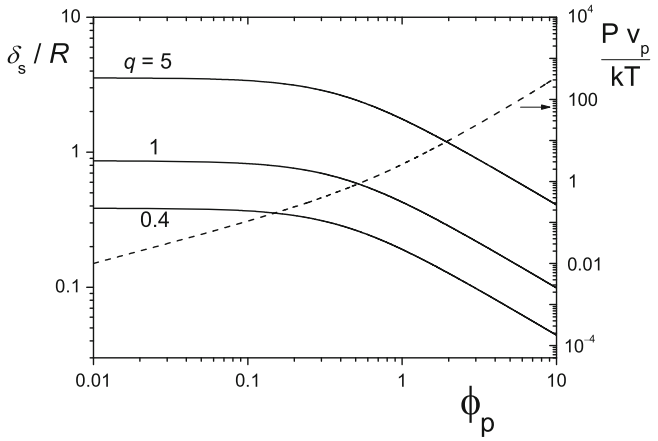

Fig. 4.9 Depletion thickness (*solid curves*) for three size ratios as indicated and osmotic pressure (*dashed curve*) of polymer chains in the excluded volume limit as a function of the relative polymer concentration

Although higher order C_i terms are yet unknown it is clear that the curvature effects for excluded volume and ideal chains in (4.22) and (4.23) are rather similar.

These expressions for δ/R can be easily approximated as the simple accurate power-laws [39]

$$\begin{aligned} \frac{\delta_{0,s}}{R} &= 0.938 q^{0.9} \quad \Theta\text{-solvent} \\ &= 0.865 q^{0.88} \quad \text{good solvent.} \end{aligned} \tag{4.24}$$

These power-laws hold for a wide range of q-values [39], see for instance Fig. 4.5. In combination with the concentration dependence (4.21), this approximation leads to

$$\begin{aligned} \frac{\delta_s}{R} &= 0.938\left(q^{-2} + 6.02 q^{-2}\phi_p^2\right)^{-0.45} \quad \Theta\text{-solvent} \\ &= 0.865\left(q^{-2} + 3.95 q^{-2}\phi_p^{1.54}\right)^{-0.44} \quad \text{good solvent,} \end{aligned} \tag{4.25}$$

expressing the concentration- and curvature dependence of the depletion thickness around a sphere in a solution with interacting polymers under Θ-solvent and good solvent conditions. For the good solvent situation the depletion thickness is plotted in Fig. 4.9 for three q-values.

4.3.3 Osmotic Pressure of Polymer Solutions

In the limit of dilute polymer solutions the osmotic pressure is given by the ideal Van't Hoff law $P_{\text{id}} = n_b kT$ (see Sect. 2.2). For the osmotic pressure of non-ideal polymers in solution one can write down a general virial series

$$\frac{P}{n_b kT} = 1 + A_2 n_b + A_3 n_b^2 + \cdots, \tag{4.26}$$

where A_2 and A_3 are the second and third osmotic virial coefficients. Note that we use B_i for colloids (see for instance (1.29), Sects. 2.3.1 and 3.2.1) and A_i for polymers. The second virial coefficient is proportional to the effective excluded volume per polymer segment: $A_2 \sim \mathbf{v}$. In the good solvent limit $\mathbf{v} = 1$ this excluded volume equals the physical volume of a segment, so A_2 attains a finite positive value. In a bad solvent $A_2 < 0$. For polymer chains in a Θ-solvent the excluded volume of a segment is exactly compensated by the attractions between the segments and $A_2 \equiv 0$; in a Θ-solvent Van 't Hoff's law $P = n_b kT$ holds up to quadratic order in n_b. Higher-order virial coefficients A_3 and beyond are non-zero, so for higher polymer concentrations deviations from ideal behaviour are found also in a Θ-solvent.

Perturbation expansions in terms of the excluded volume in principle yield the second and higher order osmotic virial coefficients [38, 50]. This procedure becomes rather cumbersome for A_4 and higher-order coefficients and established scaling exponents [40] for the semi-dilute polymer concentration regime cannot be reproduced in a virial expansion.

In fact, in the semi-dilute case the picture is simple; the chains overlap to such a degree that the characteristic length scale is determined by the correlation length ξ rather than the coil size set by the chain length M. The corresponding volume ξ^3 is denoted as a blob. The osmotic pressure can then be viewed upon as an ideal gas of blobs, so $P_{\rm sd} \sim \xi^{-3}$, with the number of blobs $\sim \xi^{-3}$. Therefore the scaling result becomes $P_{\rm sd}/kT \sim \phi_p^{3\gamma}$.

A convenient expression that enables to describe both the dilute and semi-dilute polymer concentration regimes follows from a simple additivity rule $P = P_{\rm id} + P_{\rm sd}$. This additivity follows from the Flory–Huggins theory [37] for a Θ-solvent but appears to be an excellent approximation for good solvents as well [41]. This leads to the following expression for the ratio $P/P_{\rm id}$

$$\frac{P}{P_{\rm id}} = \frac{P v_p}{\phi_p kT} = 1 + \zeta \phi_p^{3\gamma - 1}, \tag{4.27}$$

with

$$\begin{aligned} \zeta &= 4.10 \quad \Theta\text{-solvent} \\ &= 1.62 \quad \text{good solvent.} \end{aligned} \tag{4.28}$$

The numerical coefficient ζ follows from Flory–Huggins theory for a Θ-solvent and from RGT for a good solvent. Equation (4.28) turns out to be extremely accurate in comparison with experimental and computer simulation data [41]. For a good solvent the result is plotted in Fig. 4.9. Under Θ-solvent conditions Flory–Huggins theory reproduces (4.27).

The osmotic compressibility that we need in (4.4) now follows straightforwardly

$$\begin{aligned}\frac{\partial(Pv_p/kT)}{\partial\phi_p} &= 1 + 3\gamma\zeta\phi_p^{3\gamma-1} \\ &= 1 + 12.3\phi_p^2 \qquad \Theta\text{-solvent} \\ &= 1 + 3.73\phi_p^{1.31} \quad \text{good solvent.}\end{aligned} \tag{4.29}$$

Exercise
Derive (4.29) from (4.27), (4.28) and (4.14).

4.3.4 Phase Diagrams

Below we summarize the results for the osmotic pressure and depletion thickness and subsequently we consider the implications for the phase behaviour.

4.3.4.1 GFVT Ingredients; Θ-Solvent

For polymer chains in a Θ-solvent the scaling exponent γ takes its mean-field value $\gamma = 1$. The polymer concentration derivative of the reduced osmotic pressure follows from (4.29) as

$$q^3 \frac{\partial \widetilde{P}}{\partial \phi_p} = 1 + 12.3\phi_p^2, \tag{4.30}$$

and the ratio between the depletion thickness and the colloid radius is

$$\frac{\delta_s}{R} = 0.938\left(q/\sqrt{1 + 6.02\phi_p^2}\right)^{0.9}. \tag{4.31}$$

Equation (4.31) follows directly from (4.25).

4.3.4.2 GFVT Ingredients; Good Solvent

The De Gennes scaling exponent γ equals 0.77 under good solvent conditions. Therefore, we have from (4.29)

$$q^3 \frac{\partial \widetilde{P}}{\partial \phi_p} = 1 + 3.73\phi_p^{1.31} \tag{4.32}$$

and from (4.25)

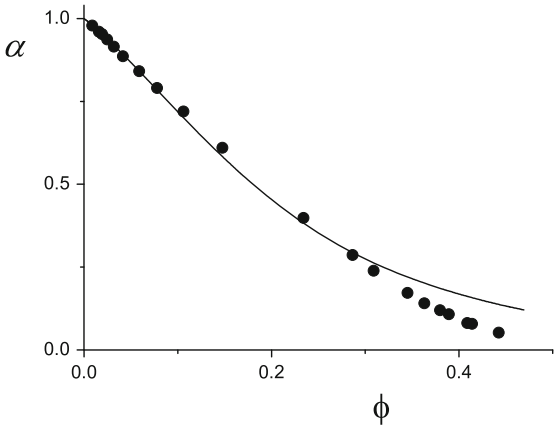

Fig. 4.10 Free volume fraction α as a function of colloid volume fraction for $q = 1.05$. GFVT (*dashed curve*) compared to Monte Carlo computer simulations (data points) [51]

$$\frac{\delta_s}{R} = 0.865\left(q/\sqrt{1+3.95\phi_p^{1.54}}\right)^{0.88}. \tag{4.33}$$

Note that in contrast to the classical FVT [18], $\partial\widetilde{P}/\partial\phi_p$ and δ_s/R in (4.30)–(4.33) now depend on the polymer concentration ϕ_p.

In Fig. 4.10 we compare the free volume fraction α calculated from (4.6), in the good solvency limit with δ_s/R in (4.7) from (4.33), with Monte Carlo simulation results of Fortini et al. [51] for $q = 1.05$ along the binodal gas-liquid curve. Except for some deviation at large colloid volume fractions the agreement is excellent.

4.3.4.3 GFVT Phase Behaviour

We can now compute the phase diagrams for hard spheres plus interacting polymers using the general expression (4.4) and its ingredients by computing the chemical potential $\widetilde{\mu} = (\partial\widetilde{\Omega}/\partial\phi)$ and total pressure $\widetilde{P} = \phi\widetilde{\mu} - \widetilde{\Omega}$,

$$\widetilde{\mu} = \widetilde{\mu}^0 + \int_0^{\phi_p^R} g\left(\frac{\partial\widetilde{P}^R}{\partial\phi_p^{R'}}\right)\mathrm{d}\phi_p^{R'}, \tag{4.34}$$

$$\widetilde{P} = \widetilde{P}^0 + \int_0^{\phi_p^R} h\left(\frac{\partial\widetilde{P}^R}{\partial\phi_p^{R'}}\right)\mathrm{d}\phi_p^{R'}. \tag{4.35}$$

Here g and h are given by (3.48) and (3.49) with a, b and c defined in (4.7). Coexistence curves then follow from (3.41) and (3.42).

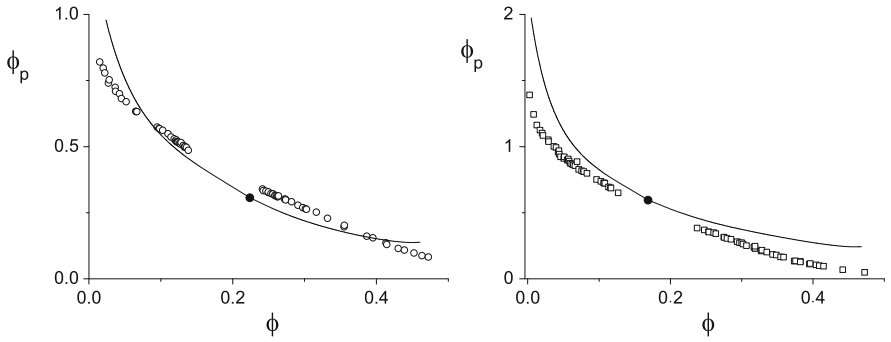

Fig. 4.11 Gas–liquid coexistence curves for hard spheres plus interacting polymers in a good solvent (Gaussian core model) from Monte Carlo simulation [52] data for $q = 0.67$ (*left*) and $q = 1.05$ (*right*) versus GFVT predictions (*curves*). The GFVT critical point is marked by a *filled circle*

We compare gas–liquid coexistence curves from GFVT in the good solvent limit with Monte Carlo simulation results of Bolhuis et al. [52] in Fig. 4.11 for $q = 0.67$ and 1.05. It is clear GFVT is capable of predicting the location of the phase boundaries reasonably well.

The critical end points for Θ-solvent and good solvent conditions are rather close to the one for penetrable hard spheres:

$$\begin{aligned} q_{\text{cep}} &= 0.328 \quad \text{penetrable hard spheres} \\ &= 0.337 \quad \Theta\text{-solvent} \\ &= 0.388 \quad \text{good solvent.} \end{aligned} \tag{4.36}$$

We turn back to Fig. 4.3 and make a comparison of the experimental phase diagrams with GFVT under good solvent conditions. We show the experimental data in Fig. 4.12 and inserted GFVT predictions (good solvency) for the binodals as the curves and the triple triangle as filled region. GFVT is capable of accurately describing the experimental equilibrium phase diagrams for $q = 0.57$ and 1, and constitutes a major improvement with respect to FVT for $q > 0.5$. Especially for $q = 1$ GFVT proves to be very useful since FVT completely fails to quantitatively describe the phase diagram here.

For $q = 0.57$ the composition of the colloidal liquid that coexists with a colloidal gas and crystal was determined by Moussaïd et al. [26]. In Table 4.1 we compare these data with FVT and GFVT predictions. The experimental colloid volume fraction and polymer concentration clearly deviate significantly from FVT. Especially the polymer concentration of the coexisting colloidal liquid phase is about 30 times larger than the FVT prediction. Generalized free volume theory gives a much better prediction of the composition, especially if the polymers are assumed to be in a good solvent.

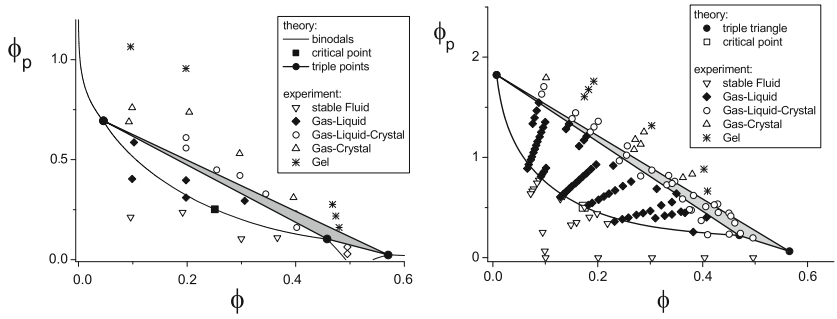

Fig. 4.12 State diagrams of colloid–polymer mixtures for $q = 0.57$ (*left*) and $q = 1.0$ (*right*) as in Fig. 4.3 but now compared to theoretical GFVT predictions (*curves*) of Fleer and Tuinier [39]. Experimental data: PMMA spheres plus polystyrene polymers in *cis*-decalin [16, 17]

Table 4.1 Liquid composition of the triple point at $q = 0.57$

	ϕ	ϕ_p
FVT	0.489	0.0037
GFVT Θ	0.470	0.048
GFVT good	0.452	0.108
Experiment	0.444	0.1

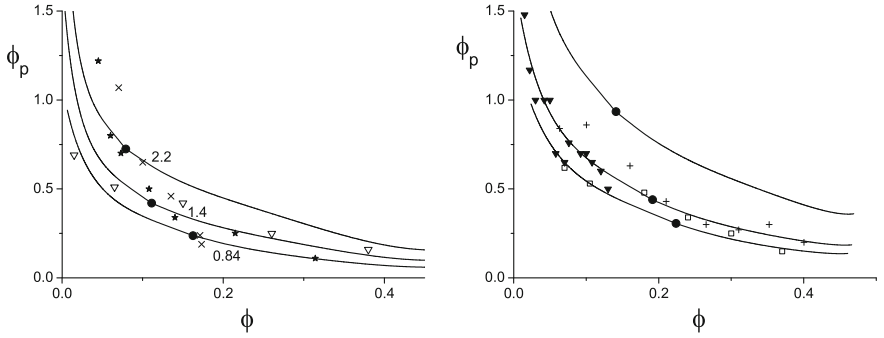

Fig. 4.13 Comparison of experimental gas–liquid coexistence binodals (data) compared to GFVT (*curves*). *Left panel*: spherical colloids mixed with polymer chains in a Θ-solvent for $q = 0.84$ (*open triangles*, [20]), 1.4 (*stars*, [21]) and 2.2 (*crosses*, [21]). *Right panel*: colloidal spheres plus polymers in a good solvent for $q = 0.67$ (*open squares*, [20]), 0.86 (*inverse filled triangle*, [54]) and 1.4 (*pluses*, [20])

One might think GFVT is useful only for describing the phase diagrams of well-defined experimental hard-sphere/random coil systems (such as PMMA + PS) or phase equilibria from computer simulations. GFVT, however, also helps to give reasonable predictions for many other colloid plus non-adsorbing polymer mixtures [39]. In Fig. 4.13 we compare GFVT binodals for gas–liquid coexistence

with experimental data on colloid–polymer mixtures under Θ-solvent (left panel) and good solvent (right panel) conditions. The order of magnitude of the predicted binodals is accurate in all cases. Sometimes the agreement is nearly quantitative. Aspects that give deviations are related to polymer polydispersity and the non-hard-sphere character of the colloidal particles. The colloids may for instance be somewhat sticky, or they may repel one another to some extent due to anchored brushes that are not very short or due to repulsive double layer interactions. In principle it is possible to include these effects into GFVT [53] but we shall not consider this here.

Exercise
In what directions will gas–liquid binodals and fluid–solid binodals at low ϕ shift in case of an additional weak short-ranged double layer repulsion between the spheres?

4.3.4.4 GFVT in the Semi-Dilute Regime

We now consider the large q-limit, which is the regime where ϕ_p^R along the binodals exceeds unity, so we have semi-dilute polymer solutions. The characteristic length scale in semi-dilute polymer solutions is ξ which scales as (4.15), $\xi/R_g \sim \phi_p^{-\gamma}$. For colloid–polymer mixtures this expression can be rewritten in terms of $\xi/R = q\xi/R_g$ to

$$\phi_p q^{-1/\gamma} \sim \left(\frac{\xi}{R}\right)^{-1/\gamma}. \tag{4.37}$$

It is important to note that ξ is independent of R_g. This implies the right-hand side of (4.37) is independent of q. Therefore also $\phi_p q^{-1/\gamma}$ is independent of q, yielding

$$\phi_p \sim q^{1/\gamma}. \tag{4.38}$$

For large q values it is therefore efficient to introduce a parameter Y as a rescaled polymer concentration:

$$Y = \phi_p q^{-1/\gamma}. \tag{4.39}$$

In the large q-limit Y is a constant (independent of q). It follows that $\phi_p = Yq^{1/\gamma}$ diverges as $q^{1/\gamma} = q^{1.3}$ for large q under good solvent conditions. This predicted $q^{1.3}$ scaling [55] of large q binodals is corroborated by simulation [56] and experiment [57, 58] as we demonstrate in Fig. 4.14, where in the left panel we show rescaled computer simulation data for the gas–liquid binodal [56], for hard

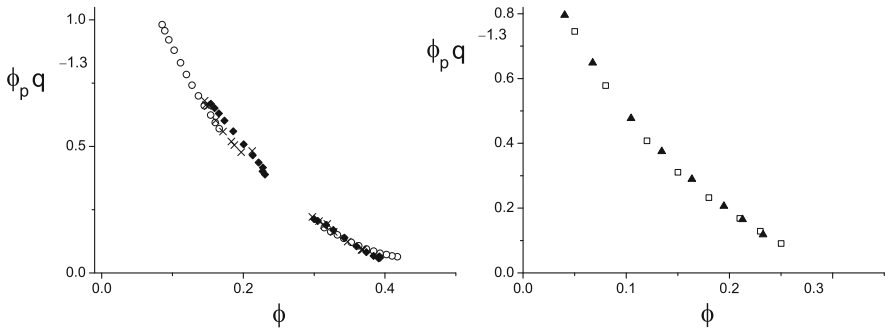

Fig. 4.14 Scaling of (*left panel*) Monte Carlo computer simulation results (see Fig. 1.22) for $q = 3.86$ (*open circles*), 5.58 (*crosses*) and 7.78 (*filled diamonds*) by Bolhuis [56] and experimental results (*right panel*) on (AOT) micro-emulsion droplets plus free polyisoprene polymer chains ($q = 10$ (*open squares*) and $q = 16$ (*filled triangles*)) by Mutch et al. [57, 58] for the gas–liquid coexistence in the protein limit regime

spheres plus polymer chains in the good solvent limit (long chains consisting of hard spherical segments). The data are binodal points from Fig. 1.22 for $q > 3$; in the rescaled form they collapse onto a universal curve. Clearly, in the colloid limit, where Y depends on q, this scaling does not apply.

In the right panel of Fig. 4.14 we plotted experimental data for the gas–liquid coexistence for two large q values. Also these data collapse onto a single curve after rescaling according to (4.39). Hence, this predicted $q^{1.3}$ scaling is corroborated by both simulations and experiments.

The parameter Y is a convenient normalised polymer concentration which has the important property that it becomes independent of the size ratio q in the high q limit [39, 55], where the polymer concentrations along the binodals are in the semi-dilute regime. The Y values along the binodals always remain order unity. Then $\delta = \xi \sim \varphi^{-\gamma}$ [40], which does not depend on R_g. Hence, δ/R does not depend on $q = R_g/R$, and δ/R reaches a constant (q-independent) level.

Analytical approximations for the phase behaviour of colloid–polymer mixtures can be found in [39] for those who need simple, approximate yet reasonably accurate descriptions of equilibrium phase diagrams. Using Y instead of ϕ_p turns all phase diagrams to more universal ones with a polymer concentration variable that is always of order unity for the relevant characteristic parts of the phase behaviour.

4.4 Effects of Polydispersity and Charges

Throughout this book we focus on monodisperse colloidal particles (and depletants) that are uncharged for didactic purposes. Accounting for polydispersity and/or charges complicates the theoretical descriptions dramatically. Still, we pay attention here to some results that have been obtained on these issues in order to get some

feeling of how polydispersity and charges affect depletion interactions and the resulting phase behaviour.

4.4.1 Polydispersity Effects

The particles and polymers in any real experiment have a finite polydispersity. The influence of polydispersity on depletion interaction and phase behaviour was investigated by extending existing approaches. The original AO theory for two parallel plates immersed in a solution of non-adsorbing ideal chains [59] could be extended to involve polymer size polydispersity [60], still providing analytical expressions for the interaction between the plates. This work was extended towards the interaction between two spheres in a solution of polydisperse ideal chains. It followed the influence of polydispersity on the interaction is rather weak. Even a polydispersity of 70% (standard deviation) only increases the attraction by less than 20%. Goulding and Hansen [61] computed the interaction potential between two spheres in a polydisperse bath of penetrable hard spheres (polydisperse phs model). Up to a polydispersity characterized by a standard deviation of 30% there is hardly an effect on the somewhat increased range and slightly deeper potential between the hard spheres. Above 30% polydispersity the effects become more significant.

Mao [62] considered the interaction between two spheres in a bath of polydisperse small hard spheres using the Derjaguin approximation. The accumulation effects due to non-adsorbing small hard spheres (see Sect. 2.3) become much less pronounced with increasing polydispersity. So, although it is known that non-adsorbing polymers contribute to an extremely weak repulsion at high polymer concentration [63, 64] it is expected that this weak repulsion is even dampened due to polydispersity as is the case for hard spheres. Goulding and Hansen [61] used DFT theory to investigate the case of depletion due to small hard spheres. Their findings correlate with Mao's analytical results but also show that Mao's Derjaguin approximation already deviates from the DFT result for a size ratio of 5.

Sear and Frenkel [65] investigated the phase behaviour of a colloid–polymer mixture by treating the polymers as penetrable hard spheres (phs) using a distribution of polydisperse phs. Their calculations demonstrated that phase separation leads to size fractionation of the phs. FVT was extended to as to model polydispersity by replacing the monodisperse polymers with bidisperse polymers by Warren [66]. Warren found that polydispersity enhances the tendency to phase separate when a bidisperse polymer mixture is compared to a monodisperse mixture having identical number-averaged molar masses. It followed that the location of the binodals of the colloid–bidisperse polymer mixture is almost identical to that of a colloid–monodisperse polymer mixture when the weight-averaged molar mass of the bidisperse mixture is taken as the monodisperse molar mass.

The phase behaviour of mixtures of monodisperse hard spheres and polydisperse ideal polymers has been investigated using original FVT [67]. At fixed mean

polymer size, polydispersity favours gas–liquid coexistence and delays the onset of fluid-solid separation. On the other hand, systems with different size polydispersity but the same mass-averaged polymer chain length have nearly polydispersity-independent phase diagrams. The influence of polymer polydispersity on the colloidal gas–liquid phase coexistence of *interacting* polymers plus spherical colloids is a complicated issue that has only been investigated using TPT by Paricaud et al. [68]. It would be interesting to study polydispersity effects in a mixture of hard spheres and interacting polymers within a framework that also allows studying the crystalline phase.

Computer simulations show that crystallization of hard spheres does not occur above a polydispersity of 11.8% in diameter [69]. Pusey [70] provided a simple argument suggesting that the maximum polydispersity $\sigma_{\max}$ depends on the close packing and melting volume fractions $\phi_{\rm cp}$ and ϕ_m, respectively,

$$\sigma_{\max} = \left(\frac{\phi_{\rm cp}}{\phi_m}\right)^{1/3} - 1. \tag{4.40}$$

Exercise
Rationalize this expression (see Sect. 3.2).

For hard spheres with $\phi_{\rm cp} = 0.74$ and $\phi_m = 0.545$, (4.40) provides $\sigma_{\max} = 0.11$, so 11%. In dispersions with large q, small colloids are needed in practice because it is difficult to synthesize model polymer chains with sizes > 200 nm in solution. Small colloids (< 100 nm) are often quite polydisperse. Therefore, systems studied with large q in general tend to be relatively polydisperse in colloidal sphere size. This implies that in experimental systems with large q, crystallisation is suppressed or absent.

The effect of particle polydispersity on the phase behaviour of mixtures of polydisperse hard spheres and ideal polymers has also been explored [71], also based on original FVT. Even modest polydispersities ($< 10\%$) can significantly change the phase diagram topology by introducing a host of new, multiphasic equilibria involving multiple solid phases. In practice, such multiphasic equilibria may show up as kinetic effects preventing the system reaching equilibrium. The non-equilibrium behaviour observed at higher polymer and particle concentrations may partly be due to this effect. Colloidal gas–liquid phase separation is however less sensitive to polydispersity [67].

4.4.2 The Interplay of Depletion and Charges

Many theories and depletion studies with model systems are based on hard-sphere like colloidal particles. In practice, many stable dispersions containing spherical

colloids consist of particles that are not 'pseudo-hard' but which can be characterised by a pair potential containing an additional soft repulsive tail. An example is a stable dispersion of charged colloids in a polar solvent. Here double layer interactions provide a soft repulsive interaction between the particles (Sect. 1.2.2). In case of an aqueous salt solution as solvent, adjusting the salt concentration influences the stability of a dispersion of charged colloids mixed with a neutral depletion agent [72–74]. Patel and Russel [75] studied the phase behaviour of mixtures of charged polystyrene latex colloids and dextran as (neutral) polymer chains and reported a significant shift towards higher polymer concentrations of the fluid–fluid binodal curve as compared to predictions for neutral polymer chains mixed with hard spheres.

Grinberg and Tolstoguzov [72] presented generalised phase diagrams of proteins mixed with neutral non-adsorbing polysaccharides in aqueous salt solutions. The miscibility or compatibility was shown to increase when the ionic strength of the solvent was lowered. The compatibility especially increased below 0.5 M. Finet and Tardieu [73] studied the stability of solutions of the lens protein α-crystallin. Adding an excess of salt to this system does not destabilise the protein dispersion. Hence, it follows that the effective attractions between the proteins are absent or are very weak in the case of screened charges. Adding PEG however induces significant attractions [73], and results in a shift of the liquid–liquid phase transition to higher temperatures [76]. Adding excess salt and PEG induces instant phase separation [73]. A similar synergetic effect of salt and PEG was found in aqueous solutions of (spherical) brome mosaic virus particles [74]. Royall et al. [77] studied the influence of double repulsion on depletion forces using confocal microscopy. In conclusion, the trend found in experimental studies on mixtures of charged 'colloids' plus neutral polymers is that the miscibility is, as expected, increased upon decreasing the salt concentration, i.e., increasing the range of the double layer repulsion.

An early theoretical depletion interaction study with polyelectrolytes as depleting agents was made by Böhmer et al. [78] who used the self-consistent field method of Scheutjens and Fleer. For high salt concentrations, the polymer concentration dependence of the depletion layer thickness matches with that of an uncharged polymer in solution. Below a salt concentration of 1 mol/L the depletion layer thickness starts to decrease with increasing polyelectrolyte concentration at lower polymer concentration. At low salt concentrations a significant repulsive barrier in the potential between two uncharged parallel flat plates was found.

A force balance theory on the Derjaguin approximation level for the interaction between two spheres in dispersion with macromolecules (regarded as hard spheres), with (like) charges on them was developed by Walz and Sharma [79]. For low concentrations of the 'macromolecules' the interaction potential curve is attractive for any salt concentration. The value of the potential at contact is increased as the Debye length increases or if the charge density on the large colloidal spheres (same sign as the 'macromolecules') increases. The range of the potential increases as the Debye length increases. At higher concentrations of the

small particles a repulsive barrier in the interaction potential curve appears for sufficiently large size ratio of small and large colloid and sufficient Debye lengths. This might lead to depletion stabilization. In the model of Walz and Sharma [79] the polymers are modeled however as hard spheres. It is therefore questionable whether this method applies to colloid–polymer mixtures where the polymer–colloid repulsion is soft.

There are only a few theoretical studies on mixtures of colloids with a screened-Coulomb repulsion mixed with neutral or charged polymer chains. Ferreira et al. [80] made a PRISM analysis up to the level of the pair interaction and computed gas–liquid spinodal curves from the effective colloid–colloid structure factor. Denton and Schmidt [81] proposed a simple theory yielding the colloidal gas–liquid binodal curve for mixed charged spheres plus free neutral polymer chains, described as penetrable hard spheres. Fortini et al. [82] extended free volume theory to account for a short-ranged soft repulsion between the spherical colloids, allowing a description of the full phase diagrams. They also made Monte Carlo simulations and the results were found to agree quite well with the extended free volume theory. It was found that especially the colloidal fluid–solid coexistence is sensitive to the screened-Coulomb repulsion.

Exercise
What happens to the miscibility region of a stable colloidal fluid with added non-adsorbing polymers upon adding a screened double layer repulsion between the spheres?

The work of Fortini et al. [82] was later extended towards highly screened charged spheres mixed with *interacting* polymers [53]. Zhou et al. [83] have shown this generalized free volume theory (GFVT) including short-ranged soft repulsion is capable of quantitatively describing the depletion-induced phase separation in mixtures of charged silica particles and non-adsorbing polystyrene polymer chains in dimethylformamide polymer (Θ-solvent conditions). They varied both the range of the double layer repulsion and the size ratio q.

Stradner et al. [84] and Sedgwick et al. [85] considered mixtures of charged spherical colloids with a long-ranged double layer repulsion mixed with very short polymer chains that induce a short-ranged depletion attraction. In such systems small equilibrium clusters are formed that can be described theoretically [86] or using Molecular Dynamics computer simulations [87]. The cluster size follows from a competition between short-ranged depletion attraction, that favours cluster growth, and long-ranged repulsion, promoting small aggregates.

Some aspects that could be relevant have not yet been incorporated in the theory for the phase behaviour. A first issue is the effect of gradients in permittivity. Croze and Cates [88] demonstrated that even the depletion zones caused by neutral polymers are affected by charged surfaces. The electrical field present between like-charged surfaces polarize the neutral polymer chains because of their

(usually) low permittivity. This enhances polymer depletion and increases the screening of double layer interactions.

The situation gets more complicated when the free polymers are (like-)charged as well. Work of Israelachvili et al. [89] revealed that the addition of free polyelectrolyte mainly decreases the effective Debye length in the aqueous salt solutions, leading to a decrease in the double layer repulsion.

Odijk [90] incorporated the effect of (like) charges on both polymer and colloid in his theory [91] for two small colloidal spheres immersed in a polyelectrolyte solution. He related the effective depletion radius for small charged spheres, immersed in a solution with oppositely charged polyelectrolytes to the Debye length, the effective number of charges on the protein, the hard sphere radius and the Kuhn length. When the effective depletion radius becomes larger than the correlation length of the polymer solution, phase separation due to depletion is expected.

In summary, it seems that at high salt concentrations like charges on polymers and colloids do not seem to strongly affect the depletion-induced attraction between colloids due to polymers. At low ionic strength however the situation becomes quite complicated and detailed theories still have to be developed that enable a computation of the stability of such systems. It is clear that there is much work left to be done on the role of (charged) depletants in (charged) systems before we arrive at a complete picture.

4.5 Phase Separation Kinetics and Long-Lived Metastable and Nonequilibrium States

So far we have considered the equilibrium phase behaviour in colloidal suspensions resulting from depletion interactions. Due to the tuneability in terms of range and strength of the depletion interaction we observed, as compared to atomic and molecular systems, new and fascinating phase behaviour such as a metastable fluid–fluid phase separation and a three-phase gas–liquid–crystal region. The predictions of phase diagrams are, however, not always realized. Systems often become trapped in metastable nonequilibrium gel and glass states. In several cases the end products strongly depend on the starting position in the phase diagram and discrepancies between predictions and actual observations are due to the intricacies of the dynamics of phase transitions. In this section we briefly consider the phase separation process and the nonequilibrium states in colloid–polymer mixtures. Taking advantage of the (large) length scales and (long) time scales involved allows us to reveal some of the secrets of the complex pathways involved in the formation of gels and glasses. Below we separate the discussion in systems where the ratio of the polymer-to-colloid size q is larger than 0.3 in Sect. 4.5.1 and where q is smaller than 0.3 (relatively large colloidal spheres) in Sect. 4.5.2.

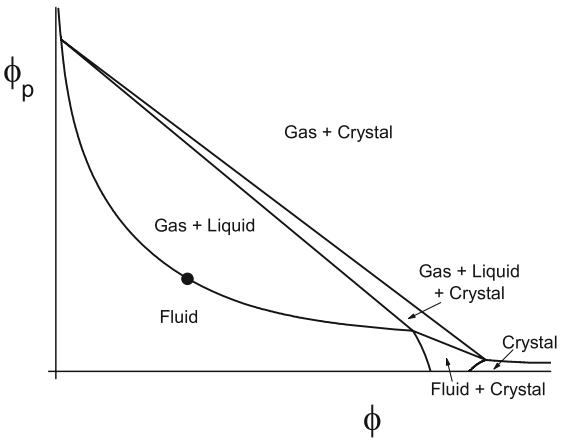

Fig. 4.15 Schematic phase diagram of a colloid–polymer mixture for large q. *Full curves* are binodals. The different phase states are indicated

4.5.1 $q > 0.3$

Quantitative predictions of demixing kinetics in colloid–polymer mixtures are fairly complicated but frequently insight of demixing mechanisms [92] can be obtained by careful inspection of the equilibrium phase diagrams of colloid–polymer mixtures. The equilibrium phase diagram for $q > 0.3$ as follows from (G)FVT is summarized in Fig. 4.15. In absence of polymer a fluid–crystal phase coexistence is found. At $\phi < 0.49$ a colloidal fluid phase exists. As ϕ_p is increased this fluid becomes unstable above a certain concentration. Then a phase separation occurs towards colloidal gas–liquid coexistence. At high ϕ_p a colloidal gas coexists with a colloidal crystal. Following Gibbs' phase rule there must be a three-phase gas–liquid–crystal coexistence region in between within which is indeed predicted and observed experimentally.

4.5.1.1 Gas–Liquid Demixing

We first focus on the phase separation in the gas–liquid region. Above the spinodal curve, long wavelength fluctuations in colloid or polymer concentration lower the free energy. After a quench in this unstable two-phase region, spontaneous long wavelength density fluctuations are no longer stable with respect to a homogeneous distribution. Concentration fluctuations with large wavelengths have a stronger thermodynamic driving force, whereas for short wavelengths the diffusion process is faster. This competition, which results in a fastest growing mode is characteristic for spinodal decomposition [93–95]. In colloidal systems, the time and length scales involved allow probing the relevant phenomena by small-angle light scattering and optical microscopy [19, 96].

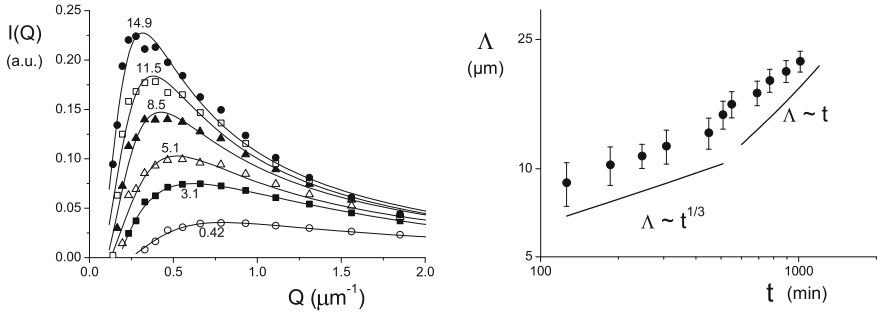

Fig. 4.16 *Left panel*: scattered intensity as a function of the wave vector Q of a dispersion of unmixing whey protein colloids ($R \approx 27\,\text{nm}$) mixed with exocellular polysaccharides ($R_g = 86\,\text{nm}$; $q = 3.2$) [19]. The time after mixing is indicated (in hours). *Right panel*: log–log plot of the characteristic length scale $\Lambda = 2\pi/Q_m$ obtained from the $I(Q)$ curves as a function of time. The diffusive growth (4.41) and viscous hydrodynamic growth (4.42) scaling regimes are indicated as *straight lines*

In Fig. 4.16 (left panel) we plot the measured scattered intensity $I(Q)$ during unmixing of a dispersion of whey protein colloids ($R = 27\,\text{nm}$) mixed with polysaccharides ($R_g = 86\,\text{nm}$), so $q \approx 3$. The overall values of the scattered intensity increase with time, implicating larger structures are being formed. At each time frame the scattered intensity passes through a maximum as a function of Q. The value of the wave vector Q_m corresponding to this maximum decreases with time corroborating an increase of the characteristic length scale $\Lambda = 2\pi/Q_m$. In Fig. 4.16 (right panel) we present this length scale Λ as a function of time. In this figure two regimes can be distinguished:

$$\Lambda \sim t^{1/3} \tag{4.41}$$

and

$$\Lambda \sim t. \tag{4.42}$$

These two time scales are characteristic for the diffusive growth (4.41) and viscous hydrodynamic growth (4.42) regimes in spinodal decomposition [97].

As indicated above the phase separation process can also be studied using optical microscopy as has been done by Verhaegh et al. [96]. They observed spinodal decomposition in a well-defined model colloid–polymer mixture of silica spheres in cyclohexane with dissolved polydimethyl siloxane chains of $q \approx 1$, and found similar results to those plotted in Fig. 4.16. Their findings agree with the picture sketched above and the characteristic length scale Λ follows the regimes of (4.41) and (4.42).

The spinodal decomposition can be studied in much more detail using confocal scanning laser microscopy (CSLM). Aarts et al. [98] studied the phase separation kinetics of a PMMA colloid plus PS polymer mixture in decalin with $q = 0.56$. In Fig. 4.17 typical spinodal structures are observed that coarsen in time.

Fig. 4.17 CSLM images (each side is 1,400 μm) of a phase separating polystyrene polymers mixed with fluorescently labeled PMMA spheres exhibiting the typical spinodal structure. The images correspond to $t = 3$ s (*left*), 11 s (*middle*) and 22 s (*right*) after homogenization. These images were kindly provided by D.G.A.L. Aarts, Oxford University, UK. See also the movies on http://www.njp.org.

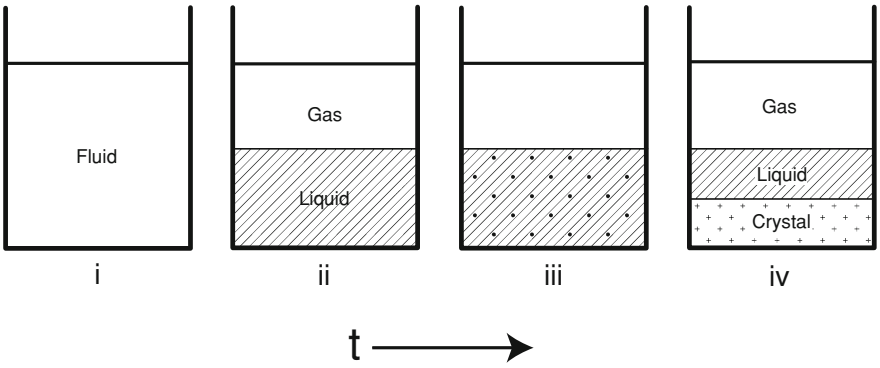

Fig. 4.18 Time evolution of phase separation kinetics in the three-phase region as observed by Poon et al. [99]

4.5.1.2 Demixing in the Three-Phase Region

We now consider the phase separation process in the three-phase colloidal gas–liquid–crystal region. This case has been analyzed experimentally and theoretically in great detail by Poon et al. [99]. By consideration of the free energy landscape they were able to distinguish several pathways for this phase separation process. The pathways were shown to depend on the location of the starting position in the three-phase region. In a large central section of the three-phase triangle (see Fig. 4.15). Poon et al. predicted and observed the scenario sketched in Fig. 4.18. Initially, the sample is a colloidal fluid (i) that phase separates into a polymer-rich colloidal gas and a colloidal liquid that is dilute in polymer (ii). This gas–liquid coexistence, however, is metastable. Soon after the formation of a

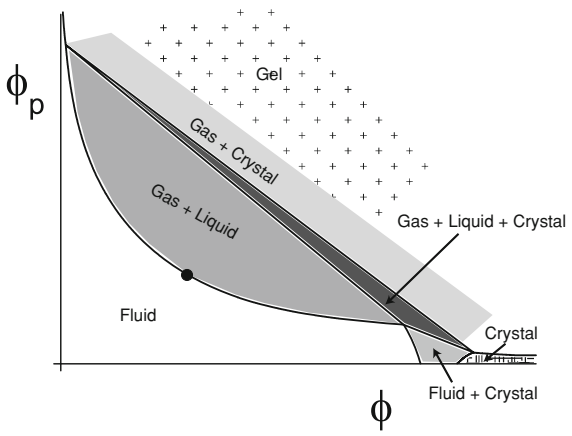

Fig. 4.19 State diagram of a colloid–polymer mixture for large q. The different observed equilibrium and long-lived nonequilibrium phase states are indicated

(sharp) gas–liquid interface, 'flashes' of light appear from the liquid (lower) phase (iii). These flashes are caused by homogeneously nucleating and growing crystallites. Subsequently, the crystallites sink to the bottom, giving rise to the final gas–liquid–crystal coexistence (iv). This is a classic example of a multi-stepped kinetic pathway.

4.5.1.3 Depletion Interaction and Gelation

Finally, we consider the large q situation at high polymer concentrations. Here kinetically arrested (gel or glass) states are observed above $\phi_p \approx 1$ $(q = 0.57)$ and $\phi_p \approx 2$ $(q = 1)$ (see Fig. 4.12). From (2.21) it follows that a contact potential of about -3 kT is required to enter the gel region. We compare this with a phase diagram of particles with a Lennard-Jones (LJ) interaction with minimum of the potential ε that can be used to describe several atomic and molecular systems. The attraction of about 3 kT implies $kT/\varepsilon \approx 1/3$. Inspection of the LJ phase diagram from simulations [100, 101] shows that this corresponds to a rather deep quench into the unstable region. In molecular or atomic systems such a strength of attraction correlates with severe undercooling. In fact, one would then expect the system gets trapped into long-lived metastable states. These states can be realized quite easily in colloid–polymer mixtures as compared to atomic systems; a huge instantaneous temperature jump is rather difficult to achieve compared to mixing a colloidal dispersion with a semi-dilute polymer solution.

In summary, the observed state diagram for large q is sketched in Fig. 4.19. Across the three-phase region a narrow concentration regime was found of equilibrium fluid–crystal phase behaviour [16, 17], see also the discussion near Fig. 4.3. The only difference with Fig. 4.15 is that an arrested state (a gel) is found at high polymer concentrations ϕ_p (or large depletion attraction) [19] (P.A. Smith, S.U.

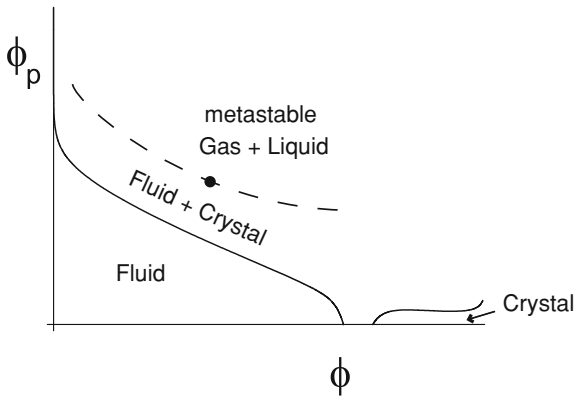

Fig. 4.20 Schematic equilibrium phase diagram of a colloid–polymer mixture for small q. *Full curve* is the fluid–solid coexistence curve, *dashed curve* is the metastable gas–liquid coexistence region

Egelhaaf, W.C.K. Poon, personal communication). The appearance of the particle gel can be explained as follows. When the attraction becomes sufficiently strong the particles stick irreversibly and form a space-spanning network. In such cases the phase separation process will not reach its equilibrium state but rather a nonequilibrium gel-like state is encountered. This has been well-studied for small q (see Sect. 4.5.2) but its appearance for $q > 0.3$ has not received much attention yet.

In practice many phase diagrams at larger q do not exhibit crystalline phases because the colloidal spheres are usually too polydisperse. At $\phi \approx 0.58$ there must be a glassy state. The influence of a depletion attraction on this state has not yet been studied for high q.

4.5.2 $q < 0.3$

At first sight the equilibrium phase diagram at low q, sketched in Fig. 4.20, appears to be dull as compared to the phase diagram for $q > 0.3$ in Fig. 4.15. However, while for large q as a rule the predictions of the phase diagram are realized, for small q nonequilibrium and metastable states dominate in large regions of the state diagram. A premonition that the pathways involved in the phase separation for small q can be intricate is provided by the presence of a metastable gas–liquid phase separation in the fluid–crystal domain of the phase diagram.

In order to sample these intricacies we consider the phase separation pathways upon increasing the polymer concentration at three colloid volume fractions $\phi, 0.02$ (low ϕ), $0.1-0.2$ (intermediate ϕ) and 0.6 (high ϕ).

4.5.2.1 Low Colloid Volume Fractions

De Hoog et al. [102] studied the phase behaviour of a mixture containing sterically stabilized fluorescent PMMA spheres ($R = 600$ nm) and polystyrene (PS) polymer

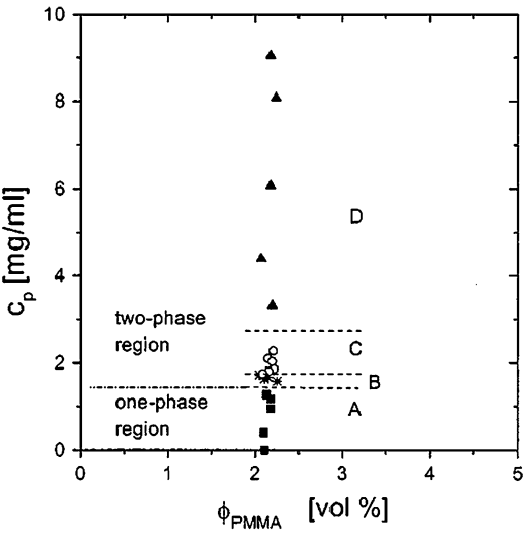

Fig. 4.21 State diagram for the $q = 0.08$ colloid–polymer mixture investigated by De Hoog et al. [102]. The different regions A−D are indicated in the plot. The PS concentration is plotted on the ordinate versus the colloid concentration on the abscissa. Reprinted from [102], copyright 2001, with permission from the American Physical Society

chains ($M_p = 2,000$ kg/mol) in a mixed solvent consisting of tetralin, *cis*-decalin and carbon tetra chloride. In this solvent mixture the PMMA spheres are nearly refractive index matched, enabling fluoresecent confocal scanning light microscopy (CSLM) measurements deep into the sample. This solvent mixture has the additional advantage that the density difference with the PMMA spheres is small to such a degree that significant sedimentation of PMMA particles only becomes apparent after months. The radius of gyration of the polymers was determined to be 46 nm. Hence $q = 0.08$ and the polymer overlap concentration of the PS chains was estimated at 8 g/L. The colloid–polymer mixture was studied at a fixed colloid volume fraction of $\phi \approx 0.02$ and PS concentrations up to 10 g/L i.e. just above the overlap concentration. From (2.21) the contact potential follows as

$$W_{\text{dep}} = W(r = 2R) = -\phi_p \frac{3}{2}\frac{R}{R_g} kT. \tag{4.43}$$

Hence the investigated polymer concentrations imply strengths of the attraction up to 20 kT. De Hoog et al. observed, depending on the polymer concentration, four characteristic scenarios. The corresponding concentration regimes A−D are identified in Fig. 4.21.

Regime (A) is the one-phase fluid region, whereas regimes (B–D) are in the two-phase region. Representative pictures of the structures found in these regions are given in Fig. 4.22. These were all taken at $t \simeq 400\tau_B$, where τ_B is the Brownian time scale, with $\tau_B = R^2/D_s$, where D_s is the self-diffusion coefficient and R is the sphere radius. In the narrow region B the formation of nucleation clusters can be observed, see Fig. 4.22. Eventually, these clusters sediment and form a colloidal crystal. In this regime, just across the fluid–crystal binodal, the contact potentials are $W_{\text{dep}} \approx -2.5\,\text{kT}$. In region C, centered at about 2 g/L (corresponding to

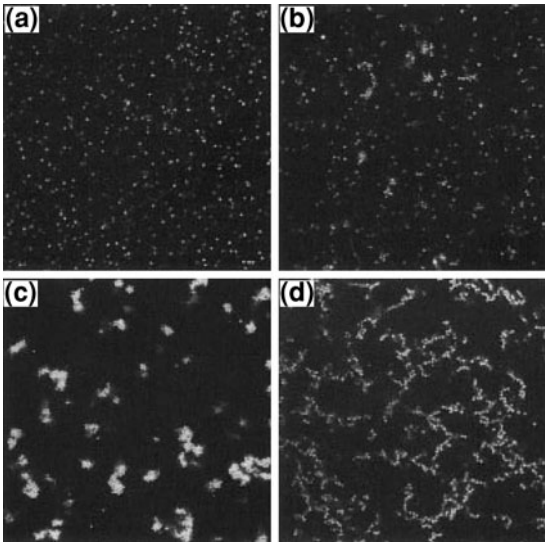

Fig. 4.22 CSLM images taken after mixing colloids and polymer at four concentrations [102] at a colloid volume fraction of 2 vol%. Polymer concentrations were 1.2 g/L (region A), 1.7 g/L (region B), 2.1 g/L (region C) and 8.1 g/L (region D). The image size is 100 μm by 100 μm These picture were taken at $t \approx 400\tau_B$. Reprinted from [102], copyright 2001, with permission from the American Physical Society

$W_{\text{dep}} \approx -4.5\,\text{kT}$), aggregates are formed from single particles, followed by growth of the clusters via subsequent aggregation. These clusters are dense but not crystalline. The sediment formed is dense but no crystallinity was observed. Above 3.3 g/L in region D, corresponding to $W_{\text{dep}} > -7.5\,\text{kT}$, aggregation is also observed but here the clusters have a more ramified or elongated strong-like shape. The sediment formed is dilute, getting denser in a few days.

4.5.2.2 Intermediate Colloid Volume Fractions

Poon et al. [103] studied a similar system as De Hoog et al. [102], this time with PMMA particles with $R = 238\,\text{nm}$ and PS polymers with $M_p = 370\,\text{kg/mol}$. We focus on their experiments carried out at a colloid volume fraction $\phi \approx 0.1$. Just as De Hoog et al. they observed four regimes. At low concentration a colloidal fluid was observed. Across the phase boundary a narrow concentration regime was found of equilibrium fluid–crystal phase behaviour.

At higher concentrations they observed a spinodal-like small-angle light scattering pattern in the region where De Hoog et al. observed aggregation. While at first surprising, Rouw et al. [104] already noted in the late 1980s that the computer simulations of Ziff [105] of colloidal aggregation phenomena appear to show a long-wavelength spinodal-like modulation of the aggregate density. This perception was turned into a quantitative framework by Carpineti and Giglio [106], who proved experimentally that colloidal aggregation exhibits the same features as spinodal decomposition, be it that the scaled structure factor $\widetilde{S}(Q/Q_m, t)$ is now described by

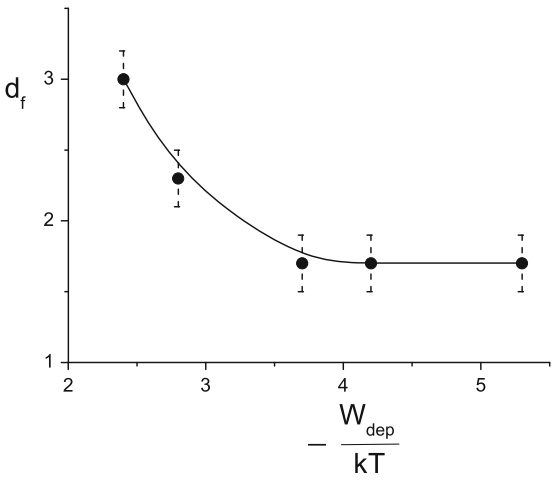

Fig. 4.23 Fractal dimension d_f inside a gel of aggregated PMMA spheres plus PS polymer chains ($q = 0.08$) as a function of the attraction at contact [103]

$$\widetilde{S}(Q/Q_m, t) = Q_m(t)^{-d}\widetilde{f}(Q/Q_m), \tag{4.44}$$

where $\widetilde{f}(Q/Q_m)$ is a time-independent scaling function. For ordinary spinodal decomposition $d = 3$ while for aggregating systems (4.44) holds if we take $d = d_f$, where d_f is the fractal dimension of the aggregates. Poon et al. [103] showed that the small-angle light scattering data of their depletion-induced aggregating system are described by (4.44) with a value of d that depends on the polymer concentration, i.e., on the strength of the depletion interaction. With increasing strength of the depletion interaction the fractal dimension decreases from $d_f = 3$ (dense clusters) to $d_f = 1.7$ (ramified clusters), see Fig. 4.23, in agreement with the visual observations of De Hoog et al. [102].

For still higher polymer concentrations Poon et al. observed the formation of a transient gel. Such a particle gel is characterized by a rapid collapse of its structure following after a delay period where no significant sedimentation occurs. This delay time can range from seconds to many months, depending upon the strength of the gel.

Verhaegh et al. [107, 108] studied transient gelation with a combination of small-angle light scattering, light microscopy and confocal scanning laser microscopy in a system of sterically stabilized silica spheres mixed with PDMS polymer chains in cyclohexane at colloid volume fractions of $\phi \approx 0.1$. Early time small-angle light scattering curves show a peak at Q_m which shifts in time to smaller values and increases slightly in intensity. This indicates the presence of a coarsening bicontinuous structure, see Fig. 4.24. Alternating dark and bright domains observed in light microscopy confirm the existence of this bicontinuous network of colloid-rich and colloid-poor domains. A slight coarsening of the domains together with an increased contrast was detected. After this initial stage, which only lasts a few seconds, the shift in the light scattering peak is arrested. Also the speckle fluctuations are arrested in time, implying that the system now

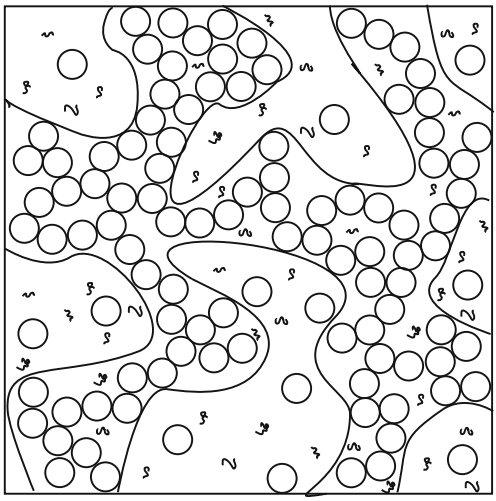

Fig. 4.24 Sketch of a gelation by arrested spinodal phase separation. A space spanning network of colloidal spheres is aggregated through depletion of non-adsorbing polymer chains

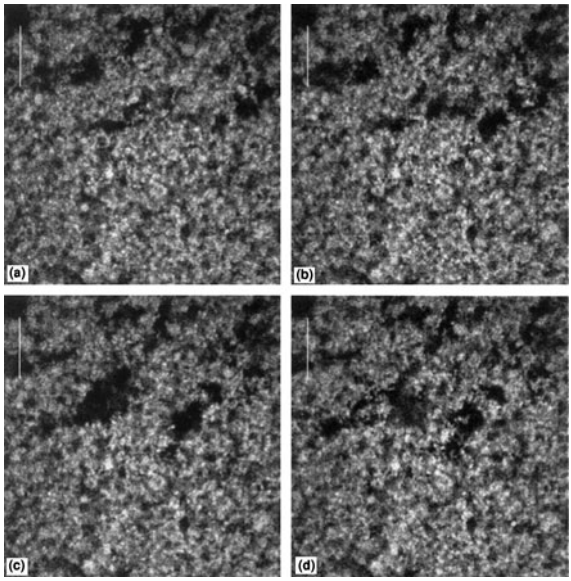

Fig. 4.25 CSLM images from a mixture of fluorescent silica spheres ($R = 115\,\text{nm}$) mixed with PDMS polymers ($R_g = 23\,\text{nm}$) in cyclohexane. The images are mixtures with $\phi = 0.125$, $\phi_p = 1.23$ (85 g/L PDMS) during gel life time. $t = 230\,\text{s}$ (**a**), 240 s (**b**), 250 s (**c**) and 260 s (**d**). The *vertical bar* corresponds to 50 µm. Picture reprinted from [108], copyright 1999, with permission from Elsevier

has a gel character. The above observations suggest that gelation results from a spinodal gas–liquid (also termed fluid–fluid) phase separation, which is arrested at some intermediate stage leaving the system in a state of microphase separation [107, 109, 110].

From CSLM pictures (see Fig. 4.25) it appears that the internal structure of particle network becomes disrupted by the formation of fractures. The number of fractures increases with time as is in agreement with an increase of scattered light

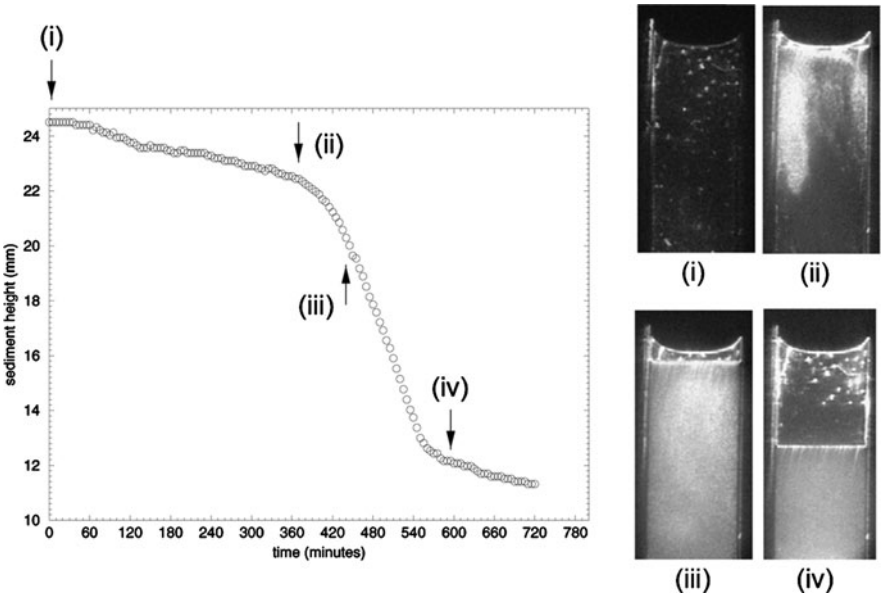

Fig. 4.26 *Left*: Sedimentation profile of PMMA spheres ($R = 186\,\text{nm}$; $\phi = 0.2$) mixed with 5 g/L PS polymers ($R_g = 17\,\text{nm}$) in a tetralin/*cis*-decalin solvent mixture. Initial sample height is 24.5 mm. *Right*: corresponding dark-field images of the structures observed during time evolution of the transient gel. Picture reprinted from [111], copyright 2002, with permission from IOP Publishing Ltd

in forward direction. This increase of the number of fractures weakens the gel strength until the elastic modulus becomes so small that in the end the gel collapses under gravity.

Using dark-field microscopy, Starrs et al. [111] studied this delayed sedimentation in a colloid–polymer mixture (PMMA spheres and PS polymers in tetralin and *cis*−decalin) with $R_g = 17\,\text{nm}$ and $R = 186\,\text{nm}$ ($q \approx 0.1$). Their results for the sedimentation profile are shown in Fig. 4.26 for a colloid volume fraction of 0.20 and PS concentration of 5 g/L. After a delay time of about 460 min the gel collapses. Note the brightening of the sample during the delay period from (i) to (ii).

From the work of Verhaegh et al. [108] it follows that it is possible to distinguish four stages in the evolution of a transient gel: birth, life (during which the gel ages), collapse, and finally macroscopic two-phase separation. In Fig. 4.27 we give a schematic representation of these stages.

The life time of the transient gel is determined by the strength of the depletion interaction and the colloid concentration and plays a role in many practical systems. For example in salad dressing, which is an oil-in-water emulsion, the depletion flocculation of the oil droplets induced by the addition of a polysaccharide such as xanthan leads to the formation of a particle network [112, 113]. The yield stress of this network (in the sense of food science) ‘stabilizes’ the

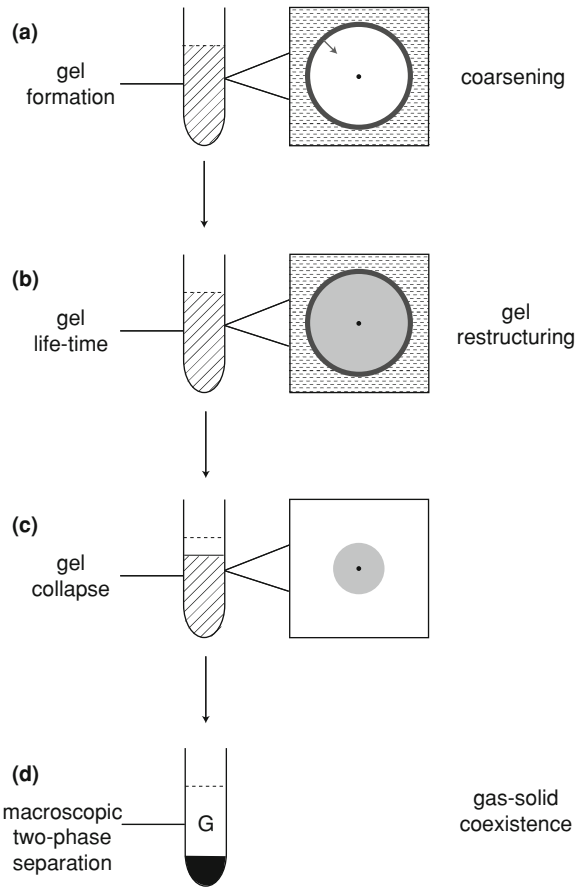

Fig. 4.27 Sketch of the demixing process observed in a sample containing a colloid polymer mixture at high polymer concentrations at $q < 0.3$. The corresponding light scattering patterns are indicated as well: **a** gel formation 'birth', **b** gel life-time 'life', **c** gel collapse 'death', **d** macroscopic phase separation. Redrawn from Verhaegh et al. [107]

dressing, i.e., prevents creaming. Buscall et al. [114] proposed a simple theory to rationalize collapse times for the delayed sedimentation of weakly aggregated colloidal gels.

4.5.2.3 High Colloid Volume Fractions

We now focus on colloid volume fractions above the fluid–crystal phase transition. As discussed in Sect. 3.2.3, Pusey and Van Megen [11] observed that above a volume of about 0.58 suspensions of hard-sphere like PMMA particles do not crystallize over several months. The explanation for this phenomenon is that particles become increasingly tightly caged as the volume fraction increases. For sufficiently high volume fractions the particles become tightly caged by their neighbours to such a degree that they are unable to move far enough to nucleate crystallization and the system is termed glassy. Mode coupling theory (MCT)

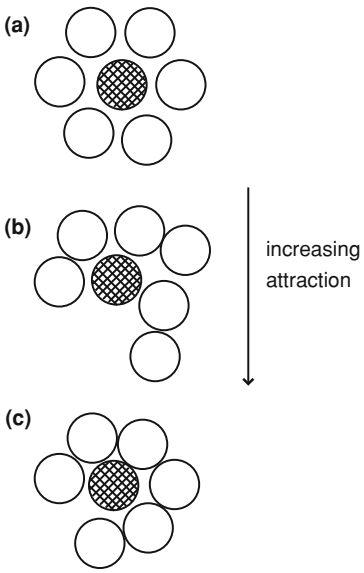

Fig. 4.28 Schematic picture of the influence of (short-ranged) attraction on the glassy state. **a** *Repulsive glass*. This corresponds to the situation where attractions are absent or very weak. There is significant free volume in the cage, but the particle can not escape this cage. **b** *Metastable fluid that crystallizes*. Adding a weak attraction leads to particles clustering in the cage. Now holes open up and particles can escape. **c** *Attractive glass*. Upon further increasing the attraction an attractive glass is formed. The attraction is now so strong that particles are tightly bound so again a cage is formed with no escape possible

[115] supports the existence of such a glass transition. Also further experimental results on hard sphere colloidal glasses [116] have been successfully interpreted with MCT [117].

Ilett et al. [16] observed that adding 1–2 g/L polystyrene ($M_p = 390\,\text{kg/mol}$, $R_g = 18\,\text{nm}$) to a concentrated ($\phi \approx 0.6$) glassy suspension of sterically stabilized PMMA colloids, with a radius of 217 nm, leads to crystallization of the initially glassy suspension. At higher polymer concentrations (above 3 g/L) the system becomes again kinetically arrested. Systems composed of hard spheres with short-range attraction display two glass states, one referred to as repulsive glass (no or very weak attraction) and one referred to as attractive glass (strong attraction), with a metastable fluid (weak attraction) in between. These two types of glasses were subsequently predicted by MCT [118–120]. These predictions were substantially confirmed by Pham et al. [121] and Eckert and Bartsch [122].

A simple physical picture of the repulsive and attractive glass and the metastable fluid was given by Pusey [123] and is depicted in Fig. 4.28. Zaccarelli and Poon [124] studied the interplay between bonding and caging. Using Molecular Dynamics simulations they were able to bridge the gap between colloidal glasses

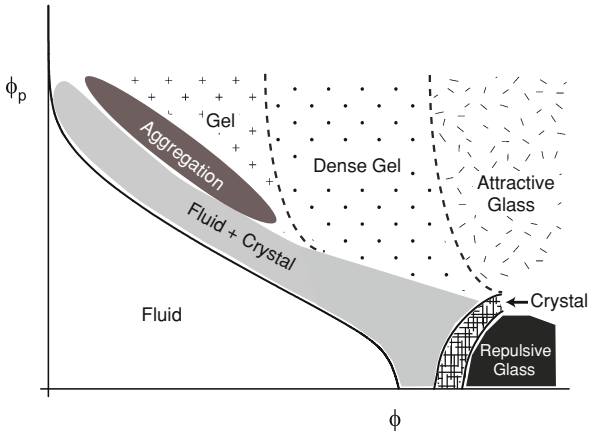

Fig. 4.29 Observed state diagram of a colloid–polymer mixture for small q

and colloidal gels with a state they refer to as dense gel. The observed overall state diagram is sketched in Fig. 4.29 and differs substantially from the equilibrium phase diagram drawn in Fig. 4.20.

Only a narrow range of concentrations is found where fluid–crystal phase transition occurs. This can be explained by the fact that the depth of the potential is quite significant for small q; it is about 4–5 kT just across the phase boundary. In retrospect it is even surprising that fluid–crystal phase transitions are observed at low volume fractions of colloids at small q for that reason.

It is intriguing and challenging that the depletion force, allowing to independently control the range and strength of the attraction, opens up new ways of structuring soft matter.

References

1. G.J. Fleer, M.A. Cohen Stuart, J.M.H.M. Scheutjens, T. Cosgrove, B. Vincent, Polymers at Interfaces. (Chapman and Hall, New York, 1993)
2. E.G.M. Pelssers, M.A. Cohen Stuart, G.J. Fleer, J. Chem. Soc. Faraday Trans. **86**, 1355 (1990)
3. P.M. Golz, Dynamics of colloids in polymer solutions, Ph.D. thesis, University of Edinburgh, Edinburgh, 1999
4. C. Gögelein, G. Nägele, J. Buitenhuis, R. Tuinier, J.K.G. Dhont, J. Chem. Phys. **130**, 204905 (2009)
5. C.M. Wijmans, E.B. Zhulina, G.J. Fleer, Macromolecules **27**, 3238 (1994)
6. A.K. Van Helden, J.W. Jansen, A. Vrij, J. Colloid Interface Sci. **81**, 354 (1981)
7. C.G. de Kruif, P.W. Rouw, J.W. Jansen, A. Vrij, J. de Physique **46**, C3–295 (1985)
8. C.G. de Kruif, R.P. Briels, A. May, Langmuir **4**, 668 (1988)
9. L. Antl, J.W. Goodwin, R.D. Hill, R.H. Ottewill, S.M. Owens, S. Papworth, J.A. Water, Colloids Surf. **17**, 67 (1986)
10. P. Bartlett, R.H. Ottewill, P.N. Pusey, J. Chem. Phys. **93**, 1299 (1990)

11. P.N. Pusey, W. Van Megen, Nature **320**, 340 (1986)
12. B.A.L. Castello, P.F. Luckham, T.F. Tadros, Langmuir **8**, 464 (1986)
13. C.G. Berry, J. Phys. Chem. **44**, 1550 (1966)
14. L. Starrs, P. Bartlett, Faraday Disc. **51**, 123 (2003)
15. W.C.K. Poon, J. Phys. Condens. Matter **14**, R859 (2002)
16. S.M. Ilett, A. Orrock, W.C.K. Poon, P.N. Pusey, Phys. Rev. E **51**, 1344 (1995)
17. R. Tuinier, P.A. Smith, W.C.K. Poon, S.U. Egelhaaf, D.G.A.L. Aarts, H.N.W. Lekkerkerker, G.J. Fleer, Europhys. Lett. **82**, 68002 (2008)
18. H.N.W. Lekkerkerker, W.C.K. Poon, P.N. Pusey, A. Stroobants, P.B. Warren, Europhys. Lett. **20**, 559 (1992)
19. R. Tuinier, J.K.G. Dhont, C.G. de Kruif, Langmuir **16**, 1497 (2000)
20. S. Ramakrishnan, M. Fuchs, K.S. Schweizer, C.F. Zukoski, J. Chem. Phys. **116**, 2201 (2002)
21. I. Lynch, S. Cornen, L. Piculell, J. Phys. Chem. B **108**, 5443 (2004)
22. Y. Hennequin, M. Evens, C.M. Quezada Angulo, J.S. Van Duijneveldt, J. Chem. Phys. **123**, 054906 (2005)
23. Z.X. Zhang, J.S. van Duijneveldt, Langmuir **22**, 63 (2006)
24. C.F. Tejero, A. Daanoun, H.N.W. Lekkerkerker, M. Baus, Phys. Rev. Lett. **73**, 752 (1994)
25. G.J. Fleer, R. Tuinier, Physica A **379**, 52 (2007)
26. A. Moussaïd, W.C.K. Poon, P.N. Pusey, M.F. Soliva, Phys. Rev. Lett. **82**, 225 (1999)
27. J.A. Thomson, P. Schurtenberger, G.M. Thurston, G.B. Benedek, PNAS **84**, 7079 (1987)
28. P.R. Ten Wolde, D. Frenkel, Science **277**, 1975 (1997)
29. C. Haas, J. Drenth, J. Cryst. Growth **196**, 388 (1999)
30. S. Auer, D. Frenkel, Nature **409**, 1020 (2001)
31. R. Sear, J. Chem. Phys. **114**, 3170 (2001)
32. A. Fortini, E. Sanz, M. Dijkstra, Phys. Rev. E **78**, 041402 (2008)
33. E. Zaccarelli, J. Phys. Condens. Matter **19**, 323101 (2007)
34. F. Leal-Calderon, J. Bibette, J. Biais, Europhys. Lett. **23**, 653 (1993)
35. M.A. Faers, P.F. Luckham, Langmuir **13**, 2922 (1997)
36. D.G.A.L. Aarts, R. Tuinier, H.N.W. Lekkerkerker, J. Phys. Condens. Matter **14**, 7551 (2002)
37. P.J. Flory, Principles of Polymer Chemistry. (Cornell University Press, New York, 1953)
38. L. Schäfer, Excluded Volume Effects in Polymer Solutions. (Springer, Heidelberg, 1999)
39. G.J. Fleer, R. Tuinier, Adv. Colloid Interface Sci. **143**, 1–47 (2008)
40. P.G. De Gennes, Scaling Concepts in Polymer Physics. (Cornell University Press, Ithaca, 1979)
41. G.J. Fleer, A.M. Skvortsov, R. Tuinier, Macromol Theory Sim. **16**, 531 (2007)
42. S.F. Edwards, Proc. Phys. Soc. **85**, 613 (1965)
43. S.F. Edwards, K.F. Freed, J. Phys. A **2**, 145 (1969)
44. M. Doi, S.F. Edwards, The Theory of Polymer Dynamics. (Clarendon Press, Oxford, 1986)
45. G.J. Fleer, A.M. Skvortsov, R. Tuinier, Macromolecules **36**, 7857 (2003)
46. J.F. Joanny, L. Leibler, P.G. De Gennes, J. Polym. Sci. Polym. Phys. **17**, 1073 (1979)
47. E. Eisenriegler, J. Chem. Phys. **79**, 1052 (1983)
48. R. Tuinier, G.A. Vliegenthart, H.N.W. Lekkerkerker, J. Chem. Phys. **113**, 10768 (2000)
49. A. Hanke, E. Eisenriegler, S. Dietrich, Phys. Rev. E **59**, 6853 (1999)
50. H. Yamakawa, Modern Theory of Polymer Solutions. (Harper and Row, New York, 1971)
51. A. Fortini, P.G. Bolhuis, M. Dijkstra, J. Chem. Phys. **128**, 024904 (2008)
52. P.G. Bolhuis, A.A. Louis, J.P. Hansen, Phys. Rev. Lett. **89**, 128302 (2002)
53. C. Gögelein, R. Tuinier, Eur. Phys. J. E **27**, 171 (2008)
54. R. Tuinier, C.G. de Kruif, J. Chem. Phys. **110**, 9296 (1999)
55. G.J. Fleer, R. Tuinier, Phys. Rev. E **76**, 041802 (2007)
56. P.G. Bolhuis, E.J. Meijer, A.A. Louis, Phys. Rev. Lett. **90**, 068304 (2003)
57. K.J. Mutch, J.S. van Duijneveldt, J. Eastoe, I. Grillo, R.K. Heenan, Langmuir **25**, 3944 (2009)

58. K.J. Mutch, J.S. van Duijneveldt, J. Eastoe, I. Grillo, R.K. Heenan, Langmuir **26**, 1630 (2010)
59. S. Asakura, F. Oosawa, J. Chem. Phys. **22**, 1255 (1954)
60. R. Tuinier, A.V. Pethukhov, Macromol Theory Simul. **11**, 975 (2002)
61. D. Goulding, J.P. Hansen, Mol. Phys. **99**, 865 (2001)
62. Y. Mao, J. Phys. **5**, 1761 (1995)
63. J. van der Gucht, N.A.M. Besseling, van J. Male, M.A. Cohen Stuart, J. Chem. Phys. **112**, 2886 (2000)
64. A.A. Louis, P.G. Bolhuis, J.P. Hansen, E.J. Meijer, Phys. Rev. Lett. **85**, 2522 (2000)
65. R. Sear, D. Frenkel, Phys. Rev. E **55**, 1677 (1997)
66. P.B. Warren, Langmuir **13**, 4388 (1997)
67. M. Fasolo, P. Sollich, J. Phys. Condens. Matter **17**, 797 (2005)
68. P. Paricaud, S. Varga, P.T. Cummings, G.J. Jackson, Chem. Phys. Lett. **398**, 489 (2004)
69. P.G. Bolhuis, D.A. Kofke, Phys. Rev. E **54**, 634 (1996)
70. P.N. Pusey, J. Phys. **48**, 709 (1987)
71. M. Fasolo, P. Sollich, J. Chem. Phys. **122**, 074904 (2005)
72. V.Ya. Grinberg, V.B. Tolstoguzov, Food Hydrocolloids **11**, 145 (1997)
73. S. Finet, A. Tardieu, J. Cryst. Growth **232**, 40 (2001)
74. M. Casselyn, J. Perez, A. Tardieu, P. Vachette, J. Witz, H. Delacroix, Acta Cryst. D **57**, 1799 (2001)
75. P.D. Patel, W.B. Russel, J. Colloid Interface Sci. **131**, 192 (1989)
76. O. Annunziata, N. Asherie, A. Lomakin, J. Pande, O. Ogun, G.B. Benedek, PNAS **99**, 14165 (2002)
77. C.P. Royall, D.G.A.L. Aarts, H. Tanaka, J. Phys. Condens. Matter **17**, S3401 (2005)
78. M.R. Böhmer, O.A. Evers, J.M.H.M. Scheutjens, Macromolecules **23**, 2288 (1990)
79. J.Y. Walz, A. Sharma, J. Colloid Interface Sci. **168**, 485 (1994)
80. P.G. Ferreira, M. Dymitrowska, L. Belloni, J. Chem. Phys. **113**, 9849 (2000)
81. A.R. Denton, M. Schmidt, J. Chem. Phys. **122**, 244911 (2005)
82. A. Fortini, M. Dijkstra, R. Tuinier, J. Phys. Condens. Matter **17**, 7783–7803 (2005)
83. J. Zhou, J.S. van Duijneveldt, B. Vincent, Langmuir **26**, 9397 (2010)
84. A. Stradner, H. Sedgwick, F. Cardinaux, W.C.K. Poon, S.U. Egelhaaf, Nature **432**, 492 (2004)
85. H. Sedgwick, S.U. Egelhaaf, W.C.K. Poon, J. Phys. Condens. Matter **16**, 4913 (2004)
86. J. Groenewold, W.K. Kegel, J. Phys. Chem. B **66**, 066108 (2002)
87. F. Sciortino, S. Mossa, E. Zaccarelli, P. Tartaglia, Phys. Rev. Lett. **93**, 055701 (2004)
88. O.A. Croze, M.E. Cates, Langmuir **21**, 5627 (2005)
89. R. Tadmor, E. Hernandez-Zapata, N. Chen, P. Pincus, J.N. Israelachvili, Macromolecules **35**, 2380 (2002)
90. T. Odijk, Langmuir **13**, 3579 (1997)
91. T. Odijk, Macromolecules **29**, 1842 (1996)
92. V.J. Anderson, H.N.W. Lekkerkerker, Nature **416**, 811 (2002)
93. J.W. Cahn, J.E. Hillard, J. Phys. Chem. **28**, 258 (1958)
94. J.W. Cahn, J.E. Hillard, J. Phys. Chem. **31**, 688 (1959)
95. J.K.G. Dhont, An Introduction to Dynamics of Colloids. (Elsevier, Amsterdam, 1996)
96. N.A.M. Verhaegh, J.S. van Duijneveldt, J.K.G. Dhont, H.N.W. Lekkerkerker, Physica A **230**, 409 (1996)
97. E.D. Siggia, Phys. Rev. A **20**, 595 (1979)
98. D.G.A.L. Aarts, R.P.A. Dullens, H.N.W. Lekkerkerker, New J. Phys. **7**, 40 (2005)
99. W.C.K. Poon, F. Renth, R.M.L. Evans, D.J. Fairhurst, M.E. Cates, P.N. Pusey, Phys. Rev. Lett. **83**, 1239 (1999)
100. J.P. Hansen, L. Verlet, Phys. Rev. **184**, 151 (1969)
101. G.A. Vliegenthart, H.N.W. Lekkerkerker, J. Chem. Phys. **111**, 4153 (1999)
102. E.H.A. de Hoog, W.K. Kegel, A. van Blaaderen, H.N.W. Lekkerkerker, Phys. Rev. E **64**, 021497 (2001)

103. W.C.K. Poon, A.D. Pirie, P.N. Pusey, Faraday Disc. **101**, 65 (1995)
104. P.W. Rouw, A.T.J.M. Woutersen, B.J. Ackerson, de C.G. Kruif, Physica A **56**, 876 (1989)
105. R.M. Ziff, in *Kinetics of Aggregation and Gelation* ed. by F. Family, D.P. Landau (Elsevier, Amsterdam, 1984), p. 191
106. M. Carpineti, M. Giglio, Phys. Rev. Lett. **68**, 3327 (1992)
107. N.A.M. Verhaegh, D. Asnaghi, H.N.W. Lekkerkerker, M. Giglio, L. Cipelletti, Physica A **242**, 104 (1997)
108. N.A.M. Verhaegh, D. Asnaghi, H.N.W. Lekkerkerker, Physica A **264**, 64 (1999)
109. C.A. Miller, D.D. Miller, Colloid Surf. **16**, 219 (1985)
110. P.J. Lu, E. Zaccarelli, F. Ciulla, A. Schofield, F. Sciortino, D.A. Weitz, Nature **453**, 499 (2008)
111. L. Starrs, W.C.K. Poon, D.J. Hibberd, M.M. Robins, J. Phys. Condens. Matter **14**, 2485 (2002)
112. A. Parker, P.A. Gunning, K. Ng, M.M. Robbins, Food Hydrocolloids **9**, 333 (1995)
113. R. Tuinier, C.G. de Kruif, J. Colloid Interface Sci. **218**, 201 (1999)
114. R. Buscall, T.H. Choudhury, M.A. Faers, J.W. Goodwin, P.A. Luckham, S.J. Partridge, Soft Matter **5**, 1345 (2009)
115. U. Bengtzelius, W. Götze, A. Sjölander, J. Phys. C **17**, 5915 (1984)
116. P.N. Pusey, W. Van Megen, Phys. Rev. Lett. **59**, 2083 (1987)
117. W. Götze, J. Phys. Condens. Matter **11**, A1 (1999)
118. J. Bergenholtz, M. Fuchs, Phys. Rev. E **59**, 5706 (1999)
119. L. Fabbian, W. Götze, F. Sciortino, P. Tartaglia, F. Thiery, Phys. Rev. E **59**, R1347 (1999)
120. L. Fabbian, R. Latz, F. Sciortino, P. Tartaglia, C. Thies, Phys. Rev. E **60**, 5768 (1999)
121. K.N. Pham, A.M. Puertas, J. Bergenholtz, S.U. Egelhaaf, A. Moussaïd, P.N. Pusey, A.B. Schofield, M.E. Cates, M. Fuchs, W.C.K. Poon, Science **296**, 104 (2002)
122. T. Eckert, E. Bartsch, Phys. Rev. Lett. **89**, 125701 (2002)
123. Pusey PN (2008) *Lecture at the 7th Liquid Matter Conference*, Lund, Sweden, 27 June–1 July
124. E. Zaccarelli, W.C.K. Poon, PNAS **106**, 15203 (2009)

Chapter 5
Phase Transitions of Hard Spheres Plus Colloids

In the previous chapter we considered the effect of added non-adsorbing polymers on the phase behaviour of suspensions of spherical colloids. The depletion effect is also operational in mixtures of large and small (hard) spheres, see Fig. 5.1 where two big spheres in a sea of small spheres are brought together. As the big spheres get close, the smaller spheres can no longer enter the gap between the big ones. The outside small particles then push the big spheres together.

When the added non-adsorbing small colloids are substantially smaller (say a factor of 5) than the major colloidal component their effect on the phase behaviour can be treated within free volume theory (FVT) [1, 2]. We stress that this treatment is limited to sufficiently asymmetric hard sphere mixtures, say, $q = \sigma_2/\sigma_1$ smaller than 0.2. For larger q values binary colloidal crystals AB_2 and AB_{13}, consisting of large colloids A with diameter σ_A and small colloids B with diameter σ_B, have been observed in the size range $0.425 \leq \sigma_B/\sigma_A \leq 0.60$ (AB_2) and $0.485 \leq \sigma_B/\sigma_A \leq 0.62$ (AB_{13}) [3–5]. Such structures cannot be treated within FVT.

The added small colloids may be of a similar colloid shape (i.e., spheres) or a different shape such as rod-like colloids. In Sect. 2.4 we found that rod-like colloids give rise to a strong depletion interaction and in this chapter we will see that rod-like colloids influence the phase behaviour of a colloidal suspension significantly at very low concentrations.

5.1 Free Volume Theory for Big Plus Small Hard Spheres

In 1964 Lebowitz and Rowlinson [6] showed that, within the Percus–Yevick treatment of hard sphere fluids [7], binary hard sphere mixtures are completely miscible for all concentrations and size ratios. This proof was later extended by Vrij [8] to hard sphere mixtures with an arbitrary number of components. Up till 1990, it was indeed generally believed that hard sphere mixtures do not phase

H. N. W. Lekkerkerker and R. Tuinier, *Colloids and the Depletion Interaction*,
Lecture Notes in Physics, 833, DOI: 10.1007/978-94-007-1223-2_5,

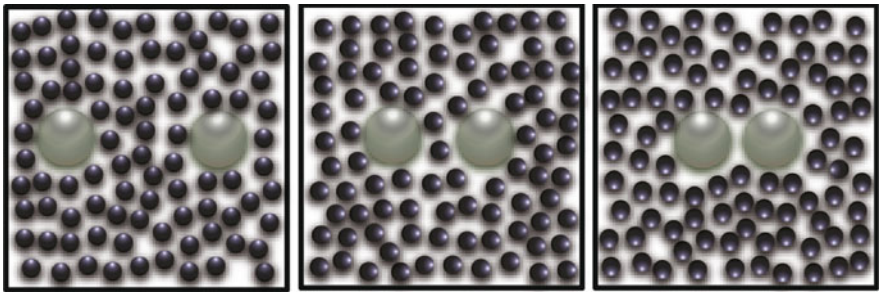

Fig. 5.1 Illustration of depletion effect in a mixture of two big hard spheres plus small hard spheres in 2D. As the big spheres approach each other (from *left* to *right*) the small spheres cannot enter the gap between the big spheres in the end

separate into two fluid phases. Biben and Hansen [9] then showed, on the basis of a thermodynamically self-consistent theory, that dense binary mixtures of hard spheres with diameters σ_1 and σ_2 phase separate into two fluid phases when the size ratio σ_2/σ_1 is less than 0.2. The physical origin of phase separation in highly asymmetric hard sphere mixtures is the depletion interaction similar to what we encountered in Chaps. 3 and 4. Throughout this chapter we refer to the depletants as the components in the reservoir (^{R}) being either small hard spheres (Sects. 5.1 and 5.2) or hard spherocylinders (Sects. 5.3 and 5.4).

The free volume treatment given for hard spheres + penetrable hard spheres can be extended to the case of asymmetric hard sphere mixtures as follows. The osmotic equilibrium system considered is depicted in a schematic way in Fig. 5.2. We assume the depletion layers are equal to the radii of the small hard spheres. Following the same steps as in Chap. 3 we obtain for the semi-grand potential of the asymmetric hard sphere mixture.

$$\Omega(N_1, V, T, \mu_2) = F_0(N_1, V, T) - P^R \langle V_{\text{free}} \rangle_0. \tag{5.1}$$

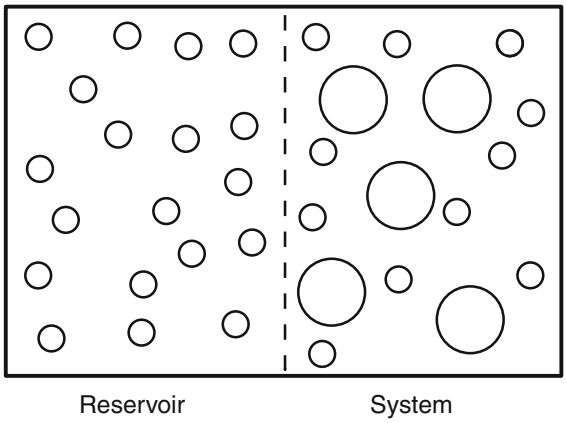

Fig. 5.2 Osmotic equilibrium system for a dispersion of big and small hard spheres in the system in equilibrium with a reservoir that consists of a small sphere dispersion. The semi-permeable membrane allows permeation of small hard spheres but is impermeable for the big hard spheres

In (5.1) N_1 is the number of large hard spheres, μ_2 is the chemical potential of the small hard spheres imposed by the (hypothetical) reservoir, F_0 is the (Helmholtz) free energy of the (large) hard sphere system without added small spheres, P^R is the pressure of the small hard spheres in the reservoir, and $\langle V_{\text{free}} \rangle_0$ is the free volume of an added small hard sphere in the system of N_1 large hard spheres in a volume V. The quantity $\langle V_{\text{free}} \rangle_0$ is given by the same expression as the free volume of an added penetrable hard sphere,

$$\langle V_{\text{free}} \rangle_0 = \alpha V. \tag{5.2}$$

Since we consider small size ratios we use expression (3.37) valid for the limit of small depletants

$$\alpha = (1 - \phi_1) e^{-3q\phi_1/(1-\phi_1)}, \tag{5.3}$$

where now $\phi_1 = n_1 \pi \sigma_1^3/6$ is the volume fraction of the large spheres. For the pressure P^R in the reservoir, which for the case of penetrable hard spheres is given by the ideal gas law, we now use the SPT expression (3.35),

$$\frac{P^R}{n_2^R kT} = \frac{1 + \phi_2^R + (\phi_2^R)^2}{(1 - \phi_2^R)^3}, \tag{5.4}$$

where n^R is the number density and $\phi^R = n^R \pi \sigma_2^3/6$ the volume fraction of the small spheres in the reservoir. In this way we account for the hard interactions between the small spheres.

We now have all the ingredients that make up the semi-grand potential (5.1) of the asymmetric hard sphere mixture. From it we obtain the pressure of the system P and the chemical potential μ_1 of the large hard spheres using standard thermodynamic relations.

$$P = -\left(\frac{\partial \Omega}{\partial V}\right)_{N_1, T, \mu_2} = P^0 + P^R \left(\alpha - n_1 \frac{\partial \alpha}{\partial n_1}\right) \tag{5.5}$$

and

$$\mu_1 = \left(\frac{\partial \Omega}{\partial N_1}\right)_{V, T, \mu_2} = \mu_1^0 - P^R \frac{\partial \alpha}{\partial n_1}, \tag{5.6}$$

where P^0 and μ_1^0 are the pressure and chemical potential of the pure (big) hard sphere system (for which we use the expressions derived in Chap. 3). The dimensionless forms of (5.5) and (5.6) are given in (3.44) and (3.45). We can now calculate the phase behaviour of the asymmetric hard sphere mixture from the coexistence equations

$$\mu_1^I(n_1^I, \mu_2) = \mu_1^{II}(n_1^{II}, \mu_2), \tag{5.7}$$

$$P^I(n_1^I, \mu_2) = P^{II}(n_1^{II}, \mu_2). \tag{5.8}$$

These expressions can, analogously to (3.46) and (3.47), be simplified to

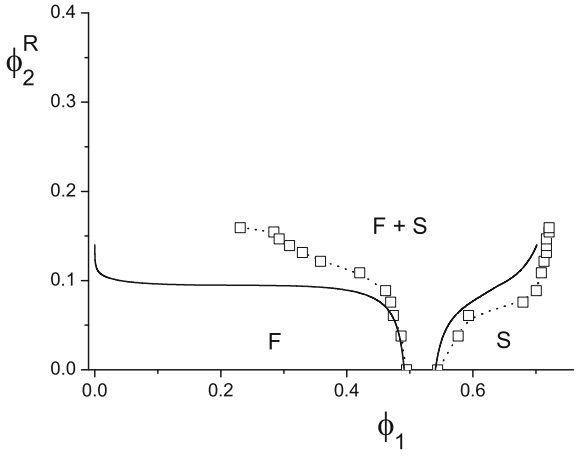

Fig. 5.3 Phase diagram of big + small hard spheres in the $\phi_2^R - \phi_1$ representation for $q = \sigma_2/\sigma_1 = 0.1$. Data points are redrawn Monte Carlo simulation results [10] guided by a *dotted curve*. The curves are the FVT predictions

$$\widetilde{\mu} = \widetilde{\mu}^0 + \widetilde{P}^R g(\phi_1), \tag{5.9}$$

$$\widetilde{P} = \widetilde{P}^0 + \widetilde{P}^R h(\phi_1), \tag{5.10}$$

with

$$g(\phi_1) = e^{-3q\phi_1/(1-\phi_1)}\{1 + 3q[1 + \phi_1/(1-\phi_1)]\} \tag{5.11}$$

and

$$h(\phi_1) = e^{-3q\phi_1/(1-\phi_1)}\{1 + 3q\phi_1/(1-\phi_1)\}. \tag{5.12}$$

The fluid–solid binodal can be obtained from

$$\widetilde{P}^R = \frac{\widetilde{\mu}_s(\phi_{1,s}) - \widetilde{\mu}_f(\phi_{1,f})}{g(\phi_{1,f}) - g(\phi_{1,s})} = \frac{\widetilde{P}_s(\phi_{1,s}) - \widetilde{P}_f(\phi_{1,f})}{h(\phi_{1,f}) - h(\phi_{1,s})}. \tag{5.13}$$

In Fig. 5.3 we give the results for $q = 0.1$. For comparison we add in these figures the Monte Carlo computer simulation results of Dijkstra et al. [10]. The agreement is reasonable although not as good as the agreement between FVT and computer simulations for the hard sphere + penetrable hard sphere system. This might be due to the fact that accumulation effects, leading to repulsive depletion contributions as we saw in Sect. 2.3 are not incorporated in FVT.

Note that for the small size ratios, for which the FVT of asymmetric hard sphere mixtures is applicable, fluid–fluid demixing (also predicted by FVT, not shown) is metastable with respect to the fluid–solid transition. The presence of this metastable transition does affect the physical properties of the mixtures. Like colloid + polymer mixtures [11–13], asymmetric hard sphere mixtures display interesting gel and glass states that are supposed to be connected with the metastable fluid–fluid transition [14, 15].

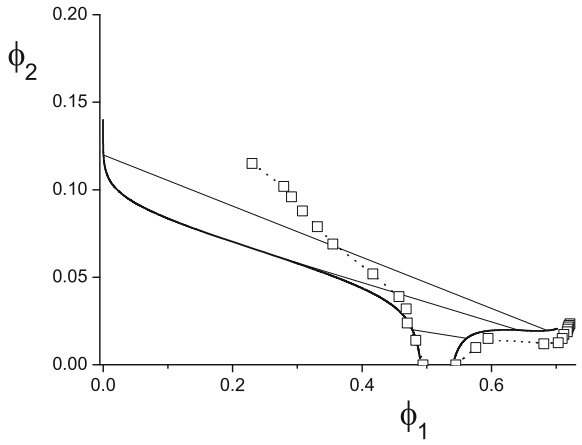

Fig. 5.4 As Fig. 5.3 but in the $\phi_2 - \phi_1$ representation. A few illustrative theoretical *tie-lines* are indicated

From an experimental point of view we are of course interested in the phase diagram in the $\phi_1 - \phi_2$ phase. By using the relation

$$n_2 = -\frac{1}{V}\left(\frac{\partial \Omega}{\partial \mu_2}\right)_{N_1,V,T} = \alpha n_2^R$$

or

$$\phi_2 = \alpha \phi_2^R,$$

we can directly convert the phase diagram in the $\phi_1 - \phi_2^R$ representation to the $\phi_1 - \phi_2$ representation. Results for $q = 0.1$ are presented in Fig. 5.4.

5.2 Phase Behaviour of Mixed Suspensions of Large and Small Spherical Colloids

5.2.1 Phase Separation in Binary Mixtures Differing only in Diameter

Sanyal et al. [16] and Van Duijneveldt [17] were the first to present experimental evidence for phase separation in bimodal hard sphere-like colloidal suspensions with a large size difference. Since then several studies [18–22] have appeared presenting experimental phase diagrams for mixed suspensions of large and small colloids. In Fig. 5.5 we give the experimental phase diagram for $q \simeq 0.1$ by Imhof and Dhont [20], which may be compared to free volume theory and Monte Carlo computer simulations. FVT overestimates the depletion activity of the small spheres at the binodal. The difference might be caused by charges on the colloidal particles in the experimental system not accounted for theoretically. Additional

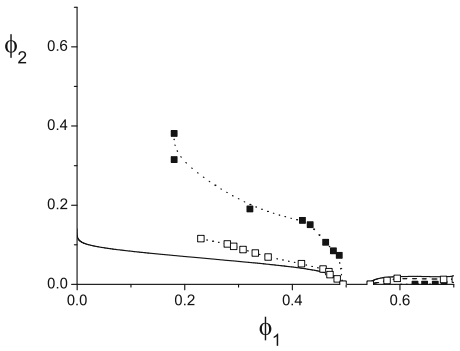

Fig. 5.5 Fluid–solid coexistence curves established from experiments (*closed squares*) with sterically stabilized silica spheres of $q \simeq 0.1$ dispersed in DMF with 10^{-2} M LiCl [20] Monte Carlo simulations ([10], *open squares*) and FVT (*solid curves*)

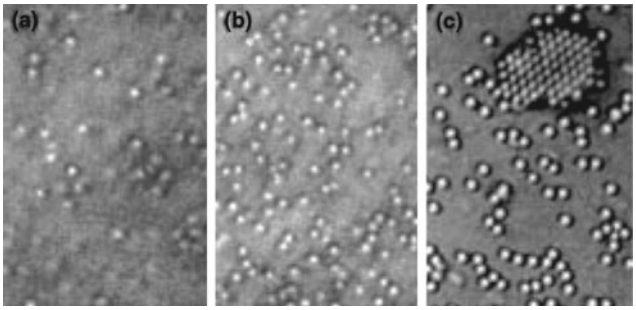

Fig. 5.6 Micrographs of polystyrene spheres ($\sigma_1 = 0.8\,\mu$m) at a glass wall with (**a**) no small spheres, and added small spheres ($\sigma_2 = 70\,$nm) with $\phi_2 = 0.08$ (**b**) and $\phi_2 = 0.16$ (**c**). The volume fraction of big spheres $\phi_1 = 0.02$. Picture reprinted from [23], web: epljournal.edpsciences.org, Copyright 1997, with permission from EDP Sciences and A.D. Dinsmore

double layer repulsion does shift theoretical FVT binodals for fluid–solid coexistence at small q upwards. Kaplan et al. [18] and Dinsmore et al. [19] observe crystallites at the sample walls at volume fractions of the small spheres significantly below the value required for the fluid–solid transition in the bulk (see Fig. 5.6). This is a manifestation of the stronger depletion interaction between a colloidal sphere and a wall than the depletion interaction between two spheres (see Chap. 2). A theoretical treatment for the wall phase behaviour based on the semi-grand potential of an adsorbed layer of colloids has been given by Poon and Warren [2]. Comparison with experiment [23] shows that also this treatment overestimates the depletion effect of the small spheres.

5.2.2 Mixtures of Latex Particles and Micelles

In 1980, Yoshimura et al. [24] reported a fluid–solid phase separation in a mixture of polystyrene latex ($\sigma_1 = 510\,$nm) and the non-ionic surfactant polyoxyethylene alkyl phenylether at KCl concentrations above 0.05 mole/l. At a surfactant

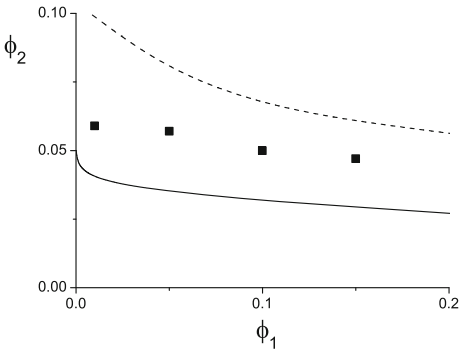

Fig. 5.7 Phase diagram for $q = 0.033$. Data points are experimental results from Piazza and Di Pietro [26], *solid curve* is the FVT prediction and the *dashed curve* represents Monte Carlo computer simulation results by Dijkstra et al. [10]

concentration of 2 wt% an iridescent bottom phase appeared which increased in amount upon further increase of the surfactant concentration. At the same time, the latex concentration in the top phase decreased. The formation of colloidal crystals in the bottom phase, which causes the iridescence, could be confirmed by direct visual observation in the microscope. A few years later, Ma [25] recognized that the origin of the phase separation is depletion interaction between the latex particles caused by the micelles. Piazza and co-workers [26] have done quantitative measurements on the depletion-induced phase separation in mixtures of latex particles and micelles. In Fig. 5.7 we give their results for a mixture of colloidal PFA (a polytetrafluoro-ethylene copolymer) spheres with diameter $\sigma_1 = 220\,\text{nm}$ and the non-ionic surfactant Triton X100 which forms globular micelles with diameters $\sigma_2 = 6-8\,\text{nm}$. In Fig. 5.7 we compare these experimental results with the FVT results.

Piazza et al. [27] have also shown that the micelle depletion-induced fluid–solid phase transition can be profitably exploited to perform an efficient size fractionation of latex particles.

5.2.3 Oil-in-Water Emulsion Droplets and Micelles of the Stabilizing Surfactant

As early as 1952, Cockbain [28] observed the reversible aggregation and creaming of soap stabilized oil-in-water emulsion droplets at soap concentrations greater than the critical micelle concentration. Fairhurst et al. [29] suggested that this reversible aggregation and creaming arises from the depletion interaction between the oil droplets caused by the soap micelles. Quantitative measurements on depletion-induced phase separation by micelles were performed by Bibette and coworkers on silicone oil-in-water emulsions stabilized by sodium dodecylsulfate (SDS) [30]. In Fig. 5.8 their experimental phase diagram in the oil-droplet vs micellar volume fraction is given for three oil-droplet sizes ($\sigma_1 = 460, 600$ and $930\,\text{nm}$) is presented together with the FVT results. The agreement is good.

It is clear that the micellar volume fraction needed to cause phase separation decreases with increasing size of the oil droplets. This is not surprising as the

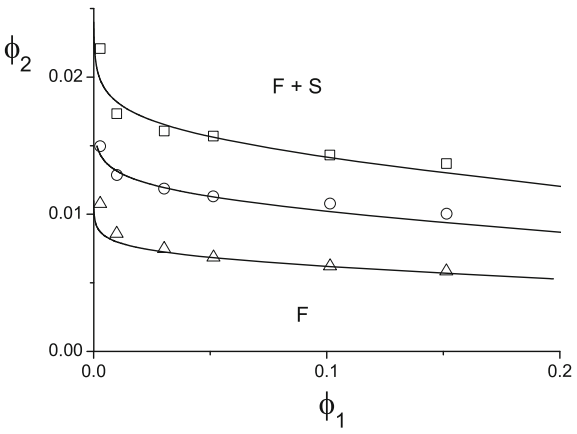

Fig. 5.8 Phase diagram of micelles (volume fraction ϕ_2) mixed with oil droplets (volume fraction ϕ_1) redrawn from Bibette et al. [30]. *Solid curves* are FVT predictions for (from *top* to *bottom*) $q = 0.014, 0.01$ and 0.006, assuming a micellar diameter of 6 nm

strength of the depletion interaction is directly proportional to σ_1/σ_2, see (2.95) with $\sigma_1 = 2R$ and $\sigma_2 = \sigma$. Bibette [31] made clever use of this fact by devising a method to size fractionate a polydisperse emulsion using the micelle depletion induced fluid–solid transition.

5.3 Free Volume Theory for Sphere–Rod Mixtures

In the introduction of this chapter we mentioned that rod-like colloids influence the phase behaviour of suspensions of spherical colloids significantly at very low concentration. For a review see [32]. This is not surprising as rod-like colloids give rise to a strong depletion interaction at low concentration, see (2.107). Here we will see that FVT (correctly) captures the above mentioned pronounced depletion effect caused by rod-like particles.

Again we start from an osmotic equilibrium where now the reservoir contains colloidal rods and the system contains colloidal spheres and rods. The osmotic equilibrium system considered is depicted in a schematic way in Fig. 5.9. Following the same steps as Sect. 3.3 we obtain for the semi-grand potential for the system represented in Fig. 5.9,

$$\Omega(N_1, V, T, \mu_2) = F_0(N_1, V, T) - P^R \langle V_{\text{free}} \rangle_0. \tag{5.14}$$

In this equation N_1 is the number of large hard spheres, μ_2 is the chemical potential of the hard rods imposed by the (hypothetical) reservoir, F_0 is the free energy of the hard sphere system without added rods, P^R is the pressure of the hard rods in the reservoir and $\langle V_{\text{free}} \rangle_0$ is the free volume of an added rod in the system of N_1 hard spheres in a volume V.

Since we are now dealing with hard rods as the depletion agent both the pressure in the reservoir and the free volume differ from the case of spheres as depletion agent. Both quantities can again be calculated conveniently using SPT [33].

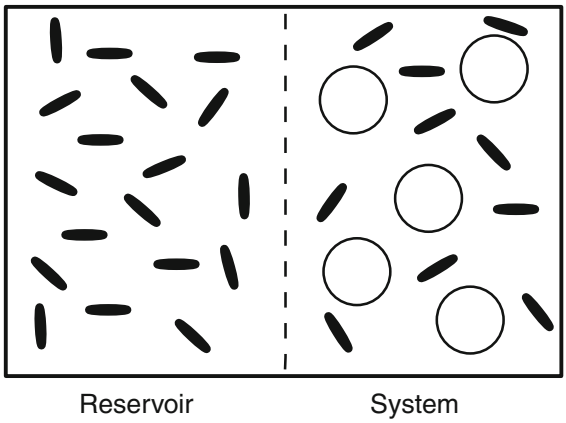

Fig. 5.9 Osmotic equilibrium system as in Fig. 5.2 but with rods replacing the small hard spheres

5.3.1 Free Volume Fraction

For the free volume we again start from expression (3.27)

$$\alpha = \frac{\langle V_{\text{free}} \rangle_0}{V} = e^{-W/kT}, \tag{5.15}$$

where W is now the reversible work to insert a rod in the hard sphere system. As explained in Sect. 3.3 this work can be calculated by expanding the particle to be inserted from zero to its final size. As a model for the rods we take spherocylinders (consisting of cylinders of diameter D and length L, capped with two hemispheres). In the case of a spherocyclinder the expansion can be described in terms of a scaling parameter λ for the length and ν for the diameter. So the scaled particle has a length λL and diameter νD. In the limit $\lambda, \nu \to 0$ the inserted spherocyclinder approaches a point particle. In this limiting case it is very unlikely that excluded volumes of a sphere + added scaled spherocylinder overlap. So

$$W(\lambda, \nu) = -kT \ln[1 - n_1 v_{\text{excl}}(\lambda, \nu)] \quad (\lambda, \nu \to 0), \tag{5.16}$$

where $v_{\text{excl}}(\lambda, \nu)$ is the excluded volume of the added scaled hard spherocylinder and a hard sphere with diameter σ_1

$$v_{\text{excl}}(\lambda, \nu) = \frac{\pi}{6}(\sigma_1 + \nu D)^3 + \frac{\pi}{4}\lambda L(\sigma_1 \nu D), \tag{5.17}$$

see Fig. 5.10. For large values of the scaling parameters λ and ν the work required to insert an additional spherocylinder is just the work to create the volume of the scaled particle against the pressure P of the hard sphere fluid

$$W(\lambda, \nu) = \left(\frac{1}{6}\pi\nu^3 D^3 + \frac{1}{4}\pi\lambda L\nu^2 D^2\right) P \quad (\lambda, \nu \gg 1). \tag{5.18}$$

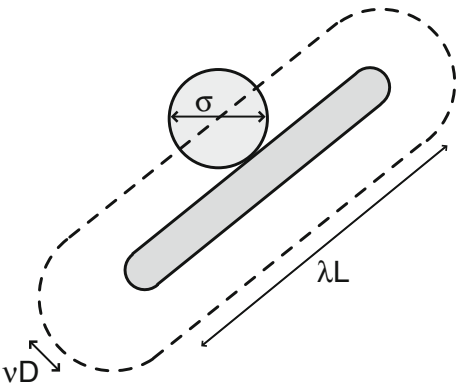

Fig. 5.10 Schematic picture of the excluded volume between a sphere with diameter σ and a scaled spherocylinder with length λL and diameter λD

For intermediate values of the scaling parameters it is assumed that the work $W(\lambda, v)$ can be found from a Taylor expansion around $\lambda = v = 0$, with the term beyond the quadratic being replaced by (5.18)

$$W(\lambda, v) = \sum_{m,n=0}^{2} \frac{1}{m!n!} \frac{\partial^{m+n} W}{\partial \lambda^m \partial v^n} \lambda^m v^n + \left(\frac{1}{6}\pi v^3 D^3 + \frac{1}{4}\pi \lambda L v^2 D^2\right) P. \tag{5.19}$$

The expression for the work to insert a spherocylinder with length L and diameter D is obtained by setting $\lambda = v = 1$. Using for P the SPT expression for hard spheres

$$\frac{P}{n_1 kT} = \frac{1 + \phi_1 + \phi_1^2}{(1 - \phi_1)^3}, \tag{5.20}$$

we obtain

$$\frac{W}{kT} = -\ln(1 - \phi_1) + a\left(\frac{\phi_1}{1 - \phi_1}\right) + b\left(\frac{\phi_1}{1 - \phi_1}\right)^2 + c\left(\frac{\phi_1}{1 - \phi_1}\right)^3. \tag{5.21}$$

Here

$$a = \left(3q + \frac{3}{2}t\right) + (3q^2 + 3qt) + \left(q^3 + \frac{3}{2}q^2 t\right),$$
$$b = \left(\frac{9}{2}q^2 + \frac{9}{2}qt\right) + \left(3q^3 + \frac{9}{2}q^2 t\right),$$
$$c = \left(3q^3 + \frac{9}{2}q^2 t\right),$$

where

$$q = \frac{D}{\sigma_1} \quad \text{and} \quad t = \frac{L}{\sigma_1}.$$

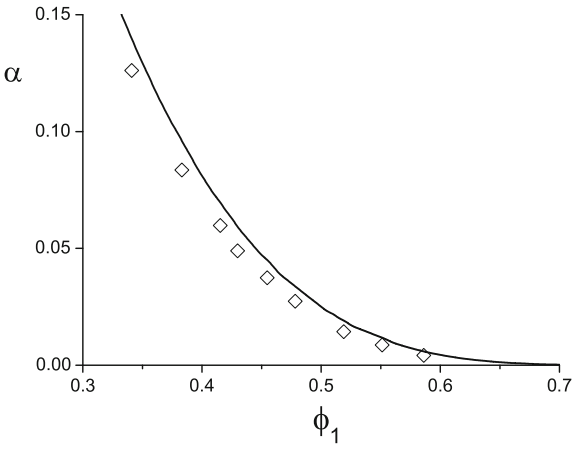

Fig. 5.11 Free volume fraction α for needles in a dispersion of hard spheres with volume fraction ϕ. Data points are Monte Carlo computer simulation results at $n_2^R L^3 = 21.6$ redrawn from Bolhuis and Frenkel [34]. *Solid curve* is the FVT result (5.23)

Exercise Verify that the above expressions for a, b and c match with those below (3.36) in the limit that a spherocylinder equals a sphere.

Using (5.15) we now obtain for the free volume fraction of a hard spherocylinder in a sea of N_1 hard spheres in a volume V.

$$\alpha = (1 - \phi_1) \exp\left[-\left\{a y_1 + b y_1^2 + c y_1^3\right\}\right], \tag{5.22}$$

where

$$y_1 = \phi_1/(1 - \phi_1).$$

In the limit $D = 0$ (and hence $q = 0$), where the spherocylinder reduces to an infinitely thin rod, the free volume fraction takes the simple form

$$\alpha = (1 - \phi_1) \exp\left[-\frac{3}{2}\frac{L}{\sigma_1}\left(\frac{\phi_1}{1 - \phi_1}\right)\right]. \tag{5.23}$$

This expression is compared to Monte Carlo computer simulations by Bolhuis and Frenkel [34] for the case $L/\sigma_1 = 2$ in Fig. 5.11.

5.3.2 Pressure of a Dispersion of Rods

We still have to find an expression for the pressure P^R of the rods in the reservoir in order to use (5.14). Since low concentrations of rods already induce phase transitions in dispersions of hard spheres we only consider dispersions of isotropic rods. Here we focus on the work of Cotter [35], who presented a thermodynamically consistent scaled particle treatment for the pressure of a system of hard

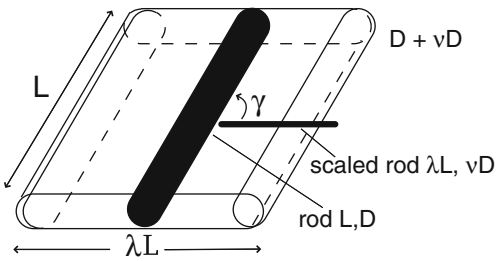

Fig. 5.12 Sketch of the excluded volume between a spherocylinder and a scaled spherocylinder

spherocylinders. The starting point is again the calculation of the work W to insert an additional spherocylinder in the system of spherocylinders to obtain the excess part of the chemical potential. The pressure can then be obtained by using the Gibbs–Duhem equation.

Again using the scaling parameter λ for the length and v for the diameter we obtain in the limit $\lambda, v \to 0$,

$$W(\mathbf{\Omega}, \lambda, v) = -kT \ln\left[1 - n_2^R \int f(\mathbf{\Omega}') v_{\text{excl}}(\mathbf{\Omega}, \mathbf{\Omega}'; \lambda, v)\, \mathrm{d}\mathbf{\Omega}'\right]. \tag{5.24}$$

The solid angle $\mathbf{\Omega}$ can be decomposed into a polar angle $\theta \in [0, \pi]$ and an azimuthal angle $\phi \in [0, 2\pi]$. In (5.24) $v_{\text{excl}}(\mathbf{\Omega}, \mathbf{\Omega}'; \lambda, v)$ is the excluded volume of the added scaled spherocylinder with orientation $\mathbf{\Omega}$ and a spherocylinder of the fluid with orientation characterized by the solid angle $\mathbf{\Omega}'$,

$$\begin{aligned} v_{\text{excl}}(\mathbf{\Omega}, \mathbf{\Omega}'; \lambda, v) = {} & \frac{1}{6}\mathbf{\Omega}(D + vD)^3 + \frac{1}{4}\pi(D + vD)^2(L + \lambda L) \\ & + (D + vD)\lambda L^2 / \sin\gamma(\mathbf{\Omega}, \mathbf{\Omega}'), \end{aligned} \tag{5.25}$$

where $\gamma(\mathbf{\Omega}, \mathbf{\Omega}')$ is the angle between the axes of the two spherocylinders (see Fig. 5.12). Further $f(\mathbf{\Omega})$ is the orientational distribution function, which gives the probability of finding a spherocylinder with an orientation characterized by the solid angle $\mathbf{\Omega}$. To distinguish between the symbols for the grand potential and the solid angle we use here the boldface $\mathbf{\Omega}$. The distribution function $f(\mathbf{\Omega})$ must be normalized

$$\int f(\mathbf{\Omega})\, \mathrm{d}\mathbf{\Omega} = 1. \tag{5.26}$$

In the isotropic phase all orientations are equally probable which implies in view of the normalization (5.26)

$$f(\mathbf{\Omega}) = \frac{1}{4\pi}. \tag{5.27}$$

For large values of the scaling parameters λ and v the work required to insert an additional particle is just the work to create the volume of the scaled particle against the pressure exerted by the fluid of spherocylinders

$$W(\mathbf{\Omega}, \lambda, v) = \left(\frac{1}{6}\pi v^3 D^3 + \frac{1}{4}\pi v^2 D^2 \lambda L\right) P^R \quad (\lambda, v \gg 1). \tag{5.28}$$

For intermediate values of the scaling parameters it is assumed that the work $W(\mathbf{\Omega}, \lambda, v)$ can be found from a Taylor expansion of (5.24) around $\lambda = v = 0$ with the terms beyond the quadratic being replaced by the expression (5.28)

$$W(\mathbf{\Omega}, \lambda, v) = \sum_{m,n=0}^{2} \frac{1}{m!n!} \frac{\partial^{m+n} W}{\partial \lambda^m \partial v^n} \lambda^m v^n + \left(\frac{1}{6}\pi v^3 D^3 + \frac{1}{4}\pi v^2 D^2 \lambda L\right) P. \tag{5.29}$$

The excess chemical potential of a spherocylinder with length L and diameter D is obtained by setting $\lambda = v = 1$ in the above expression and integrating over all possible orientations with the orientation distribution function $f(\mathbf{\Omega})$,

$$\mu_2^{\text{ex}} = \int f(\mathbf{\Omega}) W(\mathbf{\Omega}, 1, 1)\, \mathrm{d}\mathbf{\Omega}. \tag{5.30}$$

As indicated above in the isotropic phase $f(\mathbf{\Omega}) = \frac{1}{4\pi}$ and in that case the average value of the (absolute) sine of the angle between the axes of the spherocylinders is $\pi/4$. This leads to

$$\frac{\mu_2^{\text{ex}}}{kT} = -\ln(1 - \phi_2^R) + \frac{2n^R(\pi D^2 + \pi DL)(\frac{1}{2}D + \frac{1}{4}L)}{(1 - \phi_2^R)} + \frac{(n^R)^2(\pi D^2 + \pi DL)^3}{8\pi(1 - \phi_2^R)^2} + \frac{P^R(\frac{\pi}{6}D^3 + \frac{\pi}{4}D^2 L)}{kT}. \tag{5.31}$$

Using the Gibbs–Duhem relation

$$\frac{1}{kT}\left(\frac{\partial P^R}{\partial n_2^R}\right)_T = 1 + n_2^R \left(\frac{\partial \mu_2^{\text{ex}}/kT}{\partial n_2^R}\right). \tag{5.32}$$

We find

$$\frac{P^R}{n_2^R kT} = \frac{1}{1 - \phi_2^R} + \frac{n_2^R(\frac{1}{2}D + \frac{1}{4}L)(\pi D^2 + \pi DL)}{(1 - \phi_2^R)^2} + \frac{(n_2^R)^2(\pi D^2 + \pi DL)^3}{12\pi(1 - \phi_2^R)^3}. \tag{5.33}$$

Note that for $L = 0$, where the spherocylinder reduces to a sphere, the above expression reduces to the pressure of hard spheres (3.35). The dimensionless pressure $P^R v_0/kT$, where $v_0 = \pi D^3/6 + \pi D^2 L/4$ is the volume of the spherocylinder, can be written as

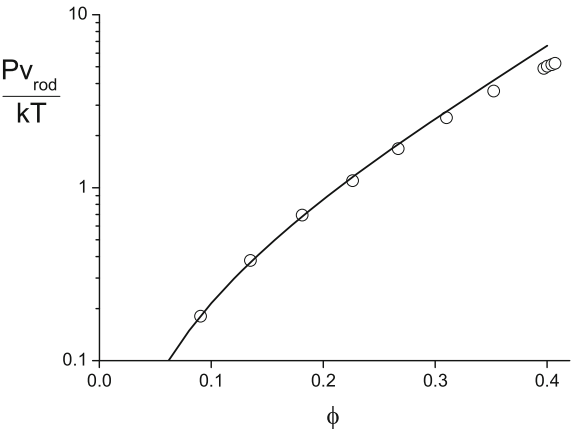

Fig. 5.13 Pressure of a dispersion of spherocylinders with $L/D = 5$ as a function of the rod volume fraction. Data points are Monte Carlo simulations from McGrother et al. [36] and *solid curve* is the SPT result (5.34)

$$\frac{P^R v_0}{kT} = \frac{\phi_2^R}{1-\phi_2^R} + A\left(\frac{\phi_2^R}{1-\phi_2^R}\right)^2 + B\left(\frac{\phi_2^R}{1-\phi_2^R}\right)^3. \tag{5.34}$$

Here

$$A = \frac{3\gamma(\gamma+1)}{3\gamma-1},$$
$$B = \frac{12\gamma^3}{(3\gamma-1)^2},$$

with

$$\gamma = \frac{L+D}{D}.$$

In Fig. 5.13 we present a comparison of the SPT result for the pressure of spherocylinders with computer simulation results of McGrother et al. [36] for $L/D = 5$. We now have all the ingredients for analyzing the properties of the semi-grand potential (5.14) of a colloidal sphere–rod mixture. From it we obtain the pressure of the system and the chemical potential μ_1 of the large hard spheres using the standard thermodynamic relations (5.5) and (5.6) (in dimensionless form (3.44) and (3.45) can be used). We can then calculate the phase behaviour of the colloidal sphere–rod mixture by solving the coexistence relations (5.7) and (5.8). As a test of the quality of the FVT for the phase behaviour of colloidal sphere–rod mixtures we present in Fig. 5.14 a comparison between FVT and simulation results for infinitely thin rods with $L/\sigma_1 = 2$ and $L/\sigma_1 = 3$ taken from the work of Bolhuis and Frenkel [34]. The agreement is, given the approximations made in FVT, remarkable.

In order to compare FVT with experiments, described in the next section, we need results for rods with a finite thickness. In Fig. 5.15 we give results [33] for spherocylinders with $L/D = 20$ and $L/\sigma_1 = 0.2, 0.5$ and 1.0 both in the $\phi^R - \phi_1$ representation as well as in the experimentally relevant $\phi_2 - \phi_1$ representation by

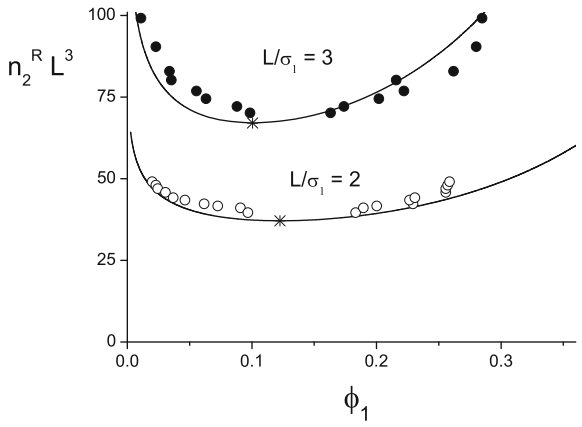

Fig. 5.14 Colloidal gas–liquid coexistence of mixtures of rods plus hard spheres for $L/\sigma_1 = 2$ and 3. Data points are Monte Carlo simulation results [34]. *Solid curves* are the FVT predictions

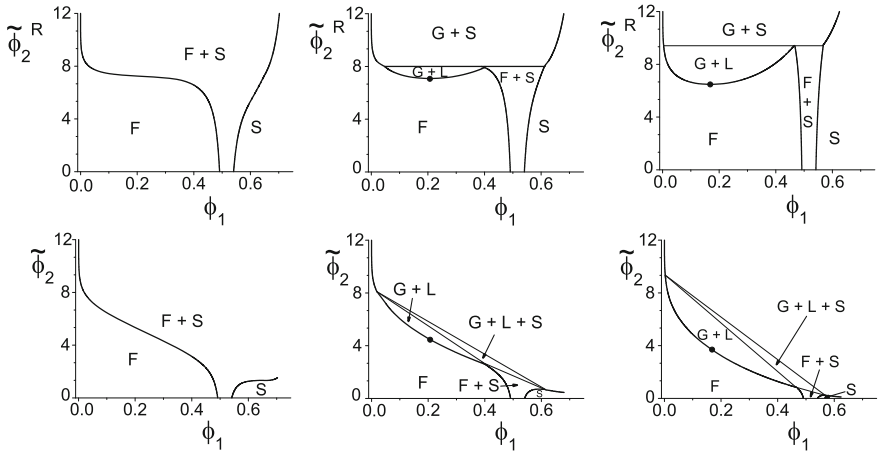

Fig. 5.15 FVT phase diagrams of mixtures of hard spheres (1) plus spherocylinders (2) for $L/D = 20$ and $q = 0.01$ (*left diagrams*), $q = 0.025$ (*middle diagrams*), $q = 0.05$ (*right diagrams*). *Upper curves* are in the $(\phi_2^R - \phi_1)$-representation and *lower curves* are in the $(\phi_2 - \phi_1)$-plane

using (5.15): $\phi_2 = \alpha\phi^R$. Given that the depletion interaction between two spheres in a sea of thin rods scales as $L\sigma_1/D^2$, see (2.107), we have scaled the volume fractions of rods by multiplication with $L\sigma_1/D^2$; $\tilde{\phi}_2^R = \phi^R L\sigma_1/D^2$. For $L/\sigma_1 = 0.2$, only fluid–solid coexistence is found. For $L/\sigma_1 > 0.3$, a region of three phase coexistence (colloidal gas–liquid–crystal) bounded by three distinct two phase regions (gas–liquid, liquid–crystal and gas–crystal) is found. The topology of these phase diagrams exhibit the same global features as those for hard spheres plus penetrable hard spheres in Chap. 3 and colloid–polymer mixtures in Chap. 4. Note that for $L/D = 20$, FVT predicts that the rods can cause a fluid–crystal transition in dilute suspensions of spheres for rod volume fractions as low as 0.003. This is confirmed experimentally as we shall see in the next section.

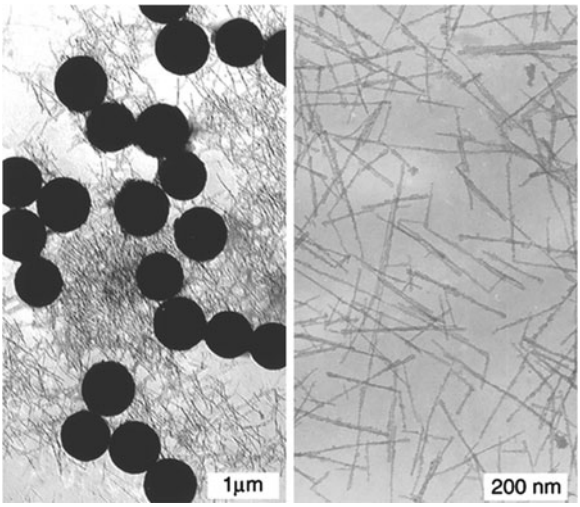

Fig. 5.16 Micrograph of (*left*) silica-coated boehmite rods mixed with silica spheres and (*right*) without silica spheres. Picture reprinted from [37], with permission from the American Chemical Society

5.4 Phase Behaviour of Colloidal Sphere–Rod Mixtures: Experiment

Koenderink et al. [37] and Vliegenthart et al. [38] studied depletion-induced crystallization in a mixture of silica spheres with a diameter of $\sigma_1 = 740\,\text{nm}$ and boehmite ($\gamma-\text{AlOOH}$) rods of length $L = 230\,\text{nm}$ and diameter $D = 9\,\text{nm}$ dispersed in DMF with 0.001 M LiCl added to screen electrostatic interactions. The rods are coated with a thin layer of silica to make them compatible with the silica spheres. The silica spheres are labeled with fluorescein isothiocyanate (FITC) to make them visible with Fluorescence Confocal Microscopy. Transmission electron micrographs of the boehmite rods and a mixture of the boehmite rods and the silica spheres are presented in Fig. 5.16.

In Fig. 5.17 a time series of confocal microscopy images is presented of a sample with a volume fraction of silica spheres of 0.025 and a volume fraction of boehmite rods of 0.0025. In the confocal microscopy images it is seen that with time the silica number density increases by sedimentation. Locally ordered structures are formed but no signs of depletion-induced phase transitions are found.

In Fig. 5.18 we present a time series of confocal microscopy images of a sample with the same volume fraction of silica spheres as in Fig. 5.17 but now for a larger volume fraction of boehmite rods of 0.005. In this case the morphology of the system is totally different. Clusters are rapidly formed (within minutes) and those aggregates rapidly transform into crystallites while they grow and coalesce [38]. The initial clusters contain typically 10^3 particles. In the final stage re-orientation of different crystalline patches and annealing of defect lines is seen. This results in large crystalline areas. The entire process does not take more than 8 min, much faster than the formation of locally ordered structures under the

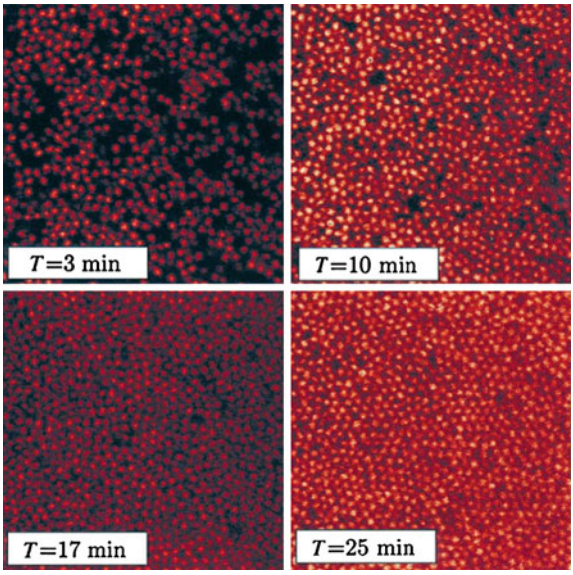

Fig. 5.17 Confocal microscopy images of fluorescently labelled silica spheres ($\sigma_1 = 740\,\text{nm}$) mixed with boehmite rods of length $L = 230\,\text{nm}$ and diameter $D = 10\,\text{nm}$ various times T after mixing at 0.25 wt% rods and 2.5 wt% spheres. Images are $50 \times 50\,\mu\text{m}$. Pictures reproduced from [38], Copyright 1999, by permission of the Royal Society of Chemistry

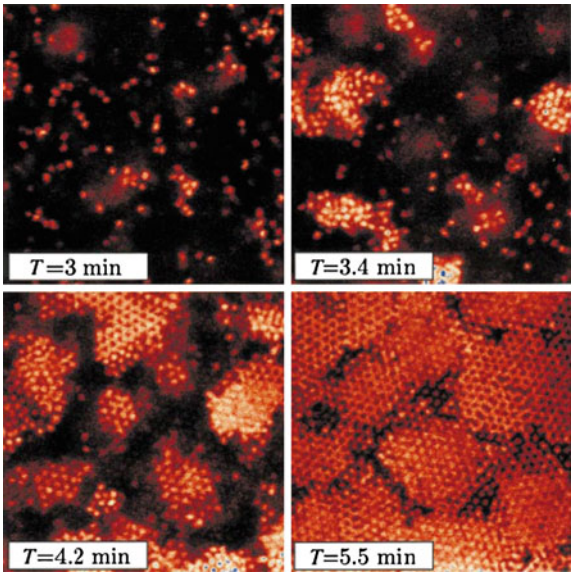

Fig. 5.18 As Fig. 5.17 but for 0.5 wt% of rods at various times. Pictures reproduced from [38], Copyright 1999, by permission of the Royal Society of Chemistry

influence of sedimentation in the system with a volume fraction of rods of 0.0025. Apparently, in the case of a volume fraction of rods of 0.005 we are in the biphasic region (fluid–solid) of the phase diagram. Let us compare this to theory. In Fig. 5.19 we present the theoretical FVT phase diagram for a mixture of hard spheres with diameter $\sigma_1 = 740\,\text{nm}$ and hard rods with length $L = 230\,\text{nm}$ and diameter $D = 10\,\text{nm}$. The experimentally investigated systems discussed above are

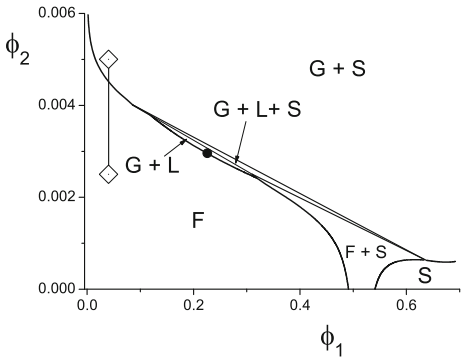

Fig. 5.19 FVT phase diagram for a dispersion of spheres plus rods for $L/D = 23$ and $q = 1/74$. The *open diamonds* indicate the mixtures studied in Fig. 5.17 (0.25 wt%) and Fig. 5.18 (0.5 wt%)

indicated by dots. The experimental observations of no phase separation ($\phi_1 = 0.025$ and $\phi_2 = 0.0025$) and phase separation ($\phi_1 = 0.025$ and $\phi_2 = 0.005$) are in agreement with theory. The experiments clearly indicate that rods are very efficient depletion agents.

References

1. H.N.W. Lekkerkerker, A. Stroobants, Physica A **195**, 387 (1993)
2. W.C.K. Poon, P.B. Warren, Europhys. Lett. **28**, 513 (1994)
3. J.V. Sanders, M.J. Murray, Nature **275**, 201 (1978)
4. S. Hachisu, S. Yoshimura, Nature **283**, 188 (1980)
5. P. Bartlett, R.H. Ottewill, P.N. Pusey, Phys. Rev. Lett. **68**, 3801 (1992)
6. J.L. Lebowitz, J.S. Rowlinson, J. Chem. Phys. **41**, 133 (1964)
7. J.P. Hansen, I.R. McDonald, Theory of Simple Liquids. (Academic Press, San Diego, 1986)
8. A. Vrij, J. Chem. Phys. **69**, 1742 (1978)
9. T. Biben, J.P. Hansen, Phys. Rev. Lett. **66**, 2215 (1991)
10. M. Dijkstra, R. Van Roij, R. Evans, Phys. Rev. E **59**, 5744 (1999)
11. E. Zaccarelli, J. Phys. Condens. Matter **19**, 323101 (2007)
12. V.J. Anderson, H.N.W. Lekkerkerker, Nature **416**, 811 (2002)
13. P.J. Lu, E. Zaccarelli, F. Ciulla, A. Schofield, F. Sciortino, D.A. Weitz, Nature **453**, 499 (2008)
14. E.K. Hobbie, M.J. Holter, J. Chem. Phys. **108**, 2618 (1998)
15. E.K. Hobbie, Phys. Rev. Lett. **81**, 3996 (1998)
16. S. Sanyal, N. Easwar, S. Ramaswamy, A.K. Sood, Europhys. Lett. **18**, 107 (1992)
17. J.S. Van Duijneveldt, A.W. Heinen, H.N.W. Lekkerkerker, Europhys. Lett. **21**, 369 (1993)
18. P.D. Kaplan, J.L. Rouke, A.G. Yodh, D.J. Pine, Phys. Rev. Lett. **72**, 582 (1994)
19. A.D. Dinsmore, A.G. Yodh, D.J. Pine, Phys. Rev. E **52**, 4045 (1995)
20. A. Imhof, J.K.G. Dhont, Phys. Rev. Lett. **75**, 1662 (1995)
21. U. Steiner, A. Meller, J. Stavans, Phys. Rev. Lett. **74**, 4750 (1995)
22. Y. Hennequin, M. Pollard, J.S. Van Duijneveldt, J. Chem. Phys. **120**, 1097 (2004)
23. A.D. Dinsmore, P.B. Warren, W.C.K. Poon, A.G. Yodh, Europhys. Lett. **40**, 337 (1997)
24. S. Yoshimura, K. Takano, S. Hachisu, in *Polymer Colloids II*, ed. by R.M. Fitch (Plenum Publishing Company, New York, 1980)
25. C. Ma, Colloids Surf. **28**, 1 (1987)
26. R. Piazza, G. Di Pietro, Europhys. Lett. **445**, 28 (1994)

27. R. Piazza, S. Iacopini, M. Pierno, E. Vignati, J. Phys. Condens Matter **14**, 7563 (2002)
28. E.G. Cockbain, Trans. Faraday Soc. **48**, 185 (1952)
29. D. Fairhurst, M.P. Aronson, M.L. Ohm, E.D. Goddard, Colloids Surf. **7**, 153 (1983)
30. J. Bibette, D. Roux, F. Nallet, Phys. Rev. Lett. **65**, 2470 (1990)
31. J. Bibette, J. Colloid Interface Sci. **147**, 474 (1992)
32. G.J. Vroege, H.N.W. Lekkerkerker, Rep. Progr. Phys. **55**, 1241 (1992)
33. G.A. Vliegenthart, H.N.W. Lekkerkerker, J. Chem. Phys. **111**, 4153 (1999)
34. P.G. Bolhuis, D. Frenkel, J. Chem. Phys. **101**, 9869 (1994)
35. M.A. Cotter, J. Chem. Phys. **66**, 1098 (1977)
36. S.C. McGrother, D.C. Williamson, G. Jackson, J. Chem. Phys. **104**, 6755 (1996)
37. G.H. Koenderink, G.A. Vliegenthart, S.G.J.M. Kluijtmans, van A. Blaaderen, A.P. Philipse, H.N.W. Lekkerkerker, Langmuir **15**, 4693 (1999)
38. G.A. Vliegenthart, A. Van Blaaderen, H.N.W. Lekkerkerker, Faraday Discuss. **112**, 173 (1999)

Chapter 6
Phase Transitions in Suspensions of Rod-Like Colloids Plus Polymers

So far we have considered the phase behaviour of colloidal spheres plus depletants. In Chap. 3 we considered the simplest type of depletant, the penetrable hard sphere. We then extended this treatment in Chap. 4 to ideal and excluded volume polymers and in Chap. 5 we considered small colloidal spheres (including micelles) and colloidal rods as depletants. In this chapter we consider the phase behaviour of mixtures of colloidal rods plus polymeric depletants. For an overview of several types of colloidal rods encountered in practice we refer to [1].

Pure hard rod suspensions exhibit interesting phase transitions themselves. Upon concentrating a dilute rod suspension for $L/D > 3.5$ the phase states schematically depicted in Fig. 6.1 will be encountered: the isotropic, nematic and smectic liquid states and a crystalline solid state [2–4]. For a description of the various liquid crystalline phases we refer the reader to standard textbooks on liquid crystals such as [5]. We mainly focus on the isotropic and nematic states and it will become clear that adding depletants will strongly affect the isotropic–nematic phase transition.

Lyotropic liquid crystalline phases were recognized a long time ago, first in suspensions of rod-like inorganic colloids (V_2O_5, Zocher [6]) and later in solutions of biological particles (tobacco mosaic virus, Bawden et al. [7]). Onsager [8] showed that an assembly of repelling rods can exhibit a transition from an isotropic to a nematic state driven by entropy. The effect of non-adsorbing polymer on this phase transition has been studied since the 1940s with a view towards the practical possibilities of isolation and separation of viruses [9, 10]. It was observed that the addition of relatively small amounts of polymer to virus suspensions lead to the 'precipitation' of the virus particles (i.e., the formation of a concentrated phase of the virus particles). Only much later, in the 1990s, experiments were started on model rod-like colloid + polymer suspensions to study this phase behaviour in depth. In this chapter we extend the treatment given in the previous chapters to rod-like colloids plus depletant and compare the results to experiment and simulation.

H. N. W. Lekkerkerker and R. Tuinier, *Colloids and the Depletion Interaction*, Lecture Notes in Physics, 833, DOI: 10.1007/978-94-007-1223-2_6,

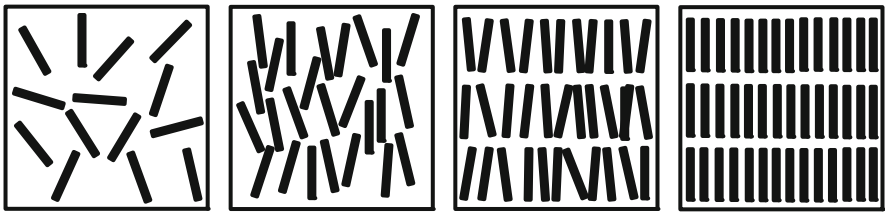

Fig. 6.1 Phase states of hard rod suspensions. From *left* to *right*: isotropic, nematic, smectic and crystal phases

6.1 Onsager Theory of the Isotropic–Nematic Transition

As we saw in the previous chapters colloidal phase transitions of hard particles are governed by entropy. This was in fact first realized by Onsager [8] for the isotropic–nematic (I–N) phase transition in a suspension of rods. He realized that an attractive force is not necessary for the I–N transition by showing that an assembly of repelling rods exhibits a transition from an isotropic to a nematic state due to a gain of packing entropy that compensates the loss of orientational entropy. Onsager also demonstrated that the I–N transition may be treated within a virial expansion of the free energy. In fact, this is one of the very few examples where a phase transition can be treated using a virial expansion. For very thin, rigid, hard particles the transition occurs at a very low volume fraction and the virial expansion may be truncated after the second virial term, leading to an exact theory for infinitely thin particles. In the following we give a brief exposition on Onsager's theory. For more details we refer to [8, 11]. The Helmholtz free energy F for a dispersion of N hard rods (which we again model as spherocylinders with length L and diameter D) in a volume V in the second virial approximation can be written as

$$\frac{F[f]}{NkT} = \text{constant} - 1 + \ln c + \sigma[f] + c\rho[f]. \tag{6.1}$$

Here we have lumped in the constant quantities that do not affect the phase transition, i.e., have the same value in the coexisting phases. Further c is the dimensionless concentration

$$c = bn, \tag{6.2}$$

where the excluded volume $b = (\pi/4)L^2D$ and $n = N/V$ is the number density of the rods. The orientational entropy per particle is expressed in $\sigma[f]$,

$$s_{or} = -k \int f(\mathbf{\Omega}) \ln[4\pi f(\mathbf{\Omega})] \mathrm{d}\mathbf{\Omega} = -k\sigma[f]. \tag{6.3}$$

where $f(\mathbf{\Omega})$ is the orientational distribution function, which gives the probability of finding a spherocylinder with an orientation characterized by the solid angle $\mathbf{\Omega}$. Finally, $-kc\rho[f]$ is the packing entropy per particle,

$$\rho[f] = \frac{4}{\pi}\int\int |\sin\gamma| f(\mathbf{\Omega}) f(\mathbf{\Omega}') \mathrm{d}\mathbf{\Omega}\mathrm{d}\mathbf{\Omega}', \tag{6.4}$$

where γ is the angle between the rods which depends on their orientations $\mathbf{\Omega}$ and $\mathbf{\Omega}'$ (see Fig. 5.12). As already remarked, the I–N transition originates from a competition between the orientational and packing entropy. For low concentrations the orientational entropy dominates and attains a maximum value for an isotropic distribution $f = 1/4\pi$, whereas for high concentrations the packing entropy becomes more important favouring a nematic orientation distribution. The orientation distribution is determined by the fact that the free energy must be a minimum. When we minimize (6.1) we obtain the integral equation

$$\ln[4\pi f(\theta)] = \lambda - \frac{8c}{\pi}\int |\sin\gamma(\mathbf{\Omega}, \mathbf{\Omega}')| f(\theta') \mathrm{d}\mathbf{\Omega}'. \tag{6.5}$$

Here we have taken into account that f does not depend on the azimuthal angle ϕ but only on the polar angle θ. Furthermore, the distribution function $f(\theta)$ must satisfy inversion symmetry, implying the angles θ and $\pi - \theta$ are equivalent. The Lagrange multiplier λ is determined by requiring that $f(\theta)$ fulfills the normalization condition

$$\int f(\mathbf{\Omega})\mathrm{d}\mathbf{\Omega} = 1.$$

It is easily seen that the isotropic distribution function

$$f = \frac{1}{4\pi}$$

satisfies (6.5) for all concentrations (although only for low concentrations this corresponds to a minimum of the free energy). For the isotropic phase σ and ρ attain the values

$$\sigma_I = 0, \quad \rho_I = 1. \tag{6.6}$$

And hence

$$\frac{F_I}{NkT} = \text{constant} - 1 + \ln c + c. \tag{6.7}$$

Exercise
Derive (6.6) from (6.3) and (6.4) using $f = 1/4\pi$.

An exact solution to the non-linear integral equation (6.5) for higher concentrations, where a nematic distribution minimizes the free energy, has not yet been found but ways to solve it numerically have appeared [12, 13]. For a didactic account on how to solve (6.5) numerically, see [14]. This allows the determination

of $\sigma[f]$ and $\rho[f]$ and from thereon the free energy in the nematic phase. To be in mechanical and chemical equilibrium, both phases must have the same osmotic pressure and the same chemical potential.

$$\begin{aligned} P_I(c_I) &= P_N(c_N) \\ \mu_I(c_I) &= \mu_N(c_N). \end{aligned} \tag{6.8}$$

These quantities can be obtained from the free energy using the standard thermodynamic relations

$$\begin{aligned} P &= -\frac{\partial F}{\partial V} \\ \mu &= \frac{\partial F}{\partial N}. \end{aligned} \tag{6.9}$$

For the isotropic phase we find from (6.7)

$$\begin{aligned} \frac{P_I b}{kT} &= c_I + c_I^2 \\ \frac{\mu_I}{kT} &= \text{constant} + \ln\, c_I + 2c_I. \end{aligned} \tag{6.10}$$

Exercise
Show that (6.10) follows from (6.7) and (6.9).

In the nematic phase (6.1) gives

$$\begin{aligned} \frac{P_N b}{kT} &= c_N + c_N^2 \rho[f] \\ \frac{\mu_N}{kT} &= \text{constant} + \ln\, c_N + \sigma[f] + 2c_N \rho[f], \end{aligned} \tag{6.11}$$

where the distribution f must be obtained numerically for each concentration from (6.5). Solving the coexistence equations (6.8) with the above expressions for the osmotic pressure and chemical potential numerically yields the coexistence concentrations

$$c_I = 3.290, \quad c_N = 4.191. \tag{6.12}$$

Further the usual measure of the ordering in the nematic phase, given by the nematic order parameter,

$$S = 4\pi \int_0^{\pi/2} f(\theta) \left[\frac{3}{2}\cos^2\theta - \frac{1}{2}\right] \sin(\theta) \mathrm{d}\theta, \tag{6.13}$$

has the value

$$S = 0.7922 \tag{6.14}$$

for the coexisting nematic phase.

More convenient calculations of the phase transition can be performed by choosing a trial function for the orientation distribution function f with one or more variational parameters. The free energy as a function of these parameters can then be minimized with respect to these parameters. Onsager [8] chose the following function

$$f_O(\theta) = \frac{\kappa \cosh(\kappa \cos \theta)}{4\pi \sinh \kappa}, \tag{6.15}$$

which gives the following results for the coexisting concentrations and nematic order parameter at coexistence

$$c_I = 3.340\ , \quad c_N = 4.486\ , \quad S = 0.848. \tag{6.16}$$

Comparison of these results with exact values (6.12) and (6.14) shows that the trial function chosen by Onsager works quite well. Odijk [15, 16] realized that for large values of κ, Onsager's orientational distribution function can be approximated by a Gaussian distribution function

$$\begin{aligned} f_G &\sim \widetilde{N}(\kappa) \exp\left(-\frac{1}{2}\kappa\theta^2\right) \quad 0 \le \theta \le \frac{\pi}{2} \\ &\sim \widetilde{N}(\kappa) \exp\left(-\frac{1}{2}\kappa(\pi-\theta)^2\right) \quad \frac{\pi}{2} \le \theta \le \pi, \end{aligned} \tag{6.17}$$

where $\widetilde{N}(\kappa)$ is a normalization constant. The advantage of this Gaussian distribution function is that for large values of κ the quantities $\sigma[f]$ and $\rho[f]$ can be represented accurately by

$$\begin{aligned} \sigma[f_G] &\sim \ln \kappa - 1 \\ \rho[f_G] &\sim \frac{4}{\sqrt{\pi\kappa}}. \end{aligned} \tag{6.18}$$

This leads to the following expression for the free energy in the nematic phase

$$\frac{F}{NkT} \sim \text{constant} - 1 + \ln c + \ln \kappa - 1 + \frac{4c}{\sqrt{\pi\kappa}}. \tag{6.19}$$

Minimizing this expression with respect to κ leads to

$$\kappa \sim \frac{4c^2}{\pi}. \tag{6.20}$$

Hence

$$\frac{F}{NkT} \sim \text{constant} + \ln\frac{4}{\pi} + 3 \ln c. \tag{6.21}$$

Using (6.9) we now obtain for the pressure and chemical potential in the nematic phase

$$\begin{aligned} \frac{P_N b}{kT} &= 3c_N \\ \frac{\mu_N}{kT} &= \text{constant} + \ln\frac{4}{\pi} + 3 + 3\ \ln\ c_N. \end{aligned} \tag{6.22}$$

Using these expressions and the expressions given by (6.10) for the pressure and chemical potential in the isotropic phase, the coexistence equations (6.8) now take the simple forms

$$\begin{aligned} c_I + c_I^2 &= 3c_N \\ \ln\ c_I + 2c_I &= 3\ \ln\ c_N + \ln\left(\frac{4}{\pi}\right) + 3. \end{aligned} \tag{6.23}$$

From this we find the following coexisting concentrations

$$c_I = 3.451, \quad c_N = 5.122, \tag{6.24}$$

implying, via (6.20), $\kappa = 33.4$. This leads to the value

$$S = 0.910 \tag{6.25}$$

for the nematic order parameter in the coexisting nematic phase. While the results for the Gaussian distribution function differ more from the exact results than the Onsager trial function (in both cases too high values for the coexisting concentrations and a too high value for the order parameter in the coexisting nematic phase), the calculations are substantially simpler [17] allowing to obtain a good estimate of the I–N transition in more complicated situations (that we will encounter in the next sections). Although the results of Onsager's theory are of great fundamental and methodological interest, they refer strictly to infinitely thin hard rods. Hence, the applicability of the theory to experimental results is limited. In real suspensions of rod-like particles we have to take into account one or more of the following aspects

- particles are not infinitely thin
- particles may be polydisperse
- particles are not hard but may show (long-range) repulsions and attractions
- particles may be semiflexible.

Onsager [8] already addressed the issues of particle repulsions and polydispersity. These and the other issues raised above have been considered extensively (for a review, see [11]).

When considering the effect of depletion attraction on the I–N transition in rod-like suspensions we must take into account that the second virial term B_2 no longer exceeds the higher virial terms. In case of attractions between the rods nearly parallel configurations are of paramount importance and B_2 is no longer the dominating virial coefficient as in the case of long, repulsive rods. It was shown

that for even slightly attractive rods the third virial coefficient B_3 is almost as large as B_2 [18]. This means that we must start from a theory that takes into account higher virial coefficients. Here we use Scaled Particle Theory (SPT) [19], which will be treated in the next section. SPT for rods plus polymers will subsequently be treated in Sects. 6.3 and 6.4, following [20, 21].

6.2 Scaled Particle Theory of the Isotropic–Nematic Transition

SPT, a convenient and tractable way to incorporate higher virial coefficients in the treatment of the isotropic–nematic phase transition was already treated for assemblies of hard rods in Sect. 5.4 to obtain the osmotic pressure of an isotropic suspension of rods. The starting point of SPT is the calculation of the reversible work W to insert an additional spherocylinder in the system of spherocylinders to obtain the excess part of the chemical potential (5.30)

$$\mu^{ex} = \int f(\mathbf{\Omega}) W(\mathbf{\Omega}, 1, 1) \mathrm{d}\mathbf{\Omega}, \tag{6.26}$$

where $W(\mathbf{\Omega}, 1, 1)$ is the reversible work to insert a spherocylinder with length L and diameter D and orientation $\mathbf{\Omega}$ in a system of hard spherocylinders. In Sect. 5.4 we considered an isotropic assembly of rods, but (6.26) applies equally well to an orientationally ordered (nematic) system of rods as long as we use for $f(\mathbf{\Omega})$ the appropriate orientation distribution function. After replacing the second virial contribution $2c\rho[f]$ in (6.11) with the chemical potential μ^{ex} we obtain

$$\begin{aligned} \frac{\mu}{kT} &= \text{constant} + \ln y + \sigma[f] \\ &\quad + (1 + 2A[f])y + \left(A[f] + \frac{3}{2}B[f]\right)y^2 + B[f]y^3. \end{aligned} \tag{6.27}$$

Here y has its usual meaning

$$y = \frac{\phi}{1 - \phi},$$

with ϕ is the volume fraction of the rods which equals nv_0, where v_0 is the spherocylinder volume given by

$$v_0 = \frac{\pi}{4} LD^2 + \frac{\pi}{6} D^3.$$

The quantities $A[f]$ and $B[f]$ are defined as

$$A[f] = 3 + \frac{3(\gamma - 1)^2}{(3\gamma - 1)}\rho[f] \tag{6.28}$$

$$B[f] = \frac{12\gamma(2\gamma - 1)}{(3\gamma - 1)^2} + \frac{12\gamma(\gamma - 1)^2}{(3\gamma - 1)^2}\rho[f], \tag{6.29}$$

where

$$\gamma = 1 + \frac{L}{D},$$

the overall length-to-diameter ratio (not to be confused with the angle γ). Using the Gibbs–Duhem equation

$$\left(\frac{\partial P}{\partial n}\right) = n\left(\frac{\partial \mu}{\partial n}\right),$$

one obtains for the pressure

$$\frac{Pv_0}{kT} = y + A[f]y^2 + B[f]y^3. \tag{6.30}$$

Exercise
Show that by setting $\gamma = 1$ (and $f = 1/4\pi$) one recovers the SPT expression for the pressure of a hard sphere fluid.

Finally, the Helmholtz free energy can be obtained from the relation

$$F = N\mu - PV,$$

leading to

$$\frac{F[f]}{NkT} = \text{constant}' - 1 + \sigma[f] + \ln\, y + A[f]y + \frac{1}{2}B[f]y^2. \tag{6.31}$$

Exercise
Show that in the limit $L/D \to \infty$ and low concentrations the above expression for the free energy reduces to the free energy in the second virial approximation (6.1) with $\text{constant}' = \text{constant} + \ln\frac{L}{D}$.

To locate the I–N transition one proceeds in exactly the same way as in Sect. 6.1 involving the following steps:

- minimize $F[f]$ numerically with respect to the orientation distribution function f,
- calculate the orientation distribution function of f,
- calculate the pressure and chemical potential, and
- solve the coexistence equations.

The results for the coexisting concentrations, which now depend on L/D, are given in Fig. 6.2 (see also [21]). In this figure we also present Monte Carlo simulation results [4] as well as the Onsager limit result $(L/D \to \infty)$. Clearly, the

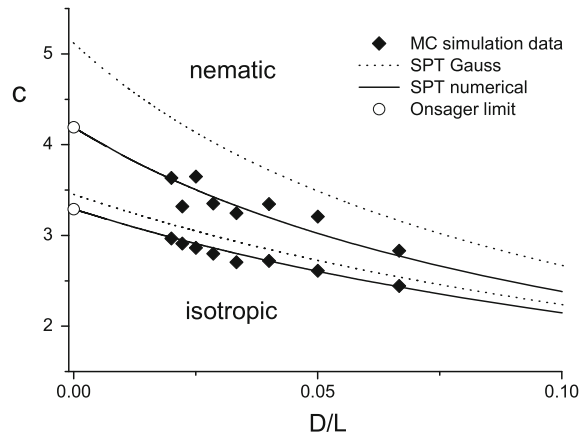

Fig. 6.2 Isotropic–nematic phase coexistence for hard spherocylinders as a function of the inverse of the aspect ratio L/D

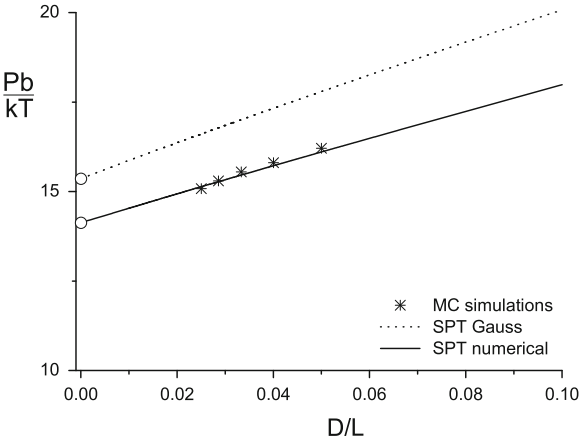

Fig. 6.3 Pressure Pb/kT at isotropic–nematic coexistence for hard spherocylinders as a function of D/L. *Note* $v_0 = b[D/L + (2/3)(D/L)^2]$

agreement is quite good. In Fig. 6.3 we give the pressure at isotropic–nematic coexistence for hard sphere cylinders as a function of the aspect ratio L/D.

It is interesting to compare the results obtained with the numerical orientation distribution function with the results obtained with the Gaussian orientation distribution function (6.17). Substituting the expressions for $\sigma[f_G]$ and $\rho[f_G]$ given by (6.18) in (6.31) and minimizing the free energy with respect to κ yields

$$\kappa = \frac{36}{\pi}\frac{(\gamma-1)^4}{(3\gamma-1)^2}\left(y + \frac{2\gamma}{3\gamma-1}y^2\right)^2. \tag{6.32}$$

Exercise

Show that in the limit $L/D \to \infty$ and low concentrations the above expression for κ reduces to (6.20).

Using (6.32) for κ in $\sigma[f_G]$ and $\rho[f_G]$ and substituting these expressions in (6.27) and (6.30) provides us with analytical expressions for the chemical potential and

pressure in the nematic phase. The expressions for these quantities in the isotropic phase are obtained by setting $\sigma = 0$ and $\rho = 1$ in (6.27–6.30). We then can solve the coexistence equations (6.8). The results for the coexisting concentrations and the coexistence pressure obtained using the Gaussian orientational distribution function are also given in Figs. 6.2 and 6.3.

As in the Onsager limit, the results lie somewhat above the numerical solution. Given the fact that the Gaussian approximation is transparent and simple, it provides a valuable method to scan through a large parameter space as we shall see in the next section.

6.3 Isotropic–Nematic Phase Behaviour of Rods Plus Penetrable Hard Spheres

We now consider the effect of added polymer on the phase behaviour of a system of hard rods. We first consider the simplest representation of a polymer: the penetrable hard sphere (phs) with diameter σ (see Sect. 2.1 for details about this model).

The starting point for the calculation of the phase behaviour is the semi-grand potential for the system of colloidal rods + phs in osmotic equilibrium with a reservoir with phs, which sets the chemical potential of the phs. This system is depicted in Fig. 6.4. In the free volume approximation (see Sect. 3.3) we can write (3.24)

$$\Omega(N_1, V, T, \mu_2) = F_0(N_1, V, T) - P^R \langle V_{\text{free}} \rangle_0, \tag{6.33}$$

where N_1 stands for the number of rods, μ_2 represents the chemical potential of the depletants (penetrable hard spheres), P^R is the pressure in the reservoir and $\langle V_{\text{free}} \rangle_0$ is the free volume for the penetrable hard spheres in the system of rods schematically illustrated in Fig. 6.5. For $F(N_1, V, T)$ we use the SPT expression (6.31) [19] and the osmotic pressure of the penetrable hard spheres in the reservoir is given by

$$P^R = n_2^R kT,$$

where ${n_2}^R$ of the number density of phs in the reservoir. The free volume is again calculated using the relation

$$\frac{\langle V_{\text{free}} \rangle_0}{V} = \alpha = e^{-W/kT}, \tag{6.34}$$

where W is the reversible work for inserting the phs in the hard rod suspension. An expression for the work of insertion W can again be conveniently obtained using scaled particle theory. The work W is calculated by expanding the phs to be inserted form zero to its final size. By writing the size of the scaled phs as $\lambda\sigma$ in the

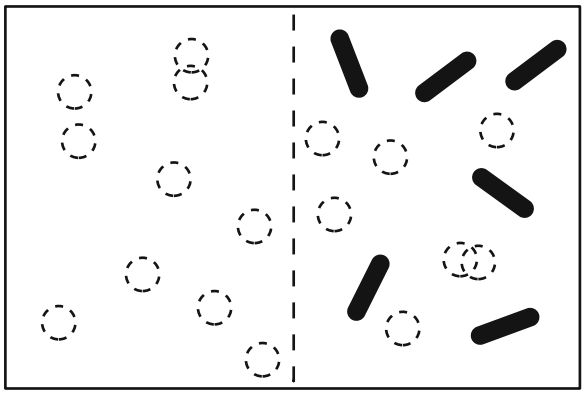

Fig. 6.4 Osmotic equilibrium between a dispersion of hard rods plus penetrable hard spheres (system) and a reservoir containing a penetrable hard sphere dispersion

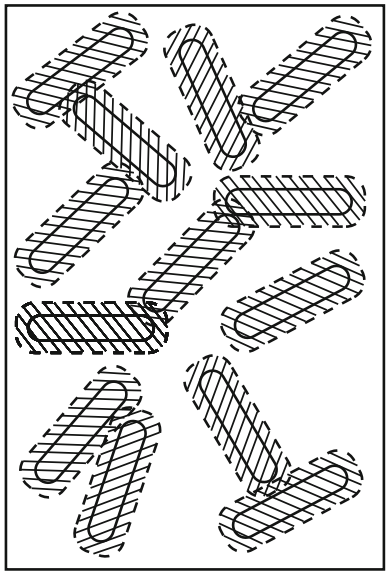

Fig. 6.5 Illustration of the available free volume (the unshaded volume) in a dispersion of hard spherocylinders

limit that $\lambda \to 0$, the inserted sphere approaches a point particle. In this limit it is very unlikely that excluded volumes of the hard rods + added scaled phs overlap. So,

$$W(\lambda) = -kT \ln[1 - n_1 v_{\text{excl}}(\lambda)] \quad \text{for } \lambda \ll 1, \tag{6.35}$$

where $v_{\text{excl}}(\lambda)$ is the excluded volume of the added scaled phs and a hard spherocylinder with length L and diameter D

$$v_{\text{excl}}(\lambda) = \frac{\pi}{4}(D + \lambda\sigma)^2 L + \frac{\pi}{6}(D + \lambda\sigma)^3. \tag{6.36}$$

The opposite limit $\lambda \gg 1$ corresponds to the case when the size of the inserted phs is very large. Then W is, to a good approximation, equal to the volume work needed to create a cavity

$$\frac{\pi}{6}(\lambda\sigma)^3$$

and is given by

$$W = \frac{\pi}{6}(\lambda\sigma)^3 P \quad \text{for } \lambda \gg 1, \tag{6.37}$$

where P is the (osmotic) of the hard rod system given by (6.30). In SPT the above two limiting cases are connected by expanding W in a series in λ

$$W(\lambda) = W(0) + \left(\frac{\partial W}{\partial \lambda}\right)_{\lambda=0}\lambda + \frac{1}{2}\left(\frac{\partial^2 W}{\partial \lambda^2}\right)_{\lambda=0}\lambda^2 + \frac{\pi}{6}(\lambda\sigma)^3 P. \tag{6.38}$$

This yields

$$\frac{W(\lambda=1)}{kT} = \ln(1-\phi_1) + \left[\frac{6\gamma q}{3\gamma-1} + \frac{3(\gamma+1)q^2}{(3\gamma-1)}\right] y_1 + \frac{1}{2}\left(\frac{6\gamma}{3\gamma-1}\right)^2 q^2 y_1^2 + \frac{2q^3}{3\gamma-1}\frac{Pv_0}{kT},$$

where

$$y_1 = \frac{\phi_1}{1-\phi_1}$$
$$q = \frac{\sigma}{D}$$
$$\gamma = \frac{L}{D} + 1.$$

Inserting (6.30) for the pressure of spherocylinders leads to the following expression for the free volume fraction

$$\alpha = (1-\phi_1)\exp[-Q(\phi_1)], \tag{6.39}$$

where

$$Q(\phi_1) = a y_1 + b y_1^2 + c y_1^3$$

with

$$a = \frac{6\gamma}{3\gamma - 1}q + \frac{3(\gamma + 1)}{3\gamma - 1}q^2 + \frac{2}{3\gamma - 1}q^3$$
$$b = \frac{1}{2}\left(\frac{6\gamma}{3\gamma - 1}\right)^2 q^2 + \left(\frac{6}{3\gamma - 1} + \frac{6(\gamma - 1)^2}{(3\gamma - 1)^2}\rho[f]\right)q^3$$
$$c = \frac{2}{3\gamma - 1}\left(\frac{12\gamma(2\gamma - 1)}{(3\gamma - 1)^2} + \frac{12\gamma(\gamma - 1)^2}{(3\gamma - 1)^2}\rho[f]\right)q^3.$$

Exercise
Check that in the appropriate limit this expression for α reduces to (3.36) with a, b and c given below (3.36).

We now have all the contributions to construct the semi-grand potential $\Omega(N_1, V, T, \mu_2)$ given in (6.33). In order to obtain the phase behaviour we proceed along the same lines as for the system of pure rods involving the following steps

- minimize Ω with respect to the orientation distribution function f. Note that in (6.33) both the free energy the pure rod system F_0 and the free volume $\langle V_{\text{free}}\rangle_0$ depend on the orientation distribution function f,
- evaluate the orientation distribution function f,
- calculate the (osmotic) pressure and chemical potential of the rods which are now given by

$$P = -\left(\frac{\partial\Omega}{\partial V}\right)_{N_1,\mu_2} = P^0 + P^R\left(\alpha - n_1\frac{\mathrm{d}\alpha}{\mathrm{d}n_1}\right), \tag{6.40}$$

$$\mu_1 = \left(\frac{\partial\Omega}{\partial N_1}\right)_{V,\mu_2} = \mu_1^0 - P^R\frac{\mathrm{d}\alpha}{\mathrm{d}n_1}, \tag{6.41}$$

  where P^0 and μ^0 are the pressure and chemical potential of the pure rod system, and
- solve the coexistence relations

$$\mu_1^I(n_1^I, \mu_2) = \mu_1^{II}(n_1^{II}, \mu_2), \tag{6.42}$$

$$P^I(n_1^I, \mu_2) = P^{II}(n_1^{II}, \mu_2). \tag{6.43}$$

Instead of formal minimization of the free energy leading to an integral equation for the orientation distribution function f we will first use the Gaussian distribution function which simplifies the calculations considerably, while leading to reasonably good results. This is illustrated in Fig. 6.6, where we plot the isotropic–nematic phase coexistence curve for $L/D = 10$ and $q = 1$. On the ordinate the relative reservoir concentration of penetrable hard spheres is plotted versus the

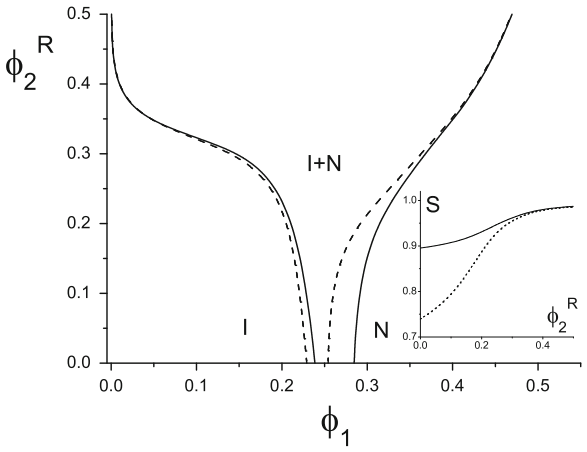

Fig. 6.6 Isotropic–nematic phase coexistence for $L/D = 10$ and $q = 1$ in the reservoir representation. The Gaussian orientational distribution function result (*solid*) is compared to the coexistence computed using formal minimisation of the oriental distribution function (*dashed curves*). In the *inset* we plot the nematic order parameter S as a function of ϕ_2^R of the nematic phase that coexists with the isotropic phase

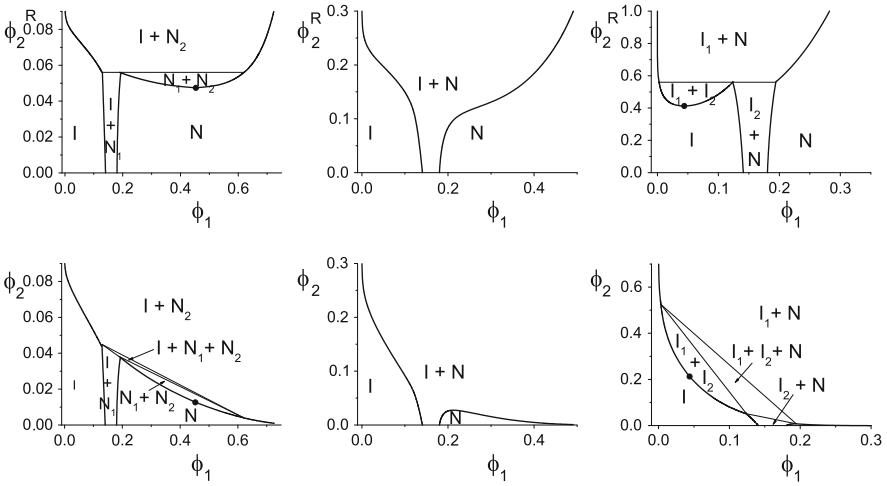

Fig. 6.7 Phase diagrams calculated using free volume theory for spherocylinders with $L/D = 20$ plus penetrable hard spheres at three size ratios $q = 0.3$ (*left*), $q = 1$ (*middle*) and $q = 2.5$ (*right*). The *upper three curves* are in the reservoir representation, the *lower curves* are the system results. The Gaussian form for the ODF was used to minimize the semi-grand potential and compute the coexistence concentrations

volume fraction of hard spherocylinders on the abscissa. The solid curves are the results for the binodals using the Gaussian distribution function, while the dotted curves were obtained using formal minimization. In Fig. 6.2 we have seen the Gaussian overestimates the I–N concentrations somewhat for the pure hard spherocylinder dispersion. For a pure rod dispersion the Gaussian approximation provides a too sharply peaked orientation distribution function f, reflected by a too large value for the nematic order parameter S. Hence, the loss of orientational entropy is overestimated for the pure rod dispersion.

As the depletant concentration becomes significant and attractions play a dominating role f becomes sharply peaked. This is reflected in a strong increase of the nematic order parameter S, see the inset in Fig. 6.6. Hence, the Gaussian orientational distribution function is accurate at larger depletant concentrations.

Phase diagrams for $L/D = 20$, computed using the Gaussian f, are plotted in Fig. 6.7 for $q = 0.3$, $q = 1.0$ and $q = 2.5$. The upper plots are the reservoir depletant-rod representations, while the lower plots are the system representations. These three size ratios reflect the different scenarios that are found in mixtures of spherocylinders plus depletants. Depending on the length-to-width ratio of the rod-like particles and the ratio of the depletant diameter over the rod diameter, we find the following types of phase behaviour:

- coexistence between two isotropic phases (dilute and concentrated, the equivalent of vapour and liquid) and a nematic phase. This phase behaviour is predicted to occur for mixtures of relatively short rods and large depletants, so long-ranged attractions.
- coexistence between an isotropic and a nematic phase.
- equilibria with two coexisting nematic phases for rods plus small depletants, so short-ranged attractions.
- coexistence between one isotropic phase and two nematic phases differing in concentration. This phase behaviour is predicted to occur for long rod-like particles and relatively small depletants.

Both for the critical isotropic–isotropic and nematic–nematic points there exists, at given L/D, a critical end point (cep). This cep identifies the conditions for which a certain phase transition ceases to exist. The occurrence of the three different regimes as a function of the geometrical parameters L/D and q is shown in Fig. 6.8, as marked by the isotropic–isotropic and nematic–nematic critical end points. As a function of L/D the cep values provide critical end curves. In Fig. 6.8 we have marked (symbols) the conditions for which we plotted the phase diagrams in Fig. 6.7.

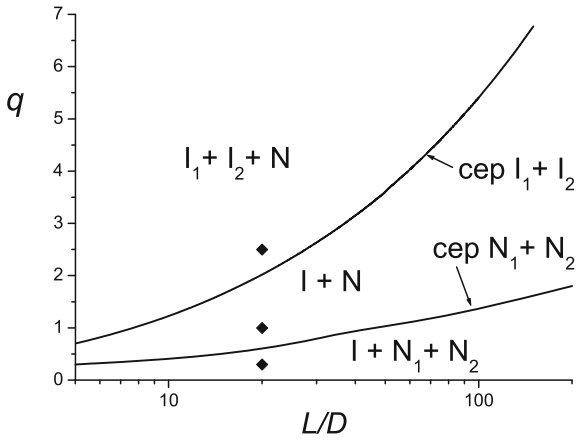

Fig. 6.8 Critical end point curves for isotropic–isotropic and nematic–nematic coexistence in dispersions of hard spherocylinders and penetrable hard spheres as a function of the aspect ratio L/D. Computed using the Gaussian approximation for the orientational distribution function

The three types of phase behaviour are illustrated in Fig. 6.7 in a representation showing colloid volume fraction ϕ_1 against depletant concentration ϕ_2^r. Experimentally, one controls the depletant (for instance non-adsorbing polymer) concentration in the system rather than the polymer concentration (chemical potential) in the reservoir. Using the relation:

$$\alpha = \frac{n_2}{n_2^R} = \frac{\phi_2}{\phi_2^R} \quad n_2 = -\frac{1}{V}\left(\frac{\partial\Omega}{\partial\mu_2}\right)_{N_2,V},$$

phase diagrams in the experimentally accessible (ϕ_1, ϕ_2) can be obtained from the results in the (ϕ_1, ϕ_2^R) plane. The resulting phase diagrams are presented in Fig. 6.7 (lower diagrams).

6.4 I–N Phase Behaviour of Rod-Like Colloids Plus Polymers

6.4.1 Rod-Like Colloids Plus Ideal Polymers

In Sect. 2.2 we discussed the relationship between phs and ideal polymers in the depletion interaction between flat plates and between spheres. It turns out that the depletion thickness δ of ideal polymers in the case of a flat plate is given by

$$\delta = \frac{2R_g}{\sqrt{\pi}},$$

where R_g is the radius of the gyration of the ideal polymer. For spheres with radius R the depletion thickness depends on the ratio

$$q = \frac{R_g}{R},$$

and can be evaluated analytically

$$\frac{\delta}{R_g} = \frac{\left(1 + \frac{6q}{\sqrt{\pi}} + 3q^2\right)^{1/3} - 1}{q}.$$

Note that in the limit $q \to 0$ one recovers, as expected, the flat plate result,

$$\frac{\delta}{R_g} = \frac{2}{\sqrt{\pi}}.$$

The depletion thickness of an ideal polymer around a cylinder requires a numerical calculation (see [21]). For practical purposes an empirical expression was given that describes the numerical data with an accuracy within a percent for $q = 2R_g/D$ values up to 100 [21],

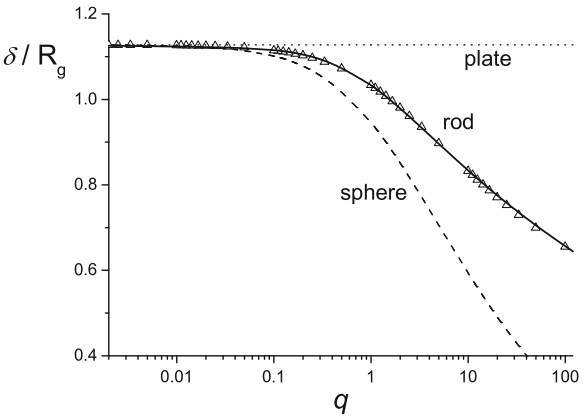

Fig. 6.9 Depletion thickness (normalised with R_g) around a spherocylinder as a function of $q = 2R_g/D$. Data points are exact numerical results. Full curve follows (6.44). For comparison the sphere ($q = R_g/R$) and flat wall results are indicated

$$\frac{\delta}{R_g} = \frac{\left(1 + \frac{4}{\sqrt{\pi}}q - k_1 q^{1.6} + k_2 q^{1.77}\right)^{1/2} - 1}{q}, \tag{6.44}$$

with the constants $k_1 = 0.62133$ and $k_2 = 1.50338$. In Fig. 6.9 the depletion thickness around a cylinder as a function of q is plotted and compared to the flat wall and sphere result. The data points are the numerical results, the curve follows (6.44). It follows that the depletion thickness around a cylinder (rod) is of order of the polymer's radius of gyration for $q < 10$. In the next subsection we extend our approach to also include interacting polymers.

6.4.2 Rod-Like Colloids Plus Interacting Polymers

As we noted in Chap. 4, expression (6.33) just like (4.5) only holds for noninteracting depletants. The general expression for the semi-grand potential for hard spherocylinders plus interacting depletants is

$$\Omega(N_1, V, T, \mu_d) = F_0(N_1, V, T) + \int_{-\infty}^{\mu_d^R} \frac{\partial \Omega}{\partial \mu_d^{R'}} \, \mathrm{d}\mu_d^{R'}, \tag{6.45}$$

with F_0 given by (6.30), see also (4.3). As in Chap. 4 we use here dimensionless free energies for convenience hence $F_0 \to \widetilde{F}_0 = F_0 v_0/VkT$ (so $F_0/NkT = \widetilde{F}_0/\phi$) and $\widetilde{\Omega} = \Omega v_0/VkT$ and we drop the explicit dependencies (N_1, V, T, μ_d) identified above. We restrict ourselves here to polymeric depletants. Analogously to the situation in Sect. 4.3 we then arrive at

$$\widetilde{\Omega} = \widetilde{F}_0 - \frac{1}{2q^3}(3\gamma - 1)\int_0^{\phi_p} \alpha[f]\left(\frac{\partial \widetilde{P}^R}{\partial \phi_p^{R'}}\right) \mathrm{d}\phi_p^{R'}, \tag{6.46}$$

using the free volume theory approximations discussed in Sect. 3.3.

Exercise
Show that $v_0/v_p = (3/2)q^{-3}(\gamma - 1/3)$.

Here we have used

- $\partial\Omega/\partial\mu_p = -N_p = -\alpha\phi_p^R V/v_p$,
- the Gibbs–Duhem relation $\mathrm{d}\mu_p^R = (v_p/\phi_p^R)\mathrm{d}P^R = (v_p/\phi_p^R)(\partial P^R/\partial\phi_p^R)\mathrm{d}\phi_p^R$, and
- $\widetilde{P}_p^R = Pv_p/kT$.

Expression (6.46) may be regarded as a generalized free volume theory (GFVT) semi-grand potential for rods plus interacting polymers. Subsequently, we can specify the quantities α and $\widetilde{P}_p^R$ for interacting polymers.

While the formalism of (6.46) appears simple and does not present any particular problem, the computations of Ω and especially the phase coexistence concentrations are involved. The reason for this is the combination of the numerical integration over the polymer concentration plus the minimisation of Ω for each rod and polymer concentration. Even within the Gaussian approximation, where the minimisation is relatively simple and there are explicit expressions for the variational parameter κ, the calculations are demanding.

For the free volume fraction α of interacting polymers in a suspension of hard spherocylinders we can write down a revised form of (6.39),

$$\alpha[f] = (1 - \phi_1)\exp[-ay_1 - b[f]y_1^2 - c[f]y_1^3], \tag{6.47}$$

with

$$a = \frac{6\gamma}{3\gamma - 1}\left(\frac{2\delta}{D}\right) + \frac{3(\gamma + 1)}{3\gamma - 1}\left(\frac{2\delta}{D}\right)^2 + \frac{2}{3\gamma - 1}\left(\frac{2\delta}{D}\right)^3$$

$$b[f] = \frac{1}{2}\left(\frac{6\gamma}{3\gamma - 1}\right)^2\left(\frac{2\delta}{D}\right)^2 + \left(\frac{6}{3\gamma - 1} + \frac{6(\gamma - 1)^2}{(3\gamma - 1)^2}\rho[f]\right)\left(\frac{2\delta}{D}\right)^3$$

$$c[f] = \frac{2}{3\gamma - 1}\left(\frac{12\gamma(2\gamma - 1)}{(3\gamma - 1)^2} + \frac{12\gamma(\gamma - 1)^2}{(3\gamma - 1)^2}\rho[f]\right)\left(\frac{2\delta}{D}\right)^3.$$

Here δ is the depletion thickness around a spherocylinder mediated by interacting polymers. At a flat wall the depletion thickness due to interacting polymers in a good solvent reads

$$\delta = \frac{1.071R_g}{\sqrt{1 + 3.95\phi_p^{1.54}}}, \tag{6.48}$$

which we used first in Sect. 4.3. To describe the depletion layer at a cylinder we need to incorporate the curvature effect. This is unknown yet for interacting polymers. The curvature effect around a cylinder by ideal polymers is known (6.44) and can be written as

$$\frac{2\delta}{D} = \sqrt{1 + \frac{4}{\sqrt{\pi}} q - 0.62133 q^{1.6} + 1.50388 q^{1.77}} - 1, \tag{6.49}$$

which is plotted in Fig. 6.9.

We now combine the correct polymer concentration dependence (6.48) with the curvature dependence (6.49) and end up with

$$\begin{aligned} \frac{2\delta}{D} = & \left(1 + 2\frac{1.071q}{\sqrt{1 + 3.95\phi_p^{1.54}}} - 0.51215 \left(\frac{1.071q}{\sqrt{1 + 3.95\phi_p^{1.54}}} \right)^{1.6} \right. \\ & \left. + 1.214 \left(\frac{1.071q}{\sqrt{1 + 3.95\phi_p^{1.54}}} \right)^{1.77} \right)^{0.5} - 1. \end{aligned} \tag{6.50}$$

The osmotic compressibility of a polymer solution in a good solvent was given in Sect. 4.3 and reads

$$\frac{\partial \widetilde{P}_p}{\partial \phi_p} = 1 + 3.7422\ \phi_p^{1.31}. \tag{6.51}$$

We do not consider θ-solvent conditions here as in Chap. 4 since the effects of accounting properly for interactions between polymers are, in contrast to the polymers plus spheres case (Chap. 4), not very strong. Therefore we restrict ourselves to the good solvency case.

We can now compute the phase diagrams for hard spherocylinders plus interacting polymers using (6.46) and its ingredients by computing the chemical potential $\widetilde{\mu} = (\partial \widetilde{\Omega}/\partial \phi)$ and pressure $\widetilde{P} = \phi \widetilde{\mu} - \widetilde{\Omega}$,

$$\widetilde{\mu}[f] = \widetilde{\mu}^0[f] + \int_0^{\phi_p^R} g[f] \left(\frac{\partial \widetilde{P}^R}{\partial \phi_p^{R'}} \right) \mathrm{d}\phi_p^{R'}, \tag{6.52}$$

$$\widetilde{P}[f] = \widetilde{P}^0[f] + \int_0^{\phi_p^R} h[f] \left(\frac{\partial \widetilde{P}^R}{\partial \phi_p^{R'}} \right) \mathrm{d}\phi_p^{R'}, \tag{6.53}$$

with g and h given by (3.48) and (3.49) with a, b and c defined below (6.47). Equations 6.52 and 6.53 depend, as specified, on the orientational distribution

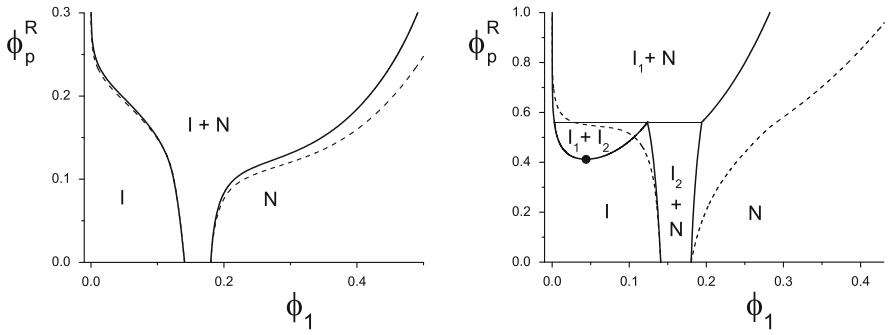

Fig. 6.10 Phase diagrams calculated using generalized free volume theory for spherocylinders with $L/D = 20$ plus interacting polymer chains in a good solvent (*dashed curves*) for size ratios $q = 1$ (*left*) and $q = 2.5$ (*right*) in the reservoir representation. Full curves are FVT results for (noninteracting) penetrable hard spheres as depletants as identical to those in Fig. 6.7. As in Fig. 6.7 the Gaussian form for the ODF was used

function f. Therefore, at each rod concentration (at given polymer concentration) (6.46) has to be minimized numerically to obtain the Gaussian variational parameter κ.

In Fig. 6.10 we plot two illustrative results shown already for noninteracting depletants (penetrable hard spheres) in Fig. 6.7 in the rod volume fraction—polymer reservoir representation for $L/D = 20$, $q = 1$ (left) and $q = 2.5$ (right). The dashed curves are the results for rods plus polymer chains in a good solvent. For $q = 1$ we observe that there is hardly any effect of accounting properly for the interactions between the polymers. This is no surprise since the binodal polymer concentrations are well below the polymer overlap concentration. Also for smaller size ratios (not shown), the effect of interactions between the polymers is negligible and describing polymers as penetrable hard spheres then is adequate. In the right panel of Fig. 6.10 we plot results for $q = 2.5$. In this case there is a more pronounced effect of accounting for the interaction between the polymers. In the good solvent description the widening of the I–N transition is enhanced and the isotropic–isotropic phase coexistence region found for penetrable hard spheres disappeared. As for $q = 1$ only I–N phase coexistence is found and the I–I demixing appears to be metastable. It follows it is only worth while to account for interactions between polymer chains in rod plus polymer mixtures for large q values ($q \gg 1$). In some cases the polymers can indeed be quite large compared to the rod diameter. We do stress that the computations are not straightforward when using the expressions used in this section, even for the Gaussian approximation for the orientational distribution function that we used.

Exercise

The ideal result is $\partial \widetilde{P}_p / \partial \phi_p = 1$. Why are the binodals for interacting polymers in Fig. 6.10 not overall shifted to significantly smaller polymer concentrations due to an increased osmotic pressure caused by interacting polymers?

6.5 Experimental Phase Behaviour of Rod/Polymer Mixtures

We now compare experimental results on the isotropic–nematic transition in mixed suspensions of colloidal rods and polymer with the theory presented in the previous sections.

The experimental results refer to three types of rod-like colloidal particles which in suspension give rise to isotropic–nematic phase separation above a critical concentration:

- stiff virus particles,
- cellulose nanocrystals, and
- colloidal boehmite (γ-$AlOOH$) rods.

The added polymers range from polysaccharides (heparin, chondroitin sulfate, dextran) to polyethylene oxide (PEO) and polystyrene (PS).

6.5.1 Stiff Virus Particles + Polymer

Probably the best examples of rod-like colloidal particles are stiff virus particles such as the plant virus tobacco mosaic virus (TMV) and the bacteriophage feline distemper (fd). In Table 6.1 we summarize the characteristics of TMV and fd, including their linear charge densities at neutral pH.

Suspensions of TMV (see Fig. 6.11, taken from [22]) have long been recognized as an interesting system to study the I–N transition [7]. TMV is a rigid cylindrical particle consisting of a protein shell enclosing double stranded RNA. Fraden et al. [23] measured the coexisting isotropic and nematic concentrations over a wide range of ionic strengths. As the ionic strength increases the concentration of virus in the coexisting phases increases. Without added salt an isotropic phase of 15 mg/ml TMV coexists with a nematic phase of 23 mg/ml, while at an ionic strength of 60 mM the coexisting concentrations are 90 mg/ml in the isotropic phase and 125 g/ml in the nematic phase. Replacing the electrostatic potential between TMV particles with an appropriate effective diameter gives a reasonably good description of the experimentally observed phase boundaries [23].

As early as 1942, Cohen [9] observed, in a study directed at the isolation of TMV from infectious juice, that the addition of 5 mg/ml of the polysaccharide heparin to a dilute TMV suspension (2 mg/ml) in 0.1 M phosphate buffer (pH = 7.1) resulted in the production of needle-shaped paracrystals of length 5–20 μm

Table 6.1 Characteristics of TMV and fd-virus rods

Virus	M (Da)	L (nm)	D (nm)	L/D	Charge density(e/nm)
TMV	4×10^7	300	18	17	-1 to -2
fd	1.6×10^6	880	6.6	133	-5 to -10

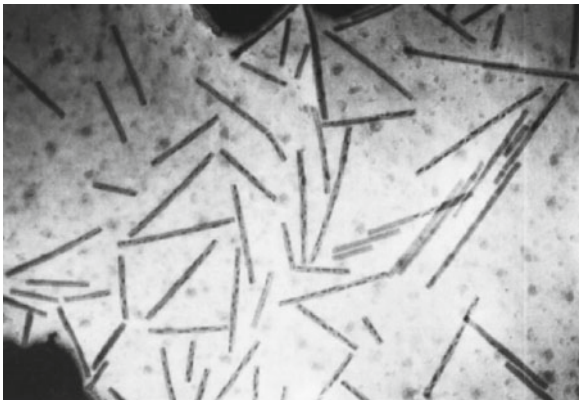

Fig. 6.11 Electron microscopy (EM) micrograph of TMV particles [22]. Reprinted with permission from Urakami et al. [22], Copyright 1999, American Institute of Physics

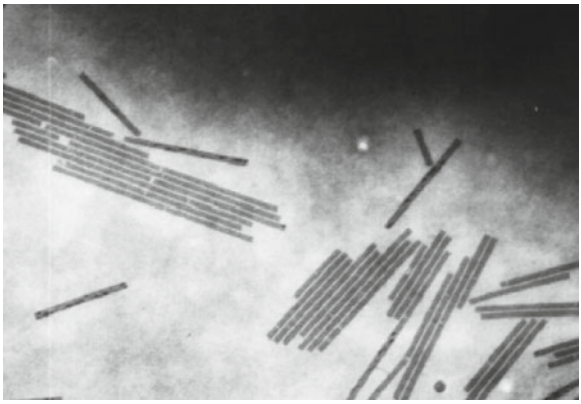

Fig. 6.12 EM picture of ordered TMV particles as induced by added chondroitin sulfate [22]. Reprinted with permission from Urakami et al. [22], Copyright 1999, American Institute of Physics

(see Fig. 1.14 [9]), which may be considered as precursors of the I–N transition [7]. In the 1990s Sano and co-workers [22, 24, 25] added the polysaccharide chondroitin sulfate (Chs) to dilute TMV suspensions with a view to establish the antiviral activity of these polysaccharides. With electron microscopy, Urakami et al. [22] observed that the addition of very low concentrations of Chs (1 mg/ml) to dilute TMV suspensions (1 mg/ml) caused the formation of large raft-like aggregates (see Fig. 6.12). The effect of Chs on infectivity may, according to Sano [24], be ascribed to these raft-like aggregates blocking the decapsulation process of TMV protein on the cell membrane surface. The fact that very low Chs concentrations lead to aggregation of TMV is attributed to the fact that it is a semirigid polymer [22, 25]. This is in agreement with the earlier theoretical and experimental observations that rod-like colloids are very efficient depletion agents, see Sects. 2.4, 5.3 and 5.4.

Leberman [10] observed that addition of 6 mg/ml of the flexible polymer polyethylene oxide (PEO), with molar mass $M = 6\,\text{kDa}$ and radius of gyration

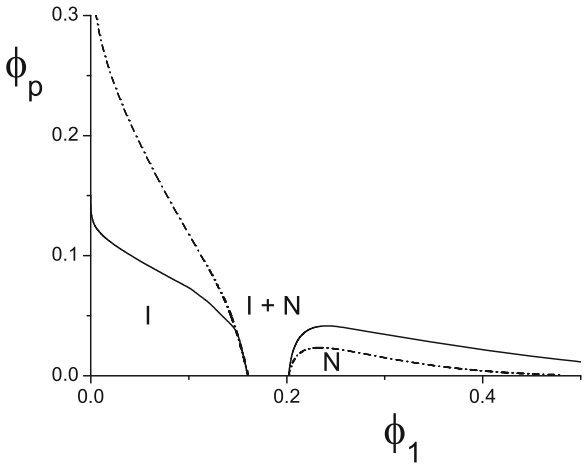

Fig. 6.13 I–N coexistence for hard spherocylinders with $L/D = 17$ mimic TMV plus penetrable hard spheres with size $q = 0.4$ (*solid curves*) and $q = 1.1$ (*dot-dashed curves*)

$R_g = 3.6\,\text{nm}$, to a dilute 1 mg/ml TMV suspension leads to precipitation of TMV, which may be considered as a sign of the I–N transition. To compare this experimental observation with theory we present in Fig. 6.13 the theoretical phase diagram for $L/D = 300/18 = 17$ and $q = 2R_g/D = 2 \cdot 3.6/18 = 0.4$, which are the relevant parameters for this mixed TMV-PEO suspension.

From this calculated phase diagram we observe that at low TMV concentrations a relative polymer concentration $\phi_p = 0.125$ is required to cause I–N phase separation which corresponds in this case to a mass concentration of $c_p = 3\phi_p M/4\pi N_A R_g^3 = 6.4\,\text{mg/ml}$ The agreement with experiment should be considered with care since in the theoretical calculation the electrostatic interactions have not been taken into account.

More extensive measurements on the I–N transition in TMV suspensions with added PEO ($M = 100\,\text{kDa}$, $R_g = 10\,\text{nm}$) were carried out by Adams and Fraden [26]. They observed at TMV concentrations of 20 mg/ml, at which the pure rod system is in the isotropic phase, the first signs of I–N phase separation at 5 mg/ml added PEO and a more definite transition for 10 mg/ml added PEO. To compare this experimental observation with theory we present in Fig. 6.13 also the theoretical phase diagram for $L/D = 17$ (TMV virus as before) but now with $q = 2R_g/D = 2 \cdot 10/18 = 1.1$, which are the relevant parameters for this mixed TMV-PEO suspension. From this calculated phase diagram we observe that at low TMV concentration a relative polymer concentration $\phi_p = 0.25$ is required to cause I–N phase separation which corresponds in this case to a mass concentration of $c_p = 3\phi_p M/4\pi N_A R_g^3 = 10\,\text{mg/ml}$. This is again in reasonable agreement with theory. As mentioned before the electrostatic interactions that certainly play a role have not been taken into account, and therefore the comparison with experiment should be considered with care.

In addition to TMV the liquid crystal phase behaviour of the semirigid cylindrical bacteriophage feline distemper (fd) has been investigated extensively. The

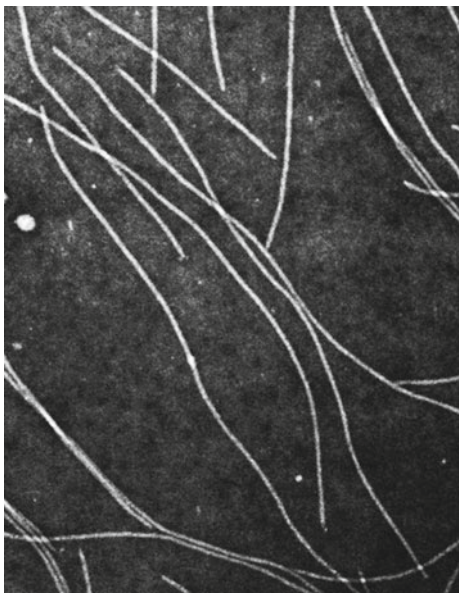

Fig. 6.14 Micrograph of fd-virus particles, reproduced from [27] with permission from the authors

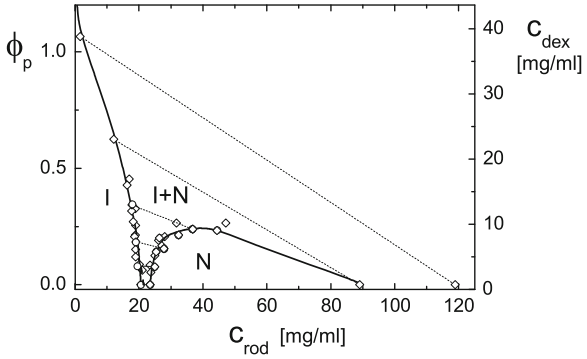

Fig. 6.15 Phase diagrams of dextran/fd-virus mixtures. Data points are measured coexistences. Phase diagram was measured at ionic strength of 100 mM at pH = 8.15 with added 500 kDa dextrans. Redrawn from [31]

fd-virus particle consists of a protein shell wound around a single ribbon of single stranded DNA. In Fig. 6.14 a microscopic image is shown of fd-viruses. Fraden and co-workers [28] measured the coexisting isotropic and (chiral) nematic concentrations over a wide range of ionic strengths. The onset of the (chiral) nematic phase occurs from 10–20 mg/ml of fd as the ionic strength is increased from 1 to 100 mM. Dogic et al. [29, 30] studied the phase diagram of mixed suspensions of fd and dextran and an example is plotted in Fig. 6.15. The used dextran polysaccharide had a molar mass M of 500 kDa and a radius of gyration R_g of 18 nm. The phase diagram with $M = 500$ kDa at ionic strength of 100 mM and pH = 8.15 [31] is redrawn in Fig. 6.15. A clear widening of the I–N transition of the fd-virus rod dispersion takes place upon increasing the dextran concentration.

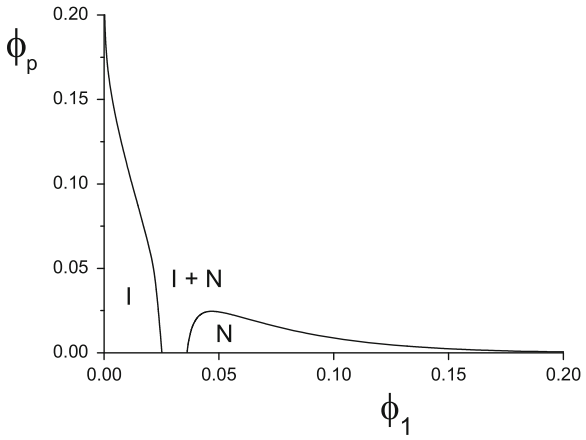

Fig. 6.16 SPT I–N phase coexistence for spherocylinders with $L/D = 133$ plus penetrable hard spheres with $q = 3.3$

At low fd concentrations the I–N transition takes place at a relative polymer concentration $\phi_p = 0.8$, which corresponds to a mass concentration of $c_p = 36\,\mathrm{mg/ml}$. To compare the experimental phase diagram we present in Fig. 6.16 the theoretical phase diagram for $L/D = 880/6.6 = 133$ and $q = 2R_g/D = 2 \cdot 11/6.6 = 3.3$. For more sophisticated theoretical descriptions, see [21, 30].

The overall agreement between theory and experiment (compare Figs. 6.15 and 6.16), while far from perfect, is satisfactory considering that we have not taken into account the electrostatic interactions and the fact that fd is not completely rigid. These factors are known to have a significant effect on the I–N phase behaviour [11].

6.5.2 Cellulose Nanocrystals + Polymer

In 1959, Marchessault et al. [32] reported on the formation of liquid crystals in suspensions of cellulose nanocrystals prepared from cellulose by acid hydrolysis in sulfuric acid (see Fig. 6.17 for a microscopic image of cellulose nanorods).

The study of the isotropic–(chiral) nematic phase transition in suspensions of cellulose nanocrystals has since developed in a blossoming and fruitful field of research (for an overview see [34]). Edgar and Gray [35] studied the effect of 2000 kDa dextran ($R_g = 34\,\mathrm{nm}$) on the phase behaviour of cellulose nanocrystals (average length $L = 110\,\mathrm{nm}$, $D = 10\,\mathrm{nm}$), prepared by acid hydrolysis of cotton filter paper. In Fig. 6.18 we redraw the I–N phase behaviour at low dextran concentrations. Above 7 wt%, suspensions of these cellulose nanocrystals start to phase separate in an isotropic and chiral nematic liquid crystal phase. At 13.3 wt% the relative volume of chiral nematic phase (compared to the total volume) is 79%. This wide biphasic range is a direct consequence of the polydispersity of the cellulose nanocrystals [15, 36] and has been observed in other dispersions containing polydisperse rod-like colloids as well [37, 38].

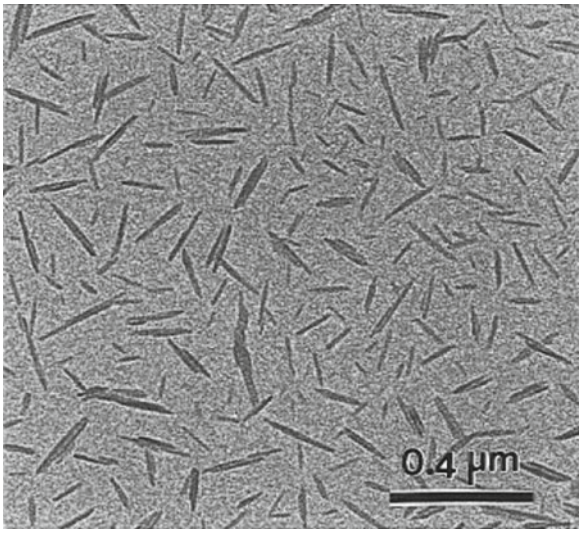

Fig. 6.17 Micrograph of a dried suspension of cellulose nanorods. Picture reprinted from Dong et al. [33] Copyright 1996, with permission from the American Chemical Society

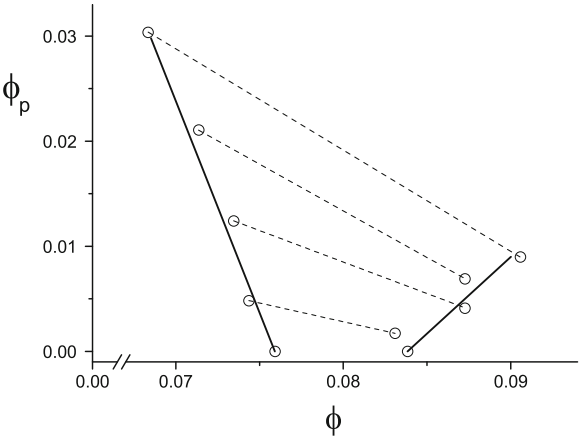

Fig. 6.18 Influence of blue dextran ($R_g/D = 3.4$) concentration (normalised to ϕ_p) on the isotropic–nematic coexistence in rod-like cellulose nanorods ($L/D = 11$) with volume fraction ϕ. Redrawn from Edgar and Gray [35]

When dextran was added to the biphasic region it leads to a significant broadening of the coexistence region and the dextran preferentially partitions in the isotropic phase. These features are in agreement with the theory described in this chapter.

6.5.3 Sterically Stabilized Colloidal Boehmite Rods + Polymer

As mentioned in the introduction of this chapter, suspensions of rod-like inorganic colloids were the first systems in which the I–N transition was observed. In the early 1960s Zocher and Torök [39–41] and Bugosch [42] observed interesting

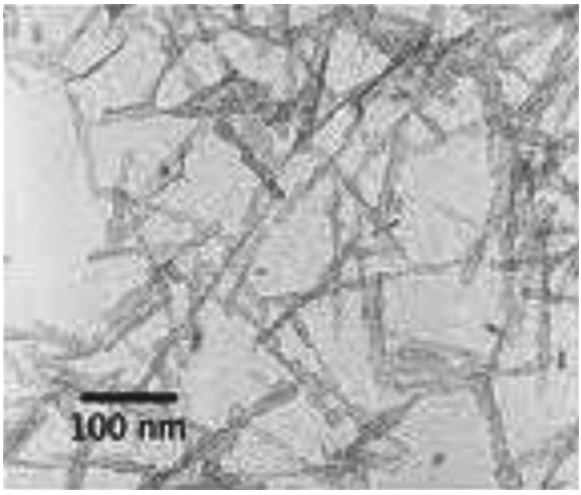

Fig. 6.19 Image of boehmite rods. Picture was kindly offered by J. Buitenhuis, IFF, Forschungszentrum Jülich, Germany

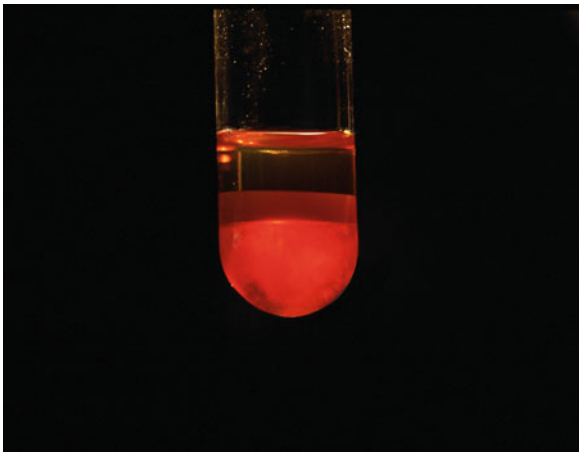

Fig. 6.20 Triphasic I_1 + I_2 + N equilibrium in dispersions of boehmite rods plus polystyrene chains in *ortho*-dichlorobenzene [43]. Picture was kindly offered by J. Buitenhuis, IFF, Forschungszentrum Jülich, Germany

liquid crystal phase behaviour in aqueous dispersions of colloidal boehmite rods, shown in Fig. 6.19.

Later, Buining and Lekkerkerker [37] observed isotropic–nematic phase separation in a dispersion of sterically stabilized boehmite rods, which approximate hard rods, in cyclohexane. Buitenhuis et al. [43] studied the effect of added 35 kDa polystyrene ($R_g = 5.9\,\text{nm}$) on the liquid crystal phase behaviour of sterically stabilized boehmite rods with average length $L = 7.1\,\text{nm}$ and average diameter $D = 11.1\,\text{nm}$ in *ortho*-dichlorobenzene. Different phase equilibria were observed. Two biphasic equilibria dilute isotropic phase I_1 + nematic N, concentrated isotropic phase I_2 + nematic N and a triphasic equilibrium $I_1 + I_2 + N$ (see photo, Fig. 6.20). In this system the boehmite rods are quite polydisperse. Therefore comparison with theory should be done with an approach including polydisperse rods. We further note no $I_1 + I_2$ coexistence was observed experimentally but

rather I_1+gel at high polymer concentrations. This behaviour resembles the behaviour of colloidal sphere/polymer mixtures, see Chap. 4.

6.6 Phase Diagrams of Rod/Polymer Mixtures Including Highly Ordered Phases

In Sects. 6.3 and 6.4 we treated the calculation of the isotropic–nematic phase transition in mixed suspensions of rod-like colloids and flexible polymers. Scaled particle theory (SPT) provided the pressure and chemical potential of the hard spherocylinder reference system and also provided a route for the calculation of the free volume fraction, the quantities required in the FVT calculation of the phase diagram. Depending on L/D and δ/D three types of phase diagrams can be obtained (presented in Fig. 6.7). For intermediate q values a significant broadening of the I–N biphasic region was found. For large q values an isostructural I–I transition arises in addition, while for small q values an additional N–N transition arises. The broadening of the biphasic I–N region and also a triphasic $I_1 - I_2 - N$ equilibrium have indeed been observed experimentally in mixed suspensions of rod-like colloids and flexible polymers [29, 35, 43]. We noted that the theoretical prediction of the N–N transition (which so far has not been observed experimentally in mixed suspensions of rod-like colloids and flexible polymers) should be treated with reservation.

The N–N transition is predicted to occur at quite high volume fractions of rods. At these high volume fractions the N–N transition may be superseded by more highly ordered (liquid) crystal phases such as the colloidal smectic phase. Experimentally, this colloidal smectic phase has been observed [28, 44, 45] in suspensions of monodisperse rods. Simulations confirmed that hard rods can form a thermodynamically stable smectic phase [2–4].

Here we outline how these more highly ordered phases can be accounted for in the phase diagram of mixtures of rod-like colloids and flexible polymers using FVT and follow the work of Bolhuis et al. [46]. The FVT requires the pressure, the chemical potential of the hard spherocylinder (HSC) reference system, and the free volume fraction (cf. (6.40) and (6.41)) as input. The computer simulations presented in [2, 4] contain the necessary information on the pressure and chemical potential of the HSC reference system and in [46] the free volume fraction was obtained using the Widom insertion method [47]. In this method one attempts to insert the polymers (represented by phs with diameter σ) at random positions in the simulation box. The fraction of insertions that does not result in an overlap corresponds to the free volume fraction. The free volume fraction measured in this way at different volume fractions of the HSC was fitted to a functional form similar to the SPT expression for the free volume fraction and used in (6.40) and (6.41). In Fig. 6.21 we present the simulation results for $L/D = 5$ and $q = 1.0$, $q = 0.65$ and $q = 0.15$ obtained in [46] using the method outline above. In the upper graph of Fig. 6.21 ($q = 1$) we compare the results for the $I_1 - I_2$ transition

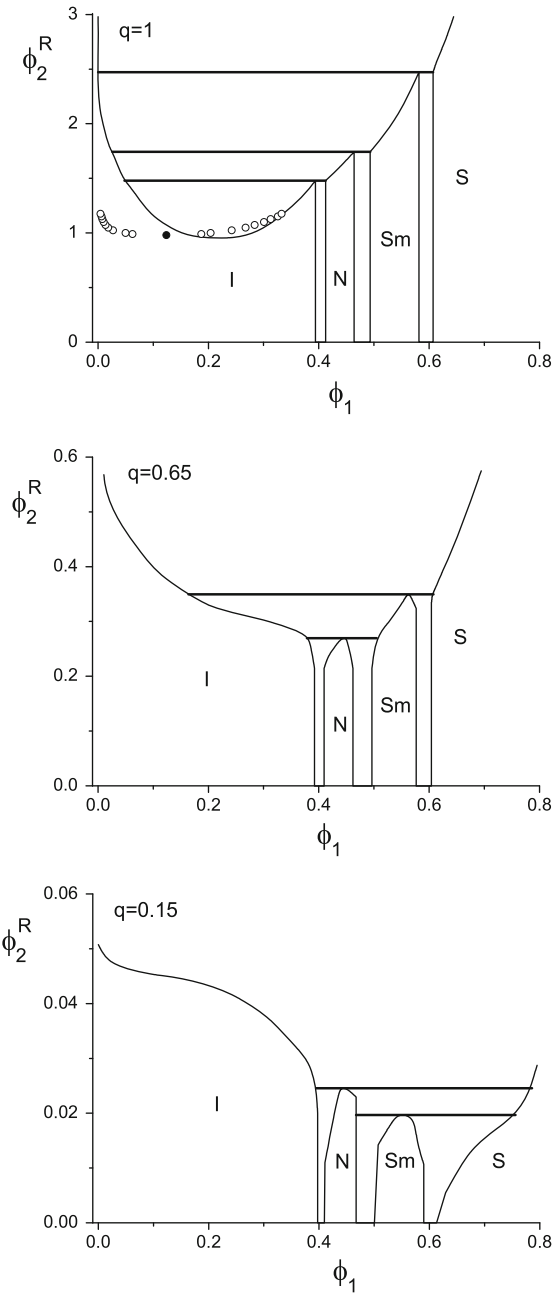

Fig. 6.21 Phase diagrams of hard spherocylinders ($L/D = 5$) mixed with penetrable hard spheres in the reservoir-phs representation for three q-values as indicated. The *curves* were obtained from perturbation theory with simulation results of the reference system. Redrawn and converted from [46]. The *thick straight lines* represent triple coexistences. Data points in the *upper graph* are direct Monte Carlo computer simulation results from [47]. *Filled circle*: critical point, *open circles*: $I_1 + I_2$ coexistence

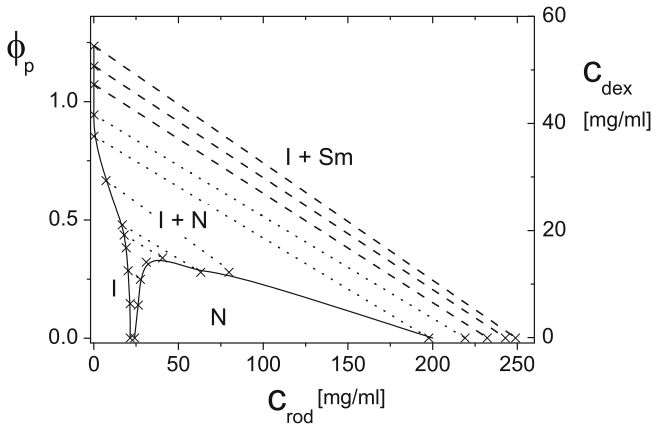

Fig. 6.22 Phase diagrams of dextran/fd-virus mixtures. Data points are measured coexistences. Complete phase diagram of fd-virus plus dextran mixture at ionic strength of 200 mM and pH = 8.10 with added dextrans. Besides the isotropic–nematic coexistence (*dotted coexistence lines*), isotropic–smectic coexistence (*dashed lines*) is found at high polymer and rod concentrations. Redrawn from [49]

with direct simulation results for that transition by Jungblut et al. [48]. The close agreement gives confidence in the FVT results.

From the results for $q = 1$ presented in Figs. 6.7 and 6.8 one expects to find a I_1-I_2 transition followed by I_1-I_2-N, and I_1-N phase equilibria. Including the more highly ordered smectic (Sm) and solid (S) phase leads to additional I_1-N-Sm, I_1-Sm, I_1-Sm-S and I_1-S phase equilibria. Again in agreement with the results presented in Figs. 6.7 and 6.8 for $q = 0.65$ there is only one isotropic phase I, which above a certain volume fraction of rods is in equilibrium with the nematic phase. Including the more highly ordered smectic (Sm) and solid (S) phases, the biphasic I–N phase equilibrium is now, upon increasing the polymer concentration, followed by I–N–S, I–Sm, I–Sm–S and I–S phase equilibria. For $q = 0.15$ we would expect a N_1–N_2 transition on the basis of the results in Figs. 6.7 and 6.8. From Fig. 6.21 we see that this transition is, however, superseded by I–N–S phase equilibrium and followed by a direct I–S transition.

We now compare this with experiment. Dogic [49] extended the earlier work of Dogic and Fraden [29] on mixed suspensions of fd and dextran to higher dextran concentrations. The phase diagram he observed is plotted in Fig. 6.22. Above dextran concentrations of 55 mg/ml the I–N transition is indeed superseded by the I–Sm transition (as predicted, see Fig. 6.23). No observations were reported on the (narrow) triphasic I–N–Sm equilibrium that is expected between the biphasic I–N and I–Sm phase equilibria.

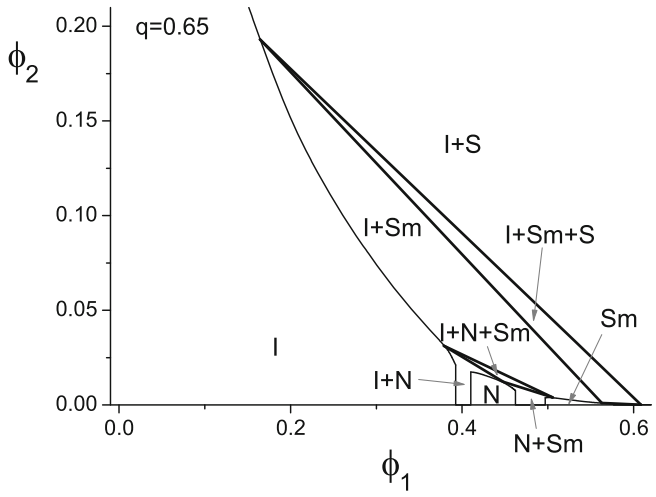

Fig. 6.23 System representation of the phase diagram for $q = 0.65$ of Fig. 6.21 computed using the SPT expression for α

6.7 Concluding Remarks

In this chapter we have concentrated on rod-like colloids plus polymeric depletants. We note that the addition of colloidal spheres to suspensions of rod-like particles also leads to novel interesting phase behaviour. For example theory [50], experiments [51] and simulations [52] demonstrate that the addition of hard spheres to hard spherocylinders leads to a smectic phase consisting of alternating two-dimensional liquid-like layers of rods and spheres. The depletion interaction is increasingly used to control self-assembly of colloidal rods as a pathway towards the engineering of new materials. For example, Baranov et al. [53] showed that by tuning the depletion attraction between hydrophobic colloidal rods of semiconductors dispersed in an organic solvent, these rods could be assembled into 2D-monolayers of close-packed hexagonally ordered arrays directly in solution. Finally, we note that suspensions of rod-like colloids plus polymers show very interesting non-equilibrium phenomena such as the formation of gels and glasses. Also the effect of shear on these systems leads to fascinating non-equilibrium phase behaviour. These topics are beyond the scope of this book and we refer the interested reader to [1, 54], where these phenomena are treated and discussed.

References

1. M.J. Solomon, P.T. Spicer, Soft Matter. **6**, 1391 (2010)
2. S.C. McGrother, D.C. Williamson, G. Jackson, J. Chem. Phys. **104**, 6755 (1996)
3. D. Frenkel, H.N.W. Lekkerkerker, A. Stroobants, Nature **332**, 822 (1988)
4. P.G. Bolhuis, D. Frenkel, J. Chem. Phys. **106**, 666 (1997)

5. P.G. De Gennes, J. Prost, *The Physics of Liquid Crystals*. (Oxford University Press, Oxford, 1974)
6. H. Zocher, Z. Anorg. Chem. **147**, 91 (1925)
7. F.C. Bawden, N.W. Pirie, J.D. Bernal, I. Fankuchen, Nature **138**, 1051 (1936)
8. L. Onsager, Ann. NY. Acad. Sci. **51**, 627 (1949)
9. S.S. Cohen, J. Biol. Chem. **144**, 353 (1942)
10. R. Leberman, Virology, **30**, 341 (1966)
11. G.J. Vroege, H.N.W. Lekkerkerker, Rep. Progr. Phys. **55**, 1241 (1992)
12. J. Herzfeld, A.E. Berger, J.W. Wingate, Macromolecules **17**, 1718 (1984)
13. H.N.W. Lekkerkerker, P. Coulon, R. van der Haegen, R. Deblieck, J. Chem. Phys. **80**, 3427 (1984)
14. R. van Roij, Eur. J. Phys. **26**, S57 (2005)
15. T. Odijk, H.N.W. Lekkerkerker, J. Phys. Chem. **89**, 2090 (1985)
16. T. Odijk, Macromolecules. **19**, 2313 (1986)
17. M. Franco-Melgar, A.J. Haslam, G. Jackson, Mol. Phys. **106**, 649 (2008)
18. P. Van der Schoot, T. Odijk, J. Chem. Phys. **97**, 515 (1992)
19. M.A. Cotter, J. Chem. Phys. **66**, 1098 (1977)
20. H.N.W. Lekkerkerker, A. Stroobants, Il Nuovo Cimento. D **16**, 949 (1994)
21. R. Tuinier, T. Taniguchi, H.H. Wensink, Eur. Phys. J. E. **23**, 355 (2007)
22. N. Urakami, M. Imai, Y. Sano, M. Tasaku, J. Chem. Phys. **111**, 2322 (1999)
23. S. Fraden, G. Maret, D.L.D. Casper, R.B. Meyer, Phys. Rev. Lett. **63**, 2068 (1989)
24. Y. Sano, Macromol. Symp. **99**, 239 (1995)
25. M. Imai, N. Urakami, A. Nakamura, R. Takada, R. Oikawa, Y. Sano, Langmuir. **18**, 9918 (2002)
26. M. Adams, S. Fraden, Biophys. J. **74**, 669 (1998)
27. J.A. Levy, H. Fraenkel-Conrat, R.A. Owens, Virology. (Prentice Hall, Englewood Cliffs, 1994)
28. Z. Dogic, S. Fraden, Phys. Rev. Lett. **78**, 2417 (1997)
29. Z. Dogic, S. Fraden, Phil. Trans. R. Soc. Lond. A, **359**, 997 (2001)
30. Z. Dogic, K.R. Purdy, E. Grelet, M. Adams, S. Fraden, Phys. Rev. E. **69**, 051702 (2004)
31. Z. Dogic, D. Frenkel, S. Fraden, Phys. Rev. E. **62**, 3925 (2000)
32. R.H. Marchessault, F.F. Morehead, N.M. Walters, Nature. **184**, 632 (1959)
33. X.M. Dong, T. Kimura, J.F. Revol, D.G. Gray, Langmuir. **12**, 2076 (1996)
34. M. Roman, W.T. Winter, TAPPI Techn. Papers. **06**(ANO09), 5 (2006)
35. C.D. Edgar, D.G. Gray, Macromolecules, **35**, 7400 (2002)
36. G.J. Vroege, H.N.W. Lekkerkerker, J. Phys. Chem. **97**, 3601 (1993)
37. P.A. Buining, H.N.W. Lekkerkerker, J. Phys. Chem. **97**, 11510 (1993)
38. Z.X. Zhang, van J.S. Duijneveldt, J. Chem. Phys. **124**, 154910 (2006)
39. H. Zocher, C. Torök, Kolloid Z. **170**, 140 (1960)
40. H. Zocher, C. Torök, Kolloid Z. **173**, 1 (1960)
41. H. Zocher, C. Torök, Kolloid Z. **180**, 41 (1962)
42. J. Bugosh, J. Phys. Chem. **65**, 1791 (1961)
43. J. Buitenhuis, L.N. Donselaar, P.A. Buining, A. Stroobants, H.N.W. Lekkerkerker, J. Colloid Interface Sci. **175**, 46 (1995)
44. G. Oster, J. Gen. Physiol. **33**, 445 (1950)
45. U. Kreibig, C. Wetter, Z. Naturforsch. **35**, 750 (1980)
46. P.G. Bolhuis, A. Stroobants, D. Frenkel, H.N.W. Lekkerkerker, J. Chem. Phys. **107**, 1551 (1997)
47. B. Widom, J. Chem. Phys. **39**, 2808 (1963)
48. S. Jungblut, R. Tuinier, K. Binder, T. Schilling, J. Chem. Phys. **127**, 244909 (2007)
49. Z. Dogic, Phys. Rev. Lett. **91**, 165701 (2003)
50. T. Koda, M. Numajiri, S. Ikeda, J. Phys. Soc. Jpn. **65**, 3551 (1996)
51. M. Adams, Z. Dogic, S.L. Keller, S. Fraden, Nature. **393**, 349 (1998)
52. Z. Dogic, D. Frenkel, S. Fraden, Phys. Rev. E **62**, 3925 (2000)
53. D. Baranov, A. Fiore, M. van Huis, C. Giannini, A. Falqui, U. Lafont, H. Zandbergen, M. Zanella, M. Cingolani, L. Manna (2010) Nano Lett. 10:743
54. M.P. Lettinga, J.K.G. Dhont, J. Phys.: Condens. Matter. **16**, S3929 (2004)

Appendix A
Statistical Mechanical Derivation of the Free Volume Theory

Here we present a statistical mechanical derivation of the grand potential. According to statistical mechanics (see for instance T.L. Hill, *An Introduction to Statistical Thermodynamics*. Addison-Wesley, New York, 1962) the grand potential is given by

$$\Omega(N_c, V, T, \mu_d) = -kT \ln \Xi(N_c, V, T, \mu_d), \tag{A.1}$$

where Ξ is the grand canonical partition function

$$\Xi = \sum_{N_d=0}^{\infty} \exp(\mu_d N_d/kT)\, Q(N_c, V, T, N_d). \tag{A.2}$$

Here Q is the canonical partition function

$$Q = \frac{1}{\Lambda_c^{3N_c}\Lambda_d^{3N_d} N_c! N_d!} \int \exp[-(U_c + U_{cd})/kT] \quad \mathrm{d}\mathbf{R}^{N_c}\mathrm{d}\mathbf{r}^{N_d}, \tag{A.3}$$

where U_c is the interaction between the N_c hard spheres and U_{cd} the interaction between the N_c hard spheres and the N_d (depletants). The latter term in the interaction limits the integration over the position of the penetrable hard spheres to the free volume which is a function of the positions $\mathbf{R}^{N_c}$ of the N_c hard spheres. This leads to

$$Q = \frac{1}{\Lambda_c^{3N_c}\Lambda_d^{3N_d} N_c! N_d!} \int \exp[-U_c/kT] \quad \langle V_{\mathrm{free}} \rangle^{N_d} \mathrm{d}\mathbf{R}^{N_c}. \tag{A.4}$$

Substituting (A.4) in (A.2) and taking into account that

$$\sum_{N_d=0}^{\infty} \frac{\exp(\mu_d N_d/kT)\langle V_{\mathrm{free}} \rangle^{N_d}}{\Lambda_d^{3N_d} N_d!} = \exp[P^R \langle V_{\mathrm{free}} \rangle / kT], \tag{A.5}$$

where we have used that the right hand side of (A.5) is just the grand canonical partition of the penetrable hard spheres with chemical potential μ_d in a volume $\langle V_{\text{free}} \rangle$, we obtain

$$\begin{aligned} \Xi &= \frac{1}{\Lambda_c^{N_c} N_c!} \int \exp[-(U_c - P_d^R \langle V_{free} \rangle)/kT] \quad \mathrm{d}\mathbf{R}^{N_c} \\ &= Q(N_c, V, T) \left\langle \exp\left(\frac{P^R \langle V_{\text{free}} \rangle}{kT} \right) \right\rangle_0, \end{aligned} \tag{A.6}$$

where $Q(N_c, V, T)$ is the canonical partition function of the N_c hard spheres and the pointed brackets with subscript 0 indicate an average over the unperturbed configurations of the hard spheres. Substitution of (A.6) in (A.1) leads to

$$\begin{aligned} \Omega &= -kT \ln Q(N_c, V, T) - kT \ln \left\langle \exp\left(\frac{P^R \langle V_{\text{free}} \rangle}{kT} \right) \right\rangle_0 \\ &= F_0(N_c, V, T) - kT \ln \left\langle \exp\left(\frac{P^R \langle V_{\text{free}} \rangle}{kT} \right) \right\rangle_0. \end{aligned} \tag{A.7}$$

This expression for Ω is exact but, from a point of view of calculating it, difficult to handle. To make progress we replace the average of the exponent by the exponent of the average and obtain the following approximate expression for the grand potential

$$\overline{\Omega} = F_0(N_c, V, T) - P^R \langle V_{\text{free}} \rangle_0 \tag{A.8}$$

This is precisely expression (3.24) we obtained from the thermodynamic integration route using the approximation (3.22). Using the well-known result that for an arbitrary probability distribution the following inequality holds

$$\langle \exp(x) \rangle \geq \exp(\langle x \rangle)$$

it follows immediately that the approximate grand potential obeys the inequality

$$\overline{\Omega} \geq \Omega. \tag{A.9}$$

We could have surmised this result also from our thermodynamic integration approach. As addition of depletants leads to some "clustering" of the hard spheres one expects that

$$\langle V_{\text{free}} \rangle \geq \langle V_{\text{free}} \rangle_0$$

and hence using the approximation (3.22) in the integration (3.18) leads to an approximate grand potential that is larger than the exact one. The statistical mechanical derivation presented above presents a rigorous proof of this supposition.

Index